Structural health monitoring of onshore wind turbine foundations

Jack McAlorum

A thesis submitted for the degree of Doctor of Philosophy to the

University of Strathclyde

Department of Electronic and Electrical Engineering

December 2018

Declaration

This thesis is the result of the author's original research. It has been composed by the author and has not been previously submitted for examination which has led to the award of a degree.

The copyright of this thesis belongs to the author under the terms of the United Kingdom Copyright Acts as qualified by University of Strathclyde Regulation 3.50. Due acknowledgment must always be made of the use of any material contained in, or derived from, this thesis.

Signed:

Date:

Acknowledgments

Thanks firstly to my supervisor Pawel for this fantastic opportunity. You believed in me from the start and supplied constant support and mentorship throughout the entirety of the research.

Also thanks to senior researchers, Grzegorz and Marcus, who made me feel welcome and were always available to help and provide guidance. To my fellow doctorate students, Iain and Tim, thank you for simultaneously experiencing this great ordeal with me.

A special thanks to my parents, Alison and Paul and my brother Ben, for the encouragement and belief you provided throughout the entirety of my studies. Not to mention providing me with a place to live and food for my belly.

The biggest thanks to my fiancè, Ashleigh. For keeping me grounded and sane, for putting up with my stress induced panics and for giving me a reason to continually push myself to achieve the best life for the future. I only hope I have made you proud and can repay you for all the waiting around!

Finally, thanks to you for picking this up, whether by choice, or because you are required to for assessment purposes...you are the best!

Abstract

Ongoing concern regarding humanity's impact on the environment and declining fossil fuel reserves has inspired a global adoption and continual support of renewable power generation. Onshore wind is a major contributor to the world's renewable capacity. Ensuring or possibly extending the lifetime of current assets is key in gaining the most efficient power generation. Structural health monitoring (SHM) systems can be employed to identify the health state of a structure and provide information regarding lifetime. Many such systems are already incorporated into various infrastructure.

Regarding onshore wind turbines, the supporting concrete foundations represent an integral structural feature, where failure could cause collapse of the entire turbine. Severe cracks on such foundations are, therefore, of great concern to turbine operators. SHM of such foundation cracks may provide a more detailed insight into the lifetime of the turbine as a whole. Sub-surface cracks are conventionally monitored using intermittent excavation and visual inspections that are carried out during turbine downtime. Other methods, such as fracture mechanics, consider the critical failure point of a cracked specimen and fail to provide an indication of increasing severity. Research presented in this thesis demonstrates the application of optical fibre Bragg grating (FBG) strain sensors for crack displacement monitoring on an operational wind turbine foundation. The primary original contribution to knowledge of this work is the development of a novel methodology in order to categorize and quantify crack deterioration measured by subsurface crack displacement sensors deployed on an operational asset with visually severe cracks. Results from this methodology should help decision making procedures in regards to acceptable crack displacements, repairs and the overall lifetime of the turbine.

Accompanying investigation into the effectiveness of epoxy and metallic bonding for FBG attachment demonstrates that purely metallic bonding may provide an improved sensor design. Particularly, a humidity dependence was observed in industry standard epoxies in the form of swelling, with the metallic bonding technique immune to such effects but producing similar performance for strain measurement during direct static and fatigue experimentation. To validate industrial results and further test metallic bonding of FBGs, a unique low-cost small-scale fatigue testing machine is designed and demonstrated for cracked concrete beam fatigue tests.

Transitioning from reactive to preventative methods for initial or additional damage is an important topic and could potentially constitute most future SHM work, including for wind turbine foundations. Prediction methodologies are explored using lab test-benches at this early stage, presenting promise for future application in SHM for preventing critical events.

Further development of the sensors, deterioration methodology and prevention techniques as part of a limit alert system for cracks in an onshore wind turbine foundations is suggested.

Contents

List of Figures

List of Tables

Glossary of Abbreviations

FBG	Fibre Bragg grating
SHM	Structural health monitoring
CO_2	Carbon dioxide
PV	Photovoltaic
RC	Reinforced concrete
WDM	Wavelength division multiplexing
TDM	Time division multiplexing
FWHM	Full width at half maximum
FC	Ferrule connector
SCADA	Supervisory control and data acquisition
PSD	Power spectral density
FFT	Fast Fourier transform
MSS	Magnetic stainless steel
RH	Relative humidity

Chapter 1:   Thesis introduction

Designed service lifetime of an engineering structure is initially evaluated using complex simula-
tions, calculations, models and experimentation, accomplished by using known mechanical and
material properties and site-specific environmental data. As structures age and inevitably incur
damage, this predicted lifetime comes into question and encourages further investigation. Struc-
tural health monitoring (SHM) is the act of carrying out this investigation by applying distinct
systems and methodologies, providing specific data regarding the current health state of the struc-
ture [1]. Over time, SHM has progressed to applying sensors to monitor the features in question,
rather than the conventional visual inspections. Sensors provide many advantages over visual
inspection, including: continuous monitoring, accuracy and specificity, reliable cost, dynamical in-
formation (with high sampling rate) and are generally less intrusive. Some potential disadvantages
include: higher initial costs, high complexity, required analysis methodology and maintenance [2].
Commonly, SHM systems incorporate strain measurement devices which can be either electrical-
or optical-based, with the latter becoming popular over the last decade. SHM can eventually in-
form decision making tools to determine the best course of action for the structure, which could
constitute a repair or replacement of specific components, immediate decommissioning of the entire
structure, or further lifetime extension procedures [3].

In the last few decades there has been significant investment in renewable power generation
methods due to the realization of human environmental impact and dwindling fossil fuel reserves.
Onshore wind power generates a significant share of the worlds renewable power [4]. Ensuring a
long or extended lifetime of these assets will improve efficiency, increase profit and ensure a lower
environmental footprint. Such assets would benefit from SHM activities. To date, the majority of
SHM systems applied to onshore wind turbines focus on components with higher failure rates [5].
Foundations, despite presenting the most severe failure consequences, are not subjected to large
monitoring campaigns.

Concrete foundations will inevitably crack, the most severe of which are promptly repaired.
Turbine operators may request anonymity regarding cracking of foundations, meaning issues are
scarcely disclosed. However, reports such as by Elforsk [6], Currie et al. [7, 8] and Miceli [9]
demonstrate that such an issue exists in a number of existing foundations. Additionally, cracking
is observed in numerous forms, such as at the embedded ring interface, on the concrete pedestal
or on subsurface faces. Visual inspections are used to assess the severity and deterioration of
cracks by periodically observing the width during turbine downtime. Overall structural impact
of cracks is unknown as monitoring is not carried out during operation. However, the general
ramifications of cracks in concrete, such as weakening the integrity of the cracked section, water
ingress to steel, diminishing aesthetics and increased maintenance costs will apply to cracks in
onshore wind turbine foundations. Regarding the increased maintenance costs - the economic

impact of cracks will depend on the severity and deterioration of said crack. An outcome of the SHM system may be to provide information to an economic model that defines the cost-benefit on repairing the crack immediately, or to delay repair. Cracks are also known to displace during loading; therefore, measuring crack width during turbine downtime may be inadequate for identifying particular damage states. Monitoring crack displacements continuously during normal operational conditions over a long-term period may provide a more informative view of crack severity state and the rate of deterioration. Current crack monitoring campaigns provide insufficient evaluation of deterioration and focus exclusively on observable crack widths. Cracks can undergo transitional, as well as varying displacements during turbine operation, both of which have not previously been considered. Fracture mechanics is a related established field; however, the methods focus on the point of fracture and do not allow observations of any progression towards the fracture. Therefore, a methodology that monitors the multiple crack features in a progressive manner is desired for SHM of cracks in an onshore wind turbine foundation.

Conventional SHM practices remain mostly reactive, providing information subsequent to an event occurring. In most cases, this is sufficient for the operator to restrict further issues. Progressing from detection to prevention is of particular interest to the industry. Prediction methodologies are developed and used in many other industries, such as finance [10], meteorology [11], medicine [12] and technology [13]. Potentially, such methods could be evolved to be used in SHM. Combining such predictive techniques with the previously discussed deterioration methodology could provide the ability to predict and prevent a critical degradation from occurring.

The objective of this project is to design and implement sensors on to an onshore wind turbine foundation with visibly degrading cracks in order to monitor crack displacements over time. Sensors were specifically designed to segregate and measure independent crack displacement modes. Deterioration of a crack was defined based on the initial characteristics observed in the displacement data and a methodology was developed to extract this information. The work described in this thesis can be used to further develop SHM practices for cracks in onshore wind turbine foundations, but could also be evolved for application to cracks in other structures. Predictive methodologies are explored in experimental environments related to SHM applications. Future work will be more focused towards applying these predictive methods to real-world data in an attempt to predict a known deterioration event, previously detected using the deterioration methodology. Both methods may work in conjunction to prevent further crack deterioration.

1.1 Justification for research

In affiliation with industrial partners, it is desired to monitor cracks in an onshore wind turbine foundation. The foundations in question consist of visually severe cracks appearing relatively early in their lifetime and, from visual inspections, are perceived to be degrading. With the required lifetime of around 20 years for a turbine, ensuring the foundations are safe to continue operation

is of the utmost importance. Visual inspections are carried out during turbine downtime and do not provide information to confirm crack severity and behaviour during operation. A sensor system is proposed to continuously monitor crack displacements, including during operation. A displacement sensor can be expressed as a strain measuring device fixed between two linear points at a known distance apart. Many devices are available: optical sensors, fibre Bragg gratings (FBG) in particular, present an electromagnetically immune, small sized and multiplexable strain measuring device. FBGs are well researched and have previously been successfully applied to concrete structures for crack initiation detection purposes [14]. Adaptation of the FBG sensor for crack displacement monitoring of multiple modes is desired.

At present, no methodology exists that quantifies crack deterioration. Fracture mechanics is a related field, but focuses on establishing the point of criticality of a crack where fracture occurs. In this work, the cracks are required to be repaired prior to this point, so a methodology of monitoring the progress towards fracture is more suitable. Establishing acceptable crack displacement limits and comparing to sensor measurements may also provide correct and fully justified repair intervals to the operator, should this information be required.

Justification can be summarized by important research questions, based on the discussion above:

- What are the conventional strain sensing options and should they be used as opposed to a bespoke design?

- What sensor systems are currently applied in SHM applications as a whole?

- What sensor systems are currently applied for concrete crack monitoring, if any?

- Are any systems already applied for concrete crack monitoring in an onshore wind turbine foundation?

- How do foundation cracks behave under turbine operational conditions compared to downtime?

- Can a sensor be designed to segregate between independent crack displacement modes?

- How can deterioration of a crack be quantified?

- Can crack deterioration be prevented/predicted?

Work in this thesis attempts to answer these research questions by initially performing a thorough literature review of real-world applications of SHM. An investigation into cracks in an onshore wind turbine foundation follows, including installation of sensors and subsequent design and implementation of a unique methodology for quantifying crack deterioration. Results merited further investigation into sensor design and experimental work replicating real-world conditions - which includes the design of a customisable fatigue testing machine. Prevention is also explored in the form of prediction methodologies applied to a test-bench more related to SHM.

1.2 Research contribution

The contributions to knowledge by the research in this thesis can be outlined as follows:

- Classification of the SHM sensor subsystem to provide a more productive process when analyzing real-world applications.

- An extensive literature review considering the sensor systems applied in a broad spectrum of real-world applications before focusing on applications to onshore wind turbines and, in particular, concrete foundations. This produced key learning points to advise on a more effective future sensor design and implementation.

- Design of a subsurface crack displacement FBG sensor capable of distinguishing between independent displacement modes using trigonometric equations.

- Implementation of sensors to surface cracks in an onshore wind turbine foundation, monitoring during operational conditions.

- Insight into previously overlooked instantaneous frequent loading during start-stop procedures causing rapid transitions in tower strain and crack displacements that may not be considered during initial foundation design.

- Novel methodology for categorizing and quantifying crack deterioration in an onshore wind turbine foundation, based on observed operational displacements. Variation in instant displacements are represented by "Reactive" deterioration. Changes in the rest state (dead load) is represented by "Permanent" deterioration. Deviations from a predicted value during rated operation is represented by "Behavioural" deterioration.

- Demonstration of the negative effects of humidity to industrial grade strain gauge epoxies and the design of a humidity-immune, purely metallic-bonded attachment method for FBG strain gauges.

- Design and demonstration of a low-cost small-scale fatigue testing machine capable of an adjustable shape, frequency and amplitude loading cycle for extensive long-term fatigue testing of materials, sensors and structures. This includes thorough FEM modelling, long-term life validation experimentation and commercial evaluation.

- Validation of metallic-bonded FBG strain gauge for concrete crack displacement monitoring.

- Implementation and development of prediction methodology in two unique test-benches, demonstrating the potential of predicting critical transitions for SHM applications.

1.3 Publications

The following outlines publications from this PhD research:

Journal

- [15] J. McAlorum, M. Perry, G. Fusiek, P. Niewczas, I. McKeeman and T. Rubert, "Deterioration of cracks in onshore wind turbine foundations", *Engineering Structures*, 167, May 2018.

- [16] J. McAlorum, T. Rubert, G. Fusiek, P. Niewczas and G. Zorzi, "Design and demonstration of a low-cost small-scale fatigue testing machine for multi-purpose testing of materials, sensors and structures", *MDPI Machines*, 6, July 2018.

Conference

- [17] J. McAlorum, I. McKeeman, M. Perry, L. Clayburn and P. Niewczas, "Predicting Freeze-Thaw Damage using Tipping Point Analysis of Strain Data", *Fourth international conference on smart monitoring, assessment and rehabilitation of civil structures*, Zurich, Switzerland, 2017.

- [18] J. McAlorum, T. Rubert, G. Fusiek, I. McKeeman, L. Clayburn, M. Perry and P. Niewczas, "Comparison of epoxy and braze-welded attachment methods for FBG strain gauges", *16th IEEE International Conference on Sensors*, Glasgow, UK, 2017.

- J. McAlorum, G. Fusiek, T. Rubert and P. Niewczas, "Concrete fatigue experiment for sensor prototyping and validation of industrial SHM trials", *Instrumentation and Measurement Technology Conference (I2MTC)*, New Zealand, 2019, Under Review.

Co-authored

- [19] M. Perry, J. McAlorum, G. Fusiek, P. Niewczas and T. Rubert, "Crack monitoring of operational wind turbine foundations", *MDPI Sensors*, August 2017.

- [20] M. Perry, G. Fusiek, P. Niewczas, T. Rubert and J. McAlorum, "Wireless Concrete Strength Monitoring of Wind Turbine Foundations", *MDPI Sensors*, December 2017.

- [21] T. Rubert, M. Perry, G. Fusiek, J. McAlorum, P. Niewczas, A. Brotherston and D. McCallum, "Field Demonstration of Real-time Wind Turbine Foundation Strain Monitoring", *MDPI Sensors*, December 2017.

- [22] G. Fusiek, T. Rubert, P. Niewczas, J. McAlorum and M. Perry, "Preliminary characterization of metal-packaged fiber Bragg gratings under fatigue loading", *Instrumentation and Measurement Technology Conference (I2MTC)*, Turin, Italy, 2017.

1.4 Thesis overview

The thesis begins with a general outline of commercial renewable technologies and their principal operational procedures, emphasizing the importance of such technologies for the future of the world. Specific contributions of each technology are discussed, providing insight into the great influence of onshore wind power and the motivation for ensuring each assets lifetime is reached and/or extended.

Following this, Chapter 3 describes the nature of concrete, beginning with the manufacturing and distribution processes. Basic material mechanics are introduced before considering the complex concrete cracking phenomenon. Cracks have a variety of physical appearances, which are dependent on the initiation source. Fracture mechanics is highlighted as an established field for studying the critical failure point of cracked materials. Development of a unique methodology is suggested to consider the deterioration of cracks below critical limits and to provide an indication of increasing severity.

Chapter 4 initially explains SHM as a whole, based on previously defined categorisation considering a systems capabilities. Three independent subsystems in SHM are introduced, of which the sensing system will be thoroughly examined. The large range of sensor technologies appropriate for SHM, strain measurement in particular are then debated, considering the benefits and flaws of each with regard to a future crack displacement monitoring implementation.

An extensive review of real-world SHM sensor applications is presented in Chapter 5. Multiple factors are considered in order to classify the SHM sensor subsystem. These are examined during the review of reported applications. The review is separated into types of civil structures, beginning with a broad spectrum of the most commonly monitored before focusing on wind turbines and specifically considering previous work on foundation monitoring. In each case, the sensor system is described and categorized with any benefits, flaws or other particular aspects to be retained for future sensor system design for crack monitoring.

Chapter 6 presents the industrial application of a sensor system for monitoring crack displacements in an onshore wind turbine foundation. Initially, the particular foundation design in this work along with the model equations for tower strains based on wind loading are presented. The unique crack formations are discussed, outlining the decision making behind the choice of cracks to monitor. Design, fabrication and installation of the long-gauge, crack displacement sensor used is detailed. Trigonometric equations are derived in order to segregate between two crack modes: opening and tearing. Sensor measurements are verified using previously described loading model equations. Deterioration of cracks is classified into three distinct characteristics, based on operational displacements of the cracks. Methodology for quantifying deterioration is applied to the sensors over the initial 9 month period.

Following the results from the industrial application, further investigation into the sensor design for crack displacement monitoring is warranted. Chapter 7 initially introduces a pure metallic-

bonded fibre Bragg grating (FBG) as an improved sensor design and is compared to epoxy attachment in three direct experimental procedures: static, fatigue and humidity. To validate industrial results and test the new sensor in direct crack displacement measurements, a machine for fatigue testing of concrete specimens is demonstrated. This low-cost machine will provide the capability of long-term testing and thorough investigation prior to any future applications. A single pre-cracked concrete specimen, instrumented with both sensor designs, was then tested in the bespoke machine. Results validated the conclusions from Chapter 6 as a more severe crack did not deteriorate under similar loading. The metallic-bonded sensor was shown to be suitable for crack displacement monitoring applications.

In the penultimate Chapter 8, focus on the progression from reactive to preventative SHM in the form of possible prediction methodology is presented. Tipping point analysis is a promising area of time-series based tools that can detect dynamic changes occurring in some physical systems prior to a critical point. Two particular tools are explored using two independent custom test-benches, developing towards the potential application to crack displacement monitoring for predicting the onset of damage or deterioration.

Research carried out in this thesis is concluded in Chapter 9, isolating key findings and possible avenues for improvement and future work in crack deterioration of onshore wind turbine foundations.

Chapter 2:   Renewable power

2.1   Greenhouse effect and fossil fuel reserves

Joseph Fourier during the 1820s calculated from the size of the Earth and distance to the Sun, that such an object should be colder. This ultimately led to the discovery of the commonly phrased "greenhouse effect". Solar energy is able to penetrate the Earth's atmosphere, heating the planet and surrounding gases. Some gases within the atmosphere, known as "greenhouse gases", later emit this heat in all directions, including back towards the earth. Primarily, "greenhouse gases" include: carbon dioxide (CO_2), water vapour, clouds, nitrous oxide, methane and ozone. Lacis et al. [23] discuss the estimated contributions of each gas to the "greenhouse effect" as: 50% from water vapour, 25% from clouds, 20% from CO_2 and 5% from other sources. CO_2 is deemed as a "forcing" gas, which refers to the fact the gas forces a change in climate and varies with human activities. CO_2 is progressively generated by humans during fossil fuel burning for energy and various industrial processes. In the past century, CO_2 emissions have accelerated at an alarming rate, almost doubling the historical average [24]. Scientists argue that the coinciding increase in global temperature is due to the "greenhouse effect" caused by these additional gases and the burning of fossil fuels.

Fossil fuels refer to combustible materials found naturally on earth, predominantly: coal, crude oil and natural gas. They are formed due to the compression of organic materials such as plants and animals over a long period of time. These materials are unsustainable, or finite, as they take millions of years to reproduce. At the current rate of production, British Petroleum estimated using data sourced from the "Federal Institute for Geosciences and Natural Resources Energy Study 2016" that coal reserves are sufficient to supply consumption for a further 153 years, almost three times longer than both crude oil and natural gas [25]. Arguments are made for longer and shorter time frames, conclusively though, fossil fuels will cease to exist in the relatively near future.

The increasing "greenhouse effect" and global temperature rises, paired with decreasing fossil fuel reserve, has driven countries to reduce their carbon footprint and invest in renewable energy sources.

2.2   Renewable sources

Renewable sources are defined as resources which are infinite in nature, or are replenished in less or equal time as it takes to extract the required energy. Use of renewable sources for electricity production has been exponentially increasing in the last two decades; however, fossil fuels remain the primary source for the worlds energy. As technology develops, renewable energy is becoming a promising replacement, with the overall objective of phasing out fossil fuel use completely by mid 21st century.

Technology	World capacity (GW)	Contribution (%)	12 month change (GW)
Hydro	1096	54.34	25
Wind	487	24.14	54
Solar	308	15.27	75
Bio	112	5.55	6
Geothermal	14	0.69	0.5
Total	2017	100	161

Table 2.1: Renewable power: contribution of each technology to world's capacity [26].

According to the renewable global status report by REN21 (Renewable energy policy network), renewable energy accounted for 19.3% of the worlds energy in 2017 [26]. Contributions for each type of renewable technology to the total renewable power capacity at the end of 2016 are given in Table 2.1. Hydropower contributes half of the total renewable capacity; however, both wind and solar show faster growth between 2016-2017.

2.2.1 Wind power

Wind power is divided between onshore and offshore turbines, both of which convert the kinetic energy of the wind to electricity. According to the Renewable capacity statistics 2017 by the International Renewable Energy Agency (IRENA) [4], the proportion of wind power that is onshore is $\approx 97\%$. Therefore, onshore wind alone provides $\approx 23.42\%$ of the worlds renewable power, making it the second highest contributor behind hydro. Onshore and offshore wind turbines operate under the same principle: to harness wind forces and convert into electricity using a turbine and generator. The only difference is in location: onshore turbines are located on land and offshore in the sea, which presents contrasting foundation requirements. The most common turbines are horizontal axis, as shown in Figure 2.1: a). They operate by capturing the velocity of the wind using aerofoil shaped blades, illustrated in Figure 2.1: b). These blades are shaped to create a pressure difference producing lift on the blade, identical to the operation of an aeroplane wing. Blades are attached to a rotor, allowing the rotation of a turbine and commonly a gearbox, producing power using a generator. The electric machinery is housed within the nacelle at the top of the tower (Figure 2.1: a)).

The second, less common type of wind power plant is the vertical axis turbine, one design known as the Darrieus rotor is shown in Figure 2.2 [27]. Operational procedure is similar to the horizontal axis turbine. The blade design allows the axis of rotation to be vertical, or perpendicular to the ground. The major advantage of this type of turbine is the location of the electrical equipment (gearbox, generator) which are on ground level, allowing for easier maintenance. Disadvantages include low torque during start-up, design complexity and high cost [27].

As mentioned, $\approx 97\%$ of wind turbines in the world are located onshore. Offshore wind does
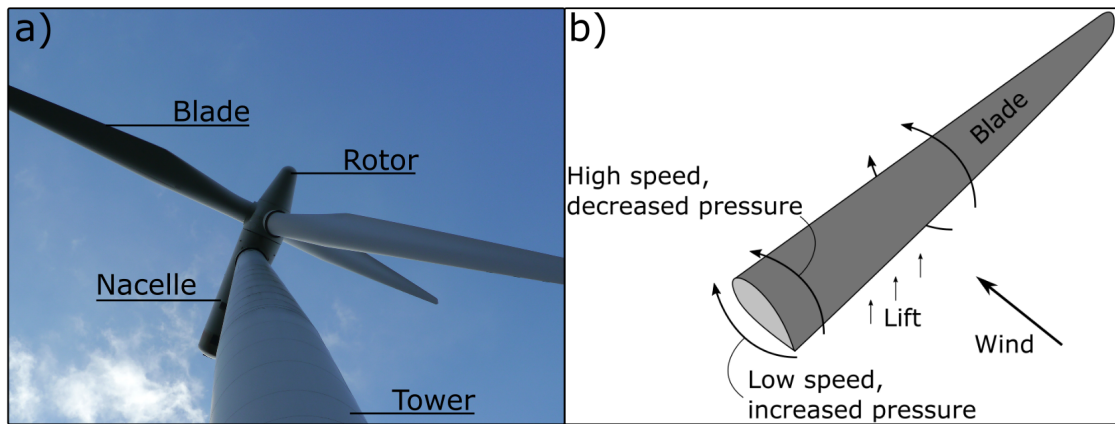
Figure 2.1: a) Horizontal axis wind turbine design. b) Aerofoil blade design.

address some major issues with onshore, including: visual impact, size restrictions, obstacles, use of land area and threats to animals. So why is onshore more common? Offshore invites a few major disadvantages. Firstly, locations present significant installation and maintenance challenges that incur large costs and time delays. Also, transporting power over the sea is difficult and expensive. Until these challenges are addressed, it is unlikely that offshore will overtake onshore in terms of operational assets. However, land area is severely limited in most countries which may compel the industry to invest more in offshore wind solutions.

Onshore wind turbines have increased in size and power output over time. A few examples of modern turbines are provided in Table 2.2. In 1990 the first onshore turbine consisted of a 40 m rotor diameter and 0.5 MW power output [28]. More recently, the Enercon E-126 demonstrates a 126 m rotor diameter and massive 7.6 MW power output [29]. On average, commercial wind farms use 2-4 MW turbines coalesced in a large array. Such large turbines require continuous development and increased size of the support structures which become more important with the increased loads.

Name	Power (kW)	Hub height (m)	Rotor diameter (m)	Data sheet
Enercon E-126	7600	135	127	[29]
Siemens SWT-2.3-93[1]	2300	80	93	[30]
Nordex N117/3600	3600	91-141	116	[31]
Vestas V117-4.2	4200	91.5	117	[32]
Doosan WinDS8000	8000	130	190	[33]
Goldwind Repower 48/750	750	50/65/75	48	[34]

Table 2.2: Details of commercial onshore wind turbines.

---

[1]Turbines considered in this work.
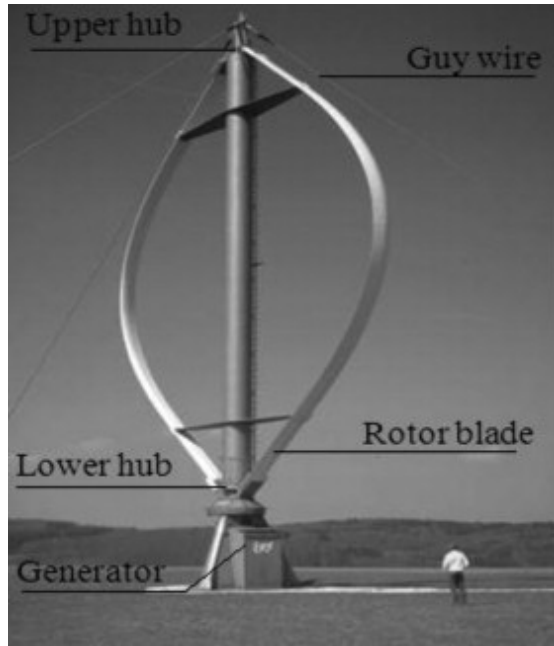
Figure 2.2: Darrieus rotor vertical turbine design. Image courtesy of Bhutta et al. [27].

2.2.2 Hydro

At a 54.34% share, hydropower is the highest contributor to renewable power capacity. Historically, water has been used for power for over two thousand years in the form of flour mills, making it one of the oldest known renewable sources. Storage hydropower is the most common modern system, which takes advantage of dams to store large quantities of water in a reservoir. Water flow is controlled via an intake, converting potential energy to kinetic energy to spin a turbine rotor and activate a generator. The largest electrical production hydroelectric dam is the Three Gorges Dam in China, which has an installed capacity of 22,500 MW and yearly production of around 95 TWh [35]. To visualize, this is enough to continually power over 80% of all UK households [36]. In addition to high potential renewable power generation, outputs are relatively constant, allowing use for base-load power. However, environments surrounding the site, such as fish ecosystems, are extremely impacted. Dam failure can also cause disastrous floods for surrounding civilizations.

2.3 Nuclear

Nuclear power represents methods for energy extraction from atomic reactions by either splitting (fission) or combining (fusion) material nuclei. Current commercialized nuclear power plants solely consist of fission reactors, with fusion proving difficult to control and incapable of producing a net energy gain. Whether current nuclear power should be considered as renewable has been the subject of debate for many decades. Arguably, it only solves one of the two issues discussed in section 2.1; nuclear power plants produce close to zero CO_2 but the fuel used (usually uranium) is not sustainable. However, Cohen argued in 1983 [37] that a source can be quoted as renewable

22

if it matches the lifetime of the Earth and Sun, approximately 5 billion years. He argued that breeder reactors, which are able to produce further materials capable of fission, could be used to ensure indefinite use of nuclear fission for the required lifetime. Radioactive waste material is an argument against this, as the purpose of renewables is to reduce the environmental impact on Earth and this waste is considered a pollutant and can be damaging. Possibly the most controversial topic though is nuclear disasters. History has shown that nuclear power plants are capable of creating devastation, both in loss of life and to the environment. For this reason alone, public opinion of nuclear power is generally negative which has potentially impeded development. Nevertheless, nuclear power is used in 31 countries, including USA, UK, France, Canada, Japan and China. France in particular captures 72% of the nations power demand from 58 nuclear power plants [38]. Total world capacity of nuclear power as of April 2017 is 391 GW, less than both hydro and wind, but greater than solar [39] (Table 2.1).

2.4   Solar

Solar power can be split into two categories: solar photovoltaic (PV) and solar thermal. The capacity alluded to in Table 2.1 of solar includes both, but over 98% of this is collected via solar PV. Technology used in both are considerably distinct but share the same concept: to generate electricity using the Sun. Solar thermal uses mirrors to concentrate heat from the Sun to a single point - enough to create steam and rotate a turbine to power a generator. Due to the distributed nature of the Sun's radiation, large arrays of mirrors are required. Since these arrays require considerable land area, it is not suitable for use in most countries. For this reason, solar PV has found significant use for renewable power generation. The technology uses particular materials known as semiconductors, which when incident with the sunlight release electrons, producing electricity. The unique trait of this technology is the ability of self-consumption: solar PV panels can be incorporated to public homes to allow personal use. However, generally large arrays of panels are grouped to create industrial-scale power stations to connect to the grid. The major disadvantage of solar PV is intermittency, since the Sun is only available for a fraction of the day. Solar power would either require a partner technology to act as base-load or a significant number of batteries to store enough energy to fulfil the downtime.

2.5   Innovations

So far, the successfully commercialized technologies for renewable power generation have been discussed. Ongoing industrial and academic research continue to produce innovative ideas and pursue further breakthroughs in the field. Hybrid solutions are of particular interest as some technologies compliment and address the issues of others. For example, work has gone into combining solar and wind as it is common for wind speeds to increase during the night, providing some compensation for the absent Sun. Essentially, the hybrid solutions attempt to remove the intermittency that ac-

companies some of the technology. One innovation by the Floating Power Plant company includes a hybrid wind-wave floating offshore power plant [40]. This idea simply sought to use the already existing platform in a floating wind turbine and install a wave power generation system. This could potentially double the power output of a single floating wind turbine and thus an entire fleet. A second hybridization in Portugal addresses the two main issues of solar PV: area requirement and intermittency by installing floating solar panels in the reservoir of a hydro dam [41]. The Kite Power Systems company have produced a new innovative method for wind power generation in order to address the concern of environmental impact of onshore wind turbine foundations [42]. The technology comes in the form of a large kite which is fit with a gearbox and generator. The rotating motion of the kite causes upward force which pulls on a tether which spools and rotates a rotor connected to a generator. The kite is retracted in the most energy efficient way to allow a net gain. They claim a 1 MW system is possible, which is comparable to some smaller wind turbines. Another benefit of this system is due to the non-necessity of huge concrete foundations, a much quicker deployment time is possible when compared to conventional wind turbines.

2.6   Future of renewables

The European Union (EU) renewable energy directive established a target of 20% contribution from renewable power to consumption by the year 2020, with a further target of 27% by 2030. The most recent progress report presented a share of 16% from renewables in 2014 [43] and as mentioned the REN21 detail a 19.3% share in 2017. To summarize the EU report, energy consumption is split into three categories: heating and cooling (49.7% share), electricity (42.2% share) and transport (8.1% share). Both heating and cooling and electricity are above projected targets and, if progress continues, will meet the 2020 target. Transport is slightly below projections, which is due to difficulties such as uncertainty and delayed progress on advanced biofuels. Only 11.3% of transport consumption is sourced by renewable electricity, with 88% from biofuels. Electric vehicles have had massive interest and publicity in recent years as technology develops, so perhaps in future more vehicles will be powered from renewable electricity generation.

2.7   SHM suitability

The previous sections have outlined the different types of renewable energy production, all of which are contributing to the goal of both reducing CO_2 emissions and replacing dwindling fossil fuels. A combination of the presented technologies will increase the probability of reaching these goals. One complication found in all methods is that the physical components of the power plants will have limited lifetimes. The longer they continue to produce energy, the more efficient and environmentally friendly they become. Ensuring these lifetimes are met or even extending them is of great importance and interest to the industry.

The focus of this thesis is onshore wind turbines which, as discussed, currently possess a high

power contribution and one of the fastest growing capacities of all renewable power methods. Particularly, the concrete foundations which support the majority of onshore wind turbines present an interesting case study. As current turbines age, the lifetime of the foundations comes in to question. Will they last for the entirety of the projected lifetime? How much of an effect does cracking actually have on the structure's integrity? Is it possible the foundation could be re-used? To answer these questions, an SHM campaign on an operational wind turbine is proposed in this research.

Chapter 3: The nature of concrete

3.1 Chapter overview

The majority of civil infrastructure, including renewable power plants, incorporate concrete in some form. Occasionally an entire structure is built solely from concrete, such as the previously mentioned Three Gorges Dam which is currently the largest single pour concrete structure in the world. In other cases, such as the majority of onshore wind turbines, it is simply the sub-surface support structure that is composed of concrete. In this chapter, discussion of the manufacturing process is given before analysing the mechanical properties of concrete. Following this, the complex phenomenon of cracking in concrete will be examined, particularly the initiation causes and displacement modes of cracks. Fracture mechanics will then briefly be explained before considering the potential for a new methodology to be developed.

3.2 Manufacturing process

Concrete is known as a composite material, created from multiple components bonded together into a single hard, coarse construction. Simple concrete is an aggregate made from crushed rocks and sand, mixed with water and cement. Cement can be described as the "glue" of concrete, binding the aggregates together. Portland cement encompasses a collection of cements which are hydraulic, reacting chemically with water through a hydration reaction [44, Chapter 4]. Cement is usually a powder-like substance made by blending mineral elements such as limestone, iron ore and clay at high temperatures within a rotary kiln (Figure 3.1 a)) and then grinding. Other additives, such as fly ash, can be added depending on the requirements of the cement both physically and environmentally. This powder is then mixed with the aggregate and water to produce concrete in a liquefied form, allowing pouring into specific forms and locations before it hardens during the hydration process. A pouring process for a wind turbine foundation is shown in Figure 3.1 b).
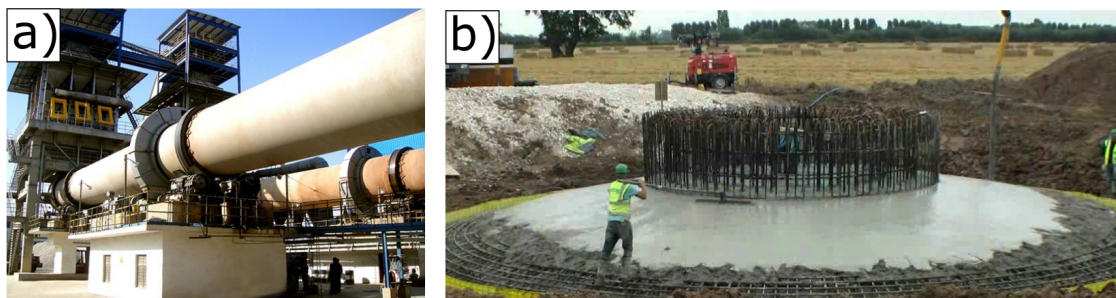
Figure 3.1: a) Rotary kiln used to blend minerals at high temperatures which are then ground into cement, image credit to KTM [45], b) concrete pouring process of an onshore wind turbine foundation, image credit to golden media productions [46].

3.2.1 Curing

Once combined, the hydration reaction of cement and water begins immediately and continues, with existence of continuous moisture, for an infinite amount of time. Exothermic hydration reactions of chemicals within the cement produce an expanding gel-like compound which adheres to the aggregates. To ensure compaction of concrete, the material is usually aggressively vibrated to remove air bubbles. Since it is exothermic, heat is expelled during the reaction, causing a rapid increase in temperature during the early stages before reaching up to $\approx 80°$C. Concrete strength gain is highly dependent on temperature, as water evaporates hydration reactions subside and temperatures decrease, causing the rate of concrete strength gain to slow. After 28 days of curing, concrete will reach close to maximum strength ($> 90\%$), which is the accepted length of time according to British standards (BS EN 206:2013+A1:2016) to perform tests. This strength is varied by many factors ranging from cement and aggregate formation, water:cement ratio and to environmental factors such as wind and temperature [47].

3.3 Concrete mechanics

In many materials, including concrete, elasticity is a crucial parameter. Elasticity refers to the ability of a material to return to its original shape following an applied stress or strain. Stress is a measure of force, F, by area, A as:

$$\sigma = \frac{F}{A} \tag{3.1}$$

with uni-directional strain represented by a change in length, ΔL with regards to overall length, L:

$$\epsilon = \frac{\Delta L}{L} \tag{3.2}$$

For an elastic material, the stress-strain relationship is linear initially, with Young's modulus constant, E, calculated as:

$$E = \frac{\sigma}{\epsilon} \tag{3.3}$$

A typical concrete stress-strain relationship is shown in Figure 3.2, accompanied by a visual comparison to a steel specimen. Generally, steel behaves similarly during tension and compression, with similar yield points [?]. Typically, the stress-strain curve for steel consists of a large linear region, prior to plastic deformation. Concrete strength refers to the ability of concrete to withstand compressive forces only, since it is inhomogeneous and weak in tension. In tension, only the cement is able to resist as aggregates will be pulled apart, causing maximum tensile stress, σ_t, to be much smaller than maximum compressive stress, σ_{max} [48]. Concrete can be described as following the
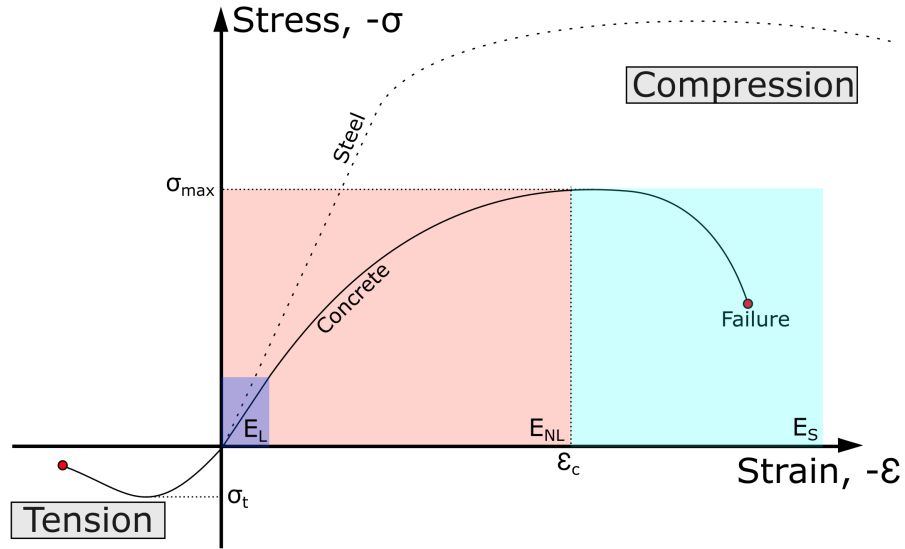
Figure 3.2: Stress-strain curve of concrete and steel. Concrete initially remains linear at relatively low stress levels, region E_L. Cracking then causes release of stress and coinciding non-linear region, E_{NL}, until maximum stress, σ_{max} is reached where failure of structures usually occurs. Softening of concrete can follow, E_S, and occurs as damage localizes.

elastic definition during small stress/strain levels. This is defined as the elastic region, E_L: the maximum stress and strain that can be applied to a material before permanent deformation. When concrete begins to inevitably crack, this behaviour becomes non-linear as the cracks cause a release of stress but do not resist elongation.

The non-linear region is represented by the area E_{NL} in Figure 3.2. During this period, equation 3.3 is not constant as the crack air pockets cause the concrete to deform progressively as stress increases. As stress continues to increase, the concrete will reach yield point, σ_{max}, where cracks have exponentially increased in size and quantity, propagating throughout the material. Overall failure can occur from this point forward, as remaining at this stress causes continuous deformation into the softening region. In this region the material continues to deform until eventual failure.

To withstand tensional forces, steel reinforcement is introduced to concrete. The stress/strain relationship of steel, shown in Figure 3.2, represents both tension and compression. With competent bonding, reinforced concrete is able to withstand tension in the same nature as compression. The process for introducing reinforcement is simple, the steel is erected in place throughout the intended area prior to pouring of concrete, allowing the liquid to flow around the steel. The concrete foundation shown in Figure 3.1 b) is an example of a pre-erected reinforcement cage which is then enclosed in concrete. Similar to binding aggregate in concrete, the gel-like substance produced during hydration also binds to the steel, effectively creating a new composite material known as reinforced concrete (RC), which has high strength in both compression and tension states. Unlike steel (which has a very predictable load response), concrete has non-linear load response over the entire size of the structure due to varying air pocket sizes throughout. Since the concrete is a

mixture of particular quantities of different materials as well as being the outcome of a rapid reaction, the same mixture can also cause varying strengths for different structures. This variance in both cases is usually minor. Generally a single structure has several samples (cubes or cylinders) extracted post-curing which are all tested to determine the overall strength of the structure.

3.4   Cracking in concrete

The focus of this research is on deterioration of cracks, rather than initiation. However, it is useful to understand why cracking occurs in concrete in order to quantify the magnitude and rate that a crack may degrade. In this section, only abnormal crack initiations are considered - occurring either due to environmental factors, excess loading or human error. Indeed micro-cracks occur in most concrete simply due to the composite nature of the material. These micro-cracks can also provide a weak point for a more severe crack to form over time due to the abnormal factors. In this section, a discussion of situations that cause different types of abnormal cracking to occur is given, including analysis of their physical appearance, before examining the behaviour of the crack in terms of modes and fracture mechanics.

3.4.1   Initiations

Hydration

During the hydration process, discussed in Section 3.2.1, microcracks can appear if the hydration reaction is not ideal. Water-cement ratio is key in determining concrete strength and workability. For example, lack of water can make concrete difficult to form leaving unintentional voids. On the other hand, excessive water may provide more workability but can decrease the concrete strength and cause cracks [44, Chapter 3].

Temperature

Temperature differences in concrete, which commonly occur during curing following initial hydration reaction, can cause crack initiation between sections with differing temperatures. Specifically in newly poured concrete during cooling, colder sections of concrete will contract more, causing a region of intense tensional stresses and subsequent cracking. This can occur randomly, or due to factors such as pouring delays or uncovered sections of concrete. Thermal cracking occurs rarely in later stages, usually only due to extreme weather conditions causing rapid changes in surface temperatures. In terms of physical appearance, thermal cracking can vary from hairline cracks to delamination, illustrated in Figure 3.3.

Loading

Repetitive or extreme structural loading can cause crack initiation on the face of the concrete. The physical appearance of these cracks depend on the type of loading applied. Figure 3.3 displays
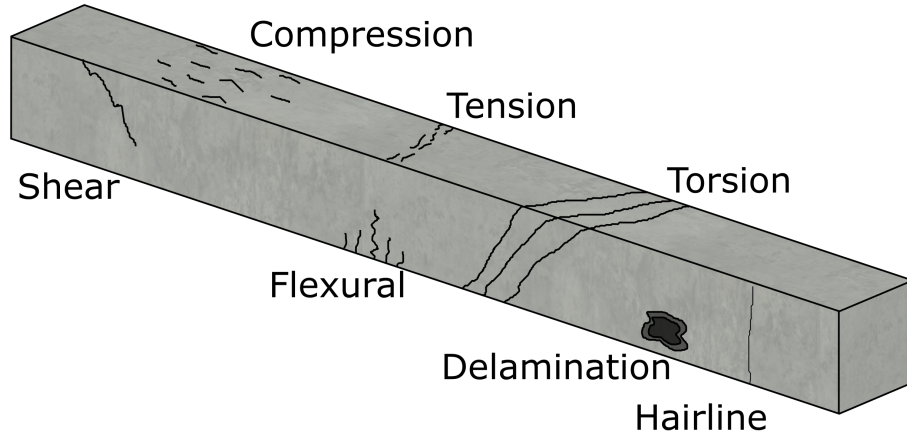
Figure 3.3: Physical appearance of cracks on a beam due to different loading types.

a concrete beam with various crack types annotated. The "Compression" and "Tension" crack formations can occur under the corresponding axial loads. During bending loads, "Flexural" cracks occur at the maximum axial stress point, with "Shear" cracks forming due to perpendicular strains. "Torsion" cracks can occur due to twisting load types.

3.4.2 Crack modes

Under loading, cracks will typically only alter in three distinct modes [49]. These are illustrated in Figure 3.4. Opening, or mode I is usually the primary and dominant displacement as it concerns the change of crack width. Sliding, or mode II, represents the movement of crack surfaces perpendicular to the face. Tearing, or mode III, depicts the movement of crack surfaces in the longitudinal direction of the crack. The overall crack displacement, or distance between centre points of each crack surface, ΔL_C will be the sum of squares of each independent mode displacement:

$$\Delta L_C = \sqrt{\Delta L_O^2 + \Delta L_S^2 + \Delta L_T^2} \tag{3.4}$$

In literature, any crack analysis work only considers these, commonly concentrating primarily on opening and ignoring sliding and tearing. Any crack surface rotation is generally disregarded as measurement would be difficult or obscured by other modes.

3.4.3 Crack ramifications

Cracking in concrete is undesired for a variety of reasons. In terms of structural integrity, cracks weaken the concrete by causing increased elongation at lower compressional stresses (see Figure 3.2). Large movements could eventually lead to total failure of the structure. Additionally, severe cracking can cause water ingress to the steel reinforcement, which can subsequently corrode the steel. As discussed, the purpose of steel reinforcement in concrete is to provide tensional support
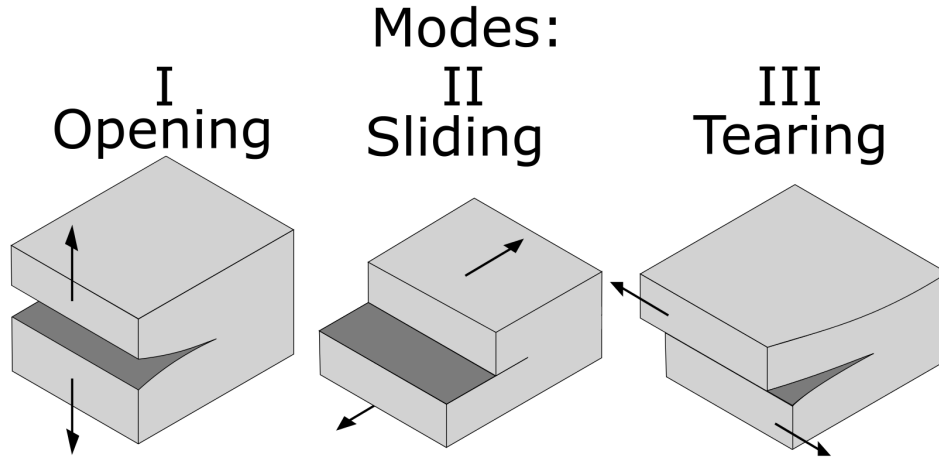
Figure 3.4: Modes of crack displacement: I) opening II) sliding and III) tearing.

strength as concrete alone is extremely weak in tension. Corrosion can completely remove this support.

Cracking has other ramifications, including diminishing aesthetics and increased maintenance costs. Typically, cracks are under evaluated and are simply repaired immediately, so an increasing number of cracks can cause unwarranted costs as cracks may be superficial.

In all cases, monitoring the cracks more closely may provide additional information to either ensure cracks are repaired before irreparable damage occurs or to reduce the costs of continual non-required repair, in the case of superficial cracks. Monitoring cracks effectively would involve the implementation of a structural health monitoring (SHM) system, including sensor system and analysis methodology.

3.4.4 Fracture mechanics of concrete

Fracture mechanics is a well established field which fundamentally studies the behaviour of a homogeneous, linear elastic cracked material under various loading procedures [50]. The objective of the analysis is to define the critical point or fracture point of a cracked specimen, similar to the yield point, σ_{max} in the stress-strain relation discussed in section 3.3. This critical point is known as the material toughness and is represented by a specific value of the stress intensity factor:

$$K_c = C_g \sigma_{ct} \sqrt{\pi a} \tag{3.5}$$

where K_c is the critical stress intensity factor for a crack with specific geometric constant, C_g and length a at critical crack tip stress level σ_{ct}. The geometric constant, C_g varies for crack modes and different types of crack. These are mainly: edge, through thickness and surface cracks [51]. Equation 3.5 states that should the crack tip stress reach the critical level, propagation of the crack will occur. To define this level, an energy state approach was proposed. This concept defined the resistance curve (R-curve), which is a plot of the energy release rate, G, against crack size a. The

energy release rate is simply the energy exhausted at fracture and can be represented by the stress intensity factor, K. Typically, a linear relationship is defined between the stress intensity factor K and crack length, a. As crack length increases, stress intensity also increases until reaching the material resistance, R, upon which fracture will occur [52].

Although concrete is not a homogeneous linear elastic material, fracture mechanics has been applied and showed suitability for concrete by adjusting the analysis to account for non-linear behaviour [53]. One model to account for this is known as the blunt crack band theory, reported by Bazant et al. [54]. Essentially, a crack is modelled by a band of densely populated parallel microcracks with blunt fronts at a width w_c and length a, illustrated in Figure 3.5 a). A stress-strain relationship is defined to determine the fracture strain dependence on z-directional stress or opening, shown in Figure 3.5 b). This method is convenient for finite element method (FEM) modelling as small blunt cracks are easily translatable. Mathematically, this stress-strain relation can be considered in a system of Cartesian coordinates:

$$\begin{Bmatrix} \epsilon_x \\ \epsilon_y \\ \epsilon_z \end{Bmatrix} = \frac{1}{E_C} \begin{bmatrix} C_{xx} & C_{xy} & C_{xz} \\ C_{yx} & c_{yy} & C_{yz} \\ C_{zx} & c_{zy} & C_{zz} \end{bmatrix} \begin{Bmatrix} \sigma_x \\ \sigma_y \\ \sigma_z \end{Bmatrix} + \begin{Bmatrix} 0 \\ 0 \\ \epsilon_f \end{Bmatrix} \tag{3.6}$$

where ϵ_x, ϵ_y and ϵ_z represents the principal strains, σ_x, σ_y and σ_z the principal stresses and ϵ_f the fracture strain of the modelled microcracks. E_C is Young's modulus of concrete and the C values represent the elastic compliance constants in each direction. From the linear stress-strain relationship in Figure 3.5 b), the fracture strain can be calculated as a function of z-directional stress:

$$\epsilon_f = f(\sigma_z) = \frac{1}{C_f}(\sigma_t - \sigma_z) \tag{3.7}$$

where σ_t is the tensile strength of concrete and the linear constant $C_f = \frac{\sigma_t}{\sigma_0}$ where σ_0 is the strain at which the micro-cracks unite into a single crack. This method can be used to characterize a crack width and define fracture strain and stress limits.

In this work, measured cracks will be far below the fracture limits. Knowing the fracture limit of a crack would be beneficial, but ensuring the crack never reaches this limit by monitoring the displacements over time is more desirable to ensure not loss of structural integrity.

3.5 Chapter summary

The manufacturing process, mechanics and cracking of concrete was discussed in this chapter. Concrete will inevitably crack and the ramifications of severe cracks can range from complete structural failure to increased costs due to unwarranted repair of superficial cracks. Fracture mechanics was briefly discussed as a methodology for identifying the fracture point of a crack. The subject of this thesis is the deterioration of cracks in an onshore wind turbine foundation,
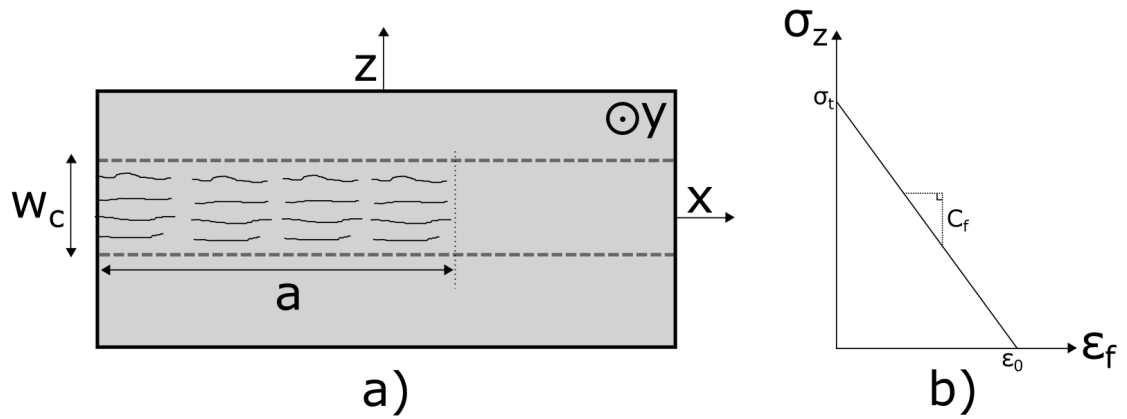
Figure 3.5: a) Crack band theory implementation, b) stress-strain relationship for model.

with the objective of monitoring the cracks and relaying the information to turbine operators. To realise this, an SHM system is proposed. This will require a thorough literature review of SHM systems, including those applied to wind turbine foundations, to determine the best strategy for crack monitoring. Following this, a new methodology for quantifying crack deterioration in a progressive manner will be developed.

Chapter 4:   Sensors for structural health monitoring

4.1   Chapter overview

This chapter aims to explore structural health monitoring (SHM) sensor systems with priority on the various devices for strain measurement. An initial overview of SHM is presented, defining each discrete subsystems found in a typical SHM system. The available strain monitoring sensors are then explored by firstly specifying the manufacturing and operational procedure for each sensor before discussing the advantages and disadvantages when utilizing the sensor in an SHM environment. Finally, secondary measurands worth considering for an SHM application are discussed, outlining additional sensors that can be employed.

4.2   Definition of SHM

SHM as a concept is well established; however, a distinct definition varies depending on the initial objectives of the system. Numerous works have been published reviewing SHM over the years [55, 56]. Housner et al. [57] described SHM in 1997 as "the use of in-situ, non-destructive sensing and analysis of structural characteristics, including the structural response, for detecting changes that may indicate damage or degradation". This definition holds up today and encompasses most approaches to SHM. Prior to the introduction of sensor technologies, the "non-destructive sensing" was mainly carried out through visual inspection of the structure. Although outdated, visual inspection is still widely used today, most likely due to uncertainty in technology and the risk involved in committing upfront costs for non-guaranteed long-term benefits. In terms of physicality, an SHM system consists of three main subsystems working collectively:

Sensing: *Monitors physical quantities.* Features are measured either by visual inspection or with technology, including characteristics of the structure or the surrounding environment.

Interrogation: *Converts physical measurements from sensors to data, saving to memory.* Sensors or interrogators will usually convert the physical quantity to an electrical signal. This electrical signal will then be converted into data files to be displayed or saved to memory. Data files will contain the original physical quantities measured in a format specific to software used.

Analysis: *Uses data to conclude the influence of the physical quantity on the health of the structure.* Subsequent to measurements, or potentially in real-time, analysis is performed using any number of algorithms or software to determine the impact the measured physical quantities have on the overall health of the structure.

The overall capabilities of an SHM system depend on each of these subsystems individually. For example, an excellent sensor may not constitute to a successful SHM system if the analysis is
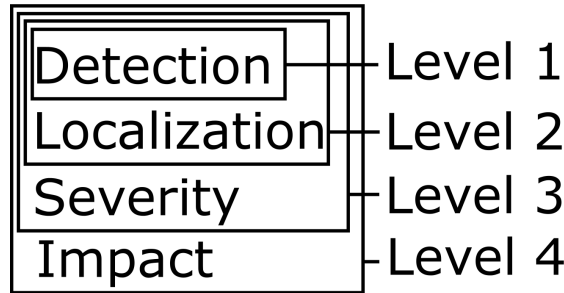
Figure 4.1: Four level representation of SHM systems, based on work in [55, 58, 59].

inadequate. Stubbs et al. [58] provide an extensive overview of work by themselves and others ([59–69]), concluding a four level system to classify SHM systems in terms of capability, illustrated in Figure 4.1. This categorisation attempts to classify the very complex process that occurs during SHM from sensors through to analysis. To explain, a level 4 system is the most complex, enclosing all four criteria: detection of damage or degradation, determining the location, estimating the severity and finally analysing the impact on the overall structure in terms of stability and safety. Arguably, monitoring damage degradation fits these criteria more effectively than monitoring for initiation. For example, it is common for initial damage in a structure to be negligible or superficial, or in other words, does not influence the structures stability or safety at all. Whereas, if this same damage is to degrade, it may develop an impact over time. Therefore, possibly a system capable of directly monitoring damage degradation could provide a more effective SHM system, than one that focuses on detecting new damage initiation.

A single SHM system is massively complex and extensive. Three subsystems (Sensing, Interrogation and Analysis) have been introduced to allow focus on a single aspect of SHM - sensors. In the following two chapters, focus will be made on the sensors applied in SHM systems, as the research involves the application of a sensing system to an onshore wind turbine foundation. Essentially, the objective is to determine the "current state" of the industry, which will aid in the design and implementation of the sensor system to the foundations. In order to effectively classify the sensor subsystem, propositions must be evidenced by literature. For that reason, the sensor subsystem classification is discussed at the beginning of the literature review in Chapter 5.

4.3   Sensing

Sensor systems may grant advantages when compared to the conventional visual inspection, depending on the sensors used. Some examples include:

- Accurate, specific data.

- Continuous measurements with little downtime.

- Dynamical information (with high sampling rate).

- Less intrusive - for example: soil excavation to access sub-surface damage is not required following installation.

- Semi-reliable cost.

To expand on these advantages: a sensor will provide specific values of a measureand to a more accurate resolution than visual methods. Additionally, once the sensor is installed it will usually continue to monitor over a long-term, rather than periodically. This also provides the capability of looking at dynamical behaviour of the structure. Furthermore, the sensor will usually not require any maintenance or human interference, so will not intrude should the structure continue to be used or operate â€" compared to the requirement of visual inspection. This specifically applies to sensors applied sub-surface, as excavation would be required for every visual inspection. The cost could also be more reliable over the long-term, since it will usually consist of a one off payment at the start. Compared to visual inspection, which may be required more or less often depending on observations.

Sensor systems do come with some major disadvantages when compared to visual inspection:

- Significant upfront costs with no guarantee of success.

- Interruptions to sensor monitoring could occur during key periods.

- Failure of sensors present a major risk if they cannot be repaired following installation.

- Requires significant knowledge for operation and analysis of sensors.

Generally, the risk of these points is outweighed by the benefits of employing the sensor system.

Sensor-based SHM systems were initially introduced to new concrete structures in order to determine when formworks could be removed [70]. As structures aged, requirements emerged for systems capable of monitoring loading in a structure and to identify locations of defects [71]. Measurands of such sensors can range from environmental factors such as wind speed to structural characteristics such as strain. In most cases, an entire system will be a combination of both, allowing for comparison and diagnosis. Strain sensing is perhaps the most developed and important component, as strain provides a comprehensive insight into a structures health. Structures are usually composed of crucial load bearing segments which are prime candidates for a strain measurement system, ensuring strain levels witnessed in these parts remain within acceptable limits over time. For this reason, particular focus will be made in the following sections to strain sensors.

4.4 Electrical strain sensors

4.4.1 Foil or thin film gauge

The most conventional and popular option for strain measurement is the electrical strain gauge. Many designs exist, but the principle for measurement remains the same: using electrical conduc-

tion to determine strain values. The foil strain gauge, shown in Figure 4.2 a), is arguably the most commonly used type. The sensor is composed of a thin, flexible plastic with a laminated metallic wire grid on one surface. Strain on the device in the annotated "sensitive direction" causes deformation of the metal wires and a proportional change in resistance, ΔR_w. Many configurations of these wires exist to allow detection of particular strain directions. The total resistance of the metal wire, R_w is given as:

$$R_w = \frac{\rho_m L_w}{A_w} \tag{4.1}$$

where ρ_m is the resistivity of the wire material, L_w is the total length of the wire and $A_w = \pi r_w^2$ is the cross sectional area of the wire with radius r_w. The change in resistance due to deformation can be expressed in terms of the change in each geometric factor:

$$\Delta R_w = R_w * \left(\frac{\Delta L_w}{L_w} - \frac{\Delta A_w}{A_w} + \frac{\Delta \rho_m}{\rho_m} \right) \tag{4.2}$$

Equation 4.2 can be simplified by means of characterization. An electrical strain gauge will be strained at particular values and resistance change will be monitored to provide the gauge factor, GF, where strain, ϵ_e in electrical gauge can be calculated as:

$$\epsilon_e = \frac{1}{GF} \frac{\Delta R_w}{R_w} \tag{4.3}$$

where $GF = 1 + 2v + \frac{1}{\epsilon_e} \frac{\Delta \rho_m}{\rho_m}$ with Poisson's ratio v. Once characterized, equation 4.3 can be used to calculate the strain for given resistance change.

4.4.1.1 Suitability of foil gauge

The application in this work of concrete foundation crack monitoring presents a few challenges when considering foil gauges. Firstly, considering the general advantages of foil gauges, which are:

- Low cost.

- Conventional, so significant research and experience available.

- Ease of use and installation.

Generally, the most convincing reason to apply foil strain gauges is cost, which alone makes for a convincing argument when applying in research. However, when contemplating the use of foil gauges for the application in this research, there are some challenges (both general and application specific):

- Accuracy of resistance measurements is dependent on the magnitude of current supplied, which is then limited by power dissipation in the gauge [72, Chapter 19].
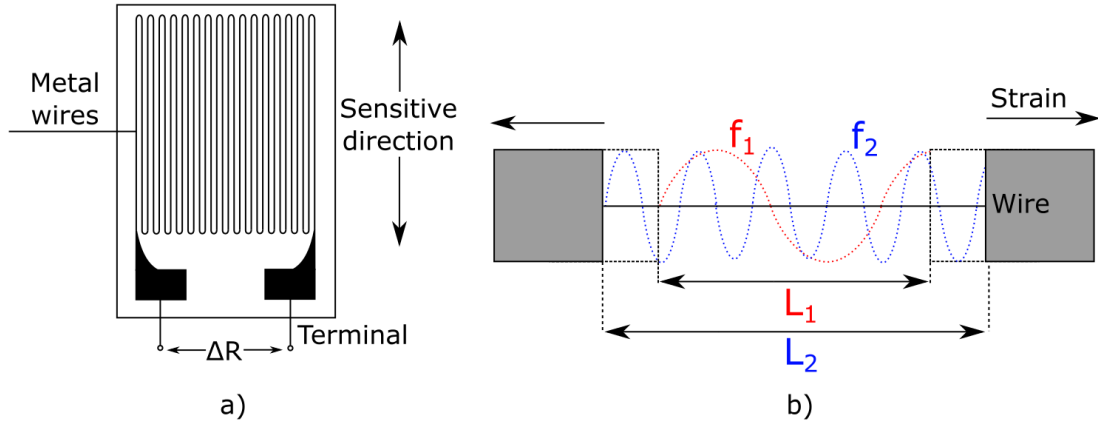
Figure 4.2: a) Thin film and b) vibrating wire electrical strain gauge designs.

- Semi-conductor based designs (which give greater accuracy than regular foil) show hysteresis/non-linearity to strain and temperature, requiring compensation and introducing some uncertainties.

- Inability to multiplex causes considerable cabling for large arrays of sensors.

- Not previously applied for long-gauge crack displacement sensing.

- Sensitivity to electromagnetic interference.

In this application of concrete crack monitoring, a long-gauge displacement transducer is required due to the inhomogeneous nature of concrete [73]. There are no reported applications of foil gauges for long-gauge displacement measurement of concrete cracks. This would require further research to deem suitability. It is preferable to use a sensor previously shown suitability for crack displacement monitoring. Furthermore, the operator requests a minimisation of noticeable, accessible hardware, since the wind turbine site is open to the public. Introducing more cabling may cause issues with regards to damage or interference by the public. Additionally, there is a requirement for measuring multiple crack modes (Chapter 3, Section 3.4.2), which will require multiple sensors in close proximity. This makes multiplexing a more attractive option.

Overall, the foil gauge presents an interesting possibility for a crack monitoring sensor. However, these application specific requirements may present challenges that other sensor types can solve more adequately.

4.4.2 Vibrating wire

A vibrating wire electrical strain gauge consists of a pre-tensioned single metallic wire fixed between two blocks. The wire is periodically excited to produce vibration at the natural frequency, initially f_1, which is measured by an interrogation unit. When strain ϵ_w is applied, the natural vibrating

frequency and length will change accordingly, to f_2 and L_2 as shown in Figure 4.2 b). The strain applied can be calculated as [74]:

$$\epsilon_w = \frac{4L_W L_1^2 \rho_w}{L_B E_S}(f_2^2 - f_1^2) \tag{4.4}$$

where L_W and L_1 are the wire lengths prior to and following pre-tensioning respectively, ρ_w is the wire density, L_B is the length measured between the centre of each block subsequent to pre-tensioning and E_S is the Young's modulus of steel. In terms of disadvantages, the vibrating wire strain gauge is similar to the thin film gauge and are increasingly being phased out for SHM purposes and were deemed inappropriate for this work.

4.5 Optical strain sensors

Optical sensors in general have become a staple in SHM systems over the last decade. Although more expensive, optical sensors usually replace conventional electrical-based sensors when factors such as large arrays, increased sensitivity, improved reliability and automation are required. They also provide improved performance in harsh environments [75]. Optical sensors can be classified into three distinct types, described in Table 4.1, based on the measurement length of the sensor. Assuming strain as the measurand, point sensors measure strain over a small length, typically up to 20 mm, long gauge up to 1 m and distributed in the magnitude of kilometres. This increased length comes at a cost of reduced strain or spatial resolution.

In the following sections, optical sensors capable of strain monitoring will be discussed in depth. In this work, the uniform fibre Bragg grating (FBG) for long gauge strain sensing was chosen due to numerous advantages over both electrical and other optical sensors:

- Heavily researched and developed sensor type providing relatively low risk.

- Linear response to both strain and temperature.

- Capability of both serial and parallel multiplexing, allowing large arrays of sensors with few optical fibres.

- Immunity to electromagnetic interference.

- Small size allows flexibility in packaging to perfectly suit measurement and environmental requirements.

- Less expensive interrogation systems when compared to distributed sensing.

4.5.1 Fibre Bragg gratings

FBGs are widely used in SHM for strain measurement due to their high flexibility. FBGs are primarily a point sensor; however, using particular packaging allows FBGs to also be used as
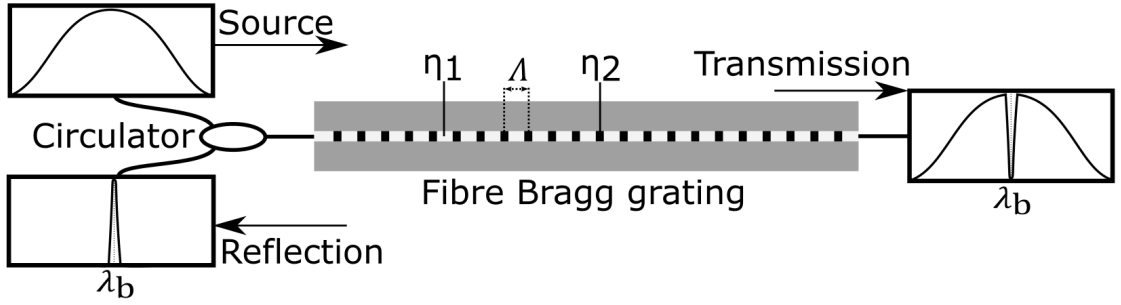
Figure 4.3: Broadband source incident on FBG causes reflection of a small band around a centre wavelength, termed "Bragg wavelength", λ_b.

long-gauge sensors. Gratings are written within an optical fibre causing a periodic modulating refractive index, illustrated in Figure 4.3 (explained in more detail in Section 4.5.1.1). Broadband light guided through said grating incites a partial reflection around a centre wavelength termed the Bragg wavelength, λ_B. Characteristics of the grating, including the grating period, Λ and effective index, η_{eff} combine in Equation 4.5 to determine the particular value of λ_B, allowing moderate customisation [76]. The wavelength of this reflection is dependent on factors such as temperature and strain, allowing a large number of unique applications such as current and pressure detectors [77, 78].

$$\lambda_B = 2\eta_{eff}\Lambda \tag{4.5}$$

4.5.1.1 Fabrication

Initial work by Metz et al. [79] demonstrated that fibre gratings could be written by using a bulk interferometer to produce an interference pattern. An interferometer is simply a device that causes precise interference of two beams of light. A photosensitive fibre is placed at the intersecting ultraviolet (UV) light from an interferometer, which reacts with an equivalent change in refractive index. Fibres are held by specially designed frames as vibrations can negatively impact the performance of the grating [80, Chapter 3]. Equation 4.6 states that the Bragg wavelength is dependent on the wavelength of the UV light used and the angle between beams, allowing

Type	Examples	Typical measurement length
Point	FBGs, Fabry-Perot Interferometers	20 mm
Long-Gauge	FBGs, SOFO Interferometers	1 m
Distributed	Rayleigh, Raman & Brillouin	1 km

Table 4.1: Optical sensor types based on work by Glisic et al. [75].
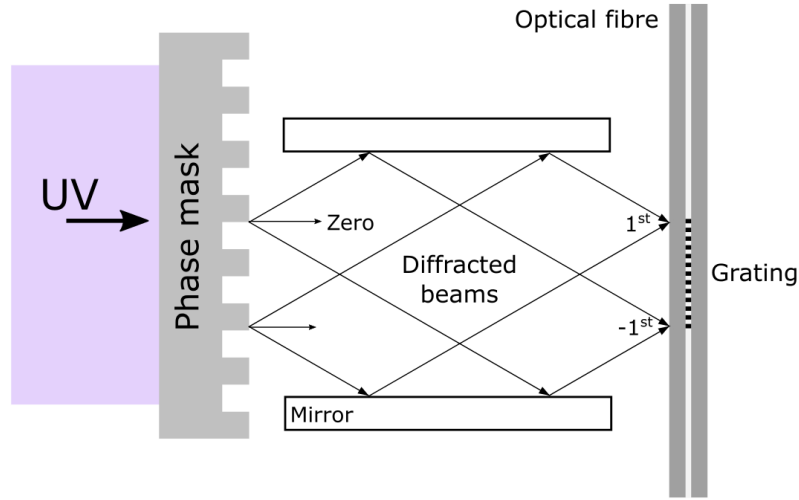
Figure 4.4: Phase mask fabrication technique for grating inscription.

adjustability by changing the UV source or adjusting interferometric mirrors.

$$\lambda_B = \frac{\eta_{eff}\lambda_{uv}}{\eta_{uv}sin(\frac{\theta}{2})} \tag{4.6}$$

Here, λ_{uv} and η_{uv} are the wavelength of UV radiation and refractive index of silica respectively, and the angle between combining beams is represented by θ.

Further work incorporated a phase mask into the interferometer method, providing improved flexibility as the Bragg wavelength could be altered regardless of the UV wavelength. The phase mask consists of a block of silica containing periodic square etchings, illustrated in Figure 4.4. In direct inscription, these etchings diffract the UV light to create the coherent beams straight onto the fibre, producing the grating. This means the phase mask characteristics alone define the Bragg wavelength. Commonly though, mirrors are used to guide the beams, allowing adjustment of the interference pattern and thus the Bragg wavelength by simply shifting the mirrors. The zero order beam is disregarded by introducing a block, or by repositioning the mirrors so beams can converge at a different location.

4.5.1.2 Grating structures

Generally, uniform gratings (shown in Figure 4.3) are used in most FBG applications. However, there are alternatives that may suit certain applications. Firstly, chirped gratings encompass a variety of FBGs where the grating period increases or decreases over the entire length. There are a large number of ways to embody the chirp, such as linearly (Figure 4.5 a)i)), quadratically or randomly [76]. The chirps allow a broader band of wavelengths to be reflected, as illustrated in Figure 4.5 b) in comparison to uniform grating reflection. Chirped FBGs, are primarily used for dispersion-compensation in optic environments. They have also been used for detection of hazardous gases [81] and crack location identification in plastic composites [82]. In the latter work,
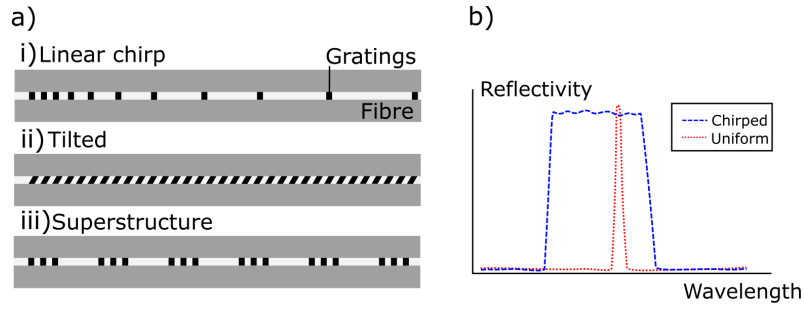
Figure 4.5: a)i) Linearly chirped, ii) tilted and iii) superstructure gratings. b) Spectrum comparison between chirped and uniform gratings.

authors take advantage of the non-uniform sensitivity of the FBG to strain, allowing translation of reflected wavelength to position over the FBG length. Essentially the FBGs become very short distributed sensors (Table 4.1).

Tilted FBGs, shown in Figure 4.5 a)ii), are another structure of grating that have many applications. These range from vibration sensors [83] to gain flattening filters for fibre amplifiers [84] and simple strain sensors [85]. In the latter, authors present the capability of measuring temperature-insensitive strain with one grating. A major drawback of uniform FBGs being the requirement of a second instrument to perform temperature compensation in post-processing. The reason for this advantageous feature is the nature of the reflection and transmission of a tilted FBG, which contains both core and cladding modes. These spectra usually encompass a large window, causing difficulty with multiplexing [86].

Another FBG grating structure with the possibility of simultaneous strain and temperature measurement was proposed by Sengupta et al. [87], based on the superstructure FBG (Figure 4.5 a)iii)). A superstructure is essentially multiple small FBGs written equally spaced along a fibre, producing equally spaced wavelength peaks. Sidebands of these spectra are usually of low reflectivity, causing potential difficulty during interrogation. Also, since multiplexing is not possible due to the bandwidth of the multiple FBGs, they are not suitable for distributed structural monitoring using sensor arrays.

For the application of this work, simple uniform gratings are capable of fulfilling the requirements. Therefore, for the future of this thesis, "FBG" refers to the uniform grating type.

4.5.1.3 Spectral properties

As mentioned, an FBG reflection consists of a small band of wavelength around a centre peak. A typical FBG spectrum is shown in Figure 4.6. The peak, λ_b is located at the highest power of the reflection, P_{max}. Sidebands (or sidelobes) are caused by harmonic reflections. Commonly, these sidebands are minimised by using Gaussian apodization [88]. The full width to half maximum (FWHM) is a bandwidth quantity which represents the reflection between half and maximum power. All of these quantities are initialised by the fabrication process. Ideally, P_{max} will be
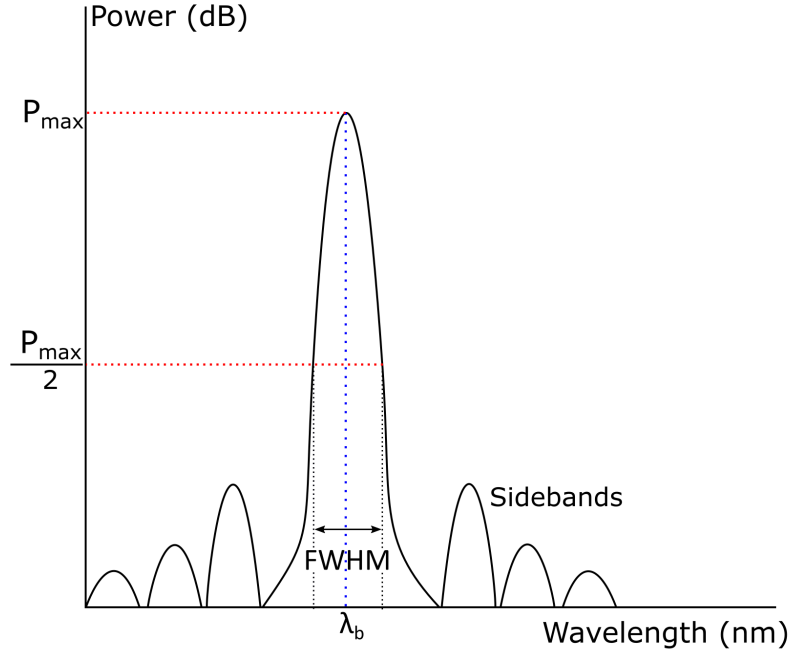
Figure 4.6: Typical spectrum of an FBG reflection, illustrating the peak (Bragg) wavelength, λ_b, and the FWHM. The sidebands can be prominent and are caused by harmonic reflections [88].

maximised, FWHM will be minimised and λ_b will be customisable during fabrication. The spectral properties will remain relatively constant throughout an FBGs lifetime, provided that no damage occurs to the FBG. Other factors such as overheating or overloading may also affect the spectrum characteristics.

4.5.1.4 Interrogation

As explained, FBGs reflect a small band of wavelengths around the respective Bragg wavelength, λ_B. The width of this band is dependent on the structure and uniformity of the grating: an accurate fabrication process accompanies a thin reflection band. Conventionally, wavelength division multiplexing (WDM) designs are used to provide the capability to interrogate a number of FBGs over one channel. Introducing time division multiplexing (TDM) into the design allows this number to be multiplied several times [89]. To continually examine the peak wavelength of each FBG, λ_B, multiple interrogation techniques have been developed. Some methodologies are provided in Figure 4.7, courtesy of work by Rao [76]. An edge filter can be used to determine the change in wavelength of the FBG by measuring the filter intensity which is dependent on wavelength position. A tuneable filter can be used by convolving the two spectra, when they match, the output will be approximately one (or maximum value over entire sweep). A scanning interferometer can also be used to determine the wavelength change [90].

Depending on the chosen interrogator system, the Bragg grating peak and any shifts will be measured at a set sampling frequency.
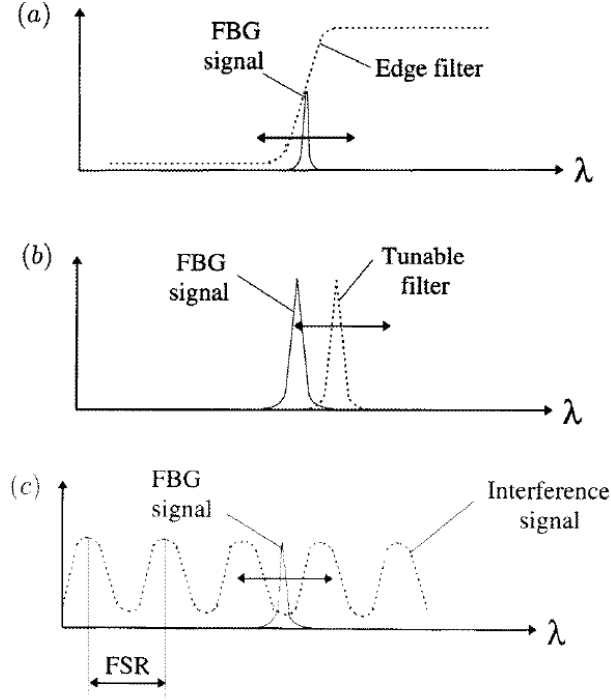
Figure 4.7: Interrogation methodologies: a) edge filter b) tuneable filter c) interferometric scanner. Image courtesy of Rao [76].

4.5.1.5 Measurands

A standalone FBG, isolated from any mechanical strain, has a reflection peak variation, $\Delta\lambda_B$, dominated by change in temperature, ΔT [91]:

$$\frac{\Delta\lambda_B}{\lambda_B} = [(1 - p_g)\alpha_g + \beta] * \Delta T \tag{4.7}$$

where p_g and α_g are the photo-elastic coefficient (0.22) and thermal expansion coefficient ($0.55 * 10^{-6}/°C$) of fused silica respectively. Refractive index sensitivity to temperature is represented by β, and is significantly higher than α_g at $\approx 7*10^{-6}/°C$. Any variation in these constants is removed by a characterization process, where an FBG is held for periods of time at different temperatures and $\Delta\lambda_B$ is recorded. An overall thermal sensitivity, K_{temp}, can then be extracted and used in future experimentation to determine the exact temperature:

$$\frac{\Delta\lambda_B}{\lambda_B} = K_{temp} * \Delta T \tag{4.8}$$

Bonding an FBG to a specimen or structure allows simultaneous measurement of temperature variations, ΔT and mechanical strain, ϵ_m:

$$\frac{\Delta\lambda_B}{\lambda_B} = K_T \Delta T + K_\epsilon \epsilon_m \tag{4.9}$$

where K_T is now a temperature sensitivity dependent on the thermal expansion coefficient, α_s of the specimen or structure and the strain transfer constant, K_ϵ in addition to the refractive index sensitivity. Directly bonding the FBG to a structure requires calculation of K_T:

$$K_T = (1 - p_g)K_\epsilon\alpha_s + \beta \tag{4.10}$$

The strain transfer constant, K_ϵ, is difficult to quantify when the FBG is directly bonded to the structure as it can vary from sensor to sensor even with identical attachment methods. Typically it will be within the range of 0.7 to 0.9. One advantage of the long-gauge sensor is the introduction of a substrate, such as a steel plate, upon which the FBG is attached to in-house before affixing to the structure. This allows initial characterization of both K_T and K_ϵ using the temperature variation method with a second unbonded FBG. The long-gauge strain dependence will be explored further in Chapter 6.

4.5.2 Interferometric sensors

Interferometric sensing refers to two distinct types: SOFO and Fabry-Perot. SOFO sensors (term originated from French phrase "surveillance d'ouvrages par fibres optiques" meaning "structural monitoring by optical fibres") are categorized as long-gauge sensors, whereas, Fabry-Perot sensors are classified as point sensors (Table 4.1) [75].

Intrinsic SOFO

The SOFO sensor consists of two single-mode optical fibres which are terminated by mirrors and attached together between two points as shown in Figure 4.8. One fibre is loose between the two points, labelled the "reference" fibre, and is isolated from strain. The second fibre is pre-stressed and will deform under tension or compression. An interrogation system is capable of determining the length difference between the fibres by way of measuring the coherence of light [92, 93].

Extrinsic Fabry-Perot

The Fabry-Perot interferometer uses a cavity and two parallel mirrors to create two reflections at a particular path difference, as shown in Figure 4.9. An interrogation system is capable of determining this path difference, which can be used to calculate the change in strain between attachment points.

4.5.3 Scattering

Scattering is an unavoidable, yet useful phenomenon that occurs in optical fibres, where light projected through the fibre collides with atoms inside the fibre. The three types of scattering cause reflections of particular wavelengths, as shown in Figure 4.10. Stoke and anti-stoke components refer to the nature of the collision, with stokes referring to an absorption by the atom thus an
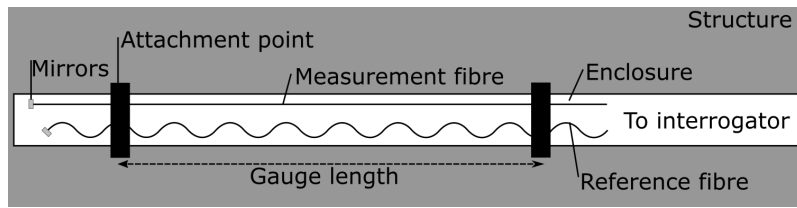
Figure 4.8: SOFO interferometer sensor: attachment points are mounted to intended structure. Measurement fibre will deform, interrogator system will determine length difference between the fibres.
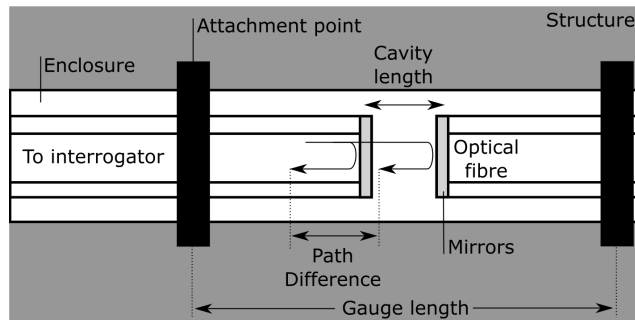
Figure 4.9: Fabry-Perot interferometer sensor: attachment points are mounted to intended structure. Interrogator evaluates strain from the path difference of the reflections which depends on the cavity length; therefore, deformation of the structure.

emitted photon with lower energy. Rayleigh-scatter is commonly used in telecommunications for determining attenuation constants, as well as providing detection of breaks in the fibre. Scattering (particularly Rayleigh and Brillouin) is also exploited to achieve distributed optical strain sensing (Table 4.1), where strain can be monitored over a long distance using a single fibre. Raman-scatter is only dependent on temperature, as this occurs due to vibrations originating from temperature changes. Brillouin-scatter is moderated by acoustic waves present in the fibre diffracting the light. This acoustic characteristic is dependent on the density of the core which is temperature and strain dependent - allowing measurement of their values.
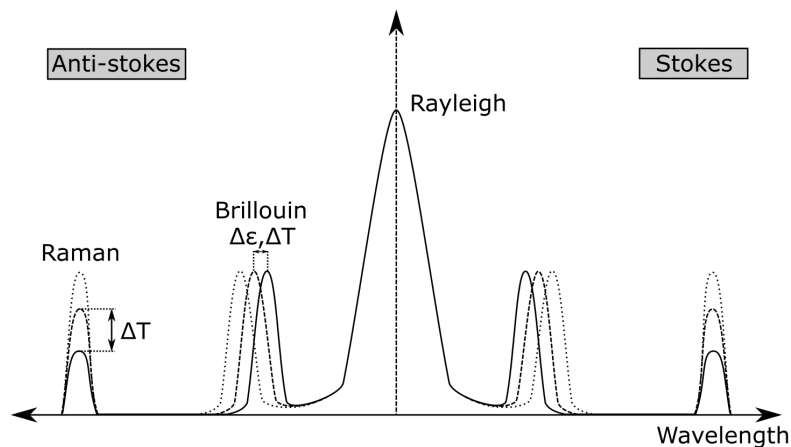
Figure 4.10: Wavelength of backscattering in an optical fibre.

4.6 Accompanying sensors

As discussed, an overall SHM sensor system is usually a combination of structural and environmental measuring devices. A combination of both provides possible validation and comparison to be made. So far, only strain measuring sensors have been considered. In order to gain an informative structural health state, other additional measurands are usually monitored. These will now be discussed.

4.6.1 Temperature

Temperature is a key measurand in SHM, not only for compensation purposes of other sensors, but for direct health state information. For example, Ranz et al. [94] demonstrated the use of temperature and humidity sensors with ultrasonic imaging for monitoring damage caused by freeze-thaw cycles. From Section 4.5.1 it was discovered that FBG strain sensors are heavily influenced by temperature; therefore, improper compensation could lead to false strain measurements. This is true for most strain sensors, meaning both are usually included in a single construction. There are a great number of methods for measuring temperature and the choice is usually dependent on either the application or the strain sensor used, or both. For example, FBGs have the capability of multiplexing, so if strain is measured with an FBG it is usually convenient to include a strain isolated FBG in series to provide temperature measurement through the same interrogation equipment. Post-measurement synchronization is also not required as the sensors are sampled simultaneously. In other cases, a simple electrical thermometer can be used, with a large number of low-cost, high accuracy thermocouples commercially available, meaning it is uncommon for an SHM application to implement a uniquely designed temperature measurement device.

4.6.2 Wind characteristics

Structures such as bridges and buildings are commonly inflicted by continuous varying forces due to wind. It is common for instruments to be used to monitor the wind speed and direction at the topmost section of the structure. An anemometer is a common device used for monitoring the wind speed, where a vertical shaft is connected to wind collecting shapes such as cups, causing rotation and measurement of wind speed in ms^{-1}. In some cases, a wind vane and anemometer are combined to provide both wind speed and direction measurement simultaneously. A wind vane simply uses a geometric shape to induce rotation, ensuring the shape remains parallel to oncoming wind allowing measurement of the direction. This data can be used to validate readings from strain sensors through the use of a mathematical model, estimating strain on the structure due to wind.

4.6.3 Acceleration

A common substitution or accompaniment for a strain sensor is the accelerometer. Although not directly monitoring a physical deformation in the structure, accelerometers can be used to monitor the motion or vibrations of tall structural components. The physical measurement is usually the displacement of a suspended mass, which can be produced in an electrical form similar to an electrical strain gauge through geometric changes in conductive components. Accelerometers can be used independently in a SHM system or in addition to strain sensors for further validation purposes.

4.7 Notable sensing options

4.7.1 Vibration-based

Vibration-based sensing for SHM is a highly developed method and is widely used today. The concept is built on the fact that the dynamic modes of a structure are dependent on the factors such as stiffness and mass. These factors will be influenced by any damage. An SHM system will involve the application of sensors to measure these dynamical modes over time, highlighting any variation that could indicate damage initiation. The main advantage of this type of sensor is the capability of global monitoring. Most of the sensors presented so far focus on monitoring local measurands. However, in some cases global monitoring is not suitable. For example, in this application of crack monitoring, the intended outcome is to ensure cracks remain above certain limits to prevent loss of structural integrity. Applying a global type sensor will monitor structural characteristics, which will not be affected by superficial cracks. Therefore, a local-based sensor is more suitable.

Basic strain gauges can be used for vibration-based sensing; however, some exclusive sensors have been introduced for this purpose. Possibly the most popular type of sensor for vibration testing is the piezoelectric transducer. Piezoelectric materials generate a small charge when subjected to stresses, allowing vibrational testing [95]. The primary advantage of this type of sensor is the self-powering property - meaning a power supply is not required. The charge is very low, requiring amplifiers for measurement, introducing uncertainties and a frequency limit.

The laser Doppler vibrometer is a possible sensing solution for vibrational testing. A laser is directed at a reflective surface on the structure, allowing measurement of the surface velocity and dynamical modes. Such a system is non-destructive and provides a very high resolution [71]. The main disadvantage of this sensor system is the requirement for a clear path for the laser to meet the surface.

4.7.2 Wave propagation

Wave propagation techniques, specifically guided ultrasonic waves, have received wide attention for SHM applications. Elastic waves, such as Lamb waves, can be propagated through a medium - interacting with any defects producing reflections. Such systems are capable of monitoring structures over a long distance [96, Chapter 5].

4.8 Chapter summary

A thorough investigation into available sensor systems and their operational procedures for strain measuring is presented in this chapter. Initially, the conventional electrical strain gauge is introduced and compared to optical sensors. Optical sensors provide many advantages over electrical and has rapidly become a justifiable alternative and the staple for SHM applications in the last decade. Optical strain sensors can be categorized by incrementing gauge length: point (≈ 20 mm), long-gauge (≈ 1 m) or distributed (≈ 1 km). FBGs in particular are commonly implemented due to their high flexibility, relatively low cost and small size. Although primarily a point sensor, with particular packaging they present effective long-gauge sensors. FBGs consist of a grating of modulating refractive index, written into an optical fibre usually using a phase mask fabrication technique. The grating causes a particular wavelength of light to be reflected, known as the Bragg wavelength, which can be customised to vary the characteristics of the reflection. Monitoring this reflection over time can provide information on the temperature and strain subjected to the FBG. Similarly, the interferometric sensor uses light reflection to measure long-gauge strain. Distributed sensors exploit the scattering phenomenon that occurs in optical fibres. Light scatters when incident on impurities in the fibre glass, some of which is reflected backwards and can be monitored to provide measurements over the entire length of the fibre. A single strain sensor is effectively useless without accompanying environmental characteristics such as temperature, wind speed and structural loads/accelerations - such measurands are discussed with relevant sensors. Overall this chapter provides an insight into the typical techniques used for strain measurement and the accompanying environmental measurands useful for SHM purposes.

Chapter 5:   Real-world SHM sensor applications: a review

5.1   Chapter overview

In this chapter, a review of various reported sensor systems in real-world SHM applications is presented. Initially, a definition and classification of the SHM sensor subsystem will be presented. This can be used during the discussion of the reported sensor systems and can also serve as an initial design step in determining the best approach to the SHM problem in this work. SHM of civil infrastructure such as bridges and buildings will firstly be considered before concentrating on applications to onshore wind turbines. This will establish benefits and flaws to contemplate during the design of such a system for monitoring cracks in an onshore wind turbine foundation and also highlight the uniqueness of such a system.

5.2   Classifying the sensor subsystem

Over the years, the definition of an SHM system has been contemplated and adapted. Extensive reviews are available and have been summarized in Chapter 4, Section 4.2. During this summary, SHM was split into three subsystems: Sensing, Interrogation and Analysis. The purpose of this review is to assess and discuss sensors applied in real-world SHM systems, so focus will primarily be on this subsystem. In some cases, the sensor system may be solely chosen for the related interrogation or analysis, if so this will be discussed. The objective of this review is to study previous methods of sensing and define which were most and least effective in determining the health state of the instrumented structure. Possible improvements that could be made to the system will also be discussed. The identified strengths and flaws of the system will be used to aid in the design of a sensor system to be applied to monitor cracks in an onshore wind turbine concrete foundation. As mentioned previously, visual inspection is still widely used today for SHM. Generally, it is a reliable method for determining the approximate health state of a structure and requires little commitment from site owners. However, the cost is difficult to quantify, the process can be time consuming or disrupting and the measurements are intermittent [97]. As outlined in Chapter 4, Section 4.3, sensor systems could potentially provide many benefits over the long-term when compared to visual inspection. These benefits have attracted companies to invest in sensor systems to be employed for SHM purposes. The overarching objective of SHM, including visual inspection, is to determine the current health state of the structure, ensure efficient operation of the structure and provide notifications when repairs are required.

To build on the previous four level representation of SHM systems discussed in Chapter 4, Section 4.2 and visualized in Figure 4.1, further categorisation has been devised by the author and introduced in this thesis for the sensor subsystem itself. The purpose of this classification is to provide a clear distinction when analysing real-world systems and allow a more effective comparison.

This classification was conceived simultaneously to the literature review and is therefore based on the observations of the author during said review. The classification is presented initially to aid the reader.

5.2.1 Measurands

The first definition concerns measurands, in other words, what the sensors are capable of measuring. This will of course depend heavily on the intended application. These can be split into three incrementally complex categories:

Environmental: The simplest of sensor system involves measuring environmental features only, such as temperature, wind speed or humidity. This can be used directly for SHM, such as for damage detection. For example, if wind speeds greater than a certain level are deemed excessive for a structure and are known to initiate damage, this can be alerted. Usually environmental factors are measured in conjunction with other data types to allow verification and correlations to be made.

Structural: The second level of measurands regards structural characteristics. This can include acceleration, strain or displacement. Many methods will be explored during the review where these characteristics provide SHM possibilities, but an example would be monitoring strain in a key structural element which may change if cracks appear.

Direct: The final level of measurands introduces direct damage monitoring. The key difference in this level is the addition of detecting damage degradation, rather than only initiation. Distinction between the two is required due to the fact the severity of newly formed cracks can be superficial and may not affect the structure's health as a whole. Sensors can measure damage directly in a number of ways which will be discussed during the review, but one example would be to measure the width of a crack or many cracks over time.

5.2.2 Timing

Timing encompasses two major factors that constitute to an effective sensor system: sampling frequency and length. To put this in perspective, using the SHM system definition from Chapter 4, Section 4.2 and assuming a system with fourth level capabilities (detecting, localizing, determining severity and impact of crack or crack degradation). Such a system may employ a sensor subsystem with slow periodic measurements and limited data storage. This sensor system may not be suitable in some applications - such as if dynamical analysis is desired. Therefore, a second categorisation can be introduced which describes varying available data acquisition rates and measurement lengths of sensor systems. These particular characteristics may also be limited by current interrogation and storage technology available. Categories are described in Table 5.1.

Sensor System	Definition	Example sensor
Static	Single measurement, no memory	Liquid-in-glass thermometer [98]
Progressive	Limited sampling frequency, limited memory	wireless hygro thermometer [99]
Express	High (kHz) sampling frequency, limited memory	NA[2]
Historical	Limited sampling frequency, historical memory	Brillouin scattering (Section 4.5.3)
Extensive	High (kHz) sampling frequency, historical memory	FBG (Section 4.5.1)

Table 5.1: SHM systems and examples based on timing capabilities

To provide an overview, a static sensor would only be capable of providing the user with a single measurement point, regardless of frequency, without saving this data point for future reference. A progressive sensor system would have limited periodic sampling rate and be capable of saving a limited amount of data (without manual intervention these data points will either be lost or overwritten, or the sensor will cease to log). An express sensor system would be capable of high sampling rates (which is defined as in the range of kHz) but have limited memory. It is worth noting that this system is counter-intuitive and niche as large frequencies require more memory. A historical system introduces the ability to continually save the data over long periods of time, but with limited sampling frequency. Finally, an extensive sensor system would be capable of high frequency measurements and have the ability to save long-term historic data. The reason for segregating these factors is to provide a more distinguished sensor system categorisation. For example, if a system is required with the intended application of measuring vibrational loads in a tower during a predicted earthquake for the purpose of detecting and locating any magnitude of damage (level 2, Figure 4.1), an express system would be appropriate in this application, provided that there is sufficient memory for the earthquake period. An extensive system would also be suitable, but may introduce further considerations such as cost and complexity in installation. Although counter-intuitive (since high frequency will require more memory), an express system should be possible and would fit certain requirements.

5.2.3 Complexity

When considering a sensor system for SHM, complexity is a key definition. To clarify, this involves how ambitious the system is in terms of: number of observed measurands, total number of sensors, type of multiplexing (serial or parallel) i.e. cabling requirements and finally the type

---

[2]Possible, but counter-intuitive.

of attachment (amount of structural interference). When studying complexity, it is paramount that the application is disregarded when possible, since some applications will introduce significant complications initially. For example, measuring strain over the entire length of a sub-surface water pipe introduces significant complications immediately. The focus here is to identify how broad the system is for a particular application, for example, measuring strain at one point in a structure compared to measuring strain in every wall of the structure. This represents two distinct systems with different complexities. To categorize this, Table 5.2 is used as an approximate guide of sensor system complexity depending on each component. The systems overall complexity is then a combination of each separate component. An example of a real world system portraying each conceived complexity level from literature is also provided. These will be discussed in more detail during the review that follows.

Component	Low	Medium	High
Measurands	1	2-3	4+
Sensors	≤ 6	7-14	15+
Multiplexing/cabling	Wireless or serial only	Serial and parallel	Parallel only
Attachment	Isolated	Retrofitted	Embedded
Examples	$[7, 100]$	$[101, 102]$	$[103, 104]$

Table 5.2: SHM system complexity factors

5.2.4 Application

The intended application will most likely influence sensor design. Due to the large number of possible applications, this cannot be categorized in the same way as the previous definitions. These restrictions will be unique for every intended application and can possibly be the most important feature. For example, a characteristic such as sensor size belongs in this category as it will vary depending on application. Also, the conditions of installation may vary the sensor design - which is also due to the application. For example, attaching a sensor to a large scale bridge presents great complexity with regards to safety, installation procedures etc. and is impossible to categorize.

5.2.5 Other

There are various other notable dependencies that are improbable to categorize but require noting. Firstly, the measurement accuracy of a sensor system is important. Measurement accuracy can be described as the error in each recorded sample due to the sensor alone, or the minimum change the sensor is capable of recording. Generally, the accuracy of a sensor is given as a "resolution". It is key that the applied sensor system has adequate resolution for the intended purpose, as changes below the resolution are usually indistinguishable. Other errors in measurement are also worth considering, such as losses due to connections and cabling, noise from environmental factors, or

drifts. It is often difficult to characterize these losses prior to installation (in order to perform future compensation), as causes can be random or sporadic. Generally, prevention methods are put in place to reduce the impact of these errors. For example, employing topologies to reduce the number of cables/connections, ensuring sensors are protected/sealed from the environment or applying filtering to reduce noise.

Finally, the economics of a sensor system may greatly influence its suitability in a project. In fact, it may be the most important factor when choosing a sensor to employ. Most companies pursue a profitable SHM project, either monetary or indeed academically (the more useful the information gained from the project, the more money will be supplied). The budget at the beginning of an SHM campaign may restrict or grant access to particular sensors. It will also have a great effect on the previous classifications. For example, the complexity of a system (i.e. number of sensors installed) will depend on the available funds and the net gain on increasing the complexity.

More dependencies are likely to exist; however, at this stage of the research, the presented categorization is sufficient to assist the literature review. Any further research in this regard is outside the scope of the thesis.

5.3   Structural health monitoring of civil structures

SHM is performed in many industries, particularly engineering categories such as civil, aerospace or nuclear. In this review, concrete civil infrastructure will be the broad focus: such as bridges and buildings, before narrowing to applications in onshore wind turbines. This review will outline the initial need and eventual benefits of monitoring each structure, before assessing and categorizing the sensor system chosen using the previously defined classification from Section 5.2. Other varying design factors will also be mentioned when appropriate, such as sensor encapsulation, interrogation methods and data analysis algorithms.

5.3.1   Conventional method and opportunity for sensors

Monitoring the health of a civil structure is essential if prolonged life is desired. Since damage is inevitable in concrete, one important reason for monitoring is to provide information on the immediate requirement of repair. This can prevent irreparable damage which would require the demolishing and rebuilding of the damaged section or perhaps the entire structure. As previously mentioned, common practice is visual inspection; however, this process does not identify underlying issues that may not be viewable, such as sub-surface damage. One example of this was discussed by Yukio, reviewed in [105], where seismic activity caused excessive damage to the Hanshin Expressway Public Corporation highways. Overall around 300 highways required repairs, all of which consist of many concrete piles which were driven and secured into the ground. The damage was visually inspected, and it was found that hidden damage occurred on the section of piles underground. This demonstrates first hand the main problem with visual inspection, specifically for large structures:
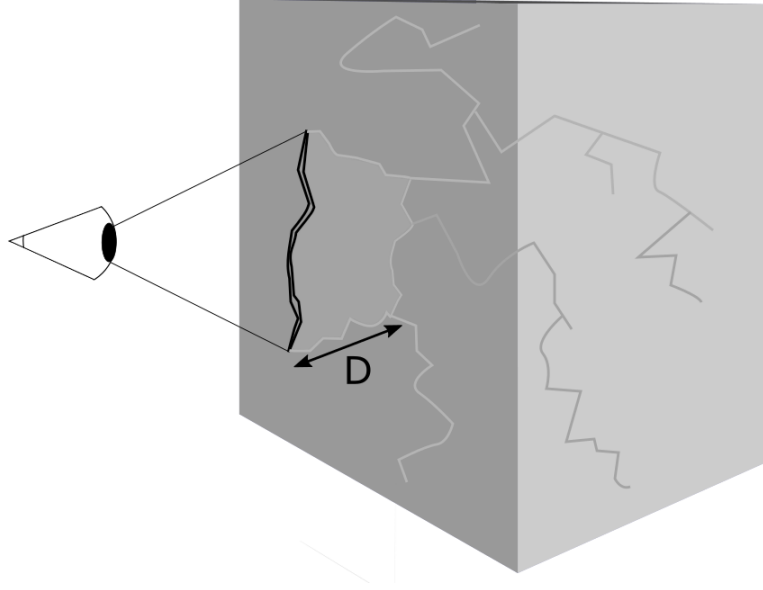
Figure 5.1: Crack network formation beneath the surface.

the only way to gather knowledge on sub-surface damage is to excavate the section, meaning every time this information is required, the section will require excavation. Not only is this accumulating expense over time, some of this expense and effort is unwarranted, as it is possible some sections will not be damaged. Should sensors be installed initially, this can be avoided as the damaged and undamaged sections would be identified without the need for further excavation, lowering long-term superfluous costs. Additionally, this information will be more comprehensive and precise.

A second issue with visual inspection in regards to crack monitoring is the fact the crack is assessed from the surface. Usually, cracks will penetrate the concrete in a multitude of networks branching in many directions. These may affect the displacement of the surface crack during operation and may not be apparent under static conditions or be perceptible from the surface. Zhou et al. [106] used dye impregnation and digital optical microscopy to analyse the effects of loading and transport properties of concrete cylinders on crack networks. The three phase experiment included cyclic loading of the specimen and extraction of two smaller samples for transport property testing, following which cracking was observed. The method provided a crack width recognition sensitivity of 20 μm and greater. From the results and images it is clear the networks are random and vary in severity, outlining just how complicated a crack can be sub-surface. Figure 5.1 is an exaggerated example of the possible reality of a face crack. Extending to a depth D measurable by the visual inspection methods, the crack networks spanning from this can be severe and will likely affect the crack displacement during operation. For these reasons, directly monitoring crack widths during operation may provide a more accurate representation of severity and deterioration.

5.3.2 Sensor Applications in Civil Structures

5.3.2.1 Bridges

Civil infrastructure encompasses any construction that is used by the general public. Roads, buildings and bridges can be considered as civil structures. Bridges are of particular concern in terms of structural stability due to reasons such as:

Safety: many pedestrians use bridges simultaneously and may be present within the vicinity.

Loading: they may be subject to high unpredictable forces and can contain sections that are not directly supported by the ground.

Delays: a bridge repair or collapse can cause delays to a large number of people and cause large impact to surrounding civilization.

Salt water: bridges commonly span over inland sea and salt water is known to accelerate corrosion in steel, meaning it is more likely to rapidly fail.

Due to these reasons SHM systems are commonly implemented to bridges, with a vast number of reported applications. Early work on bridge monitoring by Brownjohn et al. [107] in 1994 focused on verifying computer models of the large Humber Bridge's reactions to wind. The sensor system used contained many types of sensors from anemometers and thermocouples to accelerometers and optometers meaning both environmental and structural measurands were monitored. In terms of timing, each sensor type has separate sampling frequency capabilities, but due to the low frequency nature of bridge modes and response to wind loads, the requirement was low frequency measurements. However, most sensors signals were recorded by one set of equipment, meaning storage was limited and required manual extraction following several hours of measurement, although this was upgraded to allow periods of up to 20 days. Therefore, this would be categorized as a progressive system. The sensor system itself is fairly complex, with a high number of measurands and sensors. Sensors were multiplexed in both parallel and serial configurations, but attachments varied between isolated and retrofitted for the environmental and structural sensors respectively. Understanding the overall behaviour of a structure under normal operating conditions is very useful in correlating time points where damage initiation has a high probability. The purpose of these sensor systems was to combine them to collect information on the movements of the bridge under certain loading and to better understand the day-to-day modal parameters of the bridge. In terms of relation to work in this thesis, measurement of the entire structural characteristics does not provide direct measurement of damage; therefore, damage degradation would not be possible to identify. Knowledge of the normal operating conditions would prove useful in determining any effects damage has to operating efficiency or will at least provide reference of a "healthy" structural state.

Moving on to damage detection, Ko et al. [103] reported an extensive SHM project spanning three separate bridges in Honk Kong: Tsing Ma ≈ 1377 m span suspension bridge, Kap Shui

Mun ≈ 430 m span cable-stayed bridge and Ting Kau ≈ 450 m double span cable-stayed bridge. They declare a total of more than 800 sensors over the entire project including accelerometers, strain gauges, temperature sensors, displacement transducers, anemometers and level sensors, all of which monitor continuously, epitomizing the great challenges for data management and cabling. The overall purpose of the system is to monitor dynamical behaviour of the bridge for "intelligent vibration control", which addresses the issue of stresses induced in cables due to vibrations by using dampers controlled autonomously by the sensor system. Dynamical modes of the bridges are low frequency, which combined with the large number of sensors suggests a relatively low sampling rate would be used, although this is not directly mentioned. Therefore, the system itself is most likely historical, with the capability of long-term measurement of low frequency measurands. Additionally, Ko et al. explored possible techniques for damage detection using the same sensor system, proposing a neural network based, third level approach to detect, locate and determine severity of damage from noisy vibration data. Using training data, the network was able to alarm of damage, portraying the possibility of using the system for damage detection. A second method for detecting localized damage using the strain gauges is also discussed, which was capable of alerting to anomalies caused by local damage or sensor fault. The original large sensor system consisted of only electrical devices. To improve the system, fibre Bragg grating (FBG) optical sensors have now been implemented to the Tsing Ma bridge for comparative studies. The main benefit gained is the ability to multiplex several sensors on one channel, which greatly reduces the complexity of the large sensor network. The installation was reported by Chan et al. [104] where 40 FBGs were instrumented to three strategic sections of the bridge: cables, rocker bearings and the support structure. The main objective was to determine if measuring strain in the bridge sections using FBGs could provide the capability to perform SHM, but also to assess the effectiveness of the FBGs in comparison with the existent electrical system. The sensor design encapsulates two FBGs within a box, one epoxied to measure strain and the other independently measuring strain-isolated temperature. Taking advantage of differing curing times of two epoxies (one fast and one slow) allowed a quick attachment, but a final strong overall bonding to the structure. Epoxy is generally regarded as a good choice for strain device attachment with most commercial manufacturers, such as Micron Optics and their os3200 optical strain gauge, opting for an epoxy attachment. A second type of attachment involves metallic bonding, which consists of a brazing and welding of the FBG package. Investigation into the fatigue life of epoxy and spot welding for final attachment is well documented, such as in [108]. Comparison of the attachment effectiveness for strain measuring purposes is relatively unexplored, despite being of great interest in the field. This is an avenue of research that was considered in this work. Results in this study showed that the FBG sensors multiplexing ability allowed easier and less complicated installation, cabling and data collection. Following data analysis, Chan et al. concluded that FBGs also provided comparable results to the original system and presented an enticing alternative to the conventional electrical strain gauges.

Hoult et al. [101] reported an application of a wireless sensor network applied to measure crack widths in the Ferriby road bridge in the UK, demonstrating a direct damage monitoring system. Three nodes consisting of displacement transducers are located on three main cracks on the underside of the bridge. A further three nodes containing inclinometers were attached to the bearings of the bridge. Both types of nodes also contain sensors to measure temperature and relative humidity for compensation purposes. Classifying this system - measurands are mainly environmental (temperature and humidity) and direct (crack widths). Perhaps an initial improvement would have been to include accelerometers or strain sensors to provide an indication of the structural loading in the bridge as a whole. The inclinometers were used to measure any angle changes in the bridge supports which was of concern to bridge operators. Focusing on the crack width monitoring - the chosen sensors were linear potentiometric displacement transducers (LPDT). Similar to simple electrical strain gauges, these sensors measure resistance variance due to geometric changes in an electrical circuit. The complexity of this system overall is average: 4+ measurands and around 18 individual sensors retrofitted in 6 separate nodes wirelessly transmitting the data. The choice of wireless sensors is interesting, as this will greatly reduce installation complexity but will limit either sampling frequency or memory capacity. Other drawbacks of wireless sensors include synchronization difficulties of multiple sensors and also security concerns. There was a specific reason for the choice: since the bridge crosses a busy and heavily used road, the sensor installation required partial closure of the road and would cause public delays. Therefore, minimizing the time of installation is a key requirement for this sensor system, as it reduces community disruption and installation costs to the bridge operator. This is a prime example of the application significantly controlling sensor design. To meet specific requirements the effectiveness of the sensor for displacement measurement may be decreased. Results showed crack displacements did not exceed ≈ 0.02 mm over the course of the 5 month measurement campaign. The resolution of the interrogation set up is declared as 0.01 mm, so these measurements are close to the noise threshold - suggesting if cracks deteriorated it was lower than this level. This is also a good indication to what sort of resolution may be required for detecting crack deterioration over short-term periods. During sensor design, an improved resolution value should be aimed for. Perhaps if bridge closure was less of a hindrance, sensors with improved resolution could have been implemented.

5.3.2.2 Buildings

Buildings are commonly instrumented with SHM sensor systems for the same reasons as bridges, discussed in Section 5.3.2.1. Other reasons can include:

Height: tall buildings are more susceptible to overturning moment loads from wind.

Culture: to ensure the well-being of a culturally notorious landmark.

Importance: important buildings such as government buildings or hospitals are vital for the operation of a country.

Ni et al. [109] demonstrated an SHM sensor system applied to a building meeting two of the above cases: height and importance. The Shenzhen stock exchange measures 228 m in height and consists of a floating platform 36 m from the ground surrounding the main trunk of the building. The report discusses the initial results during construction of the building. The main objective is to monitor the cantilever loading on the floating platform - including strain and deflection; however, an overall health state for the entire building is desired. This highly complex sensor system consists of 224 vibrating-wire strain gauges, implemented to the floating platform at pre-determined "critical members" alongside many temperature sensors and accelerometers. A "novel vision-based displacement tracking system" was also developed to monitor the deflection of the cantilever platform. The operation of this system is not extensively discussed, no deflection data is provided at this stage. The strain gauges are interrogated with parallel cables initially to separate acquisition units, which then wirelessly transmit the data to a central processing area. Results from the initial "unloading" of the platform provided real-time stress levels in the structure during removal of temporary supports of the floating platform. This information allowed for a faster removal than scheduled, as the stress levels could be closely monitored. Following this, a wireless accelerometer network monitoring vertical displacements of the platform allowed extraction of the modal frequencies of the structure, which were compared to predictions gathered from an FEM model, validating the initial predictions. Although there are a large number of sensors applied, only 3 variables are measured: strain, acceleration and temperature. The sampling rate of strain sensors is relatively low at 1 Hz with accelerometers sampled at 100 Hz. Interestingly, the wireless system adopted is capable of real-time transmission of the data to the central processing area for storage, meaning historical memory is possible. Therefore, this can be classified as a historical retrofitted sensor system.

Fritzen et al. [110] describe a model-based approach to damage detection in a structure affected by seismic activity. A test structure known as the "Steelquake" was designed to imitate a two-storey building consisting of vertical and horizontal beams supporting two floors of concrete slabs. A total of 15 electrical accelerometers were instrumented, described in more detail by Worden et al. [111]. Essentially an FEM model and technique known as "effective independence" are used to determine the most appropriate locations. The objective of this project was to perform level 3 SHM: detection, localization and quantification of damage. Accelerometers measured the dynamics of the structure and were compared to calculated modal frequencies, shown to match fairly accurately. An algorithm is formulated to compute particular modes in order to determine if damage has occurred in specific locations - certain modal changes represent definitive damage locations. After seismic loading, the model correctly predicted damaged members that showed physical cracks in the steel. Although this application is not concrete based, it presents an interesting approach. The complexity of the physical sensor system is fairly low, with only one structural measurand and

15 total sensors. The paper does not confer in detail the sensor capabilities: sampling frequency or memory capabilities are not mentioned. Since the sensors are measuring dynamic behaviour, with frequencies up to 22 Hz, it can be assumed the data will be collected at a fast rate and with historical memory, providing an extensive sensor system. The latter paper [111], provides an overview of similar work by authors applying the same methodology to a bridge. The important feature of these works is the focus on the analysis method applied - an effective analysis can provide useful information from the most basic sensor system.

An application of FBGs for crack monitoring was presented by Lima et al. [102] on the 300 year old church of Santa Casa de MiseriCordia. The main purpose was to ensure the well-being of this culturally significant building. Although subject to restoration activities throughout the lifetime of the church, damage continues to appear in the form of large cracks. To ensure the structural integrity of the church, an SHM system for monitoring the development of these cracks was desired. Physical appearance of cracks included tensional due to both opening and sliding modes as well as some torsional cracks due to tearing modes caused by rotation of stones (see Chapter 3, Section 3.4.2). FBGs were chosen and proven to be capable of monitoring crack width on planar and non-planar faces. Non-planar refers to cracks with sliding displacements, meaning faces are not aligned. Displacement sensor design consists of two sensor supports fixed by epoxy to each crack face, with a suspended FBG epoxied in-between. The epoxy minimises any damage to the structure that would accompany bolt fixing. A secondary requirement from this application was to minimise visual impact to the public, who were able to continue visiting the historical church. This meant FBGs remained unpackaged and bare. Sensors were implemented on to 19 pre-determined cracks, with an accompanying 5 temperature sensors. Results from a one year period showed no sharp changes in crack widths, with displacement changes not exceeding 0.12 μm over the entire year. However, some structural events are clearly measured in the displacements, including an earthquake. The sensor resolution is quoted as between 1.1 and 2.3 μm for displacement measurement, which means measured displacements are below these thresholds. Sampling rate of sensors is not mentioned, graphs show only 1-2 samples per sensor per month, which is extremely slow. The system can be described as historic since measurements span a long-term period. To classify this sensor system further, with only two measurands and 24 sensors this is a relatively small scale, medium complexity project. Sensor attachment method and packaging was heavily influenced by the application. To improve on this system, incorporating some strain sensors around the structure in order to monitor the structural response would allow comparison between structural loading and crack displacements, as well as between later and earlier damage states. It is unclear if measured displacements are expected or if the crack has deteriorated. Furthermore, analysing the sensor design, a bare FBG does indeed provide a low visual impact but can be incredibly fragile and would not be suitable for long-term measurement campaigns, especially since the public will have access to the sensor area. In terms of accuracy, it is unclear if the resolution of the interrogation

system impacts the results, as displacements are below this. Also, it is unclear if results were down-sampled from original data, as 1-2 data points per month will not identify any instantaneous changes or provide dynamical information.

5.3.2.3 Other notable applications

Aerospace

SHM is an interesting approach when caring for aerospace components. Most modern SHM systems have difficulty in providing accurate instantaneous real-time information - which would be a vital requirement in an aerospace application. Hunt et al. [112] report such an SHM sensor system implemented on the Eurofighter Typhoon jet. The objective is to provide real-time event monitoring and perform fatigue life analysis (more specifically, calculate consumed fatigue life at specific location in the Typhoon) by using data received from a number of sensor systems. This includes the highly complex electrical instruments already onboard, utilized in combination with applied strain gauges to pre-determined locations. The type of strain gauge is not declared; however, an electrical-based sensor would easily integrate with onboard systems. The onboard instruments provide altitude, velocity, acceleration, weapon configuration and fuel mass variables, all of which affect the stress on the aircraft. The analysis system is capable of determining stress levels using a memory-based approach with the provided data and using previously performed FEM models. Although dissimilar to the more common concrete structure that is the focus of most SHM, the previously defined categorisation can still be used to better understand the sensor system. There are around 6 measurands in total, with strain measured with a number of gauges (up to 10). Although real-time analysis is performed, the sensor systems sample at 16 Hz, which was validated as a sufficient rate to determine the dynamic response of the Typhoon. According to our classification, this represents a historical sensor system, but with a real-time analysis method.

Pipelines

A unique requirement for some applications such as pipelines is an extremely long sensor in order to monitor the entire length of the structure. Inaudi et al. [113] discuss multiple problems addressed in pipeline applications, such as temperature changes, leakage, intrusions, strain and deformation using distributed fibre optics. The distributed sensors are able to span the long distances (kilometres) and measure the intended components at any location. In one example, a leakage was correctly detected and alerted in a long brine pipeline by monitoring temperature changes every 30 minutes. In a second example, a different type of sensor design (but similar in operation) was installed in a gas pipeline - providing informative deformation levels of the pipe during events such as earthquakes. Measurements in this case were taken only once a month. Interestingly, the sensor system itself is relatively simple - consisting of a single long optical fibre. The complexity lies in the interrogation and data storing systems. The spatial resolution for a Brillouin scattering

based technique can be as little as 2 m, meaning 12,500 data points per sample for a 25 km cable. This means the sampling rate can exponentially increase the size of the data - hence the long time between samples in the discussed applications. A larger sample rate could also cause long, time consuming analysis. This limited sampling rate makes this sensor system inappropriate for measuring instantaneous changes. Categorisation is difficult, with 1-2 measurands and a single fibre it would at first glance seem simple. Adding the large data quantity with difficult interrogation and analysis completes a fairly complex system overall. The defining factor is the application - such a sensor system could not effectively be used in other applications such as crack monitoring, but perfectly integrates with requirements for pipeline monitoring.

Smart materials

An intriguing approach to SHM is the use of "smart materials", which encompasses a broad spectrum of applications that essentially involve the incorporation of sensors directly into a material. For SHM, this can include directly embedding sensors into a structures material initially [114] or retrofitting a material containing sensors in order to detect cracks [100, 115]. In the former [100], Zhou et al. used a web of thin enamel coated copper wires attached to a plastic film to monitor cracks on the Taipingzhuang bridge. Each patch covers 2.6 x 1 m area, with spatial resolution of 10 cm between wires. The wires will break at a onset strain and can; therefore, detect the onset of cracks. To determine crack widths, different diameters of wires are used as this will change the failure strain of the wires and thus different wires will break at different strain (i.e. crack width) levels. This is done by pre-tensioning the wires prior to applications. It is not disclosed whether the sensors were successful in detecting any cracks during monitoring. If successful, this work demonstrates a sensor capable of monitoring a large area for crack initiation. In the latter report [115], Zhang et al. proposed an improved design consisting of pre-determined various wire diameters in the one sensor - removing the difficulty encountered when attempting specific pre-tensioning. The required wire diameters are calculated by estimating the maximum crack width expected in the chosen section. This design was applied to the Jiangjin Yangtze River Highway Bridge and presented some results. A few wires were found to have broken and some cracks were discovered in these locations. However, due to the small number of broken wires, it is likely these are not large structural cracks. This sensor system is of particular interest due to the ability to distinguish varying crack displacement limits. It would be fascinating to see if the same sensor could monitor the same crack over time - with thicker wires failing as the crack deteriorated - unfortunately this is not discussed. In this system, the only measurand is the direct monitoring of crack initiation and a total of 22 modules - each with 105 single wires. There is no indication of sampling frequency or memory requirements. The main disadvantage of this sensor is the single use - if a crack with maximum detectable width initiates, the sensor can no longer be used and will require replacement. This is not ideal for a long-term SHM system.

Component	Failure rate (%)
Gearbox	19.0
Blades	11.0
Generator	7.3
Controller	6.2
Yaw system	4.1
Tower	<0.3
Foundations	<0.2

Table 5.3: Estimation of failure rates of < 1 MW wind turbine components, based on work by Reder et al. [5].

5.3.3 SHM in onshore wind turbines

So far, applications of various sensor systems in civil infrastructure such as bridges, buildings, aerospace and pipelines have been discussed. The purpose of this work is to gain a broad vision of the past sensor systems used for SHM in order to aid in the design process of a sensor system for monitoring crack deterioration in an onshore wind turbine foundation. SHM of onshore wind turbines is not original - with many reported examples. As previously mentioned - the failure rate of foundations is relatively low when compared to other components. Table 5.3 outlines estimates of a few key component failure rates as reported by Reder et al. [5]. In this review, only the following structural monitoring systems will be analysed: blades, tower and foundations.

5.3.3.1 Blades

One of the most common SHM systems applied to turbines concerns the blades. Blades are the primary interface between the structure and the wind, witnessing nondamped loads and large magnitudes of stress. For extremely large turbines, measuring this directly can prove difficult as strain sensors often have relatively low ultimate stress limits - breaking or degrading significantly upon exceeding them. One sensing method that has been put into practice by Blanch et al. [116] and also by Dutton et al. [117] is acoustic emission (see Chapter 4, Section 4.7.2). In both cases, the sensor system consists of retrofitted piezoelectric sensors that measure elastic waves emitted by a source through the intended structural component. Any structural defects will affect these elastic waves and be measured by the attached sensors. During stationary and operational tests, Blanch et al. showed that the acoustic emission sensor system could monitor the blades for damage, but no damage was detected during tests. In the latter work [117], the system was capable of successfully identifying damage in multiple wind turbine blades. The sensor system in this work can be classified as an extensive monitoring system with only one measurand. Interestingly, this measurand is the elastic wave propagated deliberately through the medium - which consecutively provides direct damage monitoring. A total of 6 sensors were attached to a single blade, which represents a relatively non-complex system; however, the procedure for installing on an operational wind turbine presents significant challenges.

A second technique for detecting damage in a wind turbine blade is using vibration-based analysis, demonstrated by Tcherniak et al. [118]. An array of accelerometers are attached to the blade, measuring vibrations which are periodically induced in the blade via a mechanical actuator. A conventional turbine blade was instrumented with 20 accelerometers under laboratory conditions. An actuator produced vibrations every second in the blade, with accelerometer data used in an anomaly detection method. This method essentially uses previous non-damaged states to determine if damage has occurred. During testing, a crack was introduced at incrementing widths of 20-120 cm over time. The method showed that all widths of damage could be detected. Artificial noise was introduced into accelerometer data, with decent performance ($> 90\%$) of the method occurring at a signal to noise ratio of 0 dB. Similar to above, the measurand is a pre-applied phenomenon in the structure which provides direct damage measurement. The sampling frequency of accelerometers is not stated; however, it is expected to be less than 1 kHz as the presented spectral density of an operational blade shows prominent frequencies below 300 Hz. This system can be classified as a historical sensor system. With one measurand, 20 sensors, parallel multiplexing and retrofitted sensors - also noting the installation on an operational wind turbine would be additionally challenging - this system is fairly complex. It has yet to be presented as a viable option for monitoring operational turbines, again due to the challenging installation.

One interesting approach to monitoring an operational turbine blade with no required installation is proposed by multiple commercial companies: drones with cameras for improved visual inspections [119, 120] and thermal imaging [121]. For this application, such an approach is more effective than when used for concrete as the material of the turbine blades is less likely to exhibit sub-surface damage. Also, conventional visual inspection of blades can be difficult to carry out as it would require equipment to lift personnel close to the blades, which can be time consuming and dangerous.

5.3.3.2 Tower

Although less commonly monitored, the tower of a turbine presents catastrophic consequences upon failure and has been the focus of some SHM campaigns. Wondra et al. [122] reported the instrumentation of a 3 MW turbine tower with wireless accelerometer nodes. Using these sensors, the modal frequencies of the tower are gathered and monitored over time. Only two nodes were installed in the tower at two different heights. The sensor nodes, one of which focusing on environmental properties is reported by Kerkez et al. [123], are not fully extrapolated, but consist of accelerometers interfaced with a commercially available processor. Results showed the sensor system was able to monitor frequency components of the tower during operation, which will be useful for adapting an FEM model which then converts these into material stresses. This can be used to ensure stress levels remain below acceptable limits. The sensor system in this work is a little different as it is less bespoke, more commercially available. There is little customisation as the application and overall installation is rather straightforward. This allows the researchers

to take advantage of the available sensors to reduce costs significantly. To classify this system: the number of sensors is not apparent - perhaps 1 per node - with the structural measurand of acceleration. The measured frequencies are extremely low (< 0.5 Hz) and so the sampling rate of the sensors will equally be low. Considering this is a wireless network, memory is most likely limited, coinciding in a progressive sensor system. Complexity is low with a single measurand, 2 sensors, wireless interrogation and retrofitted nodes. The system relies on the FEM model analysis to provide useful information from the sensor data.

5.3.3.3 Foundations

Currie et al. [7, 8] presented an application to monitor damage degradation on an onshore wind turbine foundation. A unique case, damage coalesced at the base of the embedded ring, causing excessive vertical displacement of the tower and ring. These displacements caused further cracking on the surface of the foundations. To monitor the damage, a sensor system was developed to measure the vertical displacement of the tower. Any deterioration would be represented by larger vertical displacements of the tower. Linear variable differential transformer (LDVT) sensors were used, which operate by magnetic induction as a magnetic core moves between wire coils causing a voltage differential. Monitoring this differential provides displacement measurement of the core. A total of four LVDT displacement sensors were positioned at the base of the tower, monitoring the vertical displacement of the embedded ring and tower. Results portrayed a large spike in foundation displacement during periods of either wind turbulence or start-stop procedures. Turbine operators provided set limits of 3 and 5 mm to represent intermediate and extreme displacements. During a short time period, the extreme limit was breached as a drop in rotor speed accompanied a displacement of > 5 mm. This indicates that the damage at the base of the embedded ring has deteriorated beyond acceptable limits and perhaps repair should be carried out. This sensor system and analysis is relatively simple - four displacement sensors which are monitored over time with little post-processing, illustrating the benefits of using an effective sensor system for the application. The sensors are sampled at 1 Hz and are monitored wirelessly, classifying this as a non-complex progressive sensor system. This application is highly related to the research in this thesis and a great deal can be learned from this study:

- Similar to this work, damage is unique - meaning a bespoke sensor system design will be required.

- Maximum damage opening occurred at key extreme loading events during turbine operation:

  - Unmeasurable by visual inspection (even if damage was above ground).

  - Continuous monitoring of damage at relatively high frequency to ensure events are captured.

– To determine the relation between loading events and damage displacements, environmental data should be collected (such as wind speed, direction etc.).

- A complex analysis method is not required if sensor system can provide direct damage measurement effectively.

- Method of quantifying changes in crack displacements would provide a progressive damage state which can be compared to operator limits.

Using this knowledge of a previously successful damage monitoring system will aid in the design and implementation of such a system for the application in this work.

In the above application, and in the case of this research, the initial reason for pursuing a monitoring system for foundations is due to unexpected damage levels. In contrast, research carried out by Rubert et al. [21] [3] involved instrumenting a new wind turbine foundation in order to assess the effectiveness of current foundation designs and to aid in the transition to more economical designs. In some cases, foundations can be overdesigned due to the high safety factors applied. FBG strain gauges were installed on selected rebars throughout the foundation prior to concrete pouring. These included: circumferential, radial and shear rebar. Packaging of the FBGs consists of induction brazing the FBG within a Kovar capillary, which is soldered inside a copper tube with attached steel shims. The whole construction is then spot welded to the rebar and encompassed in a protective steel half-tube sealed with silicon. Addressing fibres are fed to the centre of the plinth to be interrogated in the tower. Accompanying tower strain FBGs are installed for comparison to foundation strains. Although not all sensors in the foundation survived, results were gained and compared to tower sensors and previously produced FEM models. Compared to tower strains, the foundation circumferential strains related linearly with a correlation coefficient $\tau = 0.87$ and 0.58 and $R^2 = 0.75$ and 0.33 for two perpendicular tower sensors. The FEM model produced R^2 values > 0.99 when compared to both circumferential and shear rebar sensor data. This means the FEM model is very accurately representing the loading in the foundation. At this stage the work would require a second more successful implementation following learning outcomes gained from this installation prior to any further conclusions. The main measurand in this sensor system is the structural strain apparent in the rebars. The objective is not to measure damage, rather to determine if strain levels are as expected and continue at these levels. A total of 24 FBGs: ten foundation strain, six foundation temperature, four tower strain and four tower temperature were installed. Sampling frequency was set at 100 Hz, classifying this as a historical sensor system. With two measurands, serial multiplexing and embedded installation the system is fairly complex overall. The application specific requirements such as number of sensors and small size to reduce impact on concrete-rebar interface led to the use of FBGs. Failure was mainly due to addressing fibres undergoing large forces during concrete pouring. Wireless sensing may eliminate this hazard, but

---

[3]Author was involved in this work.

this will fail to meet other requirements such as long term and high sampling rate. The embedding of sensors during rebar installation also caused time constraints which ultimately led to ineffective protection and the loss of 75% of the foundation sensors. Moving forward it is worth noting that planning for the installation is of utmost importance and ensuring not only the sensors themselves are adequately protected, but also the connection in-between.

5.4 Chapter summary

A summary of the key sensor systems and learning outcomes explored in this review are shown in Table 5.4.

From these specific applications, a few key points reoccur and must be retained for the future sensor design and implementation on to cracks in a wind turbine foundation:

- Optical sensors favoured over electrical sensors in some applications. This was evidenced in the work by Chan et al. [104] where electrical strain gauges were directly replaced by FBGs. Lima et al. [102] also chose FBGs for crack monitoring.

- During damage monitoring, structural characteristics were usually not monitored, such as in [101] and [102]. Perhaps monitoring both would provide data to validate and compare to crack displacements, which may give a more detailed perspective of damage severity.

- Face crack monitoring so far shows extremely small displacements ([101, 102]), close to or below interrogator resolution. Ensuring the measurement system is able to detect these small changes adequately is of the utmost importance.

- In some cases, either due to the use of wireless sensors or simply due to measurement device capabilities, sampling rate of the crack displacement monitoring application was low. Long-term changes can be monitored, but short-term shifts may provide more information on the current state.

Table 5.4: Summary of sensor systems from industrial applications.

Application	Sensors	Measurands	Timing	Complexity	Note
Bridge [103, 104]	Accelerometers, strain gauges, thermocouples, FBGs...	Environmental and structural	Historical	Very high	• Large project - monitoring dynamic behaviour of three bridges • FBGs implemented as an alternative to electric for damage detection • Research epoxy attachment in comparison to metallic
Bridge [101]	LPDT, inclinometers, thermocouples	Environmental and direct damage	Progressive	Medium	• Direct damage monitoring - no structural characteristics • Wireless displacement sensors due to application - limited memory • Small crack displacements, close to interrogator resolution
Building [102]	FBGs, thermocouples	Environmental and direct damage	Historic	Medium	• Direct damage monitoring - no structural characteristics • Non-destructive attachment method, unprotective housing • Small crack displacements, below interrogator resolution • Possible low sampling frequency
Smart materials [100, 115]	Copper wires embedded in film	Direct damage	N/A	Low	• Detection of specific crack widths by breaking copper wires • Not discussed, but possible deterioration measurement by sensor • Single use - breaks after limit breach
Foundation [7, 8]	LDVT	Direct damage	Progressive	Low	• Unique damage and sensor design - no structural characteristics • Set limits decided by operator and identified by measurement system • Non-complex analysis method required due to effective sensor system

68

Chapter 6:   Crack monitoring of onshore wind turbine foundations: industrial application

6.1   Chapter overview

In this chapter, a methodology to quantify crack deterioration is proposed and applied to an industrial application: monitoring cracks in an onshore wind turbine foundation. Firstly, a general background on the type of foundation, expected load response of the entire turbine and the initial foundation crack formation that was witnessed is presented. From this, objectives of a structural monitoring sensor system are discussed. The previous literature review has provided knowledge to aid in the sensor design and implementation to crack measurement. The sensor design, construction and characterization will follow before outlining the installation procedure. The sensors will then be validated using a model based on the turbine load response analysis. A novel method for determining deterioration of the cracks is then demonstrated before applying the methodology to the initial 9-month accumulation of data and discussing results.

6.2   Onshore wind turbine foundations

6.2.1   Design

Onshore wind turbines are usually supported by concrete gravity or piled foundations. Piled foundations consist of a varying number of long reinforced concrete columns attached to the turbine and embedded deep underground to provide support when the topmost soil conditions are poor. Gravity foundations are the most commonly used and are usually wide reinforced concrete platforms that are embedded just below the surface. Figure 6.1 portrays the octagonal gravity foundation that was analysed in this work. The interface between tower and foundation also have varying designs, the most commonly used are embedded can or bolt rings. In these designs, large bolts or steel cans are cast inside the foundation and extrude from the plinth to allow interconnection with the tower section. Loads are generally estimated by using FEM modelling of the turbine structure. Depending on the results, the foundations will be sized and shaped appropriately. These foundations are normally cast onsite, with a bolt cage in place to attach the tower. Heavy Earth materials such as rocks and dirt are placed on top of the slabs, acting as a balance against the overturning moment by using gravity.

6.2.2   Turbine load response

An onshore wind turbine can be modelled as a simple fixed cantilever with overturning moment, M, due to applied bending load from wind speed V_0 on the rotor and tower, as shown in Figure
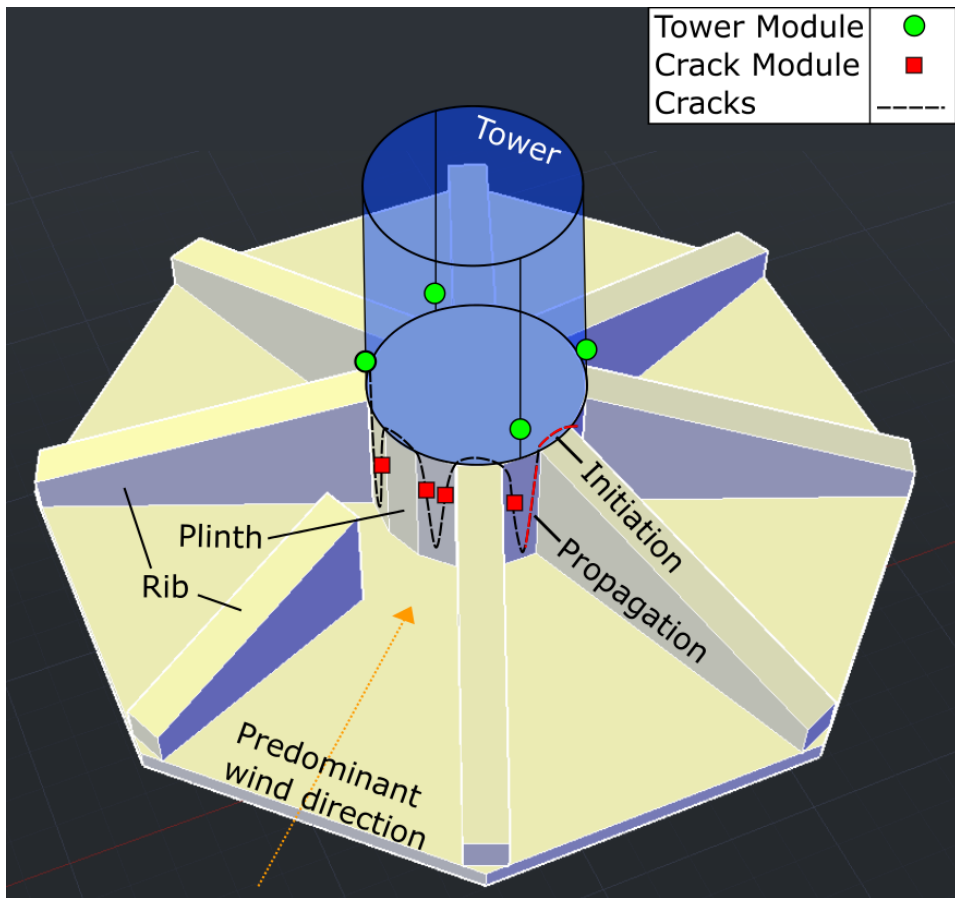
Figure 6.1: Gravity foundation design in this work with the unique crack formation and instrumented sensor module locations.

6.2 a). Mathematically, this can be expressed as [124]:

$$M = \frac{1}{2}\rho_a V_0^2 C_T(V_0) A_r H + \frac{1}{2}\rho_a d_T C_{dr} \int_0^H V(z)^2 z dz \tag{6.1}$$

where the first term describes the thrust: $\rho_a = 1.225$ kg/m^3 is the air density, $C_T(V_0) = 0$ to 0.83 is a wind speed dependent variable, unique to turbine design and theoretically illustrated in Figure 6.2 b) for the turbine in this work [125], $A_r = 9160$ m^2 is the area of the rotor and blades (which have a length of 54 m) and H is the hub height. The second term coincides with the load distribution on the tower: $d_T = 5$ m is the turbine tower diameter, $C_{dr} = 0.5$ is an approximated drag coefficient and $V(z)$ is the distributed wind profile incident on the tower [126]. To simplify, assuming stable wind conditions, $V(z)$ can be estimated [127]:

$$V(z) = V_0(\frac{z}{H})^{\frac{1}{7}} \tag{6.2}$$

substituting 6.2 into 6.1 provides the complete moment equation:

$$M = \frac{1}{2}\rho_a V_0^2 [C_T(V_0) A_r H + \frac{7}{16} d_T C_{dr} H^2] \tag{6.3}$$

Since the intended sensors are strain measuring devices, predicting strain on the tower base would be beneficial in order to validate the sensors following installation. To do this, the moment equation (6.3) is converted into strain using the second moment of inertia, I of the tower with wall thickness $T_t = 5$ cm:

$$I \approx \frac{\pi}{8} d_T^3 T_t \tag{6.4}$$

which gives tower base strain ϵ_T:

$$\epsilon_T = \frac{M d_T}{2 I E_s} cos(\alpha - \theta_S) \tag{6.5}$$

with tower second moment of inertia, $I = 2.454$ m^3, α is the wind direction (or turbine yaw) and θ_S is the tower section of interest. These equations assume steady state conditions, with the turbine outputting rated power, allowing disc theory to be applied to calculate thrust [128, 129].

6.2.3 Failure

Mechanical components of wind turbines such as the generator or gearbox are the most commonly monitored, most likely due to the higher failure rate they are prone to [5, 130]. In some work, measurement systems have been implemented on the tower and blades to monitor the relationship between dynamic loading and fatigue damage [131, 132]. Despite support structures presenting the most crucial factor in terms of safety (critical failure can cause collapse of the entire structure), they are the least monitored part of a wind turbine. Some catastrophic failures of this nature
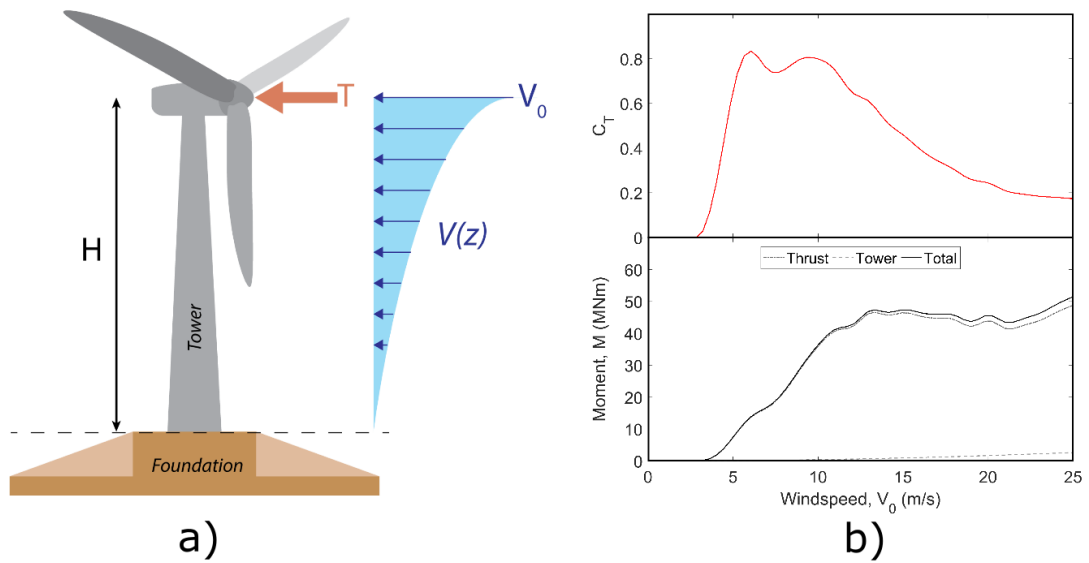
Figure 6.2: a) Cantilever model of an onshore wind turbine of hub height, H, thrust force T and distributed force $V(z)$ due to wind speed V_0. b) Theoretical thrust coefficient, C_T and overturning moment from Equation 6.3.
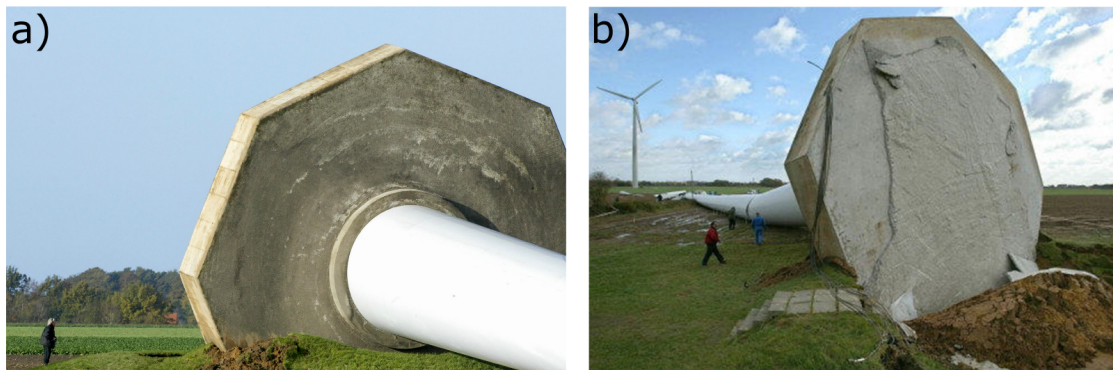
Figure 6.3: a) Foundation collapse in Goldenstedt, Germany [133] and b) another in Europe [134].

have occurred, such as shown in Figure 6.3. In these cases, most likely uncontrollable factors such as storms have caused increasing wind speeds and significant overturning moment, M above design limits. One must also consider that should the design limit change in any way, perhaps due to design errors or climatic changes, these failures could occur under mean wind conditions. As discussed in Chapter 3, concrete will crack under relatively low loads, but cracking will become more severe as it reaches failure stress. Therefore, monitoring the deterioration level and rate of multiple cracks could provide information on the proximity of the structure to this failure point. The likelihood of water ingress to reach steel is of greater concern - which could cause corrosion and weaken the tensional support the concrete gains from steel. This could possibly cause earlier failure at lower stress levels due to the weakness of concrete in tension. In both scenarios, monitoring crack deterioration can aid in preventing failure.

6.2.4 Crack formation case study

Foundations with pre-established observable surface cracks are studied in this work. The overall formation of these cracks on the foundations is illustrated in Figure 6.1. Cracks appear more defined on the side of oncoming predominant wind direction - most likely due to the tensional stresses occurring on this side. This particular foundation construction underwent a multi-stage concrete pour, with the main plinth and ribs poured independently. During this method, thermal gradients can separate these sections, causing crack initiation at the interface (denoted as "Initiation" in Figure 6.1). Additionally, there are issues in the reinforcement design including discontinuities in the level of steel and bolts that do not extend fully into the foundations. Combined with applied dynamic loading, these cracks can develop and widen, before eventual propagation to the submerged plinth faces (denoted "Propagation" in Figure 6.1). Excavation campaigns carried out by the turbine operator provided evidence of widening of the face cracks over time. The physical appearance of these cracks is shown in Figure 6.4, with the rib-plinth "Initiation" in a) and the "Propagation" to plinth face in b) identified by arrows. The major concern of these cracks is that they may represent a complete disunion of two section of the foundation. If this is the case, the face cracks may show both mode I opening displacements and large mode III tearing displacements (Chapter 3, Section 3.4.2). The face cracks are of particular concern for a number of reasons:

- Majority of rebar is located within plinth section - contains important bolt cage for tower attachment.

- Rebar is within relatively close proximity to these faces.

- They are long - in some cases spanning the entire height of the plinth.

- Multiple foundations show the same "U" shape pattern on the face.

- It is unusual for cracks to form on a face - more common at a section interface.

Also it is worth noting that a face crack is easier to instrument with sensors than one at an interface. A closer image of the face cracks is shown in Figure 6.5 a).

6.2.5 Objectives

The objectives of the project are as follows:

- Demonstrate the feasibility of a crack monitoring sensor system implemented on a single turbine for monitoring during operation.

  - Instrument multiple cracks and tower strains simultaneously.

  - Implement the capability of monitoring mode I opening and mode III tearing crack displacements.

Figure 6.4: Physical appearance of a) "Initiation" cracks at the rib-plinth interface and b) "Propagation" face cracks with "U" shape form.

> – Demonstrate long-term survivability in harsh environmental conditions such as freezing temperatures and high humidity.

- Develop a methodology for converting raw displacement data into a measure of crack deterioration.

- Collectively determine severity limits of the cracks with turbine operators.

- Continuously monitor cracks over time until limits are breached or sensors fail.

6.3 Sensor Design

Following initial inspection of the site, a sensor design capable of monitoring the face cracks of the foundations and meeting the outlined objectives was debated based on the sensor analysis and literature review from Chapters 4 and 5.

6.3.1 Crack monitoring

Concrete cracking has been discussed in Chapter 3. Specific interest in this work is given to displacement of the cracks in mode I opening and III tearing. Mode II sliding displacements (and any other types, such as surface rotations) are disregarded at this stage as a sensor capable of isolating these may not be probable as mode I will dominate. Also, mode II sliding is unlikely to be significant in this scenario due to the nature of the overturning moment loading. Monitoring the width or opening of a crack is imperative as width can be directly related to depth at small widths of up to 0.1 mm [135], which controls penetration of water or chloride to steel. Due to the inhomogeneous nature of concrete, long-gauge sensors are required to monitor large crack opening displacements and gauge length a key contributor to accuracy [73]. It was decided that the FBG
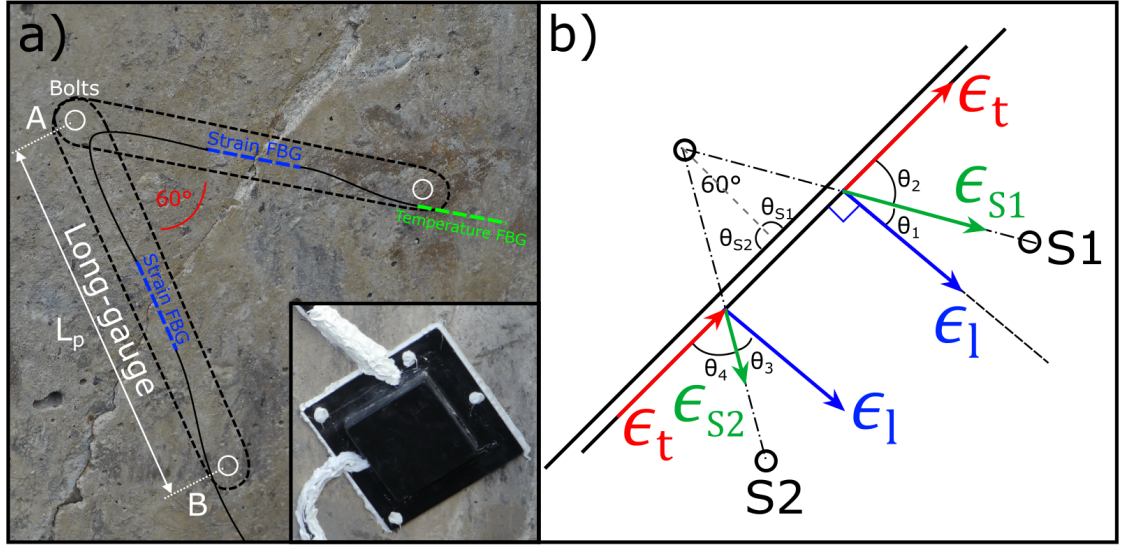
Figure 6.5: a) Intended sensor design for crack monitoring, insert: ruggedized packaging and b) trigonometry to extract mode III tearing from mode I opening displacements.

optical fibre strain sensor was most suitable for this application. Although primarily used as point strain sensors, particular packaging can allow the FBG to measure displacements as a long-gauge sensor. In comparison to electrical sensors, the multiplexing advantage of FBGs, small size and immunity to electromagnetic interference compose a prime choice for the application. In crack monitoring, aggregates and small voids can cause varying displacement changes - to ensure the large crack is effectively monitored the sensor must be adequately long.

Long-gauge FBGs

The FBG can effectively monitor the average strain at the centre of a long-gauge package anchored at two points, an example of which is illustrated in Figure 6.5 a). As discussed in Section 4.5.1, FBGs are defined by the spectral properties (including FWHM and peak position). The FBGs in this work are polyimide coated fibres with bare FBG section and a full width at half maximum (FWHM) of 300-400 pm. The data sheet for one FBG is provided in the Appendix (10.1). The strain in the package, ϵ_z, with gauge length L_p is given as [73]:

$$\epsilon_z = \frac{\Delta L_p}{L_p} = \frac{1}{L_p} \int_{x_A}^{x_B} \epsilon_C(x) dx + \frac{1}{L_p} \sum_c W_c \qquad (6.6)$$

for a displacement change, ΔL_p between anchor points A and B caused by concrete and existing crack displacements represented by the strain, $\epsilon_C(x)$. The final quantities, W_c, represent discontinuities that are difficult or impossible to predict. As discussed by Glisic et al. [73], these are caused by new crack propagations appearing between anchor points and can contribute to strain changes. Characteristically, these changes will appear as instant permanent changes in the data and are worth considering during data analysis.

The long-gauge FBG sensor will measure the value of ϵ_z as the mechanical strain factor in the

75

previously discussed Equation 4.9:

$$\frac{\Delta\lambda_B}{\lambda_B} = K_T\Delta T + K_\epsilon\epsilon_m \tag{4.9}$$

where $\epsilon_m = \epsilon_z$. Multiplying this strain by the gauge length L_p will provide the displacement between anchor points, which will be dominated by crack displacement.

Segregating crack modes

As discussed, it is possible the loading applied to these cracks could be causing both opening (mode I) and tearing (mode III) displacements of cracks. An objective outlined in Section 6.2.5 is to determine both of these displacements independently with the one sensor arrangement. To separate the tearing from opening displacements, it is possible to arrange two FBGs at an angle, as shown in Figure 6.5 a) at 60°. This particular angle is used to simplify extraction equations, as will be discussed. Trigonometry can be used to calculate the distribution of each mode by comparing FBG values. From Figure 6.5 b), the total strain in one sensor, ϵ_z, is the sum of opening (mode I) and sliding (mode II) combined, ϵ_l, and tearing (mode III), ϵ_t as:

$$\epsilon_z = \epsilon_l + \epsilon_t \tag{6.7}$$

The sliding displacement in ϵ_l was deemed improbable to distinguish from opening displacements due to the dominance of opening and difficulty in designing a capable sensor. From Figure 6.5 b), the strain in each sensor due to crack displacement modes I (ϵ_l) and III (ϵ_t) is given as:

$$\epsilon_{S1} = \epsilon_l cos(\theta_1) + \epsilon_t cos(\theta_2) \tag{6.8}$$

$$\epsilon_{S2} = \epsilon_l cos(\theta_3) - \epsilon_t cos(\theta_4) \tag{6.9}$$

where cracks are assumed to be opening ($\epsilon_l > 1$) and the polarity of ϵ_t depends on the direction of tearing displacement. For these equations the tearing shown in Figure 6.5 b) is assumed. Following the calculations and concluding a negative value for strain deduces the opposite scenario occurring (closing cracks or reversed tearing). During installation, the angle between sensors and cracks is measured (θ_{S1} and θ_{S2}). With the chosen 60° between sensors, every other angle can be associated to θ_{S1} as in Table 6.1. This specific angle will simplify the trigonometric equations.

Using the relationship: $cos(x - y) = cos(x)cos(y) + sin(x)sin(y)$, 6.9 can be subtracted from 6.8 and equivalent angles substituted to give:

$$\epsilon_{S1} - \epsilon_{S2} = \epsilon_l cos(\theta_{S1}) + \epsilon_t sin(\theta_{S1}) \tag{6.10}$$

As mentioned, this simplification is made possible due to the 60° angle between sensors. Should

Angle	Equivalent
θ_{S1}	θ_{S1}
θ_{S2}	$180° - \theta_{S1}$
θ_1	$\theta_{S1} - 60°$
θ_2	$150° - \theta_{S1}$
θ_3	$120° - \theta_{S1}$
θ_4	$\theta_{S1} - 30°$

Table 6.1: Angles in Figure 6.5 b) represented in terms of the angle between sensor and crack, θ_{S1}.

angles $\theta_{S1} = \theta_{S2} = 90°$ following sensor installation, then the extraction of tearing displacement is simply the difference in sensor strain values:

$$\epsilon_{S1} - \epsilon_{S2} = \epsilon_t \tag{6.11}$$

As will be discussed during the installation overview, this angle is sometimes not possible to achieve due to difficulties met when attempting to position sensors. In general, the relationship in Equation 6.11 can be used to provide an estimate of tearing displacements in the crack. Should these values become large and a more accurate value required, the real θ_{S1} can be used (or equivalently θ_{S2}) in combination with sensor strain values ϵ_{S1} and ϵ_{S2} to calculate the individual tearing displacement. Firstly, substituting the equivalent angles into 6.8 gives ϵ_l in terms of ϵ_t, ϵ_{S1} and θ_{S1}:

$$\epsilon_l = \frac{\epsilon_{S1} - \epsilon_t(\frac{-\sqrt{3}}{2}cos(\theta_{S1}) + \frac{1}{2}sin(\theta_{S1}))}{\frac{1}{2}cos(\theta_{S1}) + \frac{\sqrt{3}}{2}sin(\theta_{S1})} \tag{6.12}$$

which can be re-substituted into Equation 6.10 to provide the distinct tearing displacement in terms of ϵ_{S1}, ϵ_{S2} and θ_{S1}:

$$\epsilon_t = \frac{(\epsilon_{S1} - \epsilon_{S2})(-\frac{1}{2}cos(\theta_{S1}) - \frac{\sqrt{3}}{2}sin(\theta_{S1})) + \epsilon_{S1}cos(\theta_{S1})}{-\frac{\sqrt{3}}{2}cos^2(\theta_{S1}) + \frac{1}{2}sin(\theta_{S1})cos(\theta_{S1}) + (-\frac{1}{2}cos(\theta_{S1}) - \frac{\sqrt{3}}{2}sin(\theta_{S1}))sin(\theta_{S1})} \tag{6.13}$$

Although this equation appears complex, it may provide simplicity during software implementation by using a single angle variable. The independent tearing strain can also be calculated from the individual angles using the values in Table 6.1, given the angle between the sensors is 60°, as:

$$\epsilon_t = \frac{\epsilon_{S1}cos(\theta_3) - \epsilon_{S2}cos(\theta_1)}{cos(\theta_4)cos(\theta_1) + cos(\theta_2)cos(\theta_3)} \tag{6.14}$$

Applying the same method can provide isolated opening displacement as:

$$\epsilon_l = \frac{\epsilon_{S1}cos(\theta_4) - \epsilon_{S2}cos(\theta_2)}{cos(\theta_3)cos(\theta_2) + cos(\theta_1)cos(\theta_4)} \tag{6.15}$$

From these equations, any large tearing displacements can be accurately calculated by using the strain on two long-gauge FBGs over one crack at an angle of 60°.
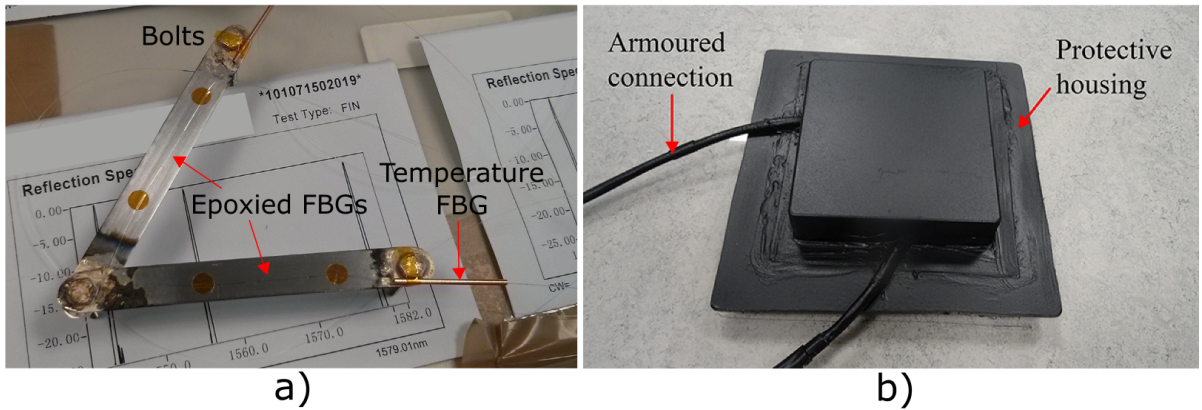
Figure 6.6: a) Physical construction of dual FBG bidirectional crack displacement monitoring module. b) Aluminium and acrylic casing sealed around FBGs to ensure protection.

6.3.2 Sensor fabrication

To fabricate the dual FBG bidirectional crack displacement monitoring sensor module, the packaging is first forged by brazing two carbon steel plates at a 60° angle with an intersecting bolt. Carbon steel was chosen to allow induction brazing, which requires a magnetic material to perform. Two more bolts were brazed at each end of the steel plates 10 cm from the intersection, providing the gauge length $L_p = 10$ cm. Following cleaning of any oxidization, three FBGs were multiplexed in series: two were epoxied at the centre of the plates to measure strain and the other placed in a copper tube - isolated from strain - to measure temperature. Each end is then terminated with a ferrule connector (FC) to allow further multiplexing with multiple modules. Particularly, angled physical contact (APC) type FC connectors are used to reduce the Fresnel reflection loss and to minimize reflections back to the source. APC connectors have an 8° angle termination instead of being perpendicular, which causes any reflection to be directed towards the cladding. However, this comes at the cost of increased transmission loss.

This construction is shown in Figure 6.6 a).

Ruggedization

Optical fibres can be extremely fragile when unprotected, so in this work an armoured sleeve is crimped onto the exposed connecting fibres. The construction in Figure 6.6 a) is encased in a protective aluminium and acrylic housing (Figure 6.6 b)) with bolts protruding to allow installation on to concrete . The casing is sealed using a combination of epoxy and silicon to minimise any moisture ingress which could degrade epoxy, steel and glass fibre components [136]. Following installation, these modules are also further sealed from the environment using silicon (Figure 6.5 a) insert).

Temperature characterization

As discussed in Section 4.5.1, FBGs are dependent on temperature changes (see equation 4.9). To
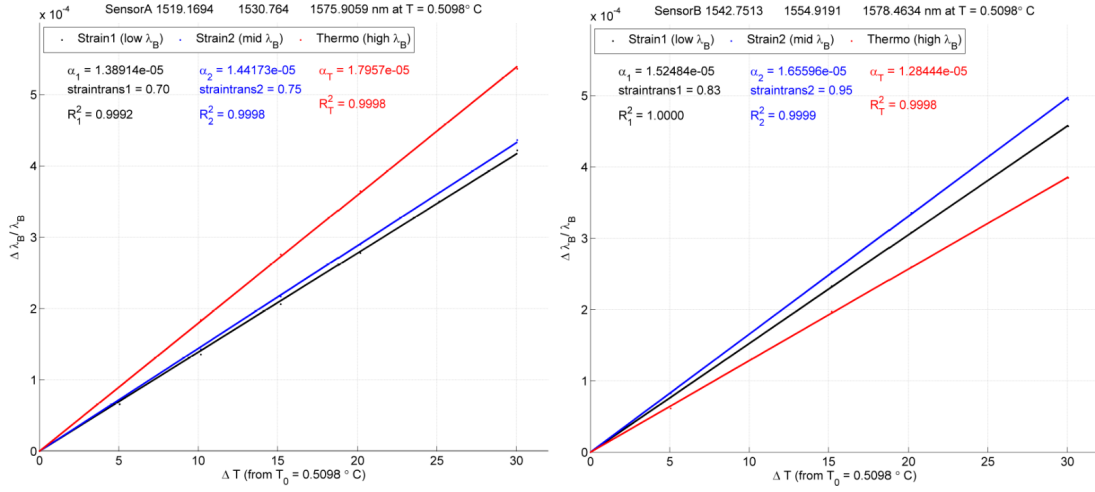
Figure 6.7: Foundation module A and B temperature characterization result.

provide temperature compensation to the strain FBGs, both a temperature measuring device (in this case a strain isolated FBG) and knowledge of the FBGs temperature coefficients, K_T, are required, which will be unique to each FBG. Also, the steel plates thermal expansion coefficients can be exploited to determine the strain transfer, K_ϵ of each strain FBG. To do this a simple lab experimentation was performed by cycling the sensors between set temperature limits $(0.5° - 30°)$ in $5°$ steps within an environmental chamber. Figures 6.7 and 6.8 contain the graphs illustrating the sensor responses from this experimentation. The individual wavelengths, temperature and strain coefficients for each sensor is then provided in Table 6.2. Due to manufacturing differences when constructing by hand, each sensor has an independent temperature and strain coefficient. The temperature coefficients are simply calculated by the gradient of the graphs in Figures 6.7 and 6.8. Strain coefficients are then calculated by:

$$K_\epsilon = \frac{K_T - K_{TF}}{\alpha_S} \tag{6.16}$$

where K_{TF} is the repeatable temperature coefficient for a bare FBG $(\approx 6 * 10^{-6}/°C)$ and α_S is the thermal expansion coefficient of carbon steel $(\approx 11 * 10^{-6}/°C)$.

These values will be used in conjunction with equations 4.9 and 6.6 to determine the displacement between bolts of each sensor and; therefore, crack displacement. Any large differences between strain FBGs in a module (for example A1 and A2) may represent tearing displacement, which can be extracted accurately using equation 6.13 or 6.14.
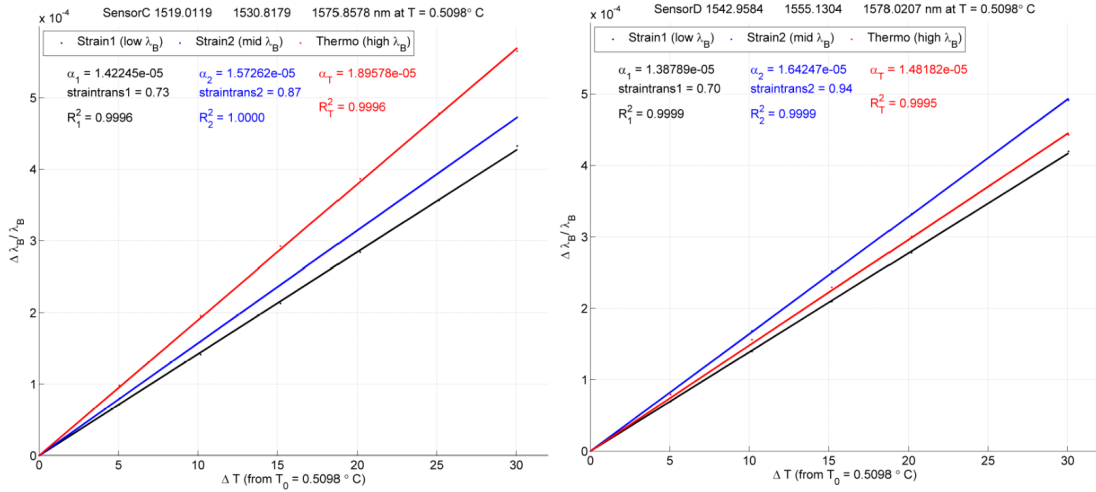
Figure 6.8: Foundation module C and D temperature characterization result.

Sensor	Wavelength @ 0.5° C (nm)	K_T (/°C)	K_ϵ (/ε)
A1	1519.169	$1.38914 * 10^{-5}$	0.717
A2	1530.764	$1.44173 * 10^{-5}$	0.765
AT	1575.906	$1.79570 * 10^{-5}$	0
B1	1542.751	$1.52484 * 10^{-5}$	0.841
B2	1554.919	$1.65596 * 10^{-5}$	0.960
BT	1578.463	$1.28444 * 10^{-5}$	0
C1	1519.012	$1.42245 * 10^{-5}$	0.748
C2	1530.818	$1.57262 * 10^{-5}$	0.884
CT	1575.858	$1.89578 * 10^{-5}$	0
D1	1542.958	$1.38789 * 10^{-5}$	0.716
D2	1555.130	$1.64247 * 10^{-5}$	0.948
DT	1578.021	$1.48182 * 10^{-5}$	0

Table 6.2: Individual wavelength, temperature and strain coefficients for each sensor in each module gained from temperature characterization experimentation.
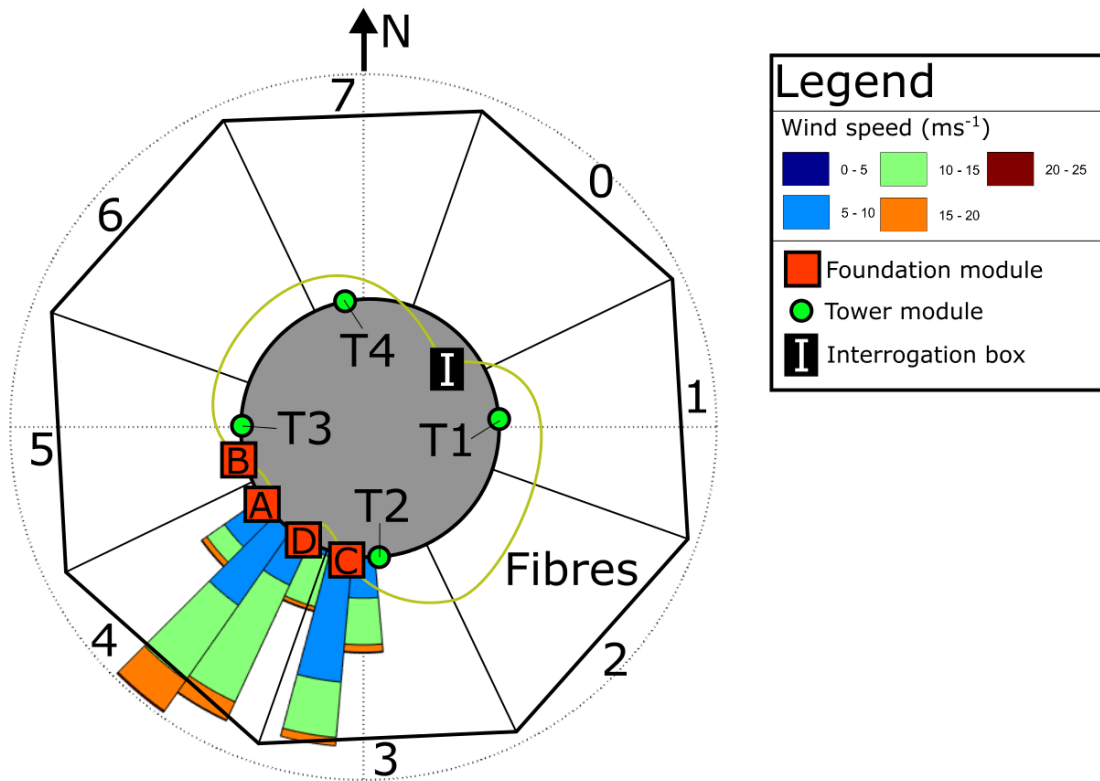
Figure 6.9: Wind rose gathered from SCADA data for the turbine in this work. Sensor locations of foundation modules (A-D) and tower sensors (T1-T4) annotated.

6.4 Installation procedure

6.4.1 Foundation modules

Each cell of the octagonal foundation design in this work was numbered from 0-7, starting from the entrance door of the turbine, as shown in Figure 6.9. The previously described foundation crack modules were installed on four face cracks. The crack locations, illustrated in Figure 6.1 and 6.9, were chosen as they visually portrayed the highest severity of all face cracks. From the wind rose in Figure 6.9, gained from supervisory control and data acquisition (SCADA) wind speed data for the turbine, it is clear the predominant wind direction is incident on the chosen severe cracks. This correlates with the overturning moment caused by the wind, meaning these cracks will be undergoing the greatest tensile forces - causing them to open. A total of four modules (labelled A-D) were installed on four cracks in cells 3, 4 and 5. Each module contained the dual FBG displacement sensors and accompanying temperature sensors described in Section 6.3. A total of 7 holes are drilled into the concrete - 3 for sensor attachment and 4 for securing the entire module - at appropriate positions depending on available area and any surrounding small cracks that could be degraded by drilling. All holes are then cleaned using compressed air. Mortar is injected into the designated sensor holes and plastic wall plugs are used for securing module. The module is fit flush to the wall over the crack and, after 24 hours of curing, silicon is applied to further protect
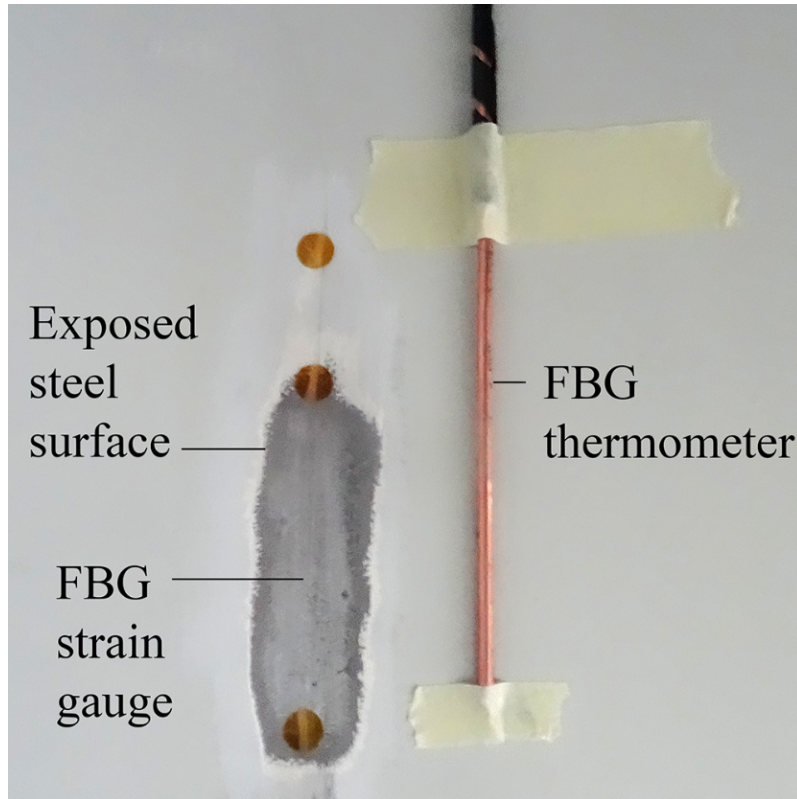
Figure 6.10: Strain and temperature sensors installed on to turbine tower.

the sensors from moisture ingress.

6.4.2 Tower sensors

During the literature review, a possible missed opportunity was witnessed from other crack monitoring applications: using structural characteristics to both validate and compare to the measured crack displacements. In this work, strain sensors were installed on the base of the turbine tower in four positions, illustrated in Figures 6.1 and 6.9. These can be used for such comparisons to crack sensor measurements. A total of four modules (T1-T4) are installed, each consisting of two FBGs - one bonded to the structure for strain measurement, the other isolated from strain to provide temperature measurements, as shown in Figure 6.10. Paint is removed from the tower to expose the steel, the area is then cleaned before epoxying the FBG directly. Since this sensor resides within the tower there is no need for environmental protection. It is also unlikely any personnel will interfere with these sensors.

6.4.3 Interrogation

The interrogator chosen for this work was the Ibsen I-MON 512 USB. The product specification or data sheet of the I-MON (10.2) quotes a sampling frequency of up to 3 kHz, a wavelength range of 85 nm, a wavelength resolution of < 0.5 pm and is reasonably inexpensive (≈ £4000). To justify this
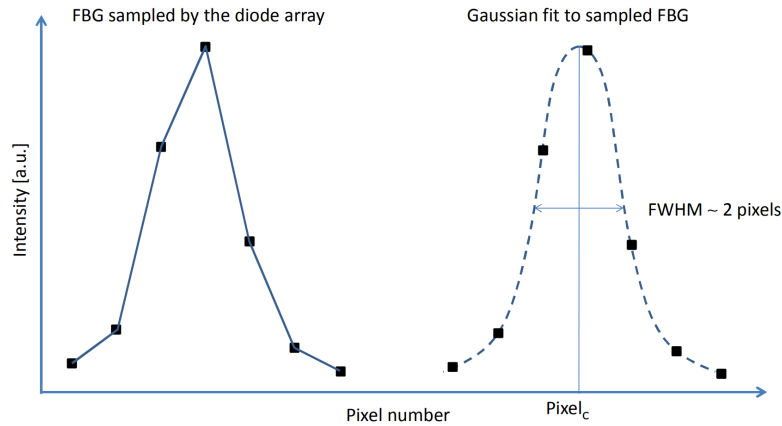
Figure 6.11: Peak detection algorithm of the I-MON interrogator from product specification (10.2). A Gaussian curve is fit over the two pixels contained within the FWHM of the FBG and neighbouring ($\pm$ 5) pixels.

choice, first consider the frequency. It is well known that natural frequencies of wind turbines are low, usually below 1 Hz. [137]. Any dynamics should be captured with 3 kHz sampling, with room for down-sampling if required. In terms of the wavelength resolution, converting the quoted ideal resolution to crack displacement (with sensor gauge length) provides an ideal crack displacement resolution of < 0.032 μm. Observed from the literature review, small crack displacements of 0.1 μm were witnessed by Lima et al. [102]. The system in this work had a resolution of 1.1 to 2.3 μm, yet was able to successfully monitor displacements. Therefore, this improved resolution of the system should be more than sufficient.

The wavelength resolution of the I-MON originates from the peak detection algorithm employed. This is presented in the product specification, given in the Appendix (10.2). To overview, firstly consider the entire bandwidth of 85 nm. The I-MON monitors this bandwidth with a series of diodes containing 512 pixels total, meaning each pixel is spaced by 166 pm. From Section 6.3.1 and Appendix (10.1), the FBGs in this work have a FWHM of 300-400 pm. This means the FBG FWHM section will contain 2 pixels, shown in Figure 6.11 left. The peak detection algorithm then fits a Gaussian curve over these and neighbouring ($\pm$ 5) pixels, providing the peak FBG wavelength value, shown in Figure 6.11 right. The quoted 0.5 pm resolution comes from the standard deviation of multiple measurements taken of a single FBG at constant temperature. This is the error of estimated peak from Gaussian fit to real FBG peak. It is emphasised that this value is ideal, and in reality will likely be larger. Therefore, any data that represents variations below or close to the ideal resolution must be considered as being influenced by interrogator resolution.

There are two other main disadvantages to using the I-MON: requirement for an independent light source and only one channel per device. The former is solved by using an adequately powerful light source to illuminate all of the sensors. The light source used in this work is the Ibsen DL-BP1-1501A superluminescent diode (SLED), which has an optical power of > 12 mW, a 3 dB spectral width of > 79 nm and a centre wavelength of 1550 nm. This source was tested prior to installation

Interrogator	Price (£)	Wavelength resolution (pm)	Bandwidth (nm)	Frequency (Hz)
SmartScan	12000	< 1	160 (40 per channel)	2500
I-MON 512 USB	4000	< 0.5	85	3000

Table 6.3: Comparison between four channelled interrogator and I-MON.

and was able to sufficiently illuminate the intended number of sensors for the chosen interrogator. With only one channel, the number of sensors that can be monitored will be limited when compared to a multi-channel interrogator. Compromise must be made regarding interrogator bandwidth and price. Knowledge of the required number of sensors prior to choosing an interrogator would be beneficial. A comparison between the I-MON and an equivalent four channelled interrogator by SmartScan is provided in Table 6.3. The most important feature in this work is the resolution, since displacements are so small. The intended number of sensors for this work was 4 crack modules and 4 tower modules, giving a total of 12 strain/displacement and 8 temperature sensors requiring a bandwidth of around 144 nm. This is based on the following assumptions: total temperature change of up to 80° C and maximum strain/displacement of 2.5 mϵ/250 μm ($\pm$ 1.25 mϵ/125 μm). This means either two I-MON or one SmartScan interrogator would be required. The two I-MON setup was chosen due to the improved resolution.

To expand on the bandwidth requirement, a total of 10 nm ($\pm$5 nm) was allocated for strain/displacement FBGs and 3 nm ($\pm$1.5 nm) for temperature FBGs. The temperature change of 80°C represents $\approx$ 2.5 and 2.12 nm of bandwidth for temperature and strain/displacement FBGs respectively. The remaining 7.88 nm bandwidth for strain/displacement sensors represents the allocated 2.5 mϵ/250 μm ($\pm$ 1.25 mϵ/125 μm).

Exploiting couplers and circulators allows a single light source to be used - given the light source is capable of illuminating all sensors. A diagram illustrating the interrogation scheme is shown in Figure 6.12 a).

Both foundation and tower modules were installed with armoured connection fibres of 30 cm length (see Figure 6.6) each terminated by an FC; therefore, each interface between fibres and modules in Figure 6.12 a) consists of such a connection. FC's are single mode, telecom connectors that can easily be interfaced to other connectors to allow multiplexing without the need to splice. These were chosen to minimise installation complexity - as it allowed every module to be installed independently and subsequently interconnected via addressing fibres. Figure 6.9 and 6.12 a) shows the organisation of these fibres, with two foundation modules serially multiplexed together, two tower sensors parallel multiplexed then subsequently parallel multiplexed with foundation sensors. Parallel multiplexing is achieved by using 50:50 couplers which split the light between outputs and re-combine the FBG reflections. The outcome: tower modules are illuminated with 12.5% of total light source power each, with foundation modules illuminated with 25%.
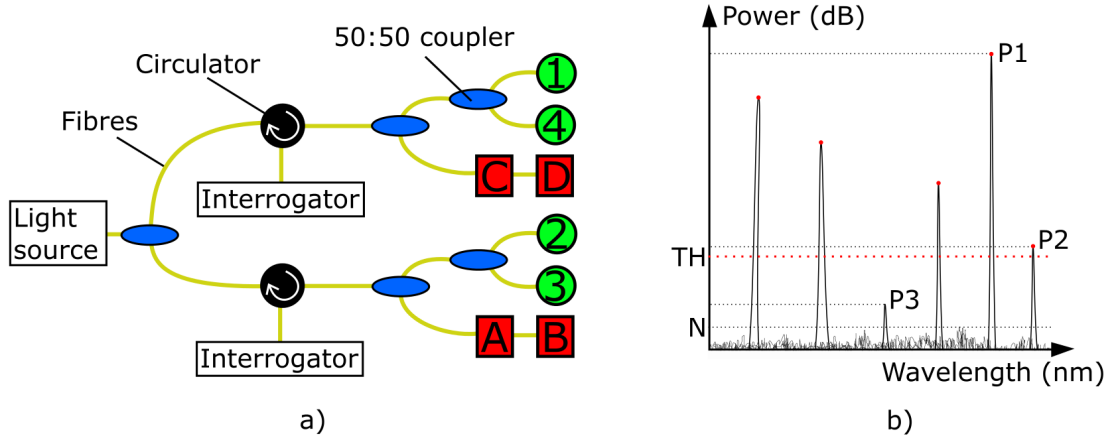
Figure 6.12: a) Schematic portraying the interrogation setup and b) example of peak detection. Two I-MON interrogators and one light source are used. Circulators send incoming light clockwise and couplers split the light into two paths at equal power distribution. Light source is projected to FBGs which reflect light backwards, which is subsequently circulated to interrogator. Interrogator post-processing measures wavelength of peaks above a threshold (TH) based on highest power (P1), which can cause difficult or undetected FBGs (P2 and P3 respectively). Peaks must remain above noise level (N) to be detected.

6.4.3.1 Connection losses and peak detection

The FC will cause power losses, categorized as [138]:

- Insertion loss - interfaces may not be perfectly aligned causing losses.

- Insertion fatigue - change in insertion loss over time after a number of reconnections.

- Temperature - connectors can be affected by temperature changes in the form of thermal expansion

- Return loss - Fresnel reflection from connector back towards source - reduced by FC/APC connectors.

The overall losses are not necessarily required in a quantitative form. One must take into account the fact that components will most likely deteriorate over time and losses will increase. FBG wavelength values are not dependent on power; however, the efficiency of detection of individual wavelength peaks is. Power of peaks must remain above the noise level of the system, otherwise they are indistinguishable. A qualitative approach can be used thanks to the interrogation software peak detection method. An example of an FBG array detected by an interrogator is shown in Figure 6.12 b), with a random noise magnitude annotated (N). The post-processing of this particular interrogator is rather simple - the highest power wavelength (P_{max}, in this case P1 from Figure 6.12 b)) defines a threshold level (TH) based on a manually entered detectable percentage (P_d):

$$TH = 0.01 P_d P_{max} \tag{6.17}$$

if a user inserts a value of 30% for P_d and the power of P_{max} is 5 dB, the threshold will be set at 1.5 dB and any FBG peak with a power < 1.5 dB will not be saved. Should this threshold be within close proximity to noise level, which upon fluctuation may exceed the threshold, then random noise peaks will be recorded and sensor measurements will be lost. The power of peaks is also not constant and will fluctuate; therefore, any peaks with a power close to TH, such as P2 in this case, may regularly be lost during measurement. Over time, due to component degradation, these powers can gradually diminish individually, so adjustment of P_d may be required. This adjustment allows for compensation of connector losses and any future changes due to component degradation.

6.5 Data processing

Prior to any analysis, the data must be processed into perceivable and useful information. Data is gathered in the form of FBG peak wavelengths, sampled at 50 Hz. Post-processing is split into 4 sub-processes.

6.5.1 Initialization

Raw wavelengths are stored in TDMS (compressed file format) files, each containing one hour of data. There are two files per hour, representing each interrogator. The initial program extracts wavelengths from the first 50 hours of every sensor and combines into a single "chunk" of data to simplify the future processing. This is carried out for the entire analysis period.

6.5.2 Down-sampling

Using the "chunks" of data, the second program is able to down-sample the data to any required rate, as 50 Hz is relatively high and will cause long computational time. To do this, an "intelligent" down-sampling method was required due to intermittent data loss that occurred randomly due to the peak detection algorithm discussed previously. This sacrifices time accuracy but is able to down-sample even with data loss. To demonstrate this, consider conventional down-sampling of a 50 Hz signal to 1 Hz, which would extract every 50th data point of the signal. If the 50th data point is missing, the "intelligent" down-sampling algorithm will instead search surrounding data points for the closest available and extract this. The range of data to search is manually set to restrict large time inaccuracy, usually to around 10% of the new sampling rate.

6.5.3 Allocation

The third program allocates each sensor to independent files and incorporates all additional information, including: sensor name, strain and temperature sensitivities, location and initial wavelength values.

6.5.4 Retrieval

Finally, each sensor is evaluated and converted into the equivalent tower strain, crack displacement or temperature. This includes temperature compensation, which was carried out using a Bayesian approach. To expand, the temperature sensitivities were initially gained in the laboratory using the methods described in Section 6.3.2. It is likely that sensors will degrade over time, which will cause variation in temperature sensitivity. To compensate, the sensors response is correlated to SCADA measurements of temperature to improve the accuracy of temperature compensation. The Bayesian method uses multiple variable linear regression, which is able to estimate the relationship between multiple, non-linear variables and a result (known as the observation). Bayesian networks can then expand on this by using prior knowledge (known as the prior) to validate the fit [139,140]. Combining these produces the posterior distribution, or an improved fit of temperature sensitivity based on known temperatures.

Bayesian networks

To mathematically describe this method, consider an observation of a linear relationship between variable X and result Y_O with slope θ_O, gained by linear regression as:

$$Y_O(X) = \theta_O X \tag{6.18}$$

where the normal distribution of the slope θ_O is described by a covariance matrix, μ_{θ_O}. Next consider that a prior guess showed the result Y_P related to the variable X with a slope θ_P:

$$Y_P(X) = \theta_P X \tag{6.19}$$

where the normal distribution of this slope is described by the covariance matrix, μ_{θ_P}. The prior and observation can be combined to provide the posterior, represented by a covariance matrix μ_{θ_R} and mean value θ_R as:

$$\mu_{\theta_R} = (\mu_{\theta_O}^{-1} + \mu_{\theta_P}^{-1})^{-1} \tag{6.20}$$

$$\theta_R = \mu_{\theta_R}(\mu_{\theta_O}^{-1}\theta_O + \mu_{\theta_P}^{-1}\theta_P) \tag{6.21}$$

This is a univariate relationship, which can be expanded by including more variables to further improve the fit. In this work, the result is the sensor output, the observation is the linear relationship between the sensor and SCADA temperatures and the prior guess is the lab estimates of temperature sensitivity.
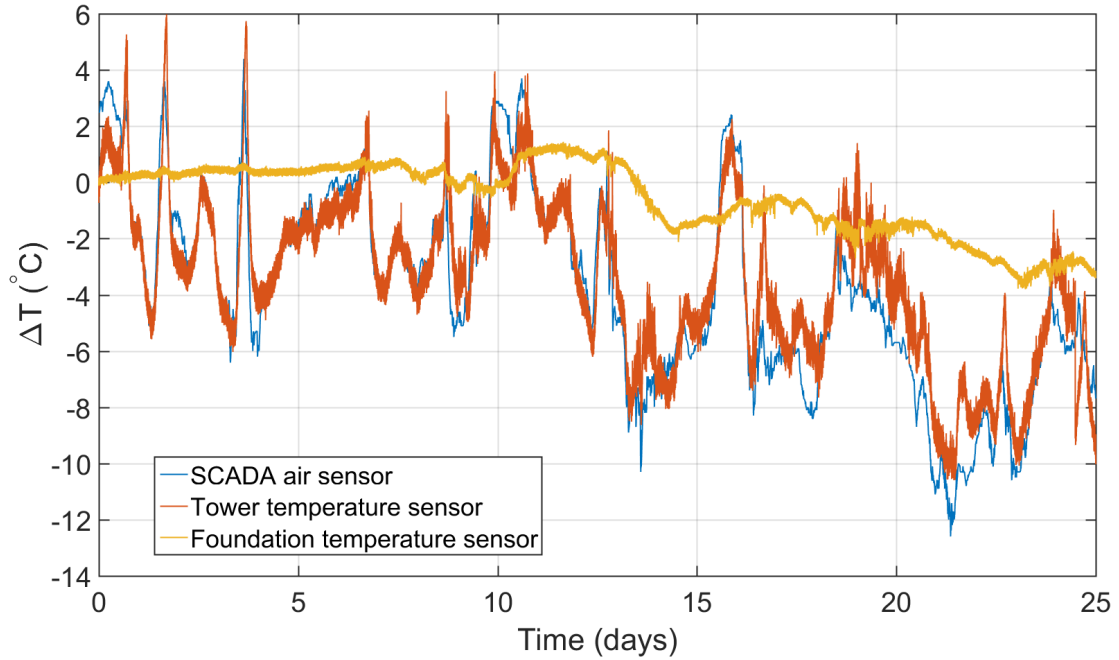
Figure 6.13: Temperature sensors in the tower and foundation compared to SCADA air temperature data over 25 day period.

6.6 Verification of sensors measurements

Now that the sensor design, manufacture, installation, interrogation and post-processing has been described, the next step is to ensure the measurements are in fact true. To do this, gathered SCADA data from the instrumented turbine is used, allowing temperatures to be correlated with temperature sensors, and strains/displacement sensors to be predicted by utilizing the previously presented model (Section 6.2.2).

6.6.1 Temperatures

SCADA air temperatures are collected and compared with tower and foundation temperature sensor data for a 25 day period, shown in Figure 6.13. In general the tower and SCADA temperatures are in good agreement, with an overall range of $-12.6 - 6\ ^\circ C$. Any differences are most likely due to the fact the air temperature is collected from a nearby weather tower. Other factors such as sunlight heating the tower will also cause differences. Foundation temperatures follow the long-term trend, remaining rather constant over the 25 day period with a range of only $-4 - 1.5\ ^\circ C$. Foundation sensors are of course buried under soil and experience a dampened temperature response [141]. Verifying these temperature measurements provides confidence in the temperature compensation calculations of strain measurements.
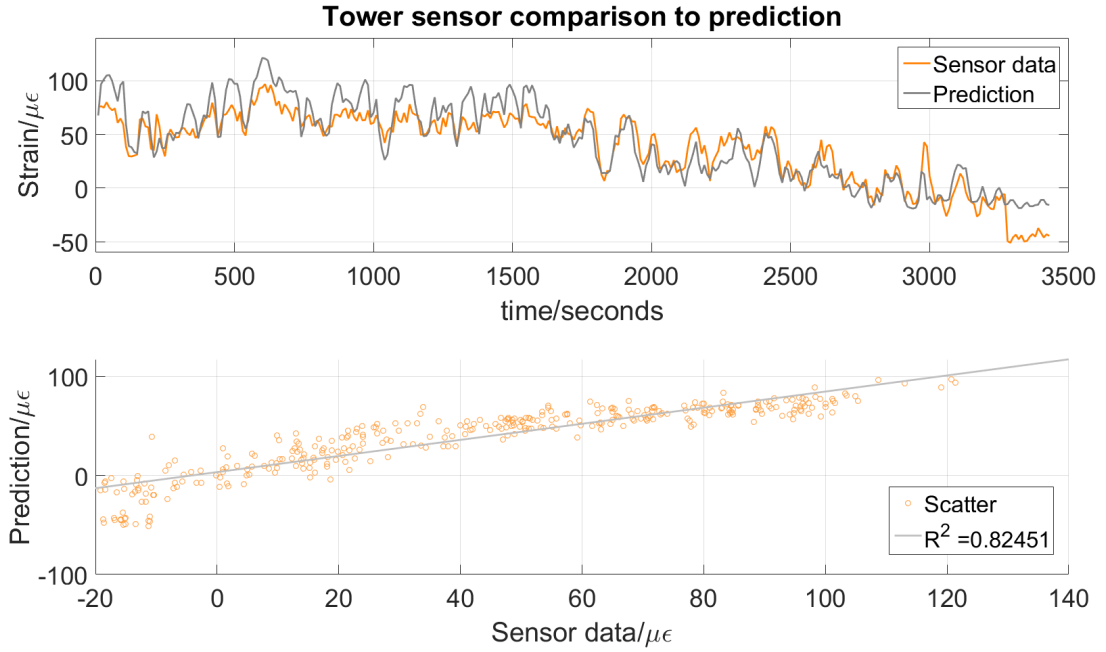
Figure 6.14: Comparison between one tower strain sensor and equivalent prediction using Equation 6.5 over a one hour time window of rated turbine power output.

6.6.2 Tower strain

Recalling Equation 6.5 from section 6.2.2:

$$\epsilon_T = \frac{M d_T}{2 I E_s} cos(\alpha - \theta_S) \tag{6.5}$$

which uses SCADA data to predict strain at the base of the tower at location θ_S. As discussed, for this prediction to be true the turbine must be under steady state operating conditions. Taking a one hour window of this prediction for one tower sensor, using the sensor location for θ_S, produces the plot in Figure 6.14. In this case a similarity constant $R^2 = 0.824$ or 82.4% was observed. It is worth noting at this stage the comparison is simply to provide a measure of validation. Since the prediction is a fairly simple estimate based on the steady state overturning moment occurring during rated operation, discrepancies will be evident. Factors such as oscillations of the turbine due to gusts, imperfect strain transfer, perpendicular turbine movements and errors in SCADA data will affect strain measurements or are not accounted for in the prediction. These rated power conditions are also rarely met, as rotor speed and wind direction in reality will not be constant. Therefore, only periods closest to rated conditions are considered.

The gradient of the linear fit line from Figure 6.14 can be used to estimate the strain transfer (≈ 0.8) of the sensor to the tower. The relationship is most likely not purely linear, due to the previously mentioned limitations - meaning this value is simply an approximation.

6.6.3 Crack displacements

Maximum measured crack displacements during early stages were around ± 3 μm, which is within the range of quoted displacements in some literature from Chapter 5. Hoult et al. [101] observed maximum displacements of 20 μm whereas Lima et al. [102] measured displacements up to 0.12 μm. One key point identified was the resolution of measurement equipment in these applications was either lower or matched the maximum displacements. In this work, the interrogator possesses a wavelength resolution of ≈ 0.5 pm, which represents an ideal displacement resolution of ≈ 0.032 μm for the sensors in this work. This resolution should be sufficient to measure crack displacements over a long-term.

6.6.3.1 Validation and relation to tower strains

At the early stage of monitoring, it is assumed the cracks are at a low severity state and behave similar to non-cracked concrete. From Chapter 3, the concrete stress-strain relationship can be expressed as linear at low forces. From this work, crack measurements are small and show a linear response to tower strains. It is then assumed that at this low severity state, the foundation strain sensors will behave linearly to the tower strain sensors as:

$$\Delta L_a = J_p \epsilon_T \tag{6.22}$$

where ΔL_a is the crack displacement change and J_p is some constant which represents the linear conversion from tower strain to foundation strain unique to sensor under consideration. Figure 6.15 shows a comparison between the crack displacement prediction using equation 6.22 and crack sensor B1 for a one hour time window of rated turbine operation, where J_p = -0.008. For module C, $J_P = 0.004$. The similarity constant when comparing foundation to tower sensors, $R^2 = 0.897$ or 89.7%. Visually, during rated turbine operation at this early stage, the correlation between tower strain and crack displacement seems reasonable, confirmed by the relatively high R^2 value. At this stage, tower strains have been validated as they match values calculated using a cantilever model. Small crack displacements have also been witnessed which seem to relate linearly to tower strains during the early stages.

6.6.3.2 Tearing displacements

Tearing or lateral displacements refer to the mode III movement of crack faces (see Chapter 3, Section 3.4.2). Whether these displacements would be witnessed in this work was unknown, but a sensor was designed that was capable of segregating the different displacement by using a certain geometry, explained in section 6.3.1. Generally, any large tearing displacements can be extracted by subtracting the measured displacement of each sensor arm. Figure 6.16 shows a comparison between two arms of sensor module B during the early stages. The measurements are extremely similar and the difference between displacements is small - verifying that each sensor is measuring
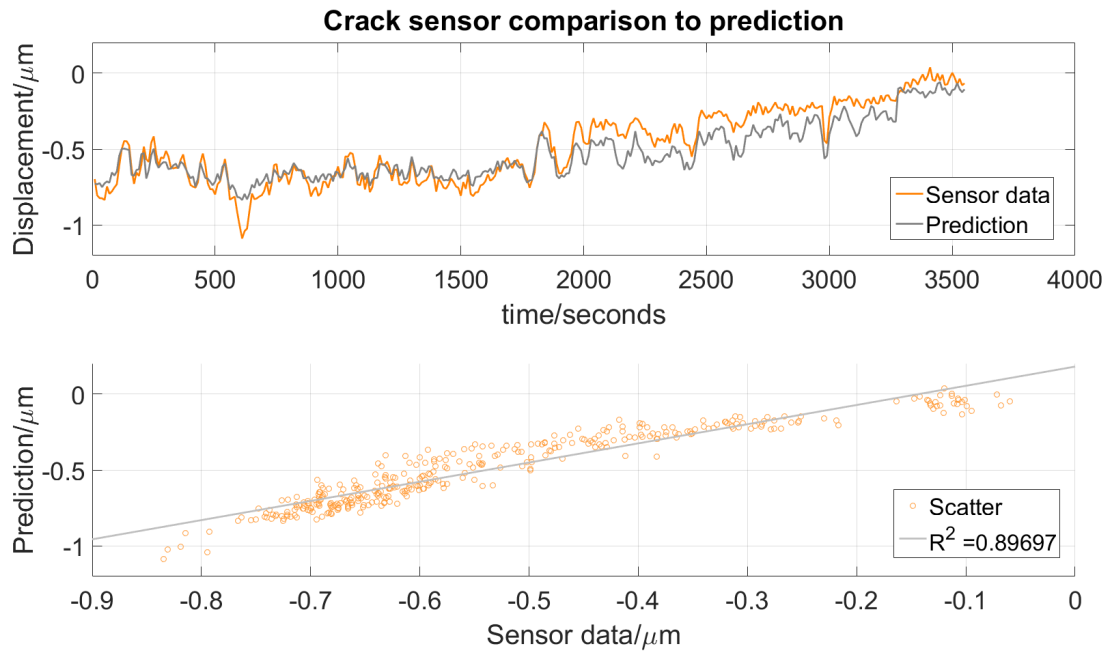
Figure 6.15: Comparison between one foundation crack displacement sensor and equivalent prediction using Equation 6.22 over a one hour time window of rated turbine power output.

crack opening and suggests no tearing displacements are occurring during these early stages.

6.7 Initial observations

Firstly, referring back to the objectives laid out in Section 6.2.5, a successful demonstration of a crack monitoring sensor system for multiple cracks apparent in an onshore wind turbine foundation has been presented. The maximum measured crack displacements are well above equipment resolutions, and during the early stage the crack displacements can be related to tower strains linearly. No tearing displacements have been observed during early stages as FBGs in modules show similar measurements. The next step is to develop an analysis method that can effectively quantify deterioration of a crack. Prior to this, a few interesting characteristics were witnessed which may aid in initial design of the method.

Start-stop procedures

Wind turbines will undergo start-stop procedures during operation, often several times per day. Generally, turbines will be switched off during periods of low wind speeds deemed too inefficient to operate or periods of high wind speeds regarded as unsafe to operate. For the turbine in this work, pitch lubrication is the most frequent cause of start-stop procedures, occurring at least once every 24 hours. Power curtailments also occur frequently and randomly when the site produces excessive amounts of power - which requires switching off a number of or all turbines on site. Other less frequent aspects such as maintenance, emergency stops or cable untwisting also cause similar procedures. An example of a typical start-stop that occurred during a blade lubrication of the
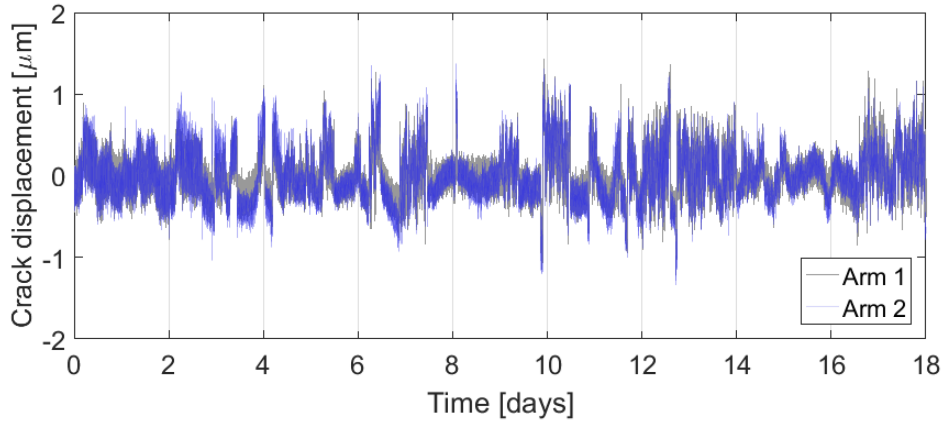
Figure 6.16: Comparison of two arms in the crack displacement module B. [4]

turbine in this work is shown in Figure 6.17 a). During this period, and similarly during other start-stop procedures, the tower strain and in fact the crack displacements react similarly, transitioning from one state to another rapidly. The magnitude of this transition will vary depending on the type of procedure. For example, an emergency stop or curtailment that occurs during a period of rated power (high wind speed) will cause the greatest transition. An example of the effect a curtailment transition has on the tower strain and crack displacement measured by sensor B1 is shown in Figure 6.17 b), where the turbine is switched off to limit power production. Clearly these defined loading events are extreme events that may impact the deterioration of cracks, but can also act as precise "markers" for comparison of the data. Also, these transitions were more prominent in module B than C, as shown in Figure 6.18. During visual assessment prior to installation, cracks were all judged as of a similar severity level. Analysis of these transitions has provided evidence that displacements of cracks during turbine operation can vary highly and cannot be identified from visual inspections. Consequences of the frequent loading events on the lifetime of the foundations is not discussed in any published works to the author's knowledge. It is also not clear whether these events were considered during the design process of foundations. Future work may explore these possibilities by analysing crack deterioration in concrete due to conventional fatigue loading (sinusoidal) compared to the same loading with additional instantaneous and frequent transitions.

Dynamics

Modal frequencies of turbines are unique to turbine design. Dynamic analysis of turbines is an extensively researched topic and is well known in the industry. A review by Tempel et al. [142] introduces the basics behind the dynamics of a turbine in terms of rotor and flexible tower. In this work, focus is on the deterioration of cracks. At this stage it is unclear whether the dynamics of a turbine can be utilized to determine if cracks deteriorate. Since most visible frequencies are caused by the rotating rotor and bending tower, it is unlikely they will change dramatically over

---

[4]Image published in co-authored paper [19].
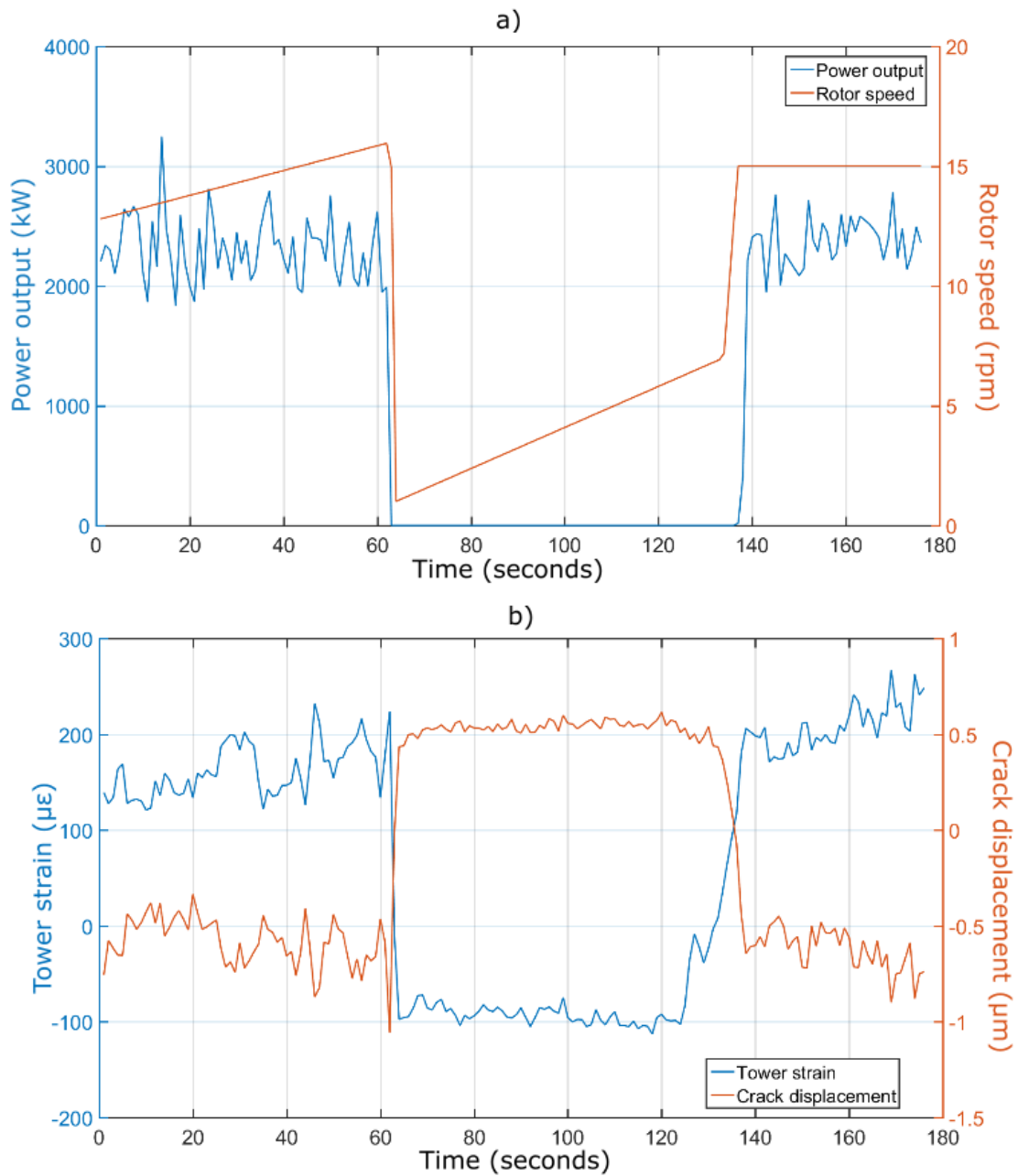
Figure 6.17: a) Example of start-stop procedure occurring during blade lubrication where the rotor is decelerated quickly before slowly restarting after a period of time. b) a separate transition clearly causing a loading event in the tower and cracks.
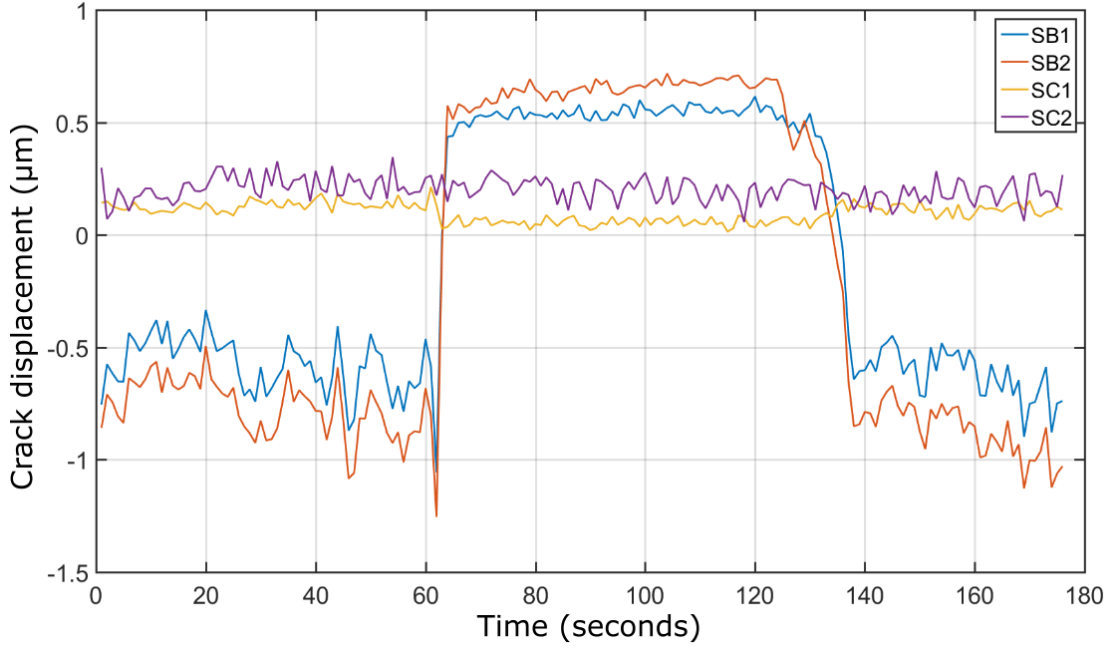
Figure 6.18: Difference in reaction of cracks monitored by modules B and C during blade lubrication. Module B shows large reaction compared to the damped reaction in module C. Suggests crack monitored by module C is less affected by start-stop procedures and may be less severe.

time when measuring cracks. Studying the visible frequencies in tower and foundations can be used for validation purposes. To extract the frequency components from the tower and crack sensors, a simple power spectral density (PSD) can be performed. This can be estimated by using the periodogram: given as the mean of the fast Fourier transform (FFT) squared:

$$P(k,f) = \frac{1}{n}|(\sum_{m=0}^{n-1} \epsilon_T(m)e^{-j(\frac{2\pi}{n})mk})|^2 \tag{6.23}$$

for k = 0,1,...,n-1, where $P(k)$ is the power of frequency, f in the tower strain signal, ϵ_T of length, n. Substituting crack displacement, ΔL_a for tower strain, ϵ_T in this equation provides the apparent frequencies in the crack displacement data. Figure 6.19 shows a comparison between the frequency components in the foundation and tower during the early stages. To effectively extract the dynamics a period during rated operation is required. Perfect rated operation rarely (if ever) occurs so some variation from the demonstrated results is likely. From the figure, it is clear the frequency components found in the tower are fairly similar to that measured in the crack displacement sensors, providing further validation. The particular frequency components found are difficult to identify, likely requiring a simulation of the turbine design in question. Such work is outside the scope of this thesis and is indeed not required to meet the objectives. Merely these dynamics can be used as a verification tool, and can also be used to determine if crack sensors continue to monitor displacements by ensuring dynamics continue to match tower sensors. It is unlikely any changes in crack width can accurately be extracted from any frequency variations.
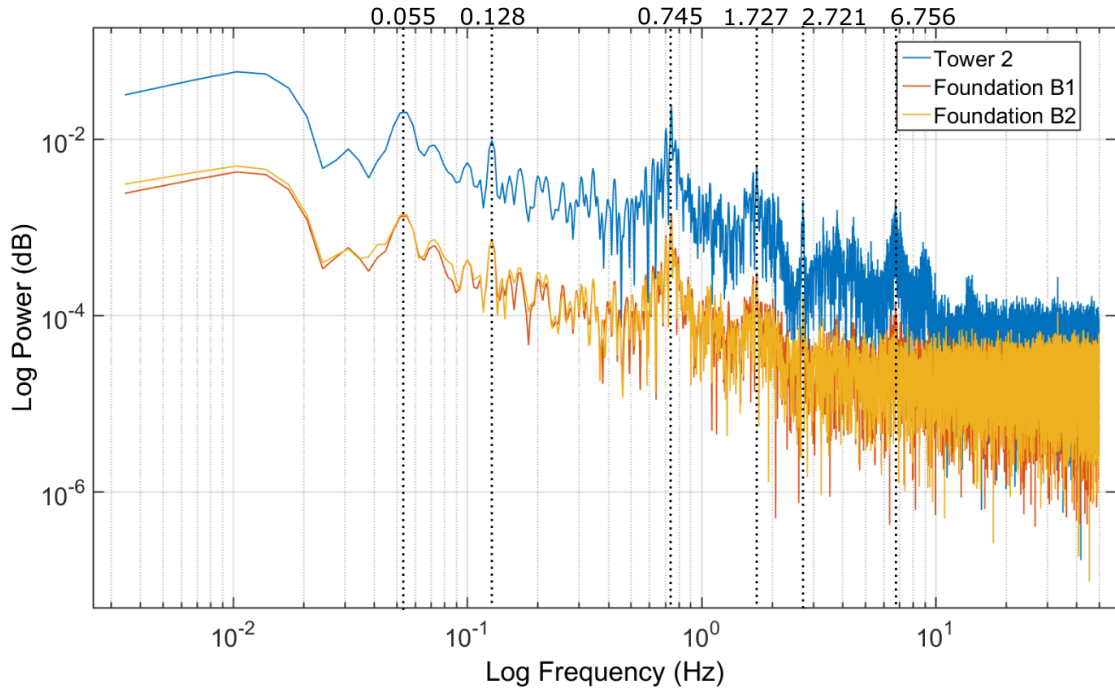
Figure 6.19: Comparison of measured dynamics in tower and foundation sensors during early stages.

6.8 Deterioration

To determine the deterioration or general change in any object, a quantity of data from at least two time periods separated by a certain amount of time is required. Any changes in the data when comparing data sets may represent deterioration of the object. The amount of time between data sets will affect the likelihood and magnitude of deterioration. For cracks, an example of visual inspection consists of collecting the steady state (turbine switched off) crack width at different time periods. An increasing crack width, or the calculated change in crack width over time, represents a quantitative measure of deterioration. In some cases, simply observing the crack width may be insufficient to determine the overall severity of the crack. For example, during operation the crack will displace between a maximum and minimum, which may increase over time should the crack become more severe. This could be accompanied by a constant steady state crack width - meaning the previous method would not identify the crack deteriorating. A more effective method for monitoring the crack would be to monitor both attributes simultaneously. Within this work, three attributes of a crack have been proposed that can be monitored for changes in order to determine deterioration. These have been categorised as "Reactive", "Permanent" and "Behavioural". Results consider the initial year of monitoring, specifically from January to October. During this period, only one interrogator was operational, meaning only tower sensors 2 and 3 and foundation modules B and C are considered (refer to Figure 6.9 and 6.12). Each deterioration concept is individually applied to time periods in January and October of modules B and C. Data for tower and foundation

sensors during these months is provided in the Appendix (10.3).

6.8.1 Reactive

Consider the previously mentioned maximum and minimum limits occurring as a crack displaces during turbine operation. The minimum will occur when the turbine is switched off (at low wind speeds) and the maximum will occur during rated operation. This is assuming the wind direction remains along the previously identified predominant angle and disregards any abnormalities such as wind gusts. These limits rarely occur; however, a common event, or "marker" that was identified (as described in Section 6.7) is the start-stop procedures when the turbine transitions between off and on states. Cracks were found to also transition during these periods. Exploiting this, an early damage state reaction of the cracks to these loading events can be ascertained and then be compared to later, similar events. Any deviation in crack reaction to similar loading over time could constitute to a quantitative measure of the deterioration, and can be monitored over time to alert of any limit breach (defined by turbine operator). For example, should a crack displace early by ΔY_E due to a blade lubrication event at the start of monitoring and then, after a period of time, displace later by ΔY_L for another blade lubrication period where $\Delta Y_L = \Delta Y_E + \Delta D_R$. Then ΔD_R is a quantity of deterioration which can be monitored over time representing the reaction change of a crack to a particular loading event. Most likely these reactions will not remain constant regardless of deterioration, so only significant variances represent a possible crack degradation. To ensure similarity between transitions, characteristics such as turbine power output, wind speed, yaw, rotor speed and temperature are recorded. These values will define the transition that should be compared.

Locating two similar transitions proved difficult with variables such as wind speed and rotor speed continuously changing. When comparing transitions, it became apparent that rotor speed was the most important factor and was required to be as identical as possible. Two similar transitions, one in January and a second in September were chosen. The start-stop procedures in both cases were curtailments. Figure 6.20 contains plots of both the module B reactions and accompanying SCADA rotor speed and turbine power output. Legends contain the magnitude of sensor transitions and the mean and standard deviation of wind speed during the transition period. The magnitude of sensor transition is calculated by taking the difference between means of 10 data point windows prior to and after the transition takes place. This method is applied to each sensor and results are shown in Table 6.4: column 2 and 3 show reaction of each sensor in January (ΔY_J) and September (ΔY_S) respectively. Deterioration (ΔD_R) is presented in the column 4 where $\Delta D_R = \Delta Y_S - \Delta Y_J$. Depending on the nature of the crack displacement (opening or closing), polarity of ΔD_R will represent different changes. In this case, the cracks are always closing upon loading, meaning a positive deterioration represents cracks "closing less" in the later transition and negative deterioration represents cracks "closing more". Figure 6.21 has been provided as a visual

Sensor	January ΔY_J (μm)	September ΔY_S (μm)	Deterioration ΔD_R (μm)
SB1	-1.1745	-0.6777	0.4968
SB2	-1.3584	-1.3174	0.0410
SC1	0.1199	0.1183	-0.0017
SC2	0.0838	0	-0.0839

Table 6.4: Reactive deterioration gained by analysing start-stop procedures at two time periods separated by 9 months.

aid to better understand this concept. Varying values of ΔD_R and transition polarity represent different types of changes.

Firstly, it is worth noting that the displacement of cracks remain relatively low. According to the Eurocode 2, BS EN 1992-1-1 clause 7.3(1), a crack width up to 0.3 mm wide is generally suggested as aesthetically acceptable. Turbine operators suggest a crack width of greater than 0.1 mm is usually repaired following inspection. These are provided as a guideline only.

In module B, the positive deterioration represents a smaller closing displacement in the later transition. This could potentially mean the cracks are becoming wider as they are less susceptible to closing. Emphasis should be made on the minuscule magnitude of these actual crack displacements and deterioration, with the maximum displacement of -1.3584 μm in sensor B2 and largest deterioration of 0.4968 μm in sensor B1. This represents $< 1\%$ of the operators suggested crack width limit (0.1 mm). Concerning the deterioration in sensor B1, at this point it is difficult to tell what the cause of this is. Simply, later data shows this sensor reacting less severely to closing transitions. The subsequent analysis methods may be able to determine if this is due to the changes in crack reaction or sensor reaction (sensitivity/drift). Since this is only evident in sensor B1, initial conclusion is that the sensor itself is the cause, perhaps due to a decrease in strain sensitivity. Module C portrayed smaller reactions throughout, including these transitions, and the deterioration is equally small. Crack sensor C2 showed no reaction during the transition in September, but also displayed infrequent reactions during transitional analysis of early data. This suggests it is not an effect of deterioration during this 9 month period, rather just a characteristic of the crack. Should a crack deteriorate to a significant state, one would expect a much larger value for the deterioration, concluding that each crack measured has not shown "Reactive" degradation.

6.8.2 Permanent

"Permanent" refers to the previously mention steady state crack width, usually measured by visual inspection methods. When using sensors, a period of "zero load" is identified and the sensor measurement recorded. In the industry, this "zero load" period is known as "dead load" conditions, where wind speed, power and rotor speed are all approximately zero with yaw remaining constant. Blade pitch is also taken into account, depending on current yaw position, as this can cause varying crack widths. For example, if a crack width is measured early as Y_E at the start of monitoring
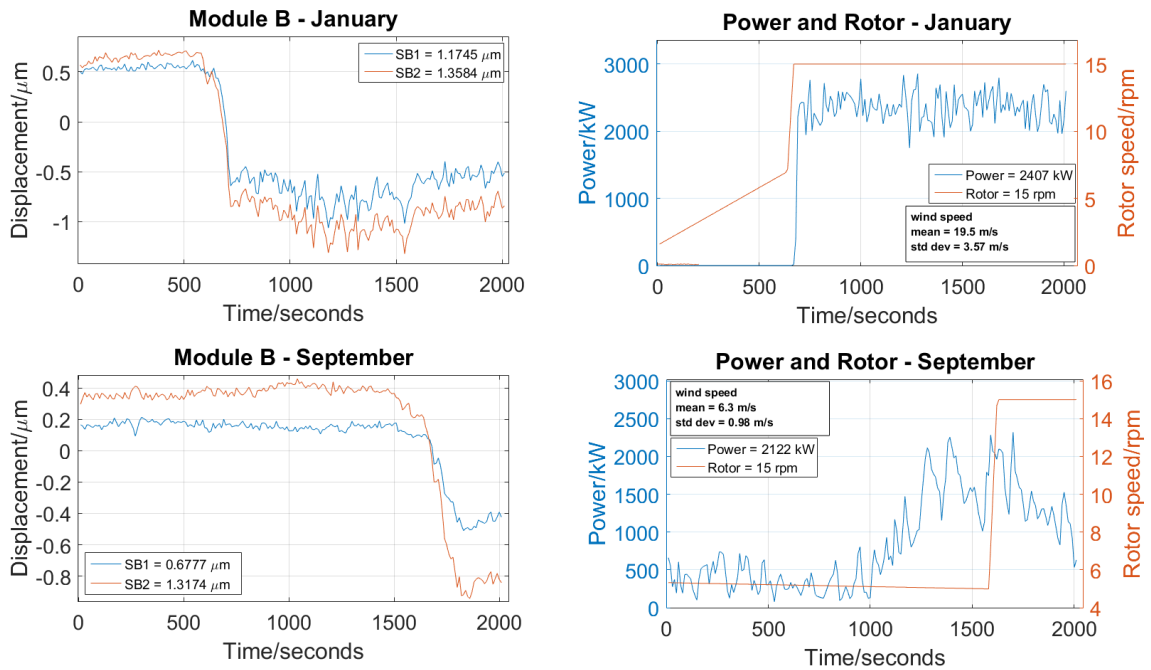
Figure 6.20: Reaction of module B to instant loading caused by a start-stop procedure occurring in January and September with similar characteristics.

Figure 6.21: A diagram illustrating the types of reaction deterioration.

Sensor	January Y_J (μm)	October Y_O (μm)	Deterioration D_P (μm)
SB1	0.4474	0.0277	-0.4197
SB2	0.6573	0.0425	-0.6148
SC1	-0.0282	-0.0228	-0.0054
SC2	-0.0271	-0.0222	-0.0049

Table 6.5: Permanent deterioration gained by analysing "dead load" conditions at two time periods separated by 9 months.

during a "dead load" period and later as Y_L under the same conditions after a period of time where $Y_L = Y_E + D_P$. Then D_P is a quantity of deterioration which can be monitored over time representing the permanent change in crack width. Again, similar to "Reactive", this crack width will most likely not remain constant regardless of deterioration, so only significant variances represent a possible crack degradation.

Similar to the "Reactive" method, locating periods of "dead load" conditions proved somewhat difficult, as these conditions rarely occur. Windows with as close to the "dead load" requirements as possible are extracted from two time periods - one early and one late during the measurement period. The mean of crack widths are then compared. Applying this method to each sensor gains the results shown in Table 6.5. Column 2 and 3 show the crack widths in January (Y_J) and October (Y_O) respectively, with column 4 portraying the deterioration (D_P), where $D_P = Y_O - Y_J$. At first glance, the negative deterioration suggests each crack has closed gradually over time. Emphasis is again made on the minuscule scale of these changes, with the maximum decrease of 0.6148 μm, again $< 1\%$ of an estimated total crack width (0.1 mm). Unlike "Reactive" deterioration, which concerns instant changes, this deterioration has larger susceptibility to uncertainties such as temperature compensation errors (drifts) or sensor degradation. It is possible that this gradual closing is evidence of such an affect. Should the crack widths significantly change, this would be identified by the "Permanent" method.

6.8.3 Behavioural

Finally, taking into account what was learned during the literature review: structural characteristics are not really considered or compared to damage monitoring. It was previously demonstrated that the tower strain and crack displacement during early stages appeared to relate linearly. In other words, the cracks behaved linearly to tower strains at a particular ratio, J_p, recalled from equation 6.22. Any large variation from this behaviour could represent deterioration of cracks and may not be observed from the previous two deterioration attributes. Essentially this method attempts to encompass any other deterioration that could be present in the sensor data by predicting crack displacements, based on the characterised crack response to tower loading, and identifying any changes. To expand on this concept: at the early stages a prediction of crack displacements is gained using the linear relationship in equation 6.22 during periods of rated operation. This was

portrayed in Figure 6.15, with $R^2 = 0.897$ and $J_p = -0.008$. If the same relationship is then used to predict and compare crack displacements during rated operation after a period of time, any significant deviations, either quantitatively by different R^2 and J_P values or simply from visual comparisons, could represent crack degradation. Also, polarity reversals will be studied (such as predicted opening accompanying a crack closing) as this could also represent a form of deterioration.

It is worth noting that rated operation rarely occurs for an extended period, if at all. Since the model used to achieve equation 6.22 assumes rated operation, it is difficult to gain ideal windows for data analysis. Figures 6.22 and 6.23 show results of module B and C respectively compared to predictions using equation 6.22. These windows represent the best values of R^2 gained from each month (January and September). The values of R^2 are provided in the legend for each sensor arm in the modules (B1/B2 and C1/C2). The magnitude difference (ΔJ_p) is only visually ascertained at this stage by using a constant value for both periods. Should J_p change, this would produce an obvious magnitude difference between sensor and prediction in the later plot. Tower strain, ϵ_T from sensor data has been used, but only during periods where these have high correlation to predictions from equation 6.5. Initial observation show that in January both sensors and prediction are very closely related, with an $R^2 \approx 90\%$. This leads us to believe that the cracks are superficial during the early stages, as expected, as they relate linearly to the tower strains. In September, a high R^2 value is also shown, suggesting the cracks are continuing to relate linearly to tower strains. Visually, sensor B2 remains close to predictions, with a more obvious difference in sensor B1. It is clear that sensor B1 has significantly *decreased* in magnitude when compared to both B2 and prediction. The decrease does not suggest cracks have deteriorated as it is unlikely cracks would close over time. There are a few explanations for this irregularity. Firstly the sensor itself (B1) could be degrading, causing a decrease in strain sensitivity, K_ϵ, from FBG displacement equation 4.9:

$$\frac{\Delta \lambda_B}{\lambda_B} = K_T \Delta T + K_\epsilon \epsilon_m \tag{4.9}$$

Secondly, the dual-FBG sensor is measuring a single crack at two different location; therefore, perhaps the crack could be behaving differently at each location. In other words, degradation at the location of sensor B1 could be greater than at B2. Again, it is unlikely deterioration would cause the crack to displace less. Finally, there is the lateral or tearing displacements to take into account, which could also affect the overall crack displacement and cause a decrease in one arm.

To further explore the case of sensor sensitivity K_ϵ decreasing, R^2 would be expected to remain high regardless of any change in K_ϵ, as R^2 is only affected by variability and not scale. For sensor B1, this is the case. To clarify, scaling measurements from B1 up to a magnitude equivalent to B2 would not change the value of R^2. Any reduction in K_ϵ would similarly not affect the R^2 value, as long as final displacements are greater than interrogator resolution. Any displacements less than the interrogator resolution will have interference from noise which would likely vary R^2.
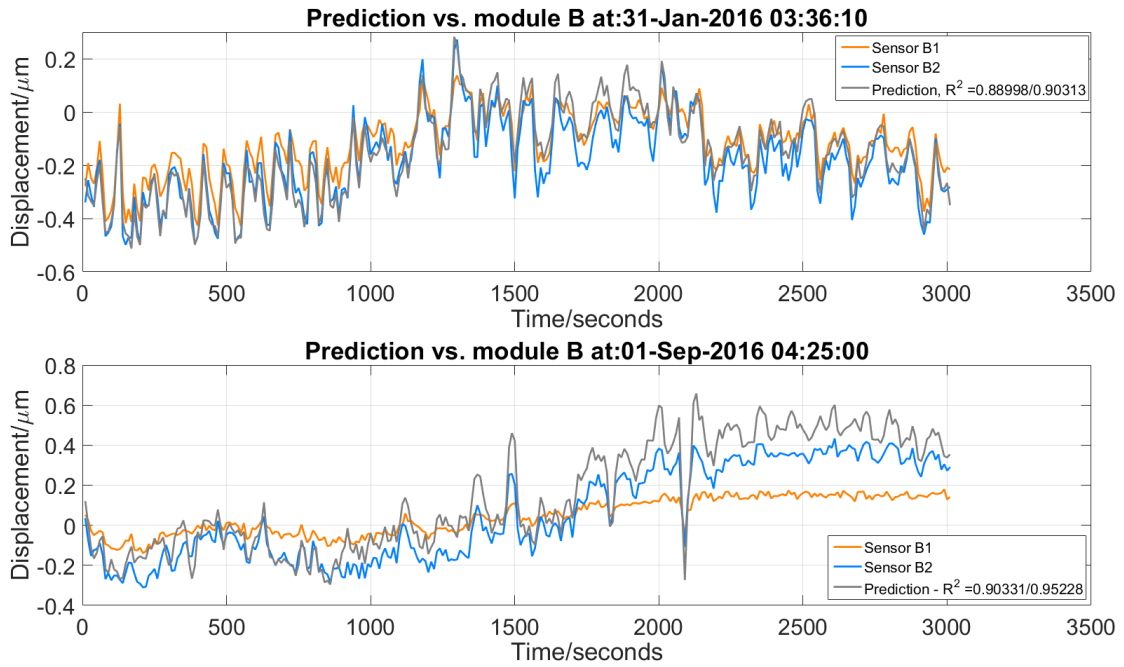
Figure 6.22: Visual comparison between prediction and sensor module B during two rated time windows: January and September. R^2 value of prediction to sensor similarity is provided in the legend.

As stated previously, the approximate ideal displacement resolution is $\approx 0.032 \ \mu m$. In this case, the measurements are very close, but greater than this limit; therefore, this decrease in magnitude could possibly be caused by sensor degradation. This result is consistent with the decrease in displacement found in sensor B1 from the previous "reactive" analysis, but not B2 which remains close to prediction and had a fairly constant reaction to loading events.

In the case of module C, results are somewhat similar, with R^2 remaining > 0.8 suggesting no deterioration in this crack. Visually, sensor magnitudes seem to also decrease in the later period, but not as severe as sensor B1. Again this likely suggests a reduction in strain sensitivity, K_ϵ of the sensors as displacements remain greater than the resolution. This reduction would mainly occur at two interfaces: bolt-concrete with mortar or sensor-steel with epoxy. The design of the bolt-concrete anchor is based on industrial standards, ACI 355.1R-91 [143] (also reported in [144, 145]). Further details are provided in the Appendix (10.4); however, the conclusion is that there is little room for improvement regarding the anchorage design, since forces are so low. No calibration or comparison exists regarding load transfer of different types of anchors in cracked concrete. Therefore, focus is shifted to the sensor-steel interface. This will be explored further in Chapter 7, where further experimentation reveals a possible impact of high humidity to strain gauge epoxies. An alternative design is also proposed in the form of metallic bonding.
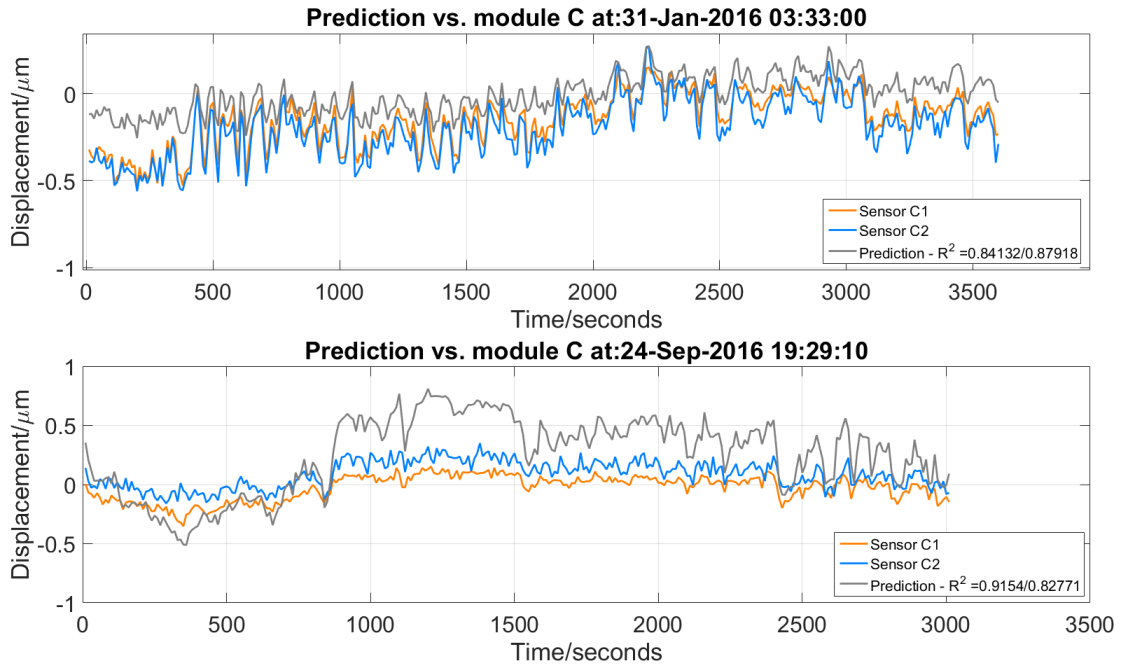
Figure 6.23: Visual comparison between prediction and sensor module C during two rated time windows: January and September. R^2 value of prediction to sensor similarity is provided in the legend.

6.8.4 Tearing displacements

The sensor design in this work has been procured in order to segregate any large tearing displacements that may be present in the monitored cracks. From section 6.3.1, a simple method of determining any apparent tearing displacements is taking the difference between arm measurements in a single module. A more accurate representation can then be gained from equation 6.13. Noting from the previous methods that a possible sensor degradation and strain sensitivity could be evident in only one arm and not the other, which makes extracting any tearing displacements more difficult. One method to check for tearing displacements is to use the "Behavioural" plots. Should a prediction be less in magnitude than one arm, but greater than the other, with a large correlation, R^2 to both, then this would suggest either large tearing displacements are occurring or the crack is behaving differently at each sensor location. At this stage, no evidence of such an aspect has been found during "Behavioural" analysis, suggesting tearing displacements are non-existent during these rated operation periods. A second method to quickly visually determine if any major tearing occurs over a large time period is to simply plot a scatter graph of the module, shown in Figure 6.24 and 6.25 for module B and C respectively. In each figure, a plot for January and September is provided for comparison. Any non-linear outliers may represent a large tearing displacement occurring. In module B (Figure 6.24, a clear linear relationship in January is shown, with possible linearity in September but at a much lower magnitude, providing further validation of the previous judgement of a decrease in strain sensitivity. There are no clear indicators of tearing
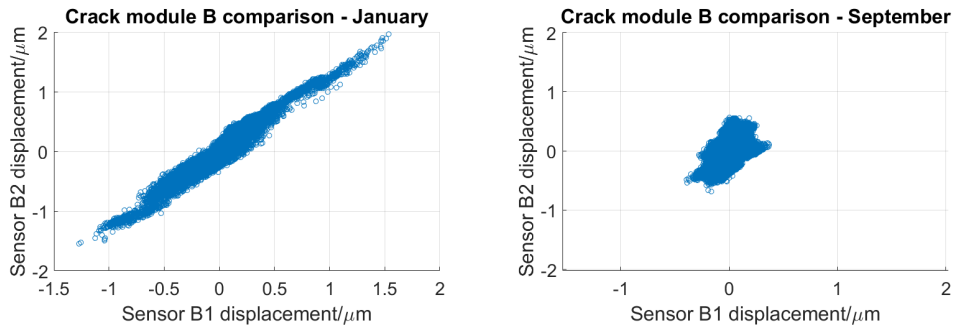
Figure 6.24: Scatter plot of module B during January and September in order to identify any non-linear outliers that may represent tearing displacements.
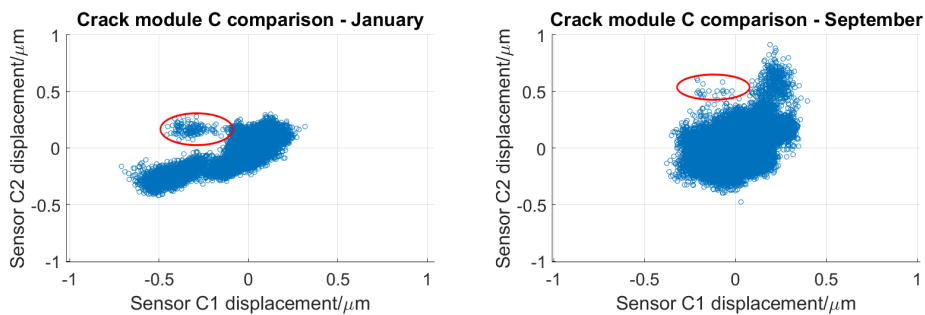
Figure 6.25: Scatter plot of module C during January and September in order to identify any non-linear outliers that may represent tearing displacements.

displacements. Module C (Figure 6.25) on the other hand does not show a clear linear relationship in either period. Discussed previously, the displacements were lower in C when compared to B, which would coincide with less similarity between arms. Interestingly, there are some outliers evident in both periods (identified by red ellipse), where measurements from each arm show a large difference. An example of one of these outlier periods is shown in Figure 6.26, which occurs during a start-stop procedure in January. Sensor C1 shows a value of -0.32 μm when C2 shows $+0.20$ μm. Perhaps during this instant load the crack undergoes a small tearing, amplified by the instantaneous nature of the event. It is worth noting that the displacement is very small and cannot be confidently defined as tearing. In future, this method can be used to identify any significant differences between sensor arms and allow determination of any tearing occurring over a long time window.

6.8.5 Dynamics

Dynamics are unlikely to provide an insight into crack deterioration, but comparing crack to tower sensors will provide validation that sensors are still measuring appropriate displacements. For example, it is possible that even with significant deterioration of the crack that the measured frequencies will remain similar to tower measurements. Figure 6.27 shows the repeated application of the method from Section 6.7 to a later period of rated operation. Frequencies may vary as the
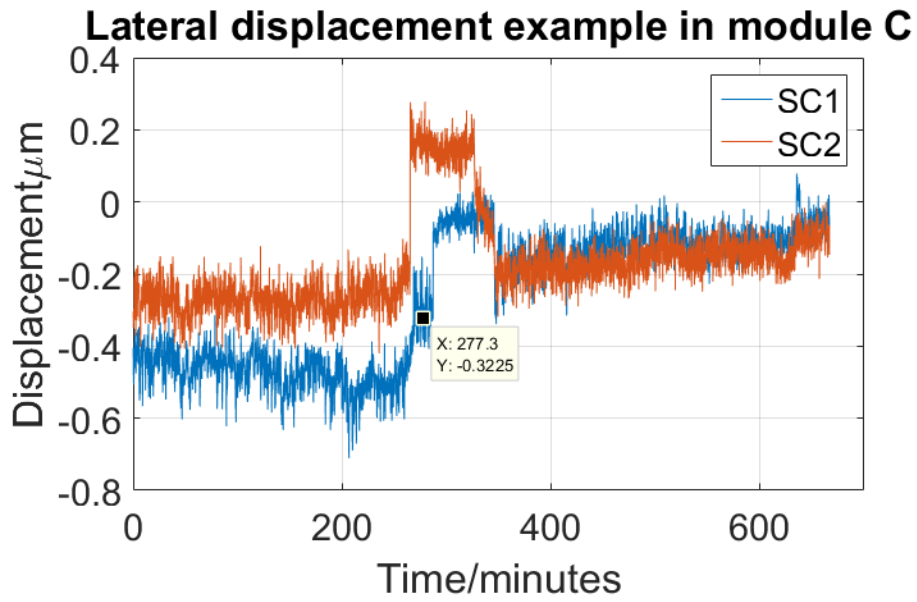
Figure 6.26: Example of a non-linear outlier detected in module C in January. During a start-stop procedure, the instant loading caused a difference between arms.

conditions are not constant. Clearly, sensor B2 remains similar to tower sensor 3, which agrees with previous analysis. The power of frequencies in sensor B1 have also decreased significantly and no real prominent frequencies appear. This further supports the conclusion of strain sensitivity decrease in the sensor.
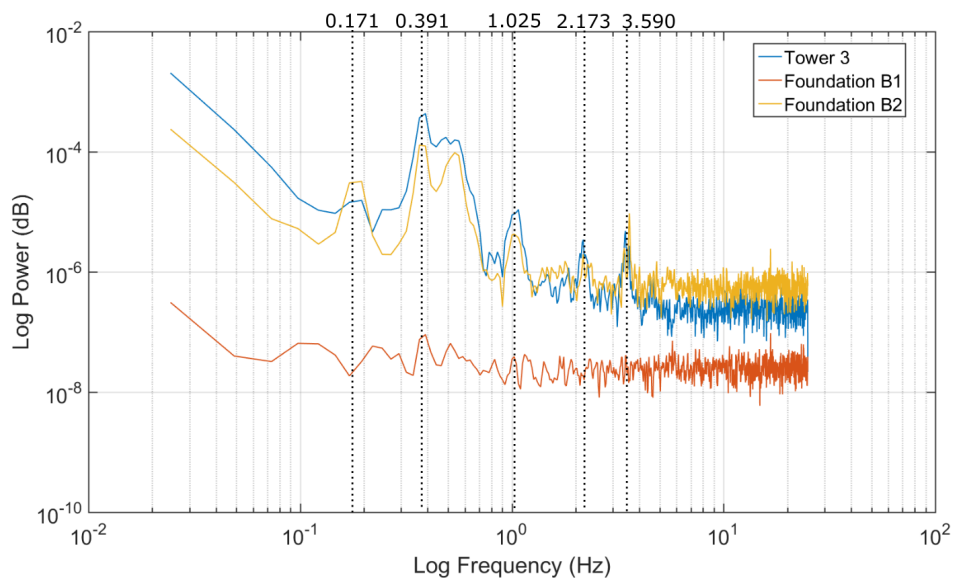
Figure 6.27: Comparison of measured dynamics in tower and foundation sensors during later stages. Referring back to Figure 6.19 shows the frequencies have varied slightly over time, but sensor B2 continues to show good similarity to tower sensor, with B1 validating previous analysis methods are perhaps losing sensitivity to strain as power has decreased significantly.

6.9 Chapter summary

An industrial application of crack monitoring in an onshore wind turbine foundation is presented in this chapter. Objectives of the installation were laid out and collectively met throughout the project. A bespoke sensor was designed and manufactured in order to segregate two modes of crack displacement: opening and tearing (Chapter 3, Section 3.4.2). Analysis showed prominently opening displacements occurring, with some possible tearing identified but inconclusive overall, as displacements were very small. Three deterioration concepts were defined: "Reactive", "Permanent" and "Behavioural". The "Reactive" method concerns instant loading events that occur during turbine start-stop procedures, such as blade lubrication and curtailments. Analysis of two time periods separated by 9 months showed that sensor B1 was "closing less" during transitions, which could suggest deterioration. Sensor B2 showed no real change during similar transitions which lead to the explanation of possible sensor degradation causing a decrease in strain sensitivity of B1. Module C showed less reaction to the defined loading events in both periods, suggesting perhaps this crack was less severe than that measured by module B, regardless of the visual inspection indicating similar severity. Overall, deterioration was extremely small at $< 1\%$ of the defined acceptable crack width of 0.1 mm. "Permanent" deterioration relates to the crack width measured during periods of close to zero external load on the turbine ("dead load" conditions). Again similar conclusions were drawn as magnitudes in all sensors decreased by a very small amount. It was suggested that the graduality of this component could mean a larger susceptibility to uncertainties such as temperature compensation errors (drifts) and sensor degradation. The "Behavioural" method investigates the relation between the tower strain and crack displacement during periods of rated operation. Specifically, analysing any changes in linearity, magnitude and polarity of crack displacements over time. All sensors continued to behave linearly to tower strains suggesting no deterioration occurring; however, further evidence of degradation in sensor B1 was found in the form of a decrease in magnitude. Dynamics evident in tower strain and crack displacement were also compared. Since modal frequencies are caused by rotating rotor and bending tower, it is unlikely they will change. This provides further validation of crack sensor measurements as frequencies were shown to match in both tower and cracks during both time periods. In the later period, sensor B1 did show a decrease in frequency power, which could also be evidence of strain sensitivity reduction.

Crack openings over time were witnessed by turbine operators during visual inspections. The length of time between these inspections is unknown, but the periodic nature of visual inspections means the true time taken for cracks to degrade is unknown. Therefore, it is possible cracks during this period are not expected to deteriorate and are at an early development stage. Monitoring of these cracks will continue in order to identify significant deterioration, should it occur. Future work would involve building and improving these early concepts and methods, such as adjusting the turbine model to include more variables such as torque to expand the number of appropriate

windows. The current model is restricted to rated operation conditions of the turbine only, which rarely occur. Information could also be used to inform an economic model to determine the optimal time to repair. Since, to the author's knowledge, no other onshore wind turbine foundation cracks of this nature have been monitored during operating conditions, there is no baseline for comparison. It is assumed that cracks are superficial at the early stages of monitoring and that any deviations from this is deterioration. Some evidence has been found to indicate sensors may have degraded in sensitivity, the cause of which is unknown at this point. Sensors have undergone alternating temperatures and humidity, which may be causes of degradation. Testing and improvements will be made to ensure this does not occur in any future installations. If such installations are undertaken, the cracks monitored should be of a much more damaged state than those measured in this work. This would increase the probability that major deterioration is present and allow for comparisons to this work.

Chapter 7:   Accelerated life and environmental assessment

7.1   Chapter overview

The industrial application in Chapter 6 has provided an insight into the average loading cycle and deterioration of cracks in an onshore wind turbine foundation monitored by a bespoke FBG sensor design over a period of 9 months. One factor that requires further investigation is the apparent evidence of sensor degradation. In this chapter, a sensor design is presented which removes the use of epoxy attachment and replaces with metallic bonding in the form of induction brazing and spot welding. Both designs are compared during direct static, fatigue and humidity experimentation. Demonstration of a low-cost small-scale fatigue testing machine follows. The purpose of the test-bench is to allow multi-purpose experimentation of materials, sensors and structures to further investigate results from the industrial application and test the metallic-bonded crack displacement sensor design applied to a crack in a reinforced concrete (RC) beam. FEM model simulations and test experiments are carried out to verify the structural integrity of the machine support structure for long-term testing. Experimental procedures replicating the in-situ loading cycles at an accelerated pace is of interest to verify the measurement system, allow currently unavailable comparisons to be made with in-situ results and test new sensor designs. Such an experiment is demonstrated on a pre-cracked RC specimen.

7.2   FBG displacement sensor

7.2.1   Sensor design

As discussed in Chapter 6, Section 6.3, crack monitoring in this work is carried out using long-gauge FBG displacement sensors. These sensors contain an FBG strain sensor attached to a substrate, which is then anchored at two points over the crack. In the industrial trial (Chapter 6) - epoxy was used as the FBG-substrate attachment method and the substrate itself was made from carbon steel. Epoxy attachment is a fundamental and highly reliable method for FBG attachment. Initial results from the industrial trial suggested a sensor sensitivity reduction. Reasons for this are unclear. With regards to sensor design, a possible unreliable protection from environmental effects could have caused corrosion on the carbon steel arms or have an effect on the epoxy. Also, the strain transfer at either FBG-to-steel or steel-to-concrete interfaces could have withered. In terms of the bolt-concrete interface, options are limited, with no real room for improvement (see Section 6.8.3). Possible enhancements then would involve replacing the carbon steel with stainless steel and epoxy with other possible attachment methods. Metallic bonding has proven to be a potential improvement to epoxy [22, 146]; however, existing designs are bespoke to particular application restraints, such as in [21, 147, 148]. Most commonly used strain gauge epoxies require specific curing conditions such as high temperatures or long time periods which can cause difficulties

during in-situ installations. Therefore, metallic bonding and spot welding is preferable to epoxy when a fast and simple attachment is required. It is possible that metallic bonding could also present increased strain-sensitivity, longer lifetime and improved resistance to environmental factors when compared to epoxy, but this would require rigorous testing. The principle of induction brazed, metallic bonding lies in using the magnetic properties of materials, such as carbon steel, to allow direct induction brazing. The process has been explained in previous work [147, 149], so will be briefly presented here. An induction coil around a carbon steel shim (thin plate) or metallic susceptor provides concentrated heating to a silver-based brazing paste, joining two or more metallic components at around 620°C. In FBG brazing, particular care is required in relation to high temperatures as they can damage the grating. The curie transition is a set material-specific temperature at which a material loses any magnetic properties it possesses. This can be manipulated during induction brazing by limiting the heating of Kovar to 435° (curie temperature), to ensure minimal thermal expansion on the encapsulated FBG and reduce reflectivity loss due to high temperatures [149].

In this work, a similar approach is used to manufacture FBG strain sensors. Firstly, a copper coated FBG (with bare FBG section) is inserted into the Kovar capillary (inner/outer diameter of 0.2/0.7 mm) with the grating centred, as shown Figure 7.1. Carbon steel shims are replaced with magnetic stainless steel (MSS) shims to provide corrosion resistance during operation. The shims are pre-applied with flow control material, which is a "paint" that restricts the area where brazing material can displace (Figure 7.2: left insert). Essentially, this "paint" ensures the brazing material is concentrated at the attachment points. This is required since the brazing area is flat and provides adequate area for spot welding and room for the fibre to trail off without being forced in direct contact with the shim's edge. Before brazing, a powdered flux is applied to protect the shims from oxidation. One shim and one side of the capillary holding the FBG are brazed together initially in one cycle (Figure 7.2). In previous work [147, 149], the brazing paste ingresses into the Kovar capillary due to direct heating from susceptors. It is unclear whether using the shim for heating (via magnetic induction) provides this ingress. This would require testing via polishing to observe inside the construction. At this stage, as long as adequate bonding of the FBG to packaging is witnessed, ingress is not important. Should ingress occur, the distance would depend on multiple factors such as temperature of brazing (varies slightly each time), size and position of heat concentrators (in this case the shims), quantity of paste used and number of impurities in the materials. Generally, from previous work, this was between 1-5 mm. The magnetic properties of the MSS enable uniform heating along the length of the shim. After cooling, the FBG at this stage can be pre-tensioned to minimise compression forces that will occur following thermal expansion and subsequent cooling. Required pre-tension strain, ϵ_{pt}, can be calculated as:

$$\epsilon_{pt} = \alpha_k \Delta T \tag{7.1}$$
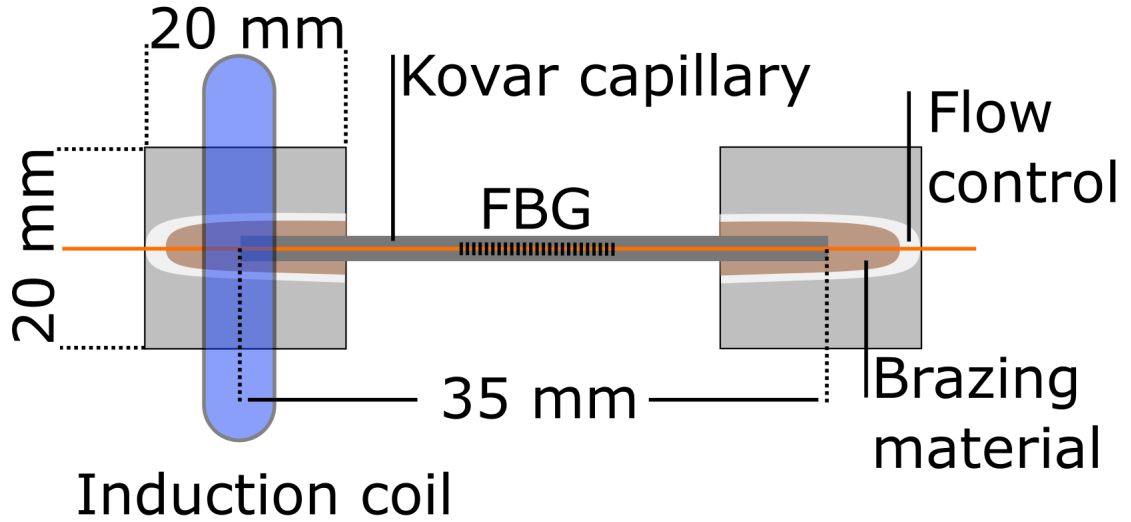
Figure 7.1: Brazing set-up for metallic-bonded FBG.

where α_k is the thermal expansion coefficient of Kovar ($\approx 5.5*10^{-6}$ m/mK) and ΔT is the change in temperature of the Kovar during brazing (435°C). This provides an approximate requirement of 2.4 $m\epsilon$ to counteract the compressive forces and avoid FBG buckling within the capillary. Pre-tensioning is accomplished by using grips and a sensitive adjustment apparatus. Following the second brazing cycle, everything is cleaned to ensure effective spot-welding (Figure 7.2: right insert).

In the previous work, the shims used were carbon steel due to the requirement to bend into small spaces [148]. If the objective in this work is to remove the possibility of corrosion, current designs are inapplicable due to the use of these shims. Common stainless steels belong to the 300 series, which are austenitic in nature meaning they have no magnetic properties. Magnetic stainless steels (ferritic and martensitic) do exist, but are difficult to acquire in thin plate dimensions. Fortunately, the nature of this application allows flat welding and thus a thicker welding shim (0.2 mm) can be used (carbon steel shim was 0.05 mm thick).

Figure 7.3 shows a) the conventional epoxy attachment, where the full length of the FBG is directly bonded to the steel substrate and b) the metallic bonding redesign with MSS shims brazed to copper coated FBG encapsulated within a Kovar capillary, then spot-welded to the stainless steel substrate. Spot-welding is used over further brazing as the substrate cannot be heated during attachment due to the large compressional forces following thermal expansion and cooling. The substrate in these photos was used for testing purposes only. In reality, this would be thinner when applied to concrete crack monitoring to minimise any resistance to crack opening. Figure 7.1 illustrates some key dimensions of the metallic-bonded FBG: the shim width/height is 20 mm, set to match the width of the steel substrate and a capillary length of 35 mm. The loss of $\approx 360°$ attachment from bending the shim around the capillary in previous work is compensated for by extending the capillary length to allow more capillary-shim bonding area. The capillary remains
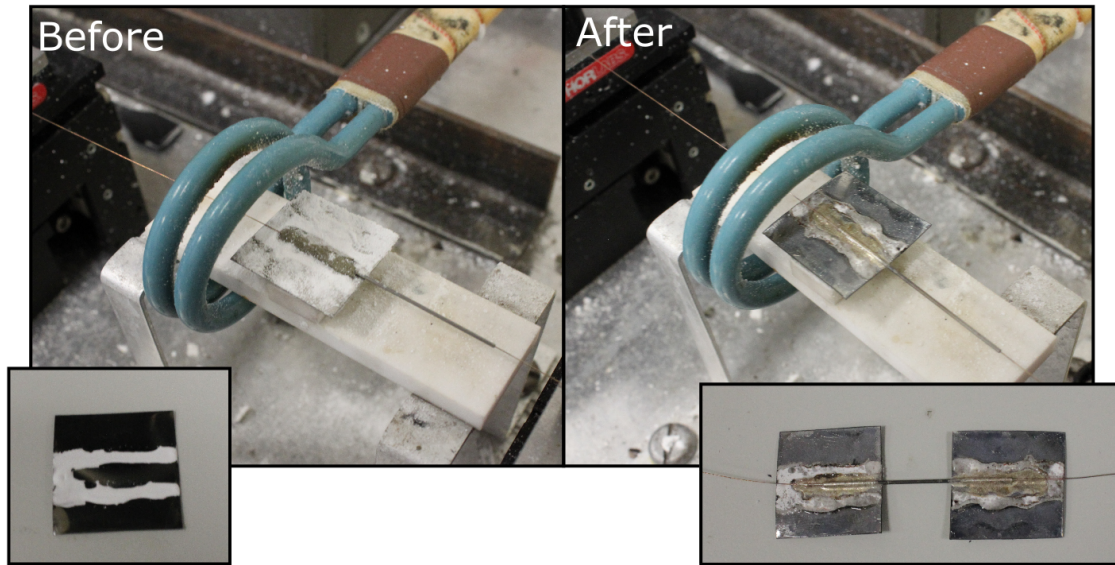
Figure 7.2: Brazing procedure, before and after induction coil operation. Left insert: application of flow control material. Right insert: completed brazing, prior to cleaning and spot-welding.
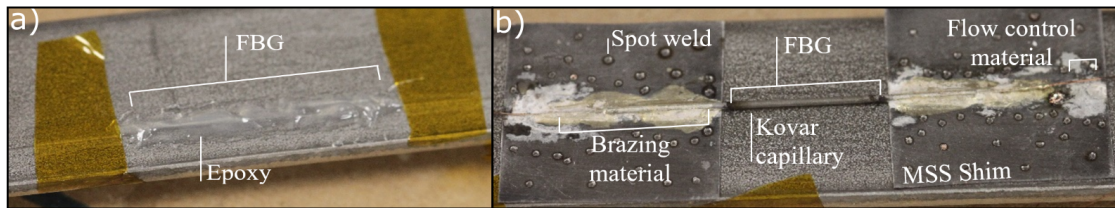
Figure 7.3: FBG bonding options: a) direct epoxy attachment, b) braze welded attachment.

with an inner/outer diameter of 0.2/0.7 mm.

7.2.2 Comparison of metallic and epoxy bonding

To determine if the metallic-bonded braze-welded design can perform to similar standards as accepted conventional epoxy attachment, some experimental tests were carried out. Firstly, Table 7.1 outlines the four chosen, well-established, strain gauge epoxies used and the curing conditions for each. Abbreviations are also provided, with an individual FBG attached with each epoxy (braze-welded is also included). Since MBOND AE-10 was used in the industrial installation reported in Chapter 6, two separate FBGs were attached using this to allow a more detailed insight. Two FBGs were also attached using the braze-welded design discussed previously.

Attachment method	Abbreviation	Curing conditions	Order
Epotek 301	E301	48 hours @ $24°C$	a)
Epotek 353ND	E353	30 minutes @ $80°C$	b)
M-Bond AE-10	MB1/MB2	48 hours @ $24°C$	c)
Epotek OG198-55	EUV	UV light for 30 seconds	d)
Braze-welded	BW1/BW2	Induction brazing @ $620°C$	e)

Table 7.1: List of attachment methods.
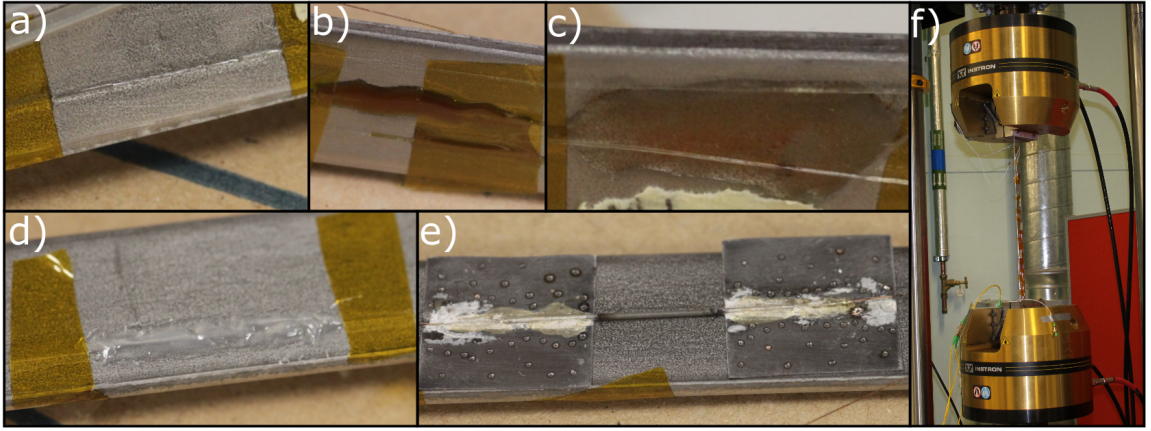
Figure 7.4: Experimental setup for fatigue experiment a-e) FBGs attached using methods in order of Table 7.1, f) Plate inserted into Instron machine.

Three separate experiments were run: fatigue, static and humidity. Fatigue experimentation consists of cycling the sensors a large number of times at a relatively low strain to deduce the consistency of attachment. A static test will evaluate the performance of sensors under static failure loading. Finally, a humidity experiment will determine the affects of a high humid environment on the sensor response. During tests, the quad-channel Smart Fibres SmartScan FBG interrogator was used. This provides a wavelength range of 40 nm, maximum sampling frequency of 2.5 kHz and repeatability of < 1 pm.

7.2.2.1 Fatigue experiment

The objective of the fatigue experiment is to determine if the attachment methods undergo any deterioration due to cyclic loading at strain levels well below failure. Strain was set at ≈ 0.5 $m\epsilon$ as a baseline. FBGs were attached to a 600 mm long, 20 mm wide, 3 mm thick structural steel plate which was inserted into an Instron 8802 servo-hydraulic machine. Figure 7.4 a-e) shows images of each attachment according to Table 7.1 and f) shows the inserted plate into the Instron machine. Force, F_1 required from the machine to produce strain, ϵ_1 (0.5 $m\epsilon$) can be calculated as:

$$F_1 = \epsilon_1 E_s A_p \tag{7.2}$$

where E_s and A_p are the Young's modulus of structural steel (200 GPa) and cross-sectional area of the plate (60 mm^2) respectively, providing required force of 6 kN.

An initial one million cycles of 0-6 kN (0 - 0.5 mϵ) trough-peak load sinusoid at 15 Hz was performed. Results from a 1 second extract of each sensor is shown in Figure 7.5. Here, 15 cycles are shown of each sensor's response which is converted into strain. To determine fatigue, the amplitude (mean-peak) of each cycle is taken for each sensor and compared. This is to negate any affects caused by inaccurate zeroing of the loading machine. Any drifts of the amplitude over time would constitute to fatigue damage to the sensor. Additionally, the variance of the amplitude
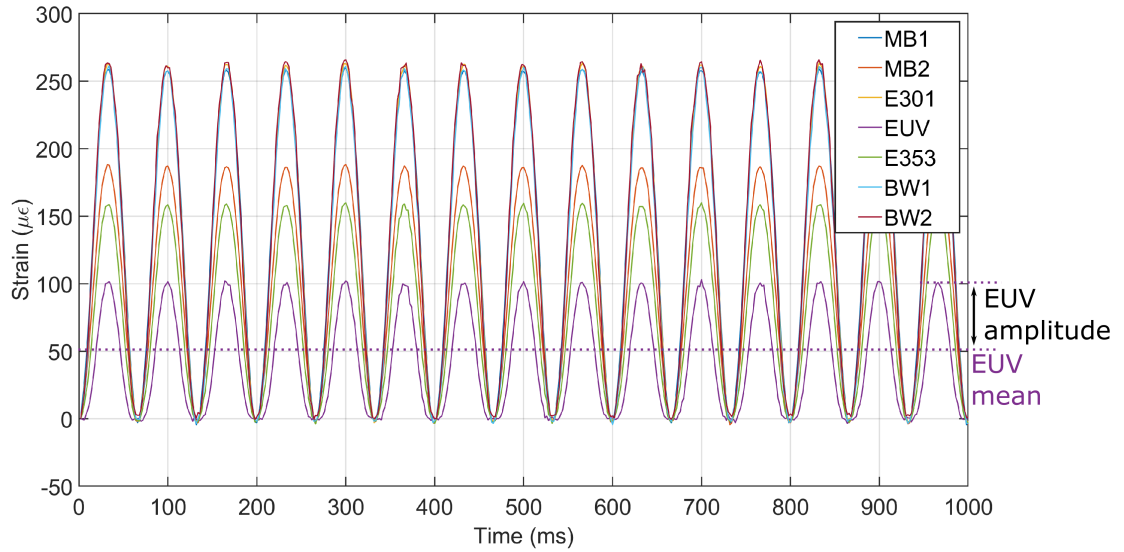
Figure 7.5: One second extract of 0 - 0.5 mϵ sinusoidal fatigue loading on sensors. This demonstrates the low strain sensitivity ($<$0.6) and the method of extracting amplitude. The amplitude of EUV is annotated (mean-peak) and is taken for each cycle during fatigue analysis.

represents the effectiveness of the attachment method.

To ascertain if any degradation occurred, an FFT was used to extract the 15 Hz sinusoid response of the sensors. The strain amplitudes (peak-mean) were extracted for each cycle and then visually assessed for each sensor, shown in Figure 7.6 a). In other words, the y-axis represents the strain amplitude of that cycle number (x-axis) of each particular sensor. A greater value in the y-axis means the sensor is more sensitive and the more stable over time represents a greater resistance to fatigue. To determine the stability of each sensor the measurements can be normalised and compared, as shown in Figure 7.6 b). The ideal wavelength resolution of this interrogator is 1 pm, which translates to ≈ 0.645 $\mu\epsilon$. From this graph, the largest variation is in sensor BW1 and BW2 at $\approx$ 2-3 $\mu\epsilon$. Both braze-welded sensors show a larger variation when compared to epoxy, however this is extremely small and negligible, since errors such as force measurement or slippage are not considered. Since sensors withstood this load phase with relatively low variation in response, a second test was run at double the strain/force (1 mϵ/12 kN), with the same number of cycles. Results for the second test are shown in Figure 7.7. In this case, all sensors vary within $\pm$ 3 $\mu\epsilon$, which remains negligible. All sensors showed excellent stability over both experiments.

With regards to the sensor magnitudes throughout, the absolute maximum cycle amplitude would be 250 $\mu\epsilon$ and 500 $\mu\epsilon$ for 6 kN and 12 kN tests respectively, assuming zero losses from machine grips. Strain transfers range from 22% to 56%. These values do not compensate for any losses from the plate-machine interface (such as slippage), machine losses (friction) or load cell measurement errors. Taking into account these losses, each strain transfer would likely improve equally. In fatigue experimentation, the factor of interest is the constancy of peak values over time, which are relatively stable for all sensors. One other interesting discovery is in regards to
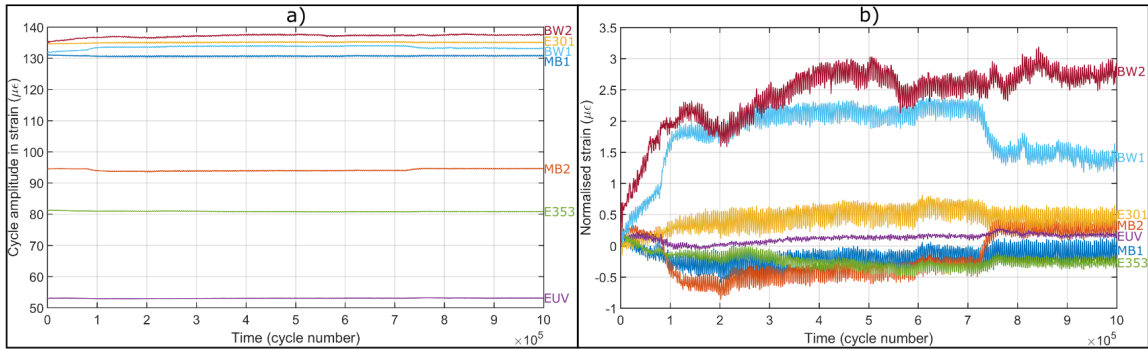
Figure 7.6: Epoxy and braze-welded comparison during 1 million cycles of 6 kN/500 $m\epsilon$ fatigue loading at 15 Hz. a) Strain amplitude of each sensor per cycle and b) normalised strain showing stability.
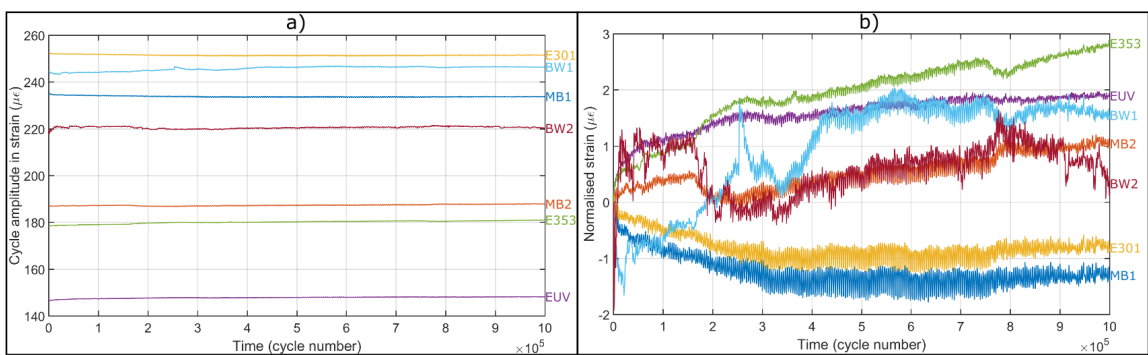
Figure 7.7: Epoxy and braze-welded comparison during 1 million cycles of 12 kN/1 $m\epsilon$ fatigue loading at 15 Hz. a) Strain amplitude of each sensor per cycle and b) normalised strain showing stability.
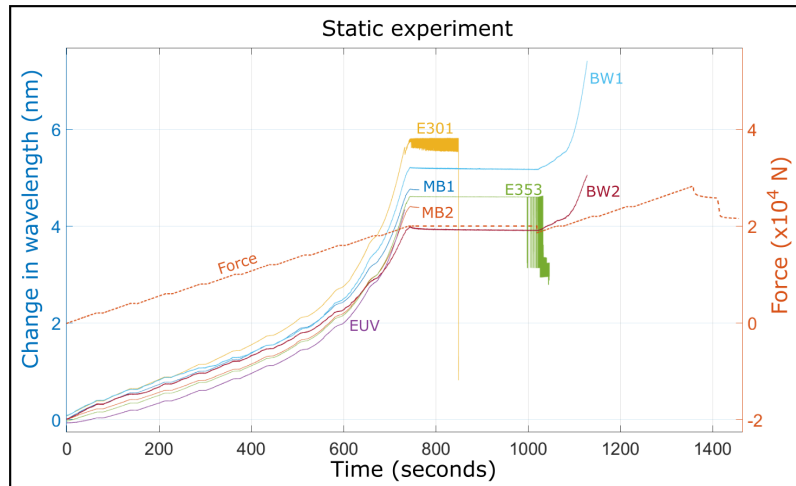
Figure 7.8: Epoxy and braze-welded comparison during static tests.

linear elastic systems, where doubling the load should double the strain (or less if losses are non-linear, which is common in slippage). Such a law is followed by all sensors other than EUV, which increased by ≈ 2.8 times, suggesting possible plastic deformation of the epoxy at these strains (this requires further investigation). Epoxies were extremely stable throughout and it is clear why they boast such popular use for strain gauge attachment. The braze-welded designs in general showed a comparable strain sensitivity to the best performing epoxies, but showed slight increase in variations during tests. This could be caused by non-uniform attachment due to spot welding, but is small and negligible.

Overall the fatigue testing has provided an insight into differences between epoxies: although all showed excellent stability, strain sensitivity was lacking (or varied in the case of MBOND AE-10). Also, both braze-welded demonstrated performance comparable to epoxy, but perhaps an improved spot-welding could further improve stability.

7.2.2.2 Static experiment

Following the completion of the fatigue experimentation, the same setup was used to perform a static ultimate failure test. It was expected that sensors would fail before the plate and far above any expected strains during application, but the purpose of the test was to determine: i) the overall strength of each attachment method and ii) any differences in linear elastic regions of each method. Results from the test are shown in Figure 7.8, steps of 2 kN were held for one minute. At 20 kN the test was paused and force retained. Sensor "EUV" failed, with all other epoxies failing subsequently. Interestingly, both braze-welded attached FBGs survived and so the test was continued, eventually failing simultaneously at 24 kN. Although this larger failure strain is not an advantage in terms of the application, it exemplifies the overall strength and sturdiness of the method and that the design performs comparable to epoxy.
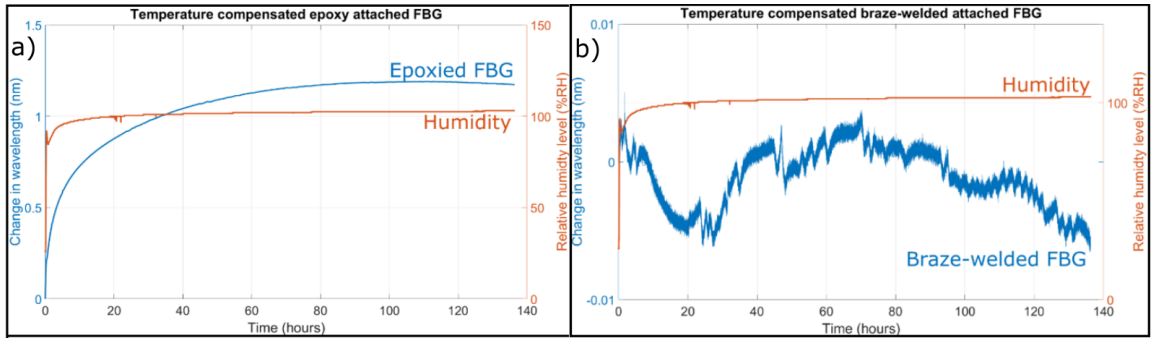
Figure 7.9: High humid environment, results for a) E301 epoxy and b) braze-welded attached FBG. Note the wavelength axis values.

7.2.2.3 Humidity

The final experiment involves an issue often overlooked in some applications: humidity. Relative humidity (RH) can be expressed as the ratio of water density in air to the saturated water density of air, both of which are dependent on temperature. In general, rainfall can increase the RH as it evaporates, both decreasing temperature and increasing moisture content. Therefore, any application of sensors outdoors should take this into account and test sensors at high humidity levels prior to implementation. To expand: according to UK Met Office [150], the annual average relative humidity in the UK from 1971-2000 varied between 76% and 88%. To simulate this high RH, enclosed salt solutions can be used in the absence of an accurate humidity control chamber. This method is well known, with the type of salt used producing a certain RH. In this work, a potassium-sulphate solution was used, supplying an RH of $\approx 96\%$ at 40°C [151]. A solubility table can be used to determine the required salt-water ratio, revealing 14.8 g of potassium-sulphate per 100 ml of water is required.

For the initial test, two sensors were attached to separate 0.2 mm thick stainless steel plates, one braze-welded and one epoxied with Epotek 301 (similar performance to braze-welded and best performing epoxy in previous experiments). The grating section of FBGs were bare and were tested prior to attachment at the high humidity showing no changes. They were also temperature cycled after attachment to remove any possible relaxation and to determine their temperature sensitivities. Sensors were then enclosed within a chamber containing the potassium-sulphate solution and held at a constant temperature of 40°C. A thermo-hygrometer with resolution $\pm 3\%$ RH and $\pm 0.5°C$ was used to monitor humidity and temperature. Sensor wavelengths and humidity were monitored over a period of 140 hours, shown in Figure 7.9.

First note the difference in wavelength axis values in both graphs and that the FBGs were temperature compensated. The braze-welded (Figure 7.9 b)) showed no influence from humidity (± 0.01 nm) with small variations most likely due to temperature compensation errors. However, the epoxy showed a large increase in wavelength, ≈ 1.2 nm, which equates to $\approx 750\mu\epsilon$. This was
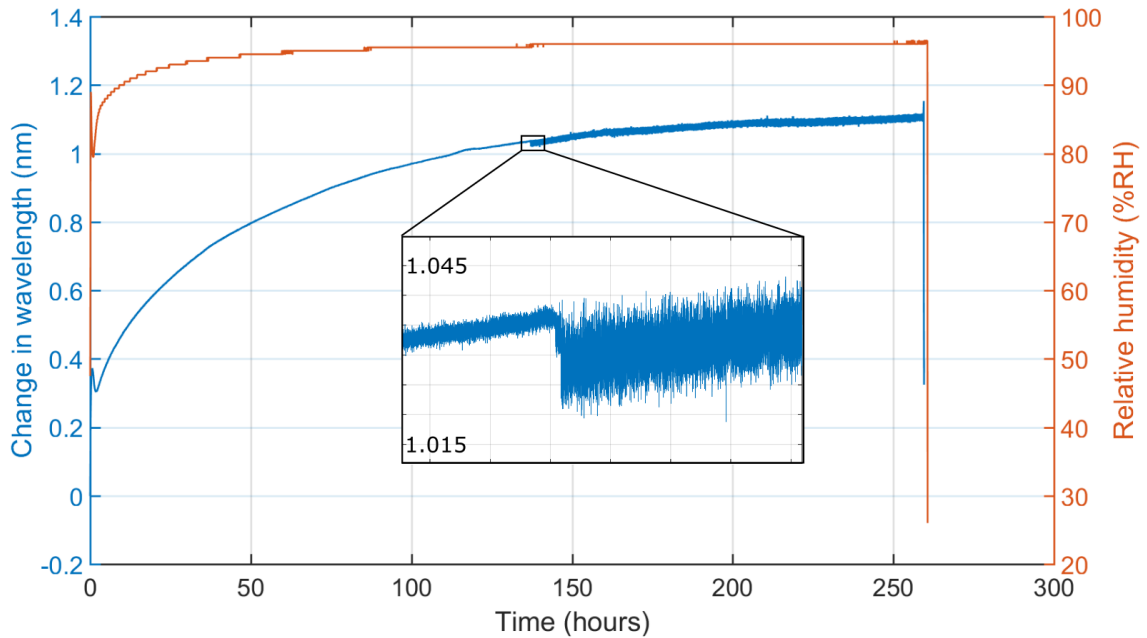
Figure 7.10: High humid environment, results for MBOND epoxy. Insert: Sudden drop and increased noise due to decreased peak power.

perhaps caused by swelling of the epoxy with the introduction of a high moisture level, causing an application of tension strain to the FBG. This signifies that the sensor has a humidity dependence, the relation of which is unclear. Clearly from Figure 7.9 a), this relation is non-linear, with a varying wavelength during periods of constant humidity. This condition would be difficult to compensate for, assuming it is repeatable. It would likely require an accurate Hygrometer.

Prior to any thorough investigations, a second test was run on the MBOND epoxy. An FBG was similarly attached to a 0.2 mm thick stainless steel plate and inserted within an enclosure with a similar salt solution. Figure 7.10 shows the response of the sensor over a 260 hour period. Results are similar to the previous test, with an increase in wavelength of 1.1 nm. Interestingly, at 137 hours a sudden drop occurred, coinciding with a decrease in FBG peak power and equivalent increase in noise. This continued for the remainder of the experiment and could possibly be caused by damage to the FBG.

Following these experiments, it is clear the popular strain gauge epoxies have a dependence on humidity, showing swelling behaviour. There are two options to compensate for this: assuming the relationship is repeatable, install an accurate humidity sensor and characterize sensors to humidity or attempt sealing with packaging, which cannot completely ensure humidity isolation as moisture will exist inside. The third option, suggested for future sensor installations, is to replace the current popular strain gauge epoxies - either with metallic bonding or humidity resistant epoxies. Humidity resistant epoxies do exist, but whether they perform well in strain gauges remains to be tested. It is suggested that this be a focus in future work (Chapter 9, section 9.2.3).

7.2.2.4 Discussion

Presented was a comparison between a custom braze-welded and popular epoxy attachment methods during fatigue, static and humidity experiments. Similar performances were witnessed from both during the fatigue experiment, with braze-welded showing high strain sensitivity but a very small variation in response over time. Static tests simply showed the strength of the braze-welded design, and again similar linear behaviour to epoxy. Finally, sensors of both types were held at high humidity, revealing a possible swelling of epoxy applying tension whilst the braze-welded was unaffected. To completely characterise the braze-welded sensor, more tests will be required.

There is one minor disadvantage of the current displacement sensor that may become more influential at larger displacements: plate bending. For this reason, an alternative design was briefly investigated during this work. The purpose of with was to replace the plate-based FBG displacement sensor with a tube. Since FBGs are attached to a thin metallic plate, any space between plate and substrate can allow the plate to bend. At large loads, significant bending may cause false measurements. For example, consider a plate bolted to a surface with an FBG attached on top. When the bolts are "pulled" in opposite directions the plate could bend in such a way that the FBG would measure compression, illustrated in Figure 7.11 a). Emphasis is made on the fact that this requires large loads and adequate space between sensor and substrate. This will most likely not affect the sensors currently employed in the field as these were fit flush to concrete and displacements are small. A possible solution to this that was investigated briefly is the replacement of plate with tube, shown in figure 7.11 b). Tubes are less susceptible to bending forces, for example, consider the equation for maximum stress, σ_m in a cantilever beam of length, L_b with applied end point load, F_e:

$$\sigma_m = \frac{F_e L_b}{I_S} \tag{7.3}$$

where I_S represents the cross-section modulus, $I_{Sb} = \frac{bh^2}{6}$ for beam of breadth, b and height h and $I_{St} = \frac{0.78(r_o^4 - r_i^4)}{r_o}$ for tube with inner, r_i and outer, r_o radius. For such a loading experiment, values for all variables are provided in Table 7.2, which provides the stress in a beam (plate) $\sigma_m = 59.88$ GPa and in a tube, $\sigma_m = 1.74$ GPa. This is confirmed with FEM models, shown in Figure 7.12.

Induction brazing was used for all attachments and the order of brazing is extremely important. Two capstan bolts were firstly brazed to the steel tube. These bolts contain holes in the head suitable for housing a tube and allow brazing material to be injected inside to firmly adhere the two components. An FBG is then fed through two Kovar capillaries and steel tube to produce the construction shown in Figure 7.11 b). The steel-capillary intersection followed by the capillary-fibre on the same side are then brazed using concentrators to reduce the heat transferred to the rest of the steel tube. Next the steel-capillary intersection on the opposing side is brazed, meaning the FBG is still unattached and will not be affected by steel expansion. After cooling, pre-tension is applied to the FBG to reduce any compressive forces caused by cooling following thermal expansion.

Concentrators should reduce any heat transferred to steel and thus reduce compression on FBG afterwards. The other fibre-capillary is then brazed in the same fashion, producing the tube displacement sensor.

Unfortunately, during prototype sensor manufacture, this design proved too difficult to build with available equipment due to the multiple brazing procedure combined with extreme weak point at each capillary end. Unlike the plate sensor, the egressing fibres are not supported by the rest of the construction. This meant the tube sensors were easily broken. Focus was shifted to improving the plate sensors from this point; however, it is possible that this concept could provide a better displacement sensor overall.

Variable	Value
b	10 mm
h	1 mm
r_i	4 mm
r_o	5 mm
L_b	100 mm
$I_S b$	1.67 x 10^{-11} m^3
$I_S t$	5.76 x 10^{-8} m^3
F_e	1 kN
Material	Steel

Table 7.2: Variable representing the conditions for the FEM model simulations.
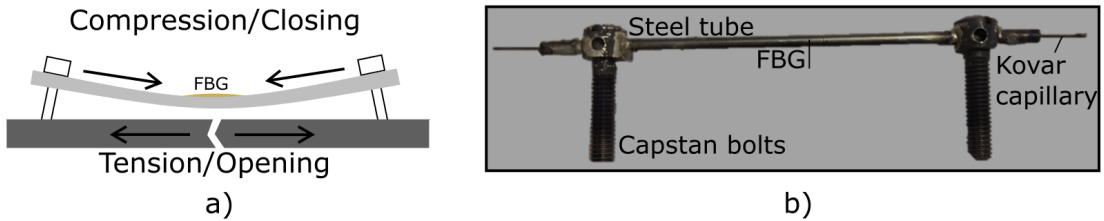
Figure 7.11: a) Possible error due to plate bending, b) replacement of plate by tube may provide more resistance to bending.
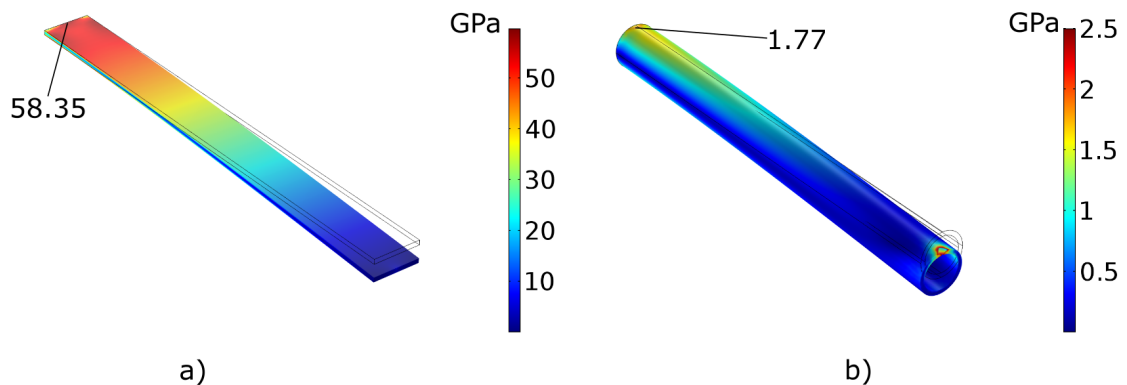
Figure 7.12: FEM simulations using values from Table 7.2 of a) plate and b) tube. Point loading caused higher stress in tube at contact point.

7.3 Fatigue machine

7.3.1 Motivation

In materials science, fatigue is defined as "a localized damage process of a component produced by cyclic loading" [152]. Crack deterioration can be similarly explained - a local damage process caused by repetitive loading. Therefore, fatigue loading applied to a crack in a concrete specimen may provide further insight into the results found from the industrial application. Customisation of the loading would allow cycles to be applied with similar characteristics as witnessed in the industrial application, rather than simply sinusoidal. Fatigue can be represented as a relationship between certain stress levels repeated for a certain number of cycles, with additional factors also contributing to a varying fatigue limit. These include: type of material, dimensions, manufacturing defects and environmental factors. Commonly, fatigue of a component is represented by an S-N curve, an example of which is shown in Figure 7.13 a). Particular stress values cause fatigue failure at a related number of cycles according to the curve. A typical fatigue test is usually run by repeatedly applying a sinusoidal stress, illustrated in Figure 7.13 b). According to the Goodman relation, a specimen will achieve infinite life if the stress amplitude σ_a remains below the endurance limit σ_e for a mean stress $\sigma_m = 0$ (Figure 7.13 c)).

Fatigue testing of materials, sensors and structures is a key element in the design and verification process in engineering [153–157]. With fatigue tests aiming for $10^6 - 10^7$ cycles and beyond, the testing processes are time consuming. This is of course dependent on the chosen cycling frequency, which will vary depending on experimental parameters. For example, in concrete structures: "cyclic frequencies are limited by the high ranges of deflection and the necessity to avoid local heating due to friction at cracks in the concrete" [158]. Therefore, in concrete testing a lower testing frequency is necessary which, in turn, is more time consuming.

Access to third party fatigue testing machines is limited and can be costly. Purchasing a commercially available machine comes with initial great expense that may not amortize for a short to medium-term project, but may decrease long-term costs overall. Many commercial machines are available on the market, with varying price that is influenced mainly by the maximum force, speed and accuracy requirements; large force, fast speeds and high accuracy that characterize the machine are accompanied by a large cost. A third option is to design and build a machine from individual components capable of producing required load cycles. Not only will this allow full control over the capabilities of the machine but it may decrease the total project cost significantly.

7.3.2 Design requirements

The design of a fatigue testing machine is highly dependent on the intended testing specimen. This includes geometry, material properties and experimental procedure, which will also define the necessary force. In this work, the machine will primarily be used to test concrete beams with
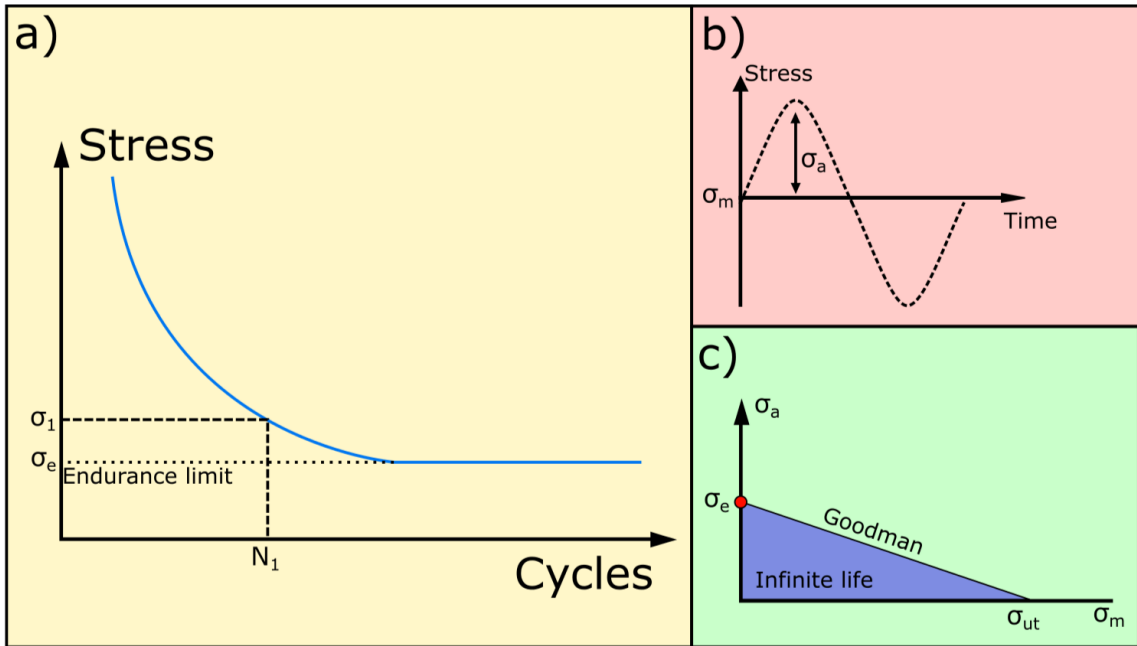
Figure 7.13: a) Example of an S-N curve illustrating fatigue of an arbitrary component where failure would occur for a stress of σ_1 after N_1 cycles. b) One cycle of a typical sinusoidal fatigue test and c) the Goodman relation. The Goodman relation states that for a stress amplitude, σ_a less than the endurance limit, σ_e, no fatigue shall occur and infinite life should be achieved.

the following maximum geometry: 1 x 0.1 x 0.1 m (length x width x height). Values are chosen to provide adequate areas for multiple sensors to be applied to beam faces. In addition, focus of research for this machine is to test sensors applied to pre-cracked concrete specimens; therefore, a key requirement is the ability to both open and close these cracks. To do this, the actuator must be capable of bidirectional force application to the specimen. The stress ratio, R, defines the type of loading:

$$R = \frac{F_{min}}{F_{max}} = \frac{\sigma_{min}}{\sigma_{max}} = \frac{\epsilon_{min}}{\epsilon_{max}} \tag{7.4}$$

where tension-tension, $0 < R > 1$, compression-compression $R > 1$ and bidirectional, $R < 0$. For equal magnitude, bidirectional force, $R = -1$. A machine capable of all ratios will allow a more thorough fatigue testing capability and a more flexible machine overall.

The standard practice for fatigue testing is the application of a sinusoidal waveform; however, loading during real-world applications is rarely absolute [159]. The British standards [160] suggest "When assessing fatigue performance a realistic estimate of the fatigue loading is crucial to the calculation of life, and all types of cyclic loading should be taken into account". Therefore, a customisable force application to produce either sinusoidal or other shaped waveform with variable amplitude and frequency is required.

Machine geometry requires adjustment depending on the yield point of the material in order

to reach the necessary strains and stresses in the sample. The initial objective was to produce an adequate strain level for testing sensors on a concrete beam face. The maximum strain level ϵ_{max} on the concrete beam face due to maximum force F_{max} can be calculated as:

$$\epsilon_{max} = \frac{M_{max}H}{2I_s E_C} \tag{7.5}$$

where maximum moment M_{Max} for 3-point bending on the centre of a fixed beam is given by:

$$M_{max} = \frac{2F_{max}a^4}{L^3} \tag{7.6}$$

for $F_{max} = +25$ kN, $M_{max} = 3125$ Nm where $a = 0.5$ m is the distance to the centre of the beam or load point and $L = 1$ m is the beam length. Substituting Young's modulus of concrete $E_C = 17$ GPa and area moment of inertia for the 0.1 m square cross section $I_s = 8.33x10^{-6}$ m^4, provides strain $\epsilon_{max} = 1.1$ mϵ. This strain should suffice for the intended sensor testing, based on knowledge from the industrial application.

7.3.3 Current state and academic benefits

A low-cost fatigue testing machine capable of ±25 kN bidirectional force on a beam with dimensions: 1 x 0.1 x 0.1 m (length x width x height) is desired as discussed previously. Reported machine designs in literature may aid in design of a custom machine and provide insight into the novelty of the work. Lee et al. [161] demonstrated the design of a structural fatigue testing machine capable of both bending and torsional loading. A hydraulic system was incorporated to both apply loading and fix the test specimen. Stress analysis of the frame is provided, with particular attention on the interface between actuator and specimen. The specified loading capability for bending is ±490 kN and the maximum specimen size is 7500 x 1500 x 950 mm. Such a machine is designed for large-scale testing, evidenced by the large force. The bidirectional capability is not demonstrated during test results, so it is unclear whether this is possible. No commercial evaluation is performed and so relative cost is unknown. It is likely to be extremely costly and benefit a long-term test period. A high initial cost may not be suitable for short-medium term testing periods. Machines are regularly designed for extremely small scale fatigue testing. For example, Vincent et al. [162] and Bhatkar et al. [163] presented machines producing maximum loading in the range of 88 - 300 N on small specimens of length < 150 mm. The main reason for custom designs is to reduce initial costs, which is less complicated for small-scale machines. Pach et al. [164] presented a unique method for applying axial loads to specimens by using a "seesaw" motion. Although they declare a design requirement of $R < 0$ (tension-compression), this was not demonstrated due to lack of correct grip attachment. Forces were also limited to 10 kN. Costs are declared to be around $3000 in comparison to a servo-hydraulic machine of $100,000$. A detailed breakdown of each section is not provided.

In terms of commercially available machines, a device capable of bidirectional loading is rare for 4-point bending applications. Cooper technology (Ripley, UK) provides a servo-hydraulic actuator capable of bidirectional loading, but only maximum loads of ± 10 kN [165]. Instron (High Wycombe, UK) provides a few available bidirectional fatigue testing machines [166]. The electrical devices are lacking the required force; however, the hydraulic systems are more suitable, such as the 8872 servo-hydraulic fatigue testing system. The main issue is the machines are not suited to beam bending and a custom frame would still be required to both load and support the beam. In some cases, the location of sourcing appropriate machines is an issue and can cause large shipping costs. Communication is also key to determine the customisation possibilities of the loading cycles which are not usually quoted.

From this review, it is believed a bespoke machine that meets the requirements of this work shows novelty in the following way:

- Bidirectional (R < 0) 4-point load cycle produces both opening and closing of a crack on a concrete specimen with adequate area for sensors.

- Economic evaluation comparing custom machine to purchasing commercially or outsourcing.

- Capability of adjustable shape, frequency and amplitude load cycles, rather than only sinusoidal, as real-world fatigue is rarely caused by pure sinusoidal loading.

7.3.4 Design process

The design, manufacturing, modelling, commissioning and testing of the machine is presented in the Appendix (10.5).

7.3.5 Commercial evaluation

Table 7.3 illustrates the breakdown of key components constituting the machine and their cost. Overall, the fatigue drive was the most expensive component with 59% of the overall costs. With regards to the decision-making of the insourcing of the machine (buying components and commissioning the machine) versus outsourcing of the testing, the business case depends upon the intended usage.

Item	Cost £
Servo Actuator	12,000
Frame	5,500
Equipment	2,000
Installation	720
Total	**20,220**

Table 7.3: Machine Expenditure

Given a mean outsourcing machine expenditure of £325/day (value gained in-house from University), the cost-benefit threshold over outsourcing is reached at 373 hours of testing. Assuming

a sample is tested at 3 Hz, this corresponds to 4 million cycles. At 10 Hz, this corresponds to $1.34*10^7$ cycles. Consequently, the lower the testing frequency, the more likely becomes the option of insourcing. As a consequence, depending on the intended total usage, the sourcing strategy may be defined.

7.4 Concrete crack monitoring

An improved sensor design was presented in Section 7.2.1 and tested in direct static, fatigue and humidity experimentation. The metallic bonding method was found to provide comparable performance, but with complete immunity to humidity variations when epoxy showed dependency and possible permanent change. The next step is to test the design for concrete crack displacement monitoring. With the now operational fatigue machine, such experimentation can be carried out with complete control. Furthermore, the deterioration methodology can be incorporated to somewhat validate the conclusions from Chapter 6. During the industrial application, mode I opening displacement of cracks were prominent (Chapter 3, Section 3.4.2). To model cracks in an experimental environment, a deliberate notch is created in the centre of a reinforced concrete (RC) beam face during curing. Using the fatigue machine the beam can be oscillated in both directions, causing opening and closing of the crack as witnessed during the industrial application. The crack can be instrumented with both old and new sensor designs for comparison.

7.4.1 Concrete beam casting

Prior to experimentation, knowledge of the maximum strain on the face of a predetermined RC beam due to maximum actuator force is required, as this will define the maximum crack displacement capability. To do this, the FEM model from section 10.5.3.2 can be modified to include the RC specimen. To accurately model the beam, details of the concrete specimen are required. Cross-sectional area is restricted by in-house concrete casting equipment. As such, the chosen concrete beam was 100 x 100 mm, with a length of 950 mm. This length provides additional room for cabling. The cast prior to concrete pour is shown in Figure 7.14 a) and subsequent to pouring and vibrating in b). An acrylic sample was used to create the notch, shown in c) which produced the final crack shown in d). Cracks were previously discussed as aesthetically acceptable up to 0.3 mm. In this work the crack is initially set as 1 mm in an attempt to provide a more accelerated vision of crack deterioration.

Concrete composition was as follows: 25 kg of 20 mm aggregate, 18 kg of 10 mm aggregate, 20 kg of sand, 10 kg of cement and 5.5 kg of water. Concrete is mixed, poured and set on a vibration table before curing over the course of 28 days. Cubes were poured from the same mix and used to determine the compressive strength of the concrete, as shown in Table 7.4. Strength values are gained from means of all cubes tested. From ACI 318-095 [70], concrete modulus of elasticity, E_C
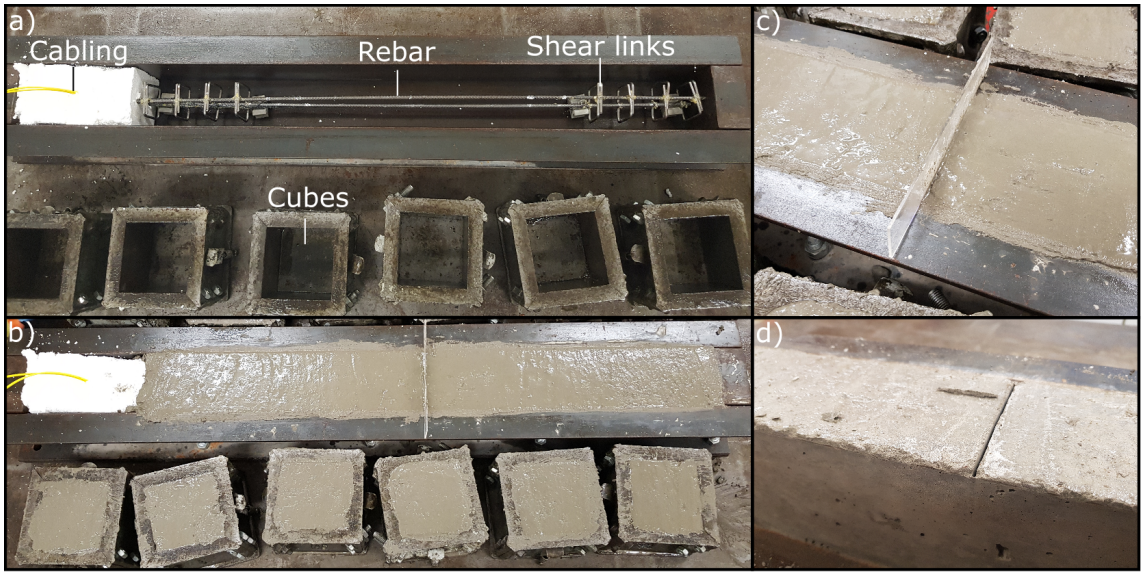
Figure 7.14: a) Cast prior to and b) following concrete pour and vibration. c) Applied notch during curing and d) final crack formed.

can be estimated in MPa as:

$$E_C = 4700\sqrt{\sigma_c} \tag{7.7}$$

for compressive strength of concrete, σ_c in MPa. This provides an $E_C \approx 27.12$ GPa for the 28 day aged concrete used in this work.

Day (no. cubes)	Force distribution (kN)	Mean strength (MPa)
7 (3)	184 - 214	20.0
14 (3)	228 - 268	25.1
28 (5)	313 - 350	33.3

Table 7.4: Concrete compressive strength.

7.4.2   Mathematical approach

The objective of this work is to replicate crack displacements witnessed during the industrial application in Chapter 6 in order to validate the conclusions. To do this, the required force must first be calculated. A crack displacement of ± 3 μm is aimed for, which is similar to maximum-minimum limits from in-situ measurements. This is equivalent to 30 $\mu\epsilon$ applied to the centre of the beam with a sensor gauge length of 0.1 m, which translates to a maximum stress, σ_M, of 0.51 MPa. The custom built fatigue machine performs 4-point bending, which can be mathematically modelled as a fixed beam with 2 point loads, F_1 and F_2 where $F_1 = F_2 = 0.5F_a$ and F_a is the force supplied by the actuator, as shown in Figure 7.15. Since point loads are equal and position $x = 0.475$ m is centred between forces $(b - x = \frac{(b-a)}{2})$, the stress at point x due to a single point load,

$\sigma_{F1} = 0.255$ MPa. Maximum moment, M_x, at location x is then given as [167]:

$$M_x = \frac{\sigma_{F1} 2 I_s}{H} \tag{7.8}$$

where $I_s = 8.33 * 10^{-6}$ m^3 is the area moment of inertia for a square cross section beam with height, $H = 0.1$ m. The required moment due to F_1 to produce σ_{F1}, $M_x = 42.483$ Nm. Relating the maximum moment to reaction characteristics for a fixed beam gives:

$$M_x = M_1 + R_1 x - F_1 (x - a) \tag{7.9}$$

where M_1 and R_1 are the reaction moment and force respectively at the fixture point, annotated in Figure 7.15, and $a = 0.375$ m is the distance from the fixture to force F_1. Expanding this provides the force, F_1 in relation to moment, M_x as:

$$F_1 = \frac{M_x}{\frac{-a(L-a)^2}{L^2} + \frac{(L-a)^2(L+2a)x}{L^3} - (x - a)} \tag{7.10}$$

here, $L = 0.95$ m represents the length of the beam. Substituting all values provides a required force $F_1 = 574$ N; therefore, $F_a = 1148$ N.
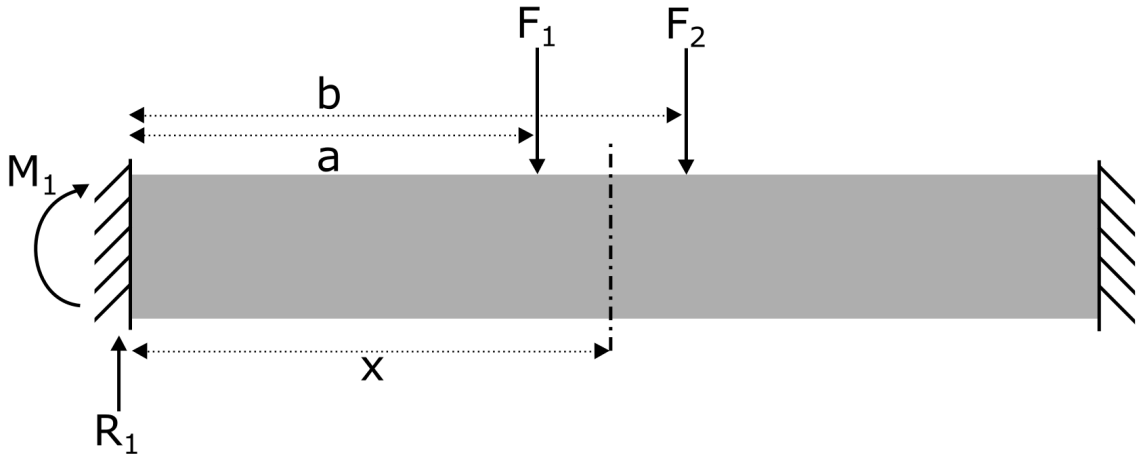
Figure 7.15: Moment diagram of fixed beam with two point loads.

7.4.3   FEM model

With details of concrete and now force known, the FEM model from Section 10.5.3.2 can be updated with the RC specimen. In this case, a more realistic model of the experiment is presented in the form of the 4-point frame and beam interaction. For this reason, the values for strain from the model may be slightly less than the mathematically calculated. Secondly, the model introduces rebar to the concrete beam, which was not in the calculation. Since steel behaves similarly to concrete during low forces, this should not cause much variation. The interaction between concrete

and rebar is extremely complicated and difficult to model. One method (specific to the software used) is to apply a truss interface to the rebar within a concrete beam, which will remove the requirement to mesh the small intersection as only axial forces are analysed. Such small meshes can cause large computational times. Simulating the RC element with the 4-point force as 1148 N provides the strain distribution shown in Figure 7.16. The maximum tension strain, located at the centre of the RC beam, was 29.76 $\mu\epsilon$ and therefore matches calculations relatively well with a small loss of 0.24 $\mu\epsilon$. This provides confidence in applying such a force on a concrete beam in the fatigue machine in order to acquire the desired crack displacements.
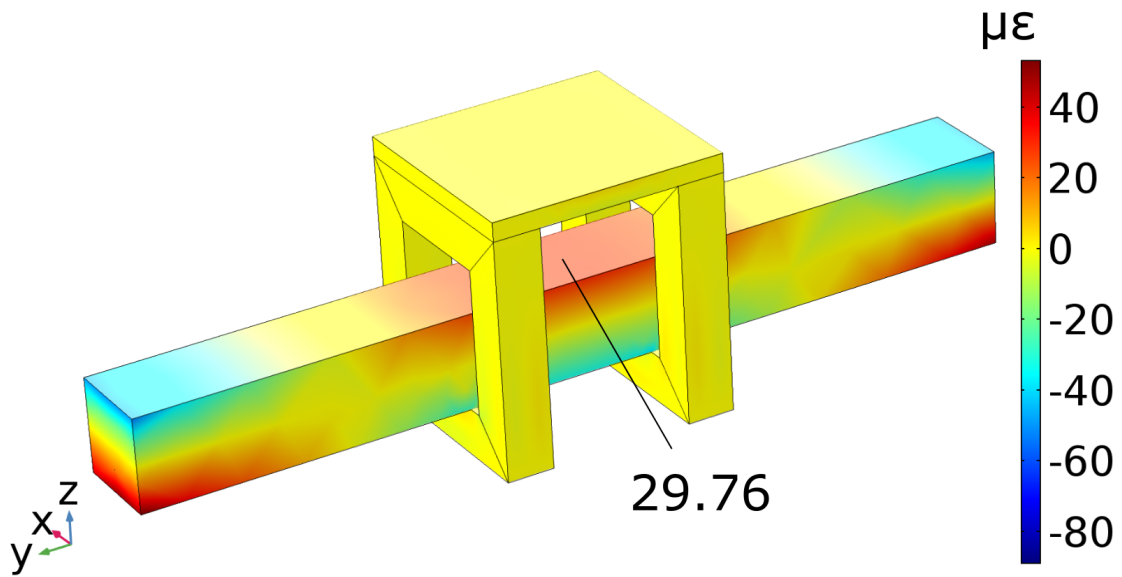
Figure 7.16: Strain distribution from FEM model of RC specimen with applied 1148 N force.

7.4.4 Experimental set-up

Two sensors were installed over the notch, one of the epoxy design used during the industrial application (Chapter 6) and the other using the metallic-bonded design presented in Section 7.2.1. In both cases a single displacement sensor was attached using bolt anchors adhered with mortar, perpendicular to the crack length and monitoring crack opening only. Figure 7.17 shows the entire experimental set up with insert displaying the sensors attachment.

7.4.5 Results

Temperature and strain characterization

Similar to Chapter 6 Section 6.3.2, sensors were characterized by cycling temperatures in order to determine the sensor temperature (K_T) and strain (K_ϵ) sensitivities. Results from these tests showed a K_ϵ of 0.7 and 0.58 for epoxy and metallic bonded respectively. This is gained by calculating the thermal expansion of each steel substrate (carbon or stainless steel) and comparing to

Figure 7.17: Experimental setup of concrete crack monitoring fatigue test. Insert: sensor attachment.

measured strain. Temperature response of each sensor is shown in Figure 7.18 a). One noteworthy point is the relaxation phenomenon of epoxy, which takes at least three full temperature cycles to become repeatable, shown in Figure 7.18 b). Metallic bonded is repeatable immediately following manufacture and showed the same response over all cycles. The smaller strain sensitivity in the metallic bonded sensor was not witnessed during work in Section 7.2.1. Possibly less effective brazing or spot welding, it is unknown at this time.

Loading

A load cycle of ±1148 N was loaded into the program presented in Figure 10.12 with speed set to
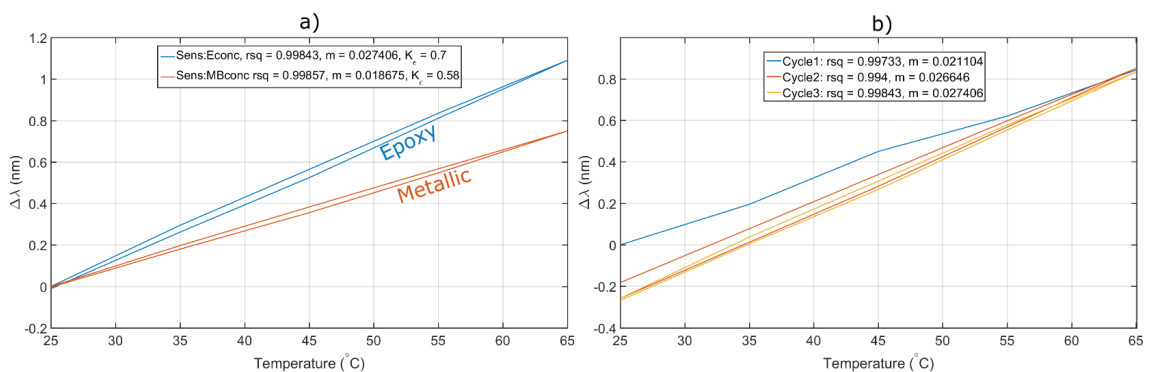
Figure 7.18: a) Final sensor response to temperature, b) epoxy relaxation.
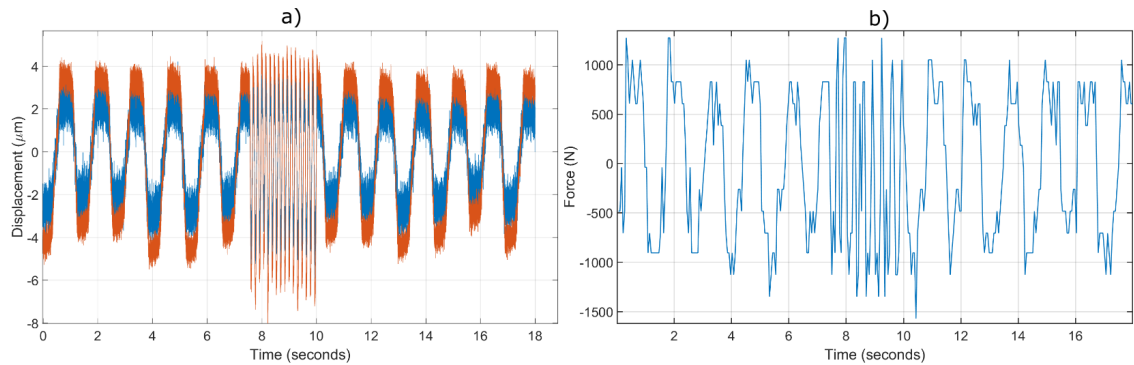
Figure 7.19: Crack displacement monitoring fatigue cycle: a) sensor response during several cycles and reaction b) load cell measurements.

provide ≈ 1 Hz cycles. Gravity is also taken into account in the program, as this will affect load cell measurements. To fully assess the deterioration methodology, all three characteristics must be apparent in the data. For "Reactive", a periodic fast transition between limits was applied once an hour (to accelerate damage). This was done by increasing the speed variable tenfold for a short time during testing. Figure 7.19 a) shows the sensor response during several cycles, with the applied reaction occurring at between 7 and 10 seconds. The increased speed is applied for several seconds due to some inaccuracies with the load cell. These will be extrapolated upon in a following sections. Essentially, it is impossible to gain an identical single transition using the current setup; therefore, the mean displacement change of a short period of several reactions will be taken. This will occur every hour, with one data point collected containing the mean reaction and compared over time. To determine any "Permanent" deterioration, data points can be collected during periods of downtime or "zero load". Finally, "Behavioural" can be gained by predicting the sensor response using FEM model from Section 7.4.3 and accompanying load cell data.

Reactive

As discussed, a short burst of fast transitions between maximum and minimum loading is applied to the concrete beam every hour. From Figure 7.19 a), it is clear the transitions are generally increased in magnitude and decreased in accuracy when compared to the slower 1 Hz cycles. There are a few reasons for this, mainly due to the load cell measurement process. A closed loop feedback system is set up, with the analogue input of the actuator controller connected to the amplified load cell voltage. This controls the direction of actuation based on load cell measurements. It is believed the main cause is the execution speed of the program itself, which is unable to process the changing load cell measurements fast enough, causing the increased magnitude and erratic limits as the actual force surpasses the set limits before the controller is able to detect it. A second concern regards the measurement resolution and conversion rate of the controller analogue input. According to the data sheet [168], the analogue input resolution is 11 bits with a ± 10 V maximum,
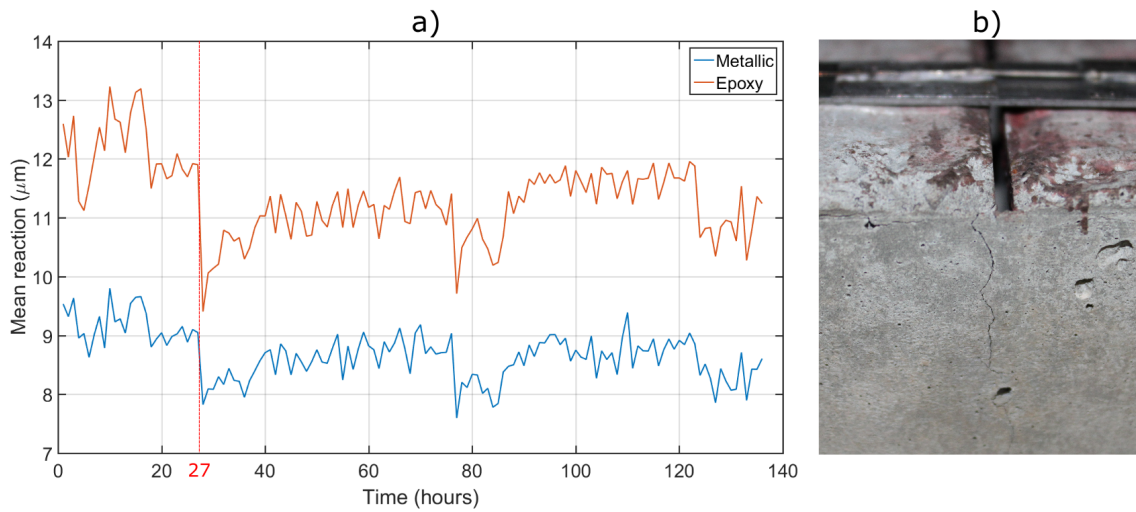
Figure 7.20: a) Reaction from crack displacement sensors over time, b) hairline crack appearance.

giving a voltage resolution of $20/2^{11} = 9.76$ mV and force resolution of 144.6 N. This matches the results in Figure 7.19 and is the equivalent of ≈ 6.3 % of the total force change. This means the force limits can range anywhere between $\pm$ 1000:1300 N, or equivalently, crack displacement limits can range between $\pm$ 2.6:3.4 μm due to resolution alone. This also does not take into account the resolution of the load cell itself. Finally, the declared conversion rate of the analogue input is 1 kHz. However, the maximum recording frequency of the load cell is 20 Hz. Therefore, it is unclear whether this measurement frequency is correct. Nevertheless, this experiment load cycle is not necessarily required to be precise, as the objective is to mimic a real world phenomenon. The crack deterioration methodology applied must be able to operate under these varying conditions.

Each transitional period is extracted and the mean change is recorded. Figure 7.20 a) shows the reaction of each sensor to these transitional periods over time. The intention is to monitor for any drastic changes. From Figure 7.19 a), displacement measurements varied by ± 1 μm during one period. It is likely that this variance may occur when comparing several periods. Over the course of the ≈ 140 hour test period, representing $\approx 500,000$ cycles, only one notable change occurred after 27 hours in both sensors. Noting that the change is extremely small (≈ 2 μm). One possible reason for this change is a hairline crack that appeared on the concrete beam, spanning from the initial notch, shown in Figure 7.20 b). Otherwise, both sensors remained within the previously defined ± 1 μm over the course of the experiment. It is clear the epoxy sensor is more sensitive to strain; however, the metallic sensor has displayed the capability to monitor the crack displacements sufficiently and provides a linear relation to the epoxy measurement, with an $R^2 = 0.82$ (Figure 7.21). From these results, despite the increased crack width and accelerated load cycle, the crack does not seem to be deteriorating under the industrial loading. This somewhat verifies the conclusions drawn in Chapter 6; however, improvements to the experimental setup is required before any further results can be gained. This will be expanded on during Chapter 9 Section 9.2.4.
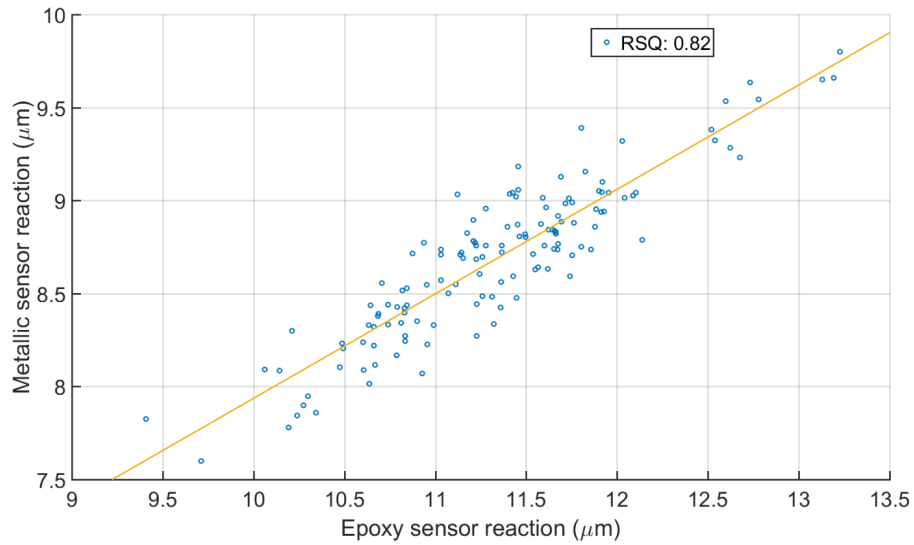
Figure 7.21: Linear relation between epoxy- and metallic- bonded sensors, with an $R^2 = 0.82$.

Permanent

Periods of zero load were also extracted every hour to determine the "Permanent" deterioration. Results again showed no major changes, with crack widths varying $< \pm 1.5 \mu$m. No permanent change was recorded at the 27 hour mark, suggesting the decrease in reaction may not be due to the hairline crack appearance. However, the crack is extremely small and may not have impacted the permanent width.

Behavioural

Unfortunately, due to the ineffective measurement of the load cell, no real prediction can be made of the crack displacement originally. To reiterate, the purpose of this method is to develop a prediction for the crack displacement during early periods of monitoring, based on a combination of sensor measurements and models. The intention was to use the load cell measurement and FEM model to produce the prediction. This prediction can then be used for comparing to sensor measurements over time. Since the load cell is both infrequently measured and extremely inaccurate (resolution of ± 500 N), this is not possible using the current setup. In order to carry out this method, a separate system would be required to independently record the load cell sufficiently (high sampling rate and improved resolution) and feed the controller when set limits are reached. This presents a future avenue of work, discussed in Chapter 9 Section 9.2.4.

7.5 Chapter summary

Following the previous chapter on the industrial application, further investigation into the crack displacement sensor design was suggested. This was due to an apparent decrease in strain sensitivity, suspected to be caused by a degradation of attachment. More specifically, the interface

between sensor-steel with epoxy.

Work in this chapter firstly proposed an alternative method that removes the epoxy and uses exclusively metallic bonding. This design was compared to epoxy in fatigue, static and humidity experimentation. Results showed a previously unknown/untested humidity dependence of the epoxy design and a possible damage initiator. The metallic design showed similar performance to epoxy designs in the fatigue and static tests, but was completely immune to humidity variations.

Following these initial experiments, it was desired to test the metallic sensor design in a direct crack monitoring application. Not only would this validate the design for crack monitoring and allow comparison to the epoxy design, it would also provide a test-bench to verify conclusions from the industrial application and further develop the deterioration methodology. To do this, a custom fatigue machine, intended for concrete specimens, was designed and implemented. This would allow full control over the experimental procedures and provide long-term reliable testing capabilities.

A concrete beam with a deliberate notch was instrumented with both crack displacement sensor designs and loaded with cycles imitating crack displacements witnessed during the industrial application. A reaction period containing fast instant transitions between limits was applied every hour. Results from sensor measurements showed despite the increased crack severity, no real deterioration occurred. A small hairline crack, spanning from the initial notch, appeared after 27 hours and was accompanied with a decrease in crack reaction. The change in displacement and hairline crack size are extremely small and not indicative of deterioration. This experiment also provided valuable information regarding the operation of the machine, with a major improvement of the load cell measurement set up required before continuing experimentation.

Chapter 8:   Prediction methodology in SHM

8.1   Chapter overview

Evolution from detection to prevention of damage is of particular interest in SHM. In most applications, evidenced by the previously performed literature review in Chapter 5, any alerts of damage detection, deterioration or even severe loads are reactive - alerting subsequently [169]. In most cases, this is sufficient for the operator to perform restrictive action to prevent further issues. Progressing to methods capable of predicting these factors in order to prevent the damage initially would be highly beneficial to the industry. In this chapter, methodology previously used in various unrelated applications is presented, known as tipping point analysis (TPA). This toolbox is employed to experimental test-benches that represent real-world SHM applications in order to develop the algorithms in anticipation of applying the methods for predicting crack initiation and deterioration.

8.2   Current state

Outside of SHM, prediction methodology is used extensively. Some examples include: in finance for forecasting stock market prices [10], in meteorology for predicting drought [11], in medicine for early detection of Alzheimers [12] and in predicting technological advancements [13]. Statistical methods such as regression analysis and several related sub-categories incorporate mathematical models for estimating relationships between variables by using large data sets. An extensive, informative explanation of regression analysis is provided by Bowerman et al. [170]. Machine learning and artificial intelligence has undergone exponential growth in popularity in recent years, even gaining large media coverage [171,172]. These terms encompass a wide variety of architectures that are built on the same principle: using data-sets and statistical techniques (such as regression) to "teach" a machine or computer to perform varying analysis processes to solve problems [173]. Such work is outside the scope of this thesis, but is worth noting as machine learning techniques may prove useful in future for crack monitoring as more data becomes available.

In SHM, no successful demonstrations of prevention methods in a real world application have been reported [169]. Work by Perry et al. [174] established the potential to apply TPA to predict cracking in a reinforced concrete element. A single experimental procedure is carried out on a reinforced element - demonstrating the capability of predicting critical failure using TPA. It may be beneficial to design a test-bench capable of producing large amounts of suitable critical transition data in order to develop and modify the techniques for SHM applications. TPA shows great promise for application in real-world SHM; however, further research is required.
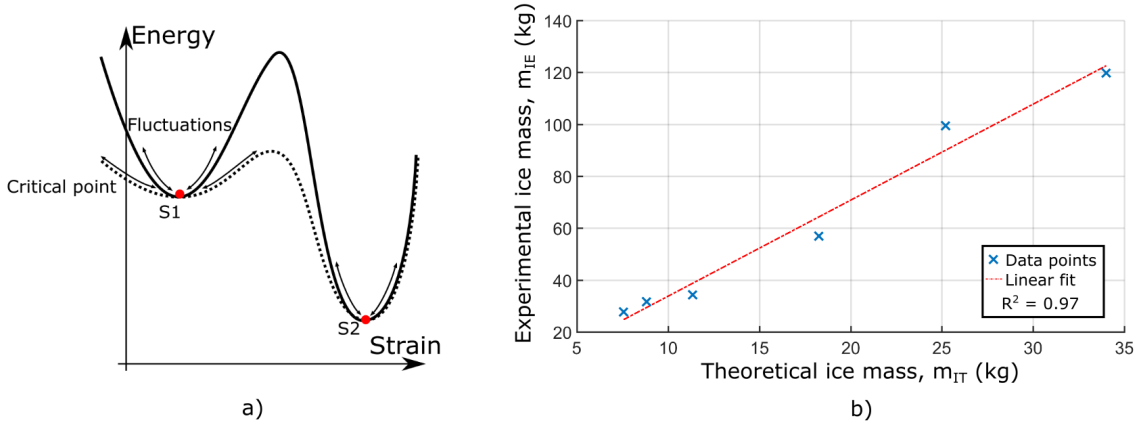
Figure 8.1: a) Double-well or saddle node representation of some systems, b) linear relation between theoretical and experimental ice mass.

8.3 Tipping point analysis

In many physical systems, critical transitions occur and are preceded by perceptible signals in time series data [175]. The established toolbox of TPA has been developed and used in many systems to predict these critical transitions by investigating the potential energy state of a system for dynamical changes [176, 177]. For example, Figure 8.1 a) illustrates a saddle-node bifurcation that can be used to represent some systems. The system will oscillate in the state (S1) causing noise. A bifurcation causes a shift to a lower energy state (S2), preceding this the surrounding walls of S1 decrease causing a period where noise "slows down" or decay rate increases. Livina et al. demonstrated two distinct methods from the toolbox: "degenerate fingerprinting" (DF) and "potential analysis" (PA) to predict climate bifurcations [178, 179]. Furthermore, Prettyman et al. [180] developed a "spectral analysis" (SA) method that comparatively demonstrated similar capabilities for data-sets when other tools failed.

8.3.1 Degenerate fingerprinting

DF involves the use of a lag-1 autocorrelation function (ACF) to detect critical "slowing down" of the dynamics of a system. For example, a strain-based system can be expressed by the time series:

$$\epsilon_T(t) = \epsilon_s(t) + \epsilon_n(t) \tag{8.1}$$

where a measured total strain, ϵ_T is the sum of static (or relatively slow changing) strain, ϵ_s (caused by external factors such as force or temperature) and some Gaussian noise ϵ_n. In conventional applications, the static component is usually independently extracted, commonly with filtering to reduce noise, for analysis purposes as it contains the required information. In DF, either the noise or indeed total without noise filtering (ϵ_n or ϵ_T for the strain-based case) are analysed using the

ACF:

$$\rho_k = \frac{\sum_{t=1}^{N}(Z_t - \mu_n)(Z_{t+1} - \mu_n)}{\sum_{t=1}^{N}(Z_t - \mu_n)^2} \tag{8.2}$$

Here, $0 < \rho_k < 1$ represents the ACF indicator where a trend towards 1 suggests dynamics of the system are "slowing down". For the case of a strain-based system, Z_t would be a window of the noise data, ϵ_n of length N, the mean of which is μ_n. Shifting the window by one data point provides, Z_{t+1}.

8.3.2 Potential analysis

A visual representation of the number of potential wells in a system can be gained by using a potential contour plot. A changing number of wells in the system can be an indicator of a bifurcation. The double-well potential example from Figure 8.1 a) shows an intermediate step of a prominent single well and decreased second well at the critical point. Livina et al. [181] demonstrated multiple artificial data-sets containing multiple numbers of wells, after which a potential contour plot illustrated a visual representation of the changing number of wells. The main disadvantage of this method compared to DF is the difficulty of automation. DF provides a simple variable that can be monitored automatically, whereas PA requires visual assessment.

8.3.3 Spectral analysis

As discussed in Section 8.3.1, one feature of some physical systems is variations in the frequency of the noise signal prior to critical transitions, such as "slowing down". Applying an ACF indicator exploits this to provide a clear indicator of any changes in noise frequency. A second method for identifying frequency changes is SA. SA represents a more direct measurement of the magnitudes of specific frequencies over time. A power spectrum is extracted from a window of data, similar to equation 6.23:

$$P(k, f) = \frac{1}{n}|X(k)|^2 \tag{8.3}$$

for $k = 0, 1, ..., n-1$ and window size, n where $P(k)$ is the power of frequency, f apparent in FFT of data, $X(k)$. Choice of window size, n is important: too small and lower frequency components will be masked, too large and effects may be obscured. Range and resolution of observable frequencies is also controlled by the window size. Prettyman et al. [180] determine changes in frequencies by plotting a linear trend of a specific frequency range $(10^{-2} - 10^{-1})$ and recording the gradient over time. This gradient can be used as an indicator, similar to DF, to ascertain if frequency magnitudes vary over time. A decreasing gradient represents an increasing magnitude of lower frequencies in the range.
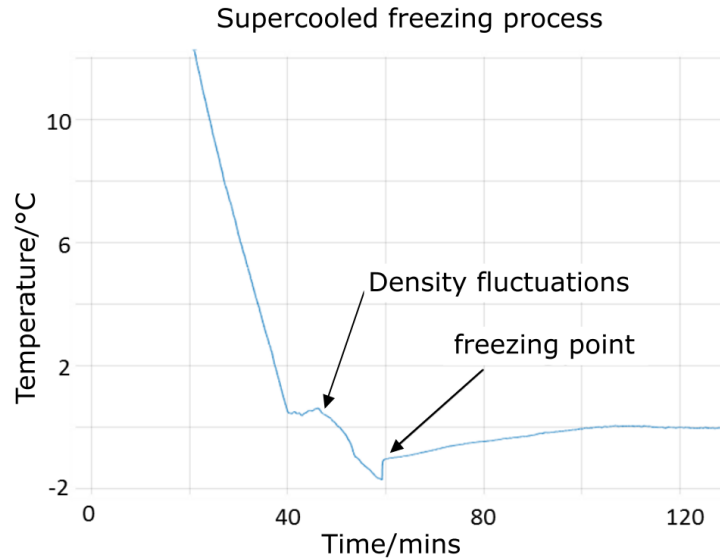
Figure 8.2: Supercooling and subsequent freezing process, defined as "supercooled freezing". Water is cooled below $0°C$ and consequently spontaneously freezes releasing heat energy causing a measurable increase in temperature. At temperatures $\approx 1to4°C$ water density fluctuations cause movement in the water and this can be seen from the thermocouple.

8.4 Test-bench: freezing process

8.4.1 Supercooling

Freezing of supercooled water provides a similar process to a crack initiation or deterioration (a gradual build to an instantaneous transition) in a more repeatable and shorter time period. Potentially this process could be used to produce large amounts of simulated data to develop the TPA methodology prior to more time-consuming crack-related experiments. Supercooling explains a phenomenon where a liquid is cooled below its freezing point without transitioning to a solid state. Freezing can then occur, either randomly or deliberately, where the solidification process causes an increase in the surrounding temperature due to release of latent heat [182]. An example of a supercooling and freezing process is shown in Figure 8.2. This instantaneous change in temperature provides a reference point for the time transition occurs. Likelihood of freezing randomly will depend on factors such as number of impurities in the water and temperature at freezing. A deliberate force or addition of impurities can forcibly cause freezing to initiate. In this work, prediction of the random instantaneous freezing of supercooled water by using the TPA methods DF and SA is attempted. Applying TPA to many freezing cycles in this way will provide a greater understanding and allow development of the methods. Furthermore, implication of a successful demonstration of predicting ice formation has the potential to be useful for external applications.
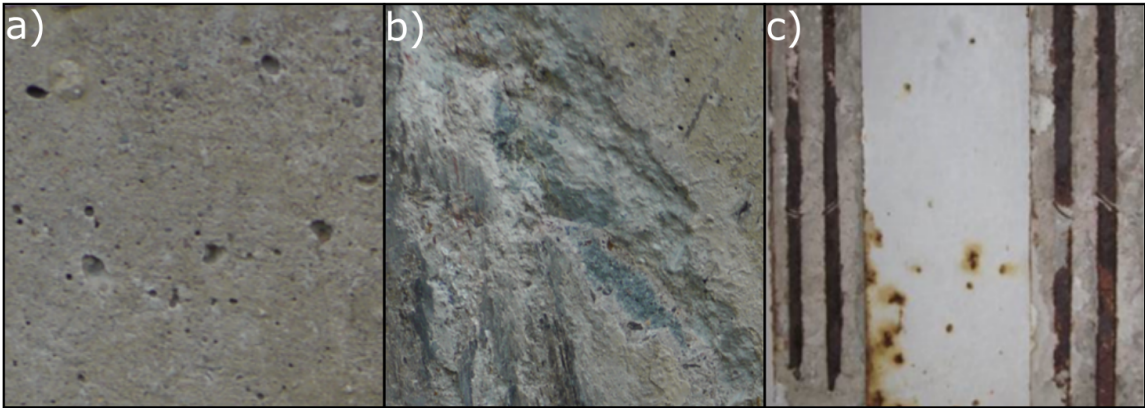
Figure 8.3: Examples of freeze-thaw damage: a) pop-outs, b) scaling and c) spalling (courtesy of Safiuddin [186])

8.4.2 Potential external applications

Although the primary aspiration for this work is to develop the TPA methodology for crack deterioration purposes, the system described has potential applications in many fields where ice formation is undesirable. Examples include aeronautical, civil and electrical power engineering; and even biochemistry and culinary science. In the context of civil engineering, a common degrader of concrete in colder climates is freeze-thaw: damage is accrued with the introduction of water, which expands upon freezing causing cyclic stress and damage over multiple freeze-thaw cycles [183]. The forms of damage caused by freeze-thaw range from exterior damage to the outer layer of concrete known as scaling, pop-outs or spalling to internal damage and crack initiation or expansion [184]. Such damage is shown in Figure 8.3 for some severe cases. Eventually, these cracks can provide a pathway for corroding agents to attack the underlying steel reinforcement, reducing the tensile strength of the concrete. Concrete freeze-thaw damage is a common and ongoing concern for infrastructure managers, since the effects only become visibly apparent after significant degradation. The method proposed here could be used to inform manual maintenance or could be used in conjunction with a simple, automatically triggered heating element to prevent ice formation. An ice detection system for wind turbine blades is another example where this system would be valuable. There are many proposed ice detector systems for turbines, reviewed by Cattin et al. [185]. They measure factors affected by ice such as: humidity changes, speed variation of rotating objects (e.g. anemometers), vibration fluctuations on a probe, refraction or blocking of light and natural frequency alterations. The common issues these sensors face is that the indirect measurements of ice cause a requirement for a significant amount of ice to form before indication is possible. Visual-inspection also follows detection to ensure existence of ice. Switching the turbine off and on is a simple way to forcibly remove the ice. In some cases, turbines have heated blades for this purpose. Our method would improve the efficiency of both of these systems as they would only need to be used when required.

8.4.3 Methodology

The phenomenon of instant freezing of supercooled water was previously discussed. In addition to an increase in temperature, it is also widely known that during ice formation the body of water/ice will expand (i.e. ice has greater volume than water, specifically around 9% larger). To increase the probability of prediction, analysis will be performed on both temperature and volume increase that occurs at the freezing point. This volume increase will produce a force acting outwards from the water body. Containing the water will concentrate this force to the walls of the container, which can be measured for strain changes. Any increase in strain due to freezing will occur instantly at the point of freezing, referenced by the increase in temperature. The magnitude of strain will be dependent on the proportion of ice that forms at freezing, since only a fraction will transition to ice at the freezing point. Bochnicek et al. [187] provided a study into the relationship between this temperature increase and the amount of ice formed, concluding:

$$m_I = \frac{m_w c \Delta T_S}{l_f} \tag{8.4}$$

where m_I is the mass of ice formed at freezing point, m_w is the initial water mass, $c = 4181 \frac{J}{kg\,°C}$ is the specific heat capacity of liquid water, ΔT_S is the change in temperature at freezing point and $l_f = 333550 \frac{J}{kg}$ is the latent heat of fusion of ice. One concern about this equation is the lack of inclusion of apparent impurities. It is known that water will freeze due to impurities, and a greater number of impurities causes an increase in the rate that ice forms, R [188]:

$$R = K_p \exp\left(-\frac{\Delta G}{k_B T}\right) \tag{8.5}$$

where K_p is a constant representing the number of nucleation sites and rate that molecules attach to the nucleus, ΔG is the change in Gibbs free energy of the nucleus at transition, k_B is the Boltzmann constant and T is temperature. Stott et al. [189] used high-speed video cryomicroscopy to determine that the rate of ice formation, R of purified water varies from $0.0006 - 0.023\ ms^{-1}$. Purified water usually consists of $\approx 10 - 50$ PPM of total dissolved solids (representing nucleation sites, K_p) whereas basic tap water is known to have $\approx 300 - 600$ PPM. So, using tap water should increase the rate that ice forms, which may vary the structure of ice crystal formation and potentially the mass of ice that forms, m_I. To test this hypothesis, equation 8.4 is compared to multiple experimental cycles of "supercooled freezing", measuring temperature change, ΔT at freezing with a thermocouple submerged in water and the mass of ice that formed, m_I by removing excess water and weighing on scales. Results are shown in Table 8.1 for constant water mass, m_w. Plotting the theoretical against experimental ice mass reveals a linear relationship with $R^2 = 0.97$, shown in Figure 8.1 b). Although the number of data points is lacking, it is clear that the theoretical value is linearly related to the measured experimental values. In these examples, the experimental ice mass that freezes is ≈ 3.48 times greater than the theory. The reason for

ΔT (°C)	Experimental ice mass, m_{IE} (kg)	Theoretical ice mass, m_{IT} (kg)
1.2	27.64	7.56
1.4	31.56	8.82
1.8	34.32	11.34
2.9	57.10	18.27
4.0	99.50	25.20
5.4	119.72	34.01

Table 8.1: Ice mass comparison
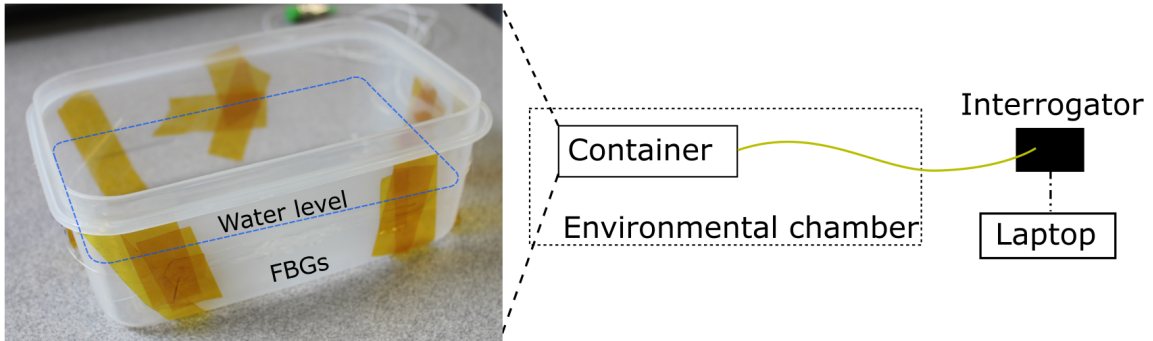
Figure 8.4: Experimental setup of freeze test-bench.

verifying this relationship is to provide some validation for future strain measurements, as strain should show dependence to mass of ice formed.

8.4.4 Experimental set-up

FBGs fit this application well since they can measure both strain and temperature changes and are unaffected by water over a short-term. Both a bonded and unbonded FBG will be applied to monitor strain and isolated temperature. The unbonded FBG can be used for temperature compensation purposes. To demonstrate the method of predicting ice formation, a polypropylene container was filled with 0.5 litres of regular tap water and instrumented with an FBG measuring strain and an FBG measuring temperature. The container was placed within an environmental chamber to ensure consistent freezing cycles and sensors were connected to an FBG interrogator with sampling frequency of 50 Hz with a laptop interface. Figure 8.4 illustrates the experimental set up. Polypropylene consists of a low Young's modulus which should allow good strain transfer from ice expansion to strain. The strain FBG was fully epoxied along the water level, whereas the temperature FBG was epoxied on one side to ensure thermal contact only. Finally, thermal grease was applied over both to ensure equal heat transfer for both sensors. A total of seven freezing cycles were run under the same conditions, with the environmental chamber programmed to begin at 25°, cool to -14° for a period of around 5 hours, before proceeding to room temperature until ice was fully melted - this cycle was then repeated.
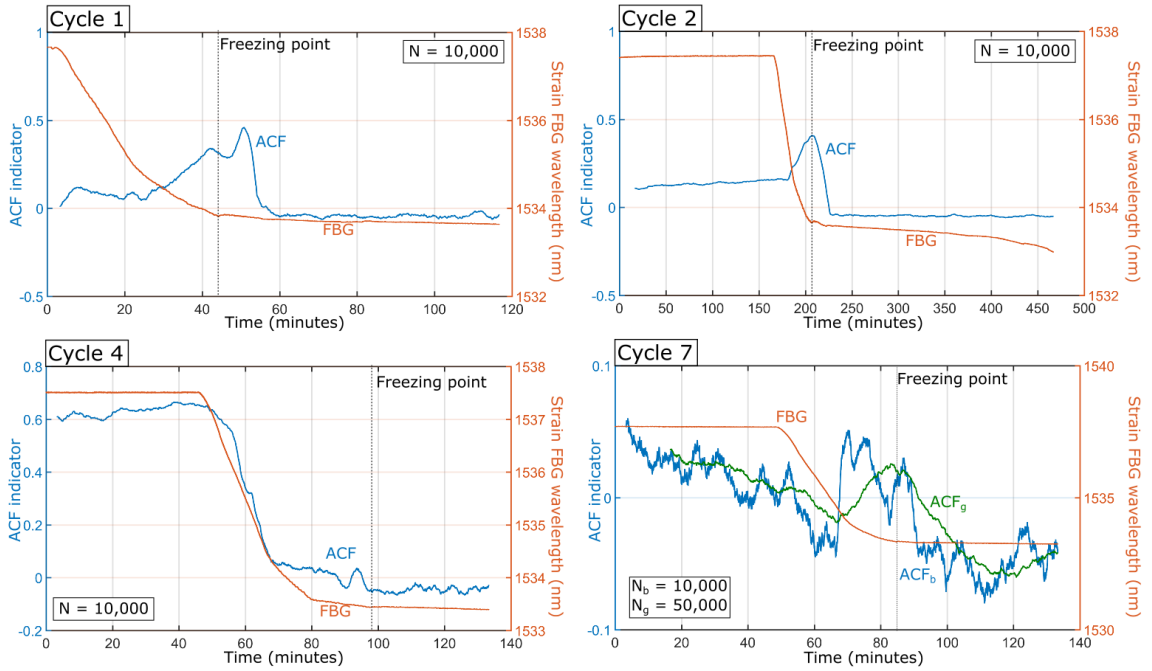
Figure 8.5: Results from four cycles of applying ACF to FBG strain noise instrumented on a container of water undergoing spontaneous freezing after supercooling. Cycle 7 shows the difference between window sizes on the same cycle.

8.4.5 Results

Data was collected from FBGs at a sampling rate of 50 Hz, which should provide sufficient data points to perform both DF and SA. Noise is extracted from raw strain/temperature data using a moving average window of 5 data points (method described in Appendix 10.6). This removes any trends due to strain or temperature and extracts independent strain noise of bonded FBG, ϵ_n (see equation 8.1).

Degenerate fingerprinting

Lag-1 ACF, Equation 8.2, is performed on the noise of each freezing cycle independently over a sliding, self-intersecting window of size $N = 10,000 - 50,000$. Window size is dependent on constant factors such as sampling rate and data length, but also on the systems dynamics which may vary for each cycle. Currently, the choice of window size can be informed through sensitivity analysis and the experimenter's understanding of the time dependence of the systems dynamics. In future, an algorithm to automatically determine the window size will be developed. The window is manually adjusted for each cycle to provide the most apparent prediction (rise to 1). The final result is the ACF indicator for each cycle, which varies from 0 to 1 and is a measure of varying dynamics, as windows separated by one data point are correlated. Figure 8.5 shows results for four cycles out of seven that showed apparent predictions prior to the freezing point, which is indicated in the graphs and is based on the point that temperature increases due to freezing described previously.

The additional three freezing cycles showed no significant rise in ACF indicator and showed no false positives. Results of these cycles are provided in the Appendix (10.7). Cycles 1, 2, 4 and 7 showed a clear rise in ACF indicator at around 5-10 minutes prior to freezing point. In terms of identification, cycles 1 and 2 would easily be detected using an automatic detection system. Cycle 4 and 7 are visually noticeable but automatic detection would depend on the sensitivity of the detection system. ACF window size in these examples is 10,000 for cycles 1, 2 and 4. In cycle 7, the most apparent prediction was witnessed with a window size of 10,000, noting the scale of the plot shows these changes are small. A window size of 50,000 is also shown for cycle 7, where the rise is more gradual but remains small in magnitude.

To understand why the ACF indicator did not rise in some cycles and rose less in cycle 4 and 7, calculated strain values and temperature rise at freezing can be considered more closely. These are provided in Table 8.2. FBG strain, ϵ_m is extracted using equation 4.9, using the unbonded FBG for temperature compensation.

$$\frac{\Delta\lambda_B}{\lambda_B} = K_T\Delta T + K_\epsilon\epsilon_m \tag{4.9}$$

Strain, (K_ϵ) and temperature (K_T) coefficients are computed in a similar method as described in Chapter 6, Section 6.3.2 by subjecting the configuration to periodic steps in temperature. Temperature increase, ΔT_S is measured by a separate thermocouple placed in the water and compared to the temperature FBG, which measures a damped temperature outside the container. Theoretical ice mass, m_{IT} is then calculated from from equation 8.4 and multiplied by 3.48 to give the estimated mass at freezing, m_{IE}, as previously discussed in Section 8.4.3. Firstly, results suggest measured strain is currently uncorrelated with the ice mass. For example, cycle 4 has the largest temperature rise, thus largest estimated mass, but has the 5th highest strain. This irregularity can be explained with a few theories: ice does not form on the single instrumented wall, it may not form on all walls equally and expansion is influenced by open air above and surrounding water which affects the distribution of force. For these reasons, the impact of ice expansion on the instrumented FBGs is unpredictable. Secondly, the ACF indicator rose for the small strain in cycle 4, but not in the largest strain in cycle 3. This is likely due to the fact the ACF is calculated based on the de-trended strain noise, ϵ_n; therefore, strain level should not influence the probability of prediction. However, from the successful predictions, cycle 4 showed the smallest increase in indicator and had the smallest strain. Perhaps the strain does influence the magnitude of the ACF indicator trend.

Spectral analysis

Equating 8.3 with $X(k)$ representing the FFT of a window of the strain noise from Section 8.4.5 provides the power spectrum. Since frequencies of interest are unknown as this methodology has never been applied to such an application, a variety of frequency ranges will be analysed visually initially. This can be done by summing a short range of frequency magnitudes for each window,

Cycle no.	Strain in FBG ϵ_m ($\mu\epsilon$)	Temperature increase ΔT_S (° C)	Theoretical mass m_{IT} 8.4 (g)	Experimental mass $m_{IE} = 3.48 m_{IT}$ (g)
1	**28.687**	**1.760**	**11.086**	**38.579**
2	**27.386**	**1.735**	**10.929**	**38.033**
3	32.604	1.443	9.090	31.633
4	**13.043**	**1.915**	**12.060**	**41.969**
5	13.042	1.750	11.020	38.350
6	6.521	1.875	11.811	41.102
7	**22.826**	**1.361**	**8.398**	**29.225**

Table 8.2: Mass and strain results

shifting the window, then repeating and subsequently plotting the magnitude over time. Window size is set at a constant value of 10 seconds (500 data points) to ensure frequencies below 1 Hz could be adequately detected. It was found that this window did not require adjustment as the ACF window size did, and adjustment did not improve results. The window is shifted for each calculation by 1 second to minimise computational requirements and ensure short changes are not overlooked. From visually assessing multiple frequency brackets, it was found that $2.5 - 3.5$ Hz showed interesting variations prior to the freezing point. Figure 8.6 shows results from applying SA to the strain noise during the same cycles that showed rises in ACF indicators. The "SA indicator" represents the sum of frequency magnitudes in the range $2.5 - 3.5$ Hz. The resolution of FFT observable frequencies, $R = \frac{F_s}{N}$ for sampling frequency, $F_s = 50$ Hz is 0.1 Hz; therefore, plots represent the sum of 10 individual frequency components. One interesting anomaly was found in Cycle 3, shown in Figure 8.7. Extremely low frequency components show a significant increase during a short time period prior to freezing point. The cause of this is uncertain but was not found in any other cycles so presumably can be explained by interference of some sort. Essentially, this method has provided the same conclusions as ACF, with only 4 of 7 cycles showing apparent predictions. Results from applying SA to the three additional cycles is provided in the Appendix (10.7).

8.5   Test-bench: brittle failure

8.5.1   Plaster

In the previous experiment, the test-bench was relatively distant from the intended application of concrete cracking. However, the knowledge and experience gained can now be applied to a system more relatable. Ideally, a new test-bench that retains the benefits of the previous is desired: easy to perform, not time-consuming and repeatable, but also introduces a measurand more closely related to the intended application. Considering the mechanical properties of concrete: which is a brittle material (more specifically, quasi-brittle [190]), meaning fracture occurs prior to any elastic behaviour. Ideally, the methodology would be tested on small samples of concrete under loading and prediction of ultimate failure attempted. Concrete typically takes a long period to cure and can be
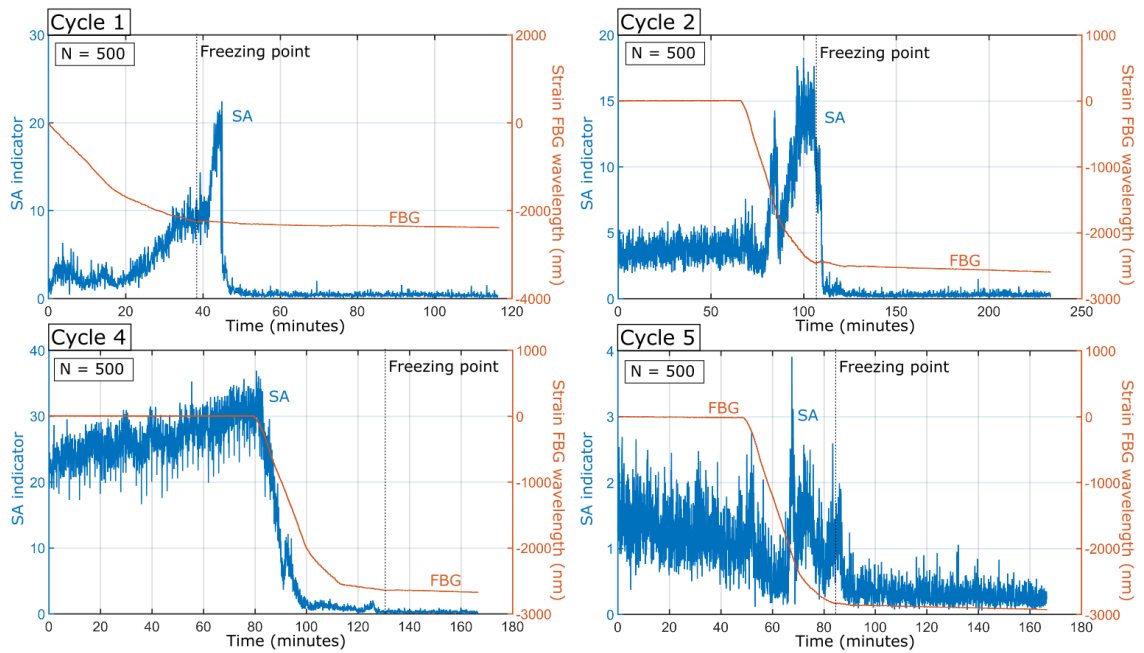
Figure 8.6: Results from the same four cycles that produced apparent predictions when ACF was applied. Comparatively, the plots look very much alike, with the both indicators rising at similar periods.
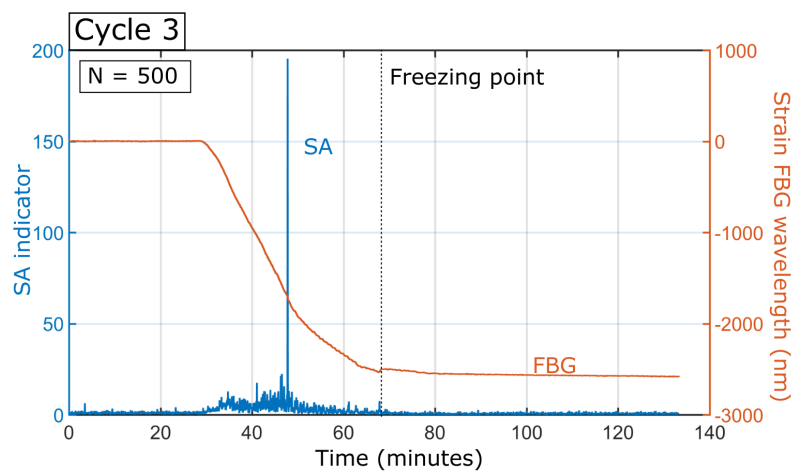
Figure 8.7: Large instant increase in extremely low frequency $(0.1 - 1\text{ Hz})$ components during cycle 3.

difficult to cure in small samples. To allow ease of experimentation and further development of the analysis methods, a material mechanically similar to concrete and easy to acquire in small samples is desired. One such material that meets these requirements is the easily sourced Gypsum plaster. Heating Gypsum to 150°C produces a fine powder, usually termed Plaster of Paris (POP). Mixing this powder with particular quantities of water forms a brittle compound. POP has a Young's modulus, $E \approx 4 - 5$ GPa [191] which is lower than concrete ($E_c \approx 17 - 40GPa$). According to Vekinis et al. [192], it also has a tensile strength of $\approx 3.2MPa$ and a tensile strain yield of ≈ 700 $\mu\epsilon$. The composition of POP will vary; therefore, these values are expected to change in reality. The tensile yield value is important since prediction of the failure requires a sensor capable of surviving to said failure point. FBGs are able to survive well above ≈ 700 $\mu\epsilon$, in addition to the small size required for a small specimen (which is limited due to loading equipment), FBGs are suitable for this application.

8.5.2 Methodology

The objective of this work is to apply the previously practiced TPA methods in order to predict critical failure in a POP specimen. In comparison to the previous freezing test-bench, the POP failure experiments provide a closer imitation to the intended application of cracking in concrete. The same methodology will be applied - noise will be extracted from an FBG bonded to the specimen. Two TPA techniques will then be applied in order to determine if prediction of the eventual failure is possible.

8.5.3 Experimental set-up

Five specimens were cast in a 2:1 ratio of plaster to water and cured for 48 hours. Specimen dimensions are illustrated in Figure 8.8 a) and are specific to fit the chosen tensile machine - Testometric M350-10CT. FBGs are attached to the centre of the POP specimens using EPO-TEK OG198-55 epoxy, which is cured by UV light and proved viscous enough to avoid absorption into plaster. FBGs were sampled at a higher rate of 2 kHz (compared to freeze tests), providing a greater insight into specific frequencies during SA as it increases frequency resolution ($\frac{Fs}{N}$). Two independent loading cycles are applied, which will identify if the predictions are load specific, including tensile (Figure 8.8 b)) and bending (Figure 8.8 c)).

8.5.4 Results

A total of 5 experiments were carried out, 3 bending and 2 tensile, where specimens were linearly loaded until critical failure. Loading is applied using displacement control of the tensile machine, meaning even if the material behaves non-linearly - loading will remain linear. Experiments were carried out over varying time periods to determine if predictions still occur for shorter experiments. Details of the experiments are provided in Table 8.3. Experiments were labelled 1-5 in order of
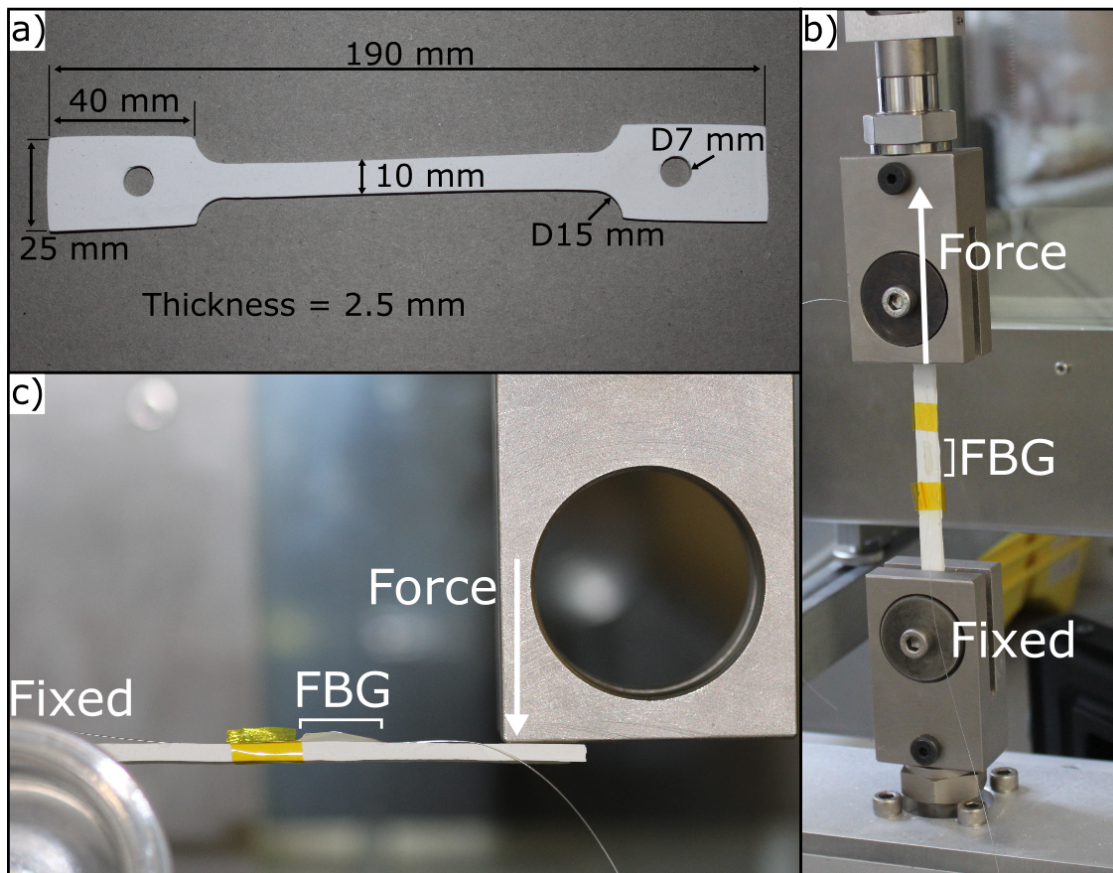
Figure 8.8: a) POP specimen dimensions, b) tensile loading and c) bending loading.

Experiment no.	Load type	Prediction time T_P (mins)	Failure time T_C (mins)	$\frac{T_P}{T_C}$	Strain @ T_P ($\mu\epsilon$)
1	Tensile	NA	3	NA	NA
2	Bending	22	34	0.65	143
3	Tensile	25	30	0.83	172
4	Bending	191	216	0.88	118
5	Bending	371	473	0.78	145

Table 8.3: Plaster experimental details and results
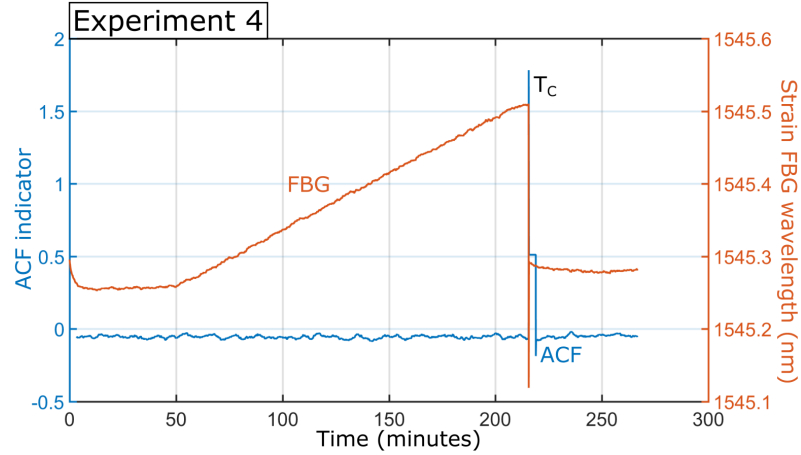
Figure 8.9: Example of ACF applied to plaster experiment 4, with indicator showing no rise.

time taken for failure, T_C. FBG strain data was collected and noise was extracted during data processing procedures using a moving average window of 5 data points (method shown in Appendix 10.6).

Degenerate fingerprinting

Since ACF does not require high frequency sampling, the data was firstly down-sampled to 50 Hz from 2 kHz, which also reduces the extreme computational complexity of the method. The ACF was performed on the strain data gathered from each experiment, but no reliable predictions occurred. An example of the ACF indicator for experiment 4 is shown in Figure 8.9, where no rise occurs at any point prior to failure time, T_C. It is unclear why this method is unsuitable for this application, it is possible any dynamic changes in the POP specimen are unmeasurable by the ACF. ACF was also carried out on the same experiment without down-sampling and the same result entailed.

Spectral analysis

SA was performed on the same experimental data without down-sampling and more promising results were observed. From applying SA to the freeze test-bench, some frequency components of interest are known to lie in the 2.5-3.5 Hz range, but also components below 0.1 Hz should be observed since these were prominent in previous work [180]. For this reason, the initial experiment
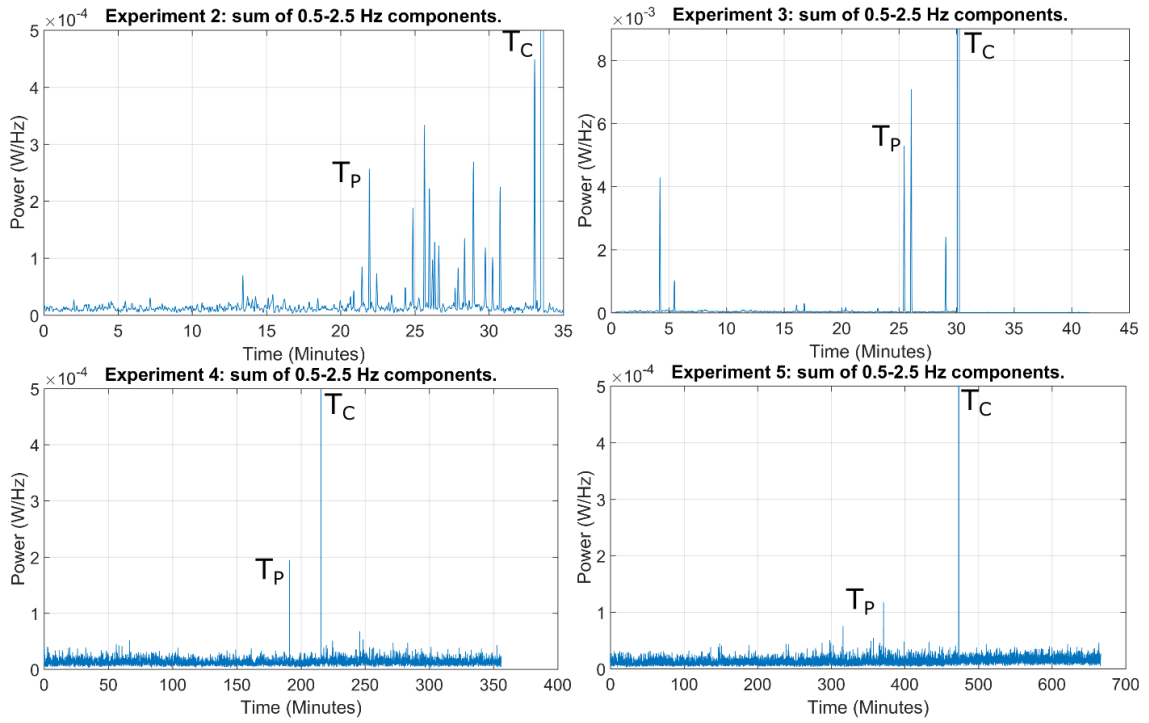
Figure 8.10: SA results

with a short failure time of 3 minutes may not be gradual enough to produce sufficient measurable dynamic changes. In fact, results showed for all other experiments (2-5) a significant rise in frequency components within the 0.5-2.5 Hz range prior to the failure time, T_C. Unlike results from the freezing test-bench, these rises were not gradual and occurred instantaneously at several points prior to failure. Figure 8.10 shows these results with most apparent changes labelled, T_P. Firstly, the only experiment that seemed to show a false positive was number 3 at around 5 minutes; however, this coincides with the onset of loading. Therefore, in all four experiments there is an apparent prediction of specimen failure, witnessed in the form of a clear rapid rise occurring in the magnitude of 0.5-2.5 Hz frequency components. The reason for this increase is unclear at this stage. It is possible there is some stress induced change in the material that causes reverberations affecting the systems dynamics, such as initial cracking. Garaga et al. [193] demonstrated that POP has an extremely large linear region before non-linear behaviour occurs. In fact, for 3 specimens the non-linear region began between 1-7 MPa. The strain in the FBG at the point of each prediction (shown in column 6 of Table 8.3) divided by the estimated Young's modulus ($E \approx 4.5$ GPa [191]) gives a range of stress at prediction, $\sigma_P = 0.53 - 0.77 MPa$. As such, it is possible the predictions are detecting the onset of non-linearity in the form of cracking in the POP specimen.

The main disadvantage of this test-bench is that each experiment causes destruction of a sensor upon completion. This limits the number of tests that can be run by the number of available sensors. Results show promise for predicting critical failures using SA where DF failed and should be investigated further for application to predict crack initiation or deterioration.

8.6   Chapter summary

Experimental implementation of two TPA techniques on two separate test-bench has been presented. Freezing of supercooled water provided a repeatable and short critical transition imitating a crack initiation or deterioration in concrete. Using this test-bench allows little investment and maximum repetition in order to practice and develop the TPA tools. Such a system has potential external applications, including concrete freeze-thaw damage prevention. Results showed that both TPA methods were identical in predicting four of seven cycles, and prediction occurred at similar time periods. Following this, a test-bench with closer relation to concrete cracking was demonstrated: brittle critical failure in a POP specimen. Results showed DF was ineffective, with no predictions in any of the experiments. However, SA showed an interesting instantaneous transition in all appropriate test cycles prior to failure, this correlated with possible onset of non-linear behaviour evidenced by monitored stress and previous literature. Both test-benches demonstrated promising results from the prediction methodology for detecting critical transitions. Further investigation is required, possibly applying the methodology in a real-world environment.

Chapter 9:   Conclusions and future work

9.1   Conclusions

Deterioration of existing cracks in an onshore wind turbine foundation are the subject of research in this thesis. The design, manufacture and implementation of optical fibre Bragg grating (FBG) displacement sensors on to pre-cracked foundations is demonstrated. Sensors are directly retrofitted over cracks for long-term monitoring. The purpose of these sensors is for monitoring crack deterioration, so any new cracks outwith the measured area will not be detected. However, any new cracks appearing within the gauge length of the sensor would indeed be detected; however, current methods will be unable to differentiate this as new damage. The inception of a methodology for quantifying deterioration is presented and applied to the collected crack displacements. The objective is to provide more detailed information on the crack state to the turbine operators.

After classifying the structural health monitoring (SHM) sensor subsystem, previous real-world sensor systems were considered, illustrating that no adequate methodology exists for crack deterioration monitoring. During this literature review, various other key factors were observed regarding the sensor system used. Firstly, structural characteristics were not mutually measured with crack displacements - which could provide data for validation and comparison purposes. Secondly, crack displacements were small and consistently lay below the equipment resolution, emphasizing the requirement for equipment displacement resolution to reach at least 0.1 μm. Crack monitoring also remained focused on mode I, opening displacements, disregarding other modes which may provide a more informative state of cracks. Additionally, sampling rates for crack monitoring were inadequate to investigate the crack dynamics, suggesting the adoption of high frequency sampling interrogation.

FBG sensors for displacement or strain measurement are conventionally available for unidirectional measurements only. To incorporate the bidirectional displacements of crack modes, a bespoke sensor design was developed using two FBGs. FBGs were epoxied to separate steel arms at a particular angle, which allowed a trigonometric relation to be used to segregate crack modes independently. Sensors were installed over four visually severe cracks in an onshore wind turbine foundation. An interrogation set up capable of high frequency (50 Hz) and low resolution ($\approx 0.032~\mu m$) measurements was used to investigate dynamic behaviour and allow measurement of the anticipated low displacement magnitudes. Strain sensors were also attached at the base of the tower. Comparing the crack displacements to the structural characteristics of the turbine, in this case the tower strain, provided continuous validation of measurements and provided a relevant (and otherwise non-existent) comparison to be made throughout the monitoring period.

In order to determine deterioration, an initial state and a comparison state are required, separated by a period of time. It was assumed that cracks were superficial from the point of instrumentation, providing the initial state. To determine a quantity of deterioration, an attribute

of the crack, such as width, is observed at a sequential time period following the initial state and any changes in the attribute are recorded. The developed methodology consisted of three defined independent crack attributes, based on initial observations of crack displacements. The methods for extracting said attributes include: "Reactive", "Permanent" and "Behavioural". Each concept examines an attribute over time, with any changes defined as deterioration. Firstly, the "Reactive" method analysed defined loading events that occurred during turbine start-stop procedures. These events caused equivalent transitions in the crack displacements. These reactions were monitored to determine if the transition magnitude varied for similar events over time. Any changes could potentially represent deterioration. In the "Permanent" method, similar to visual inspection, the permanent crack width during turbine downtime was monitored for variations over time. SCADA data is used to determine periods of "dead load" conditions, where external forces acting on the turbine are minimal. Crack widths during these periods are recorded over time, with changes potentially representing deterioration. Finally, it was observed that the tower strains and crack displacements were linearly related during early periods. A simple mathematical model was produced to predict the crack displacements during the initial state. The prediction is then compared to crack displacement during a second time period, recording any differences visually and numerically using correlation. Overall, after a 9 month period the cracks were deemed to have not significantly deteriorated. Results suggested some FBGs may have a reduced sensitivity when compared to others, proposing further investigation into sensor design, particularly the attachment method used.

A potential improved sensor design involves replacement of epoxy with purely metallic bonding. During experimental procedures, epoxy swelling was witnessed when subject to high humidity - with metallic bonding immune to such effects. Furthermore, metallic bonding was also shown to be capable of similar performance levels when compared to industry standard epoxies for strain measurement. To further test the sensors and in an attempt to validate the crack deterioration methodology, a test-bench was designed and demonstrated for concrete beam fatigue tests. Results showed the metallic-bonded sensor was capable of monitoring crack displacements and was linearly related to the epoxy design. Also, despite the increased crack severity, no deterioration occurred under the loading witnessed during the industrial application, validating the conclusions drawn during that work.

An improved SHM system would possess the ability to prevent damage degradation, rather than reactively alert the operators. Prediction methodology with the potential to be applied in SHM, known as tipping point analysis, is briefly explored in relatable test-benches, demonstrating promise for future implementation to real-world applications.

9.2 Future work

9.2.1 Deterioration methodology

The early concepts and methods for quantifying crack deterioration should continue to be developed as new data is collected. It is suggested to improve the predictions by including additional turbine variables such as torque and blade pitch. The main issue is the restricted number of time windows appropriate for analysis and including more variables will only increase this number. This work could also inform a second model that determines the economic viability of repairing the crack. The economic impact of cracks in foundations is an interesting study. As mentioned, cracks are commonly repaired immediately, regardless of information on the severity or deterioration. No real economic analysis on the benefit of repairing the crack immediately, or delaying if crack is not deteriorating exists. Results from this work suggest that cracks are not deteriorating; therefore, it may be more cost-effective to delay repairs until cracks display an increase in deterioration. This should be considered in future work when more results become available.

9.2.2 Further field trials

Investigation of more foundations displaying similar (potentially more severe) cracks is required. Due to the unique nature of the crack formations in this work, no comparisons are available for validation purposes, other than lab experiments. At the time of writing, collaboration with industrial partners is ongoing in order to determine the viability of another field trial. Significant learning has been obtained following the initial field trial and, although successful, improvements can be made to make the measurement and analysis process more effective. The infrastructure surrounding the data collection and processing procedures, such as interrogation, data loss filtering and temperature compensation is now in place and can be used in future installations, reducing the time required to produce results. Also, deterioration methodology now exists, does not require initial design and can be further developed and improved. More field trials would provide a greater insight into the results deemed from this work and further improve the ability of the system to quantify crack deterioration in onshore wind turbine foundations.

9.2.3 Humidity interference

The effect of humidity on strain gauge epoxies is only briefly investigated in two industrial standard strain gauge epoxies. In these experiments, swelling of epoxy caused a large tension strain to occur on the FBG. It is suggested to extensively research this affect and determine the cause of the tension. Humidity resistant epoxies are available; however, their effectiveness for strain gauge attachment is unknown - this should also be explored.

9.2.4   Fatigue machine improvements

The fatigue machine is a newly assembled apparatus and has only undergone a single concrete experiment. The objective of that work was to test and compare two types of crack displacement sensors and to replicate loading witnessed during the industrial application in order to attempt verification of the deterioration methodology. The experiment met these objectives, but also provided valuable information regarding machine performance and possible improvements for future experiments. Firstly, the load cell measurement set up is ineffective, with the machine controller not suitable for data acquisition purposes due to the low sampling frequency and insufficient resolution. Also, using the load cell for feedback was met with problems regarding processing speed and measurement accuracy, with an increased actuation speed causing an increase in loading. To improve on all of these factors, development of a separate system to independently monitor and record load cell measurements, outputting a digital trigger for the controller feedback, is proposed for future work. A digital trigger removes resolution issues and should be processed more quickly, providing a more accurate load cycle regardless of actuation speed. The separate system should record load cell measurements at a sufficient sample rate. Other improvements are more software based, such as creating complex programs to allow more customisable cycle shapes or synchronizing the load cell and sensor measurements.

9.2.5   Prevention

The focus of this research involves the deterioration of existing cracks. The current state of the SHM industry has seemingly exhausted the possible reactive methodologies that produce information subsequent to events. With the recent rise in popularity of artificial intelligence and machine learning, prediction methodologies are being applied in many industries. SHM presents a fruitful opportunity should a successful prediction methodology be developed - the ability to prevent damage would be highly desired in the industry. In future, work should continue on developing the TPA methods presented in this work for more closely related SHM applications. Other methods such as machine learning should also be explored. Should successful implementation of the methods in lab experimentation occur, progressing to an industrial application is suggested. Using the prediction methodology in conjunction with the reactive techniques (such as the deterioration methodology in this work) can provide validation of the ability to prevent the event.

Chapter 10:   Appendix

10.1   Data sheet of FBG

The FBGs used in the industrial application are polyimide coated with bare FBG section and FWHM of 300-400 pm. The spectrum of one FBG is shown in Figure 10.1.

Reflection Spectrum

RCWL@-3dB: 1555.02 nm   TCWL@-3dB: 1555.02 nm

RBW@-3dB: 0.35 nm   FWHM: 0.35 nm
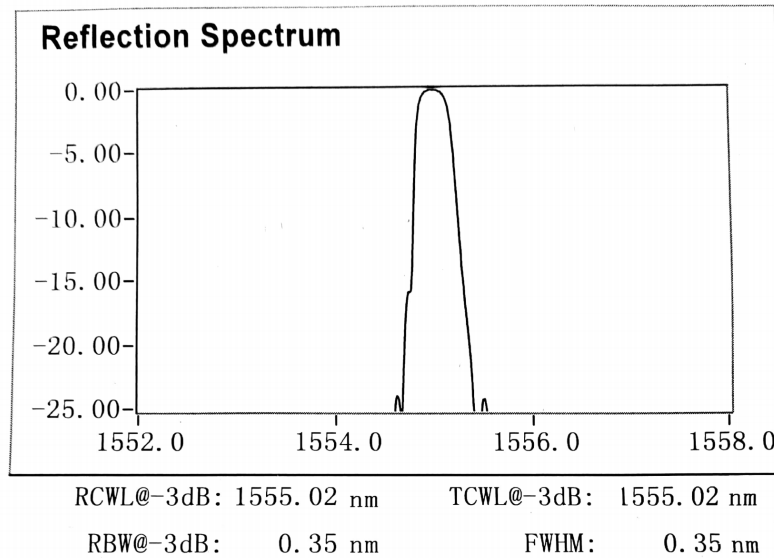
Figure 10.1: Spectrum of a single FBG.

The statistics from the data sheet for this FBG are provided in Figure 10.2.

Technica SA

Customer PO	5021199
Product type	Single FBG
No of FBGs	1
FBG length (mm)	7
CW (nm)	1555+/-0.5
FWHM (nm)	0.35+/-0.05
Ref (%)	>90
FBG profile	Apodized
Fiber type	Polyimide Fiber
Fiber recoating	Polyimide Recoat
Connector	None
Fiber end marking	None
Production S/N	1090031629007

Figure 10.2: Statistics of FBG from data sheet.

10.2   Product specification of I-MON

I-MON 256 and 512 USB

Product Specification

Table of Contents

1   Introduction

The I-MON USB Interrogation Monitor offers real-time spectrum monitoring of Fiber Bragg Grating (FBG) sensors at high speed. High spectrometer resolution combined with broad wavelength range provides a high-resolution interrogation monitor allowing measurement of a large number of FBG sensors. High sensitivity allows high resolution also at very low light levels. With its USB 2.0 interface and data acquisition software it provides easy setup with a laptop PC, and can act as stand-alone monitor in combination with a customer-selected light source.

The I-MON USB comes in two different versions as shown in the Table below

Table 1: I-MON USB versions

I-MON	Wavelength range	Detector
I-MON 256 USB	1525 – 1570 nm	Hamamatsu G11620-256DA
I-MON 512 USB	1510 – 1595 nm	Hamamatsu G11620-512DA

Other wavelength ranges can be provided.

2   Specifications

Table 2: I-MON 256/512 USB Specifications.

Parameter	Unit	I-MON 256 USB	I-MON 512 USB
Maximum Number of FBG's and Spacing		> 37 at 1200 pm	> 70 at 1000/1200 pm
Wavelength Range	nm	1525-1570	1275- 1345/1510-1595
Wavelength Fit Resolution	pm	< 0.5	
Repeatability (over any pol. state)	pm	3 (5 max)	
Wavelength Linearity	pm	5 (typ)	
Wavelength Drift[*]	pm / °C	1 (3 max)	
Dynamic Range	dB	30 (typ)	
Input Optical Power Range	dBm	-70 to –22	
Measurement Frequency[*]	kHz	6 KHz max	3 KHz max
Fiber Length	m	1	
Fiber Type		SMF-28 with Ø3 mm jacket	
Connector		FC/APC connector or specify	
Size (L×W×D)	mm	110 x 94 x 49	
Weight	g	660	700
Operating Temperature – non condensing	°C	0 to 50	
Storage Temperature	°C	-20 to 70	

(*)   By applying temperature correction the wavelength accuracy can be improved.

Specifications are subject to change without prior notice.

2.1   Measurement Definitions:

2.1.1   Maximum Number of FBG Sensors and Spacing

The I-MON optics is designed to match the bandwidth of a standard ITU-type FBG. If the Gaussian fit routine utilizes the peak pixel $\pm$ 5 neighboring pixels the minimum FBG spacing is 1200 pm as specified in Table 3. If the number of neighbor pixels is reduced to $\pm$ 3 the minimum FBG spacing is around 800 pm. For the 1310 nm version of the I-MON 512 USB the minimum spacing is 1000 pm.

If the sensing system leads the FBG peaks to traverse towards each other it should be ensured that the FBG spacing never gets below the defined minimum FBG spacing.

2.1.2   Wavelength Fit Resolution

The wavelength fit resolution is defined as the standard deviation over a series of measurements assuming that the temperature and the polarization is kept constant.

2.1.3   Repeatability

The repeatability is defined as the peak-to-peak variation in measured wavelength assuming that the polarization is rotated 360 deg and assuming the temperature is kept constant. I.e., it is the polarization induced wavelength shift, peak-to-peak.

2.1.4   Wavelength Linearity

The wavelength linearity is measured at the I-MON calibration temperature (25 deg C). The wavelength linearity is defined as the deviation from the I-MON wavelength fit and the reference wavemeter measurement.

2.1.5   Wavelength Drift

The wavelength drift is defined as a wavelength shift per degree C. By applying temperature control or temperature correction, the wavelength accuracy can be significantly improved (see Chap. 4.5).

2.1.6   Dynamic Range of Pixel Signal

The control electronics utilizes a 16 bit A/D converter. The dynamic range is defined as the full scale range (65535 counts) divided with the RMS dark noise of the pixel reading.

2.1.7   Input Optical Power Range

The image sensor integration time can be altered between 3 μs and 196 ms yielding an input optical power range is from –70 dBm to –22 dBm.

2.1.8   Measurement Frequency

The measurement frequency is set by the sum of the InGaAs reset time, exposure time and readout time.

157

3 Modes of Operation

Table 1 I-MON USB package content.

Item Description
I-MON USB Interrogation Monitor
Micro USB cable
I-MON USB– Product Specification (available for download on Ibsen Photonics' website)
I-MON USB–User Manual (available for download on Ibsen Photonics' website)
I-MON USB-Make your own software (available for download on Ibsen Photonics' website)

3.1 Operation with LabVIEW Evaluation Software

The I-MON USB content is listed in Table 1. The I-MON is supplied with LabVIEW Evaluation Software, and the Evaluation Software is described in the corresponding User Manual. The purpose of the Evaluation Software is to demonstrate the functionality of the I-MON in an easy manner without the need for tedious programming from the user and to enable the user to use the I-MON with own light source and FBG sensors using a PC as monitor. Since the LabVIEW source code of the Evaluation Software and some basic sample software is supplied too, the user may select to further develop the LabVIEW-based software. The LabVIEW version used to make the software is described in the User Manual.

3.2 Developing own Measurement Programs

The document "Make your own software" will guide through most steps necessary to develop own application software.

3.3 PC Requirements

Table 2: PC Requirements.

Parameter	Minimum Requirement	Recommended	Unit
CPU	Intel Dual Core 2.5 GHz	Intel i5 2.8 GHz	
Screen-resolution	1024x768		Pixels
Memory	1	4	Gbytes
Available slots	PCIe and/or spare GigE adaptor	PCIe and/or spare GigE adaptor	
Operating System	Windows XP/Vista/7 (32 or 64 bit)	Windows XP/Vista/7 (32 or 64 bit)	

4   Principle of Operation

4.1   FBG Sensing

Fiber Bragg Grating Interrogator
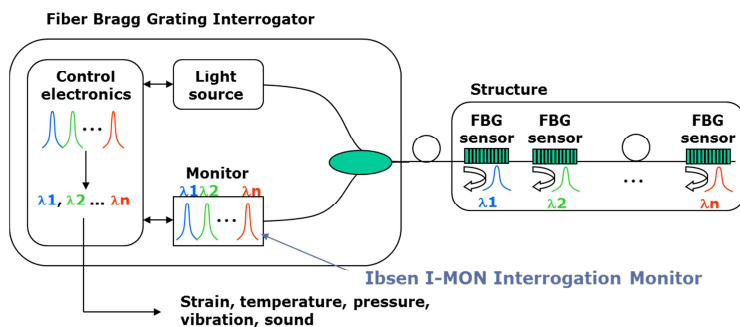
Figure 1: Using the I-MON in an FBG sensing system.

Figure 1 illustrates how the I-MON can be used in a Fiber Bragg Grating (FBG) sensing system. The FBG sensor is a short piece of optical fiber with a periodic modulation of the refractive index in the optical fiber. The periodic modulation of refractive index is generated by the interference pattern created from a phase mask (see http://www.ibsen.dk/products/phasemasks/), and it creates a narrow filter with peak reflectivity at a wavelength λi determined by the period of the FBG.

A broadband source such as a superluminescent diode (SLED) or an amplified spontaneous emission (ASE) source can be used as light source for the FBG sensing system.

When the FBG is mounted on a structure it may be stretched or compressed due to structural changes of the structure. This causes a change in the FGB period, and the peak reflectivity of the FBG is shifted accordingly to $\lambda i + \Delta \lambda$.. Each fiber can contain a multitude of FBG sensors all having different peak reflection wavelength.

Determining the peak reflection wavelength and shift in peak wavelength is the basis of FBG sensing, since the reflected wavelength can be converted to parameters such as strain, pressure, vibration and temperature. The I-MON interrogation monitor is designed to measure the reflection spectra from the FGB sensors, and will provide data to the control electronics for peak determination.

4.2   I-MON interrogation monitor
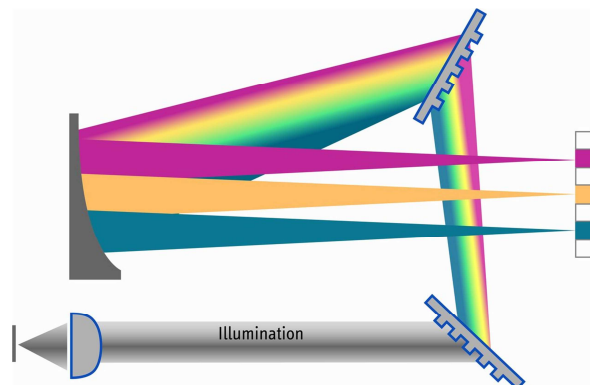
Figure 2: Optics schematic diagram for the I-MON interrogation monitor.

The schematic diagram for the optics of the I-MON is illustrated in Figure 2. The I-MON is based on Ibsen 's patented[*] high-resolution spectrometer platform. The high-resolution spectrometer platform spatially separates the wavelength spectrum utilizing multiple transmission gratings to provide a unique optimization of high optical resolution combined with compact size by turning the light 360 degrees inside a compact housing. The spectra reflected from the FBGs are focused onto a diode array, and the customer electronics reads out the diode array signals and performs a peak fit to determine the reflected FBG wavelength.

[*] Patent Numbers: US 6,978,062, US 6,842,239

4.3   Measured spectra and peak determination

The reflected FBG spectra are sampled by the diode array with either 256 pixels (I-MON 256 USB) or 512 pixels (I-MON 512 USB). The average pixel spacing in wavelength is similar for both I-MONs – about 170 pm. The optical resolution (FWHM) of the I-MON is about 330 pm, and as a typical (ITU-type) FBG has a bandwidth of 200-300 pm, this means that each FBG will be sampled by about 2 pixels, which is just enough to minimize wavelength non-linearity resulting from pixel under sampling.
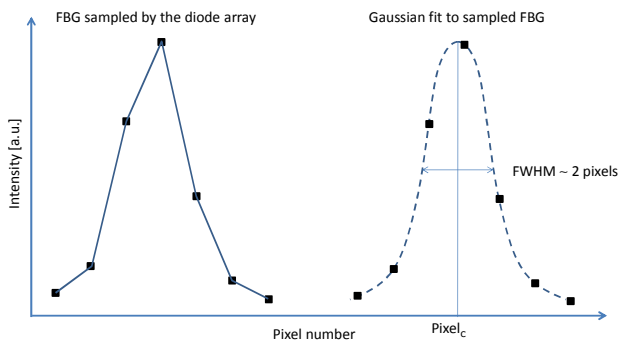
Figure 3: FBG sampled by the diode array.

Figure 3 (left) shows a typical FBG peak sampled by the diode array. Each dot represents the intensity signal from the discrete diodes in the array. The optical response of the I-MON is highly Gaussian, and as many FBGs are also Gaussian apodized, a Gaussian peak fit algorithm can determine the FBG peak position with sub-pixel accuracy. This is illustrated on the right-hand side of Figure 3.

Gaussian peak fitting is computational intensive, so it may be advisable to utilize faster algorithms such as center of gravity or centroid algorithms. It should be noted that it is important to check the robustness of the peak fitting algorithm under real test conditions.

4.4   Wavelength Calibration

The I-MON is wavelength calibrated at a fixed temperature of 25 deg C according to a polynomial of 5th degree:

Eq. 1 $$\lambda[\text{nm}] = A + B_1\,pix + B_2\,pix^2 + B_3\,pix^3 + B_4\,pix^4 + B_5\,pix^5, \quad pix = 0..255 \text{ or } 511.$$

This equation describes the relation between the beam spot position (pix) on the image sensor and the optical wavelength (λ). Under calibration the beam spot position is deStermined be applying a Gaussian fit to the image sensor response, and the input light source is a tunable laser coupled to a reference wavelength meter. The wavelength meter is set to measure the wavelength in vacuum.

The coefficients A, B_1, B_2, B_3, B_4 and B_5 are measured for each I-MON unit and are provided on the Certificate of Conformance included with the I-MON.

As a consequence of the I-MON design (placement of sensor array) the incident light of longer wavelength hits lower pixel numbers, see Figure 4.
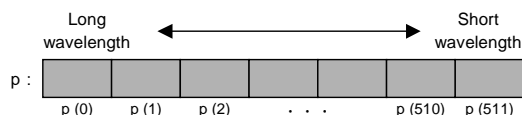
Figure 4: Pixel Arrangements illustrated for a 512 element diode array.

4.5   Compensation for Temperature Drift

The I-MON is temperature characterized, and by measuring the I-MON temperature the effects of wavelength drift (see Chap. 2.1.5) can be reduced by using the following correction equation:

Eq. 2 $$\lambda_{Corrected}\,[\text{nm}] = \frac{\lambda_{meas}\,[\text{nm}] - \beta \cdot t_{amb}\,[\text{deg C}] - \beta_0}{1 + \alpha \cdot t_{amb}\,[\text{deg C}] + \alpha_0}$$

The coefficients α, α_0, β, β_0 are provided on the Certificate of Conformance.

5   Electrical Interface

The linear InGaAs image sensor has 256 or 512 elements and is supplied by Hamamatsu Photonics. The pixel spacing is 25 μm, and they are both housed in the same type DIP housing. They are pin compatible and are interfaced with a control PCBs. The Control PCB has a USB interface and is provided by JETI Technische Instrumente GmbH. Thus, some drivers, documents, etc. used by the I-MON are also delivered by JETI Technische Instrumente GmbH, and from time to time names referring to JETI may appear. With respect to functionality this is of no concern. This message is only to avoid confusion.

5.1   Image Sensor

As written above the spectra from the FBGs are imaged onto a linear image sensor that converts the incident light into an electrical signal. The image sensor outputs a photoelectric signal from each pixel (photo diode) at a certain time interval. This time interval is called 'sample frequency' or 'measurement frequency' and determines how fast the optical signals can be detected. The signal gain of the detector is set by an on-chip charge amplifier. This charge amplifier integrates the photo diode current over a certain time interval that is called "exposure time". The output signal level can therefore be optimized by adjusting the exposure time. For example, even at low light levels, lengthening the exposure time increases the output signal to a level where the signal can be easily processed. Long integration times will reduce the sample frequency. The charge integration method for the InGaAs image sensor used in the I-MON is called "Simultaneous Integration Method.

5.1.1   Simultaneous Integration Method

In simultaneous integration mode, when an integrate pulse is send, the charges from all pixels accumulate in the charge amplifier simultaneously. The charge amplifier output is then sequentially transferred to the readout section by a clock pulse. This method is used by the InGaAs image sensors family used in the I-MON USB.

5.2   Control electronics

The I-MON USB includes Control Electronics and is operated through a USB 2.0 interface and a parallel I/O port. The USB interface is used as a command interface to configure the detector scanning parameters and also for streaming of the detector data in real-time.

The parallel I/O port is currently only supported with fast trig functionality.

In order to utilize the thermal compensation described in Chap. 4.5, a thermal sensor is included in the electronics design that can be read via the USB interface. At calibration the I-MON temperature is measured in the bulk housing.

The physical positions of the different interfaces are described in Chap 6. The pin configuration is described in Table 3:

Table 3 Pin configuration

Connector	Connector type	Pin	Description
USB	Standard micro USB		Standard USB configuration
Parallel I/O port	Molex SD-501571-001	20	GND
		18	Trig input. 3.3 V TTL (5 V tolerant)
		11	Exposure indication output. 3.3 V TTL
Power	hdr1x2 connector	1	GND
		2	6-12 V DC, max 250mA. The I-MON is powered via USB is there is no external power supply.

The I-MON USB is fully powered and controllable from a PC connected via USB interface. Ibsen Photonics A/S provides Evaluation Software (See Chap. 3.1) and a DLL that let you easily operate the I-MON USB. The Evaluation Software is based on LabVIEW. The DLL is a library that can be used with e.g. C/C++ and LabVIEW when creating your own software (See Chap. 3.2).

6   Mechanical Interface
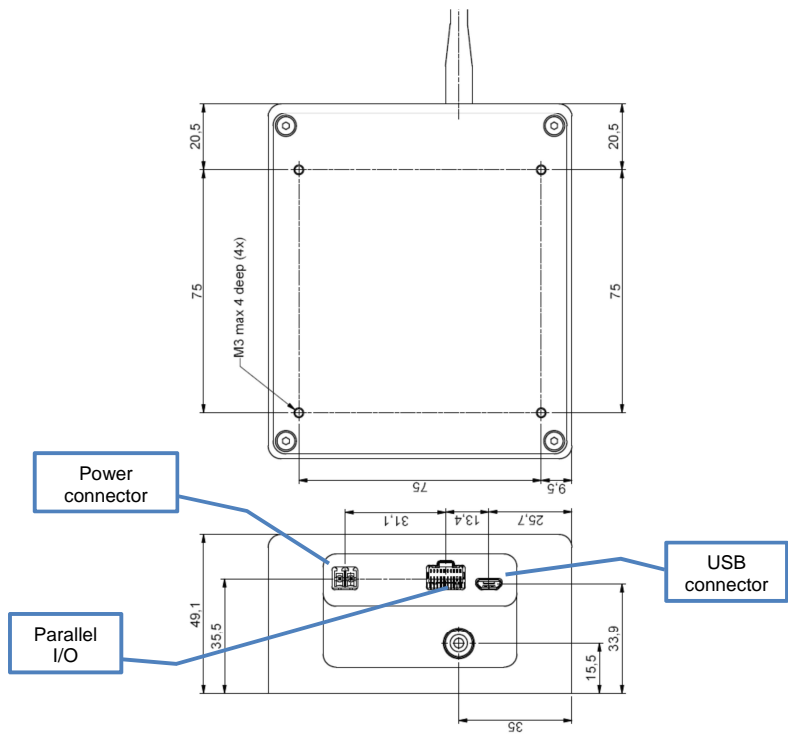
Figure 5: I-MON dimensions and connector positions.

The package dimensions are shown in Figure 5: I-MON dimensions and connector positions.. Four threaded mounting holes are placed on the housing back side. Note that all dimensions are given in mm.

7   References

Table 4: Reference documents

Subject	Document type	Document Number/Location
I-MON USB– Product Specification	Product Specification	This document
I-MON USB–User Manual	User Manual	54-100-641
I-MON USB-Make your own software	User Manual	54-100-652
D2XX_Programmer's_Guide	User Manual	54-101-226
Firmware Commands - RU60	User Manual	54-101-237
90-101-675 I-MON USB	Step file	90-101-675

8   Revision History

Table 5: Revision history

Revision	Changed by	Short description of change
1	22-11-2013/OJE	First version
2	12-12-2013/OJE	Pin no. on Molex connector corrected
3	17-09-2014/PKE	Manuals and specifications available for download

10.3   Deterioration analysis

Periods at the start and end of the year were chosen for deterioration analysis. Figures 10.3 and 10.4 show the period starting January 27th of the tower and foundation sensors respectively. Similarly, the later period starting August 23rd is shown in Figure 10.5 and 10.6 for tower and foundation sensors respectively. Again some peak detection issues caused data loss of module C.
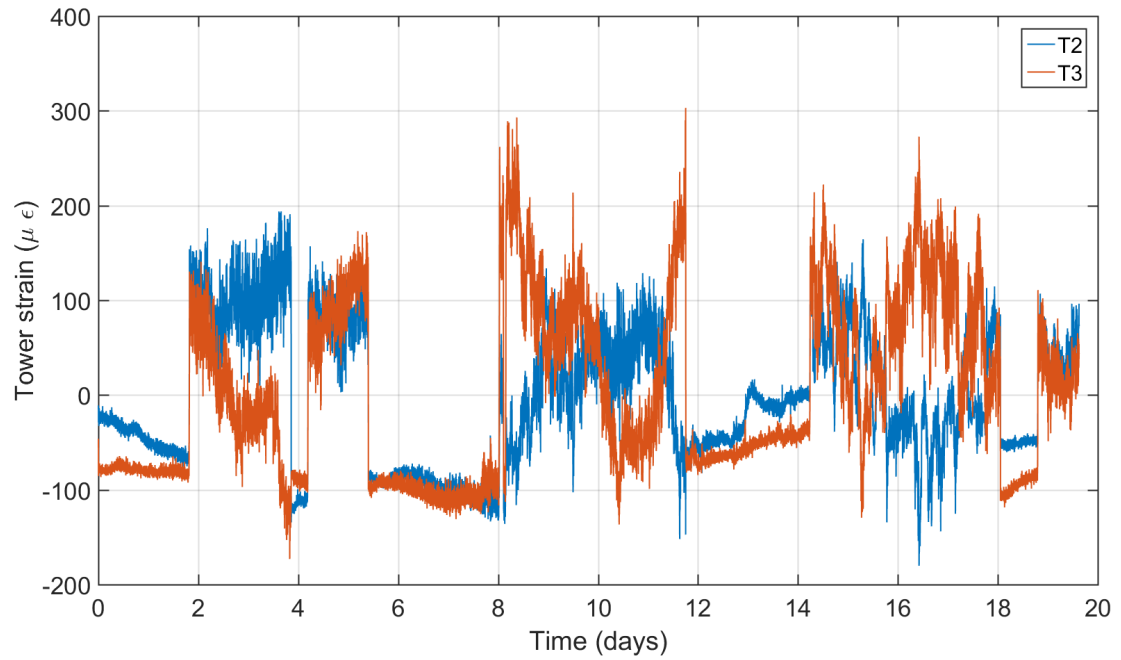
Figure 10.3: Early data starting 27th January for sensor 2 and 3.
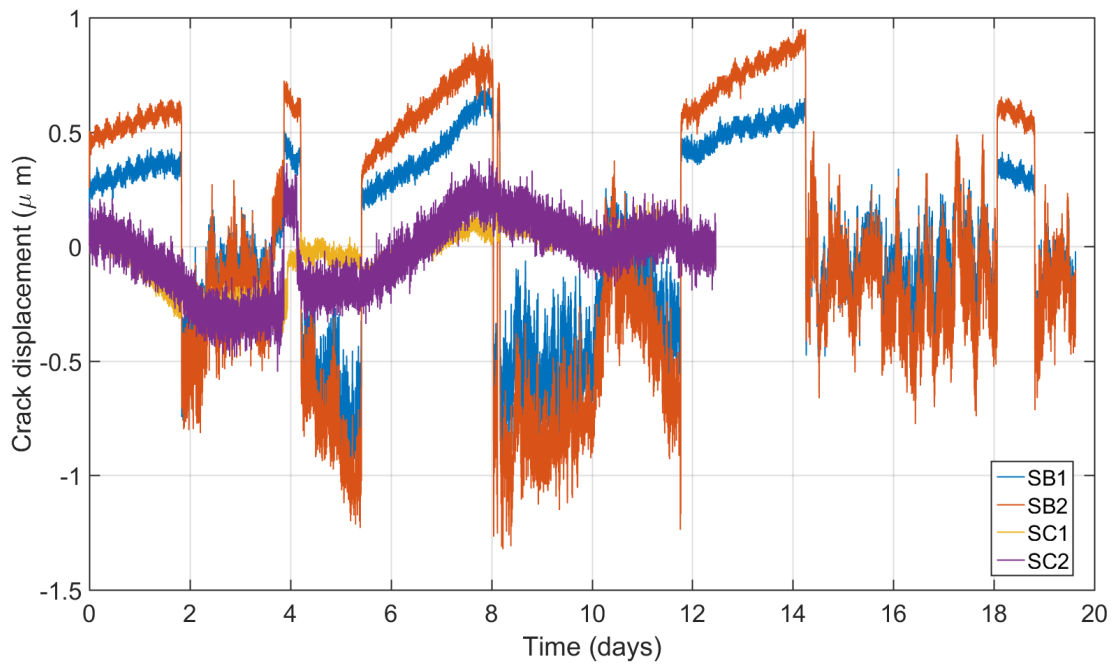
Figure 10.4: Early data starting 27th January for modules B and C. Peak detection algorithm caused some data loss of module C part-way through the period. Illustrates the significant difference in displacements between cracks.
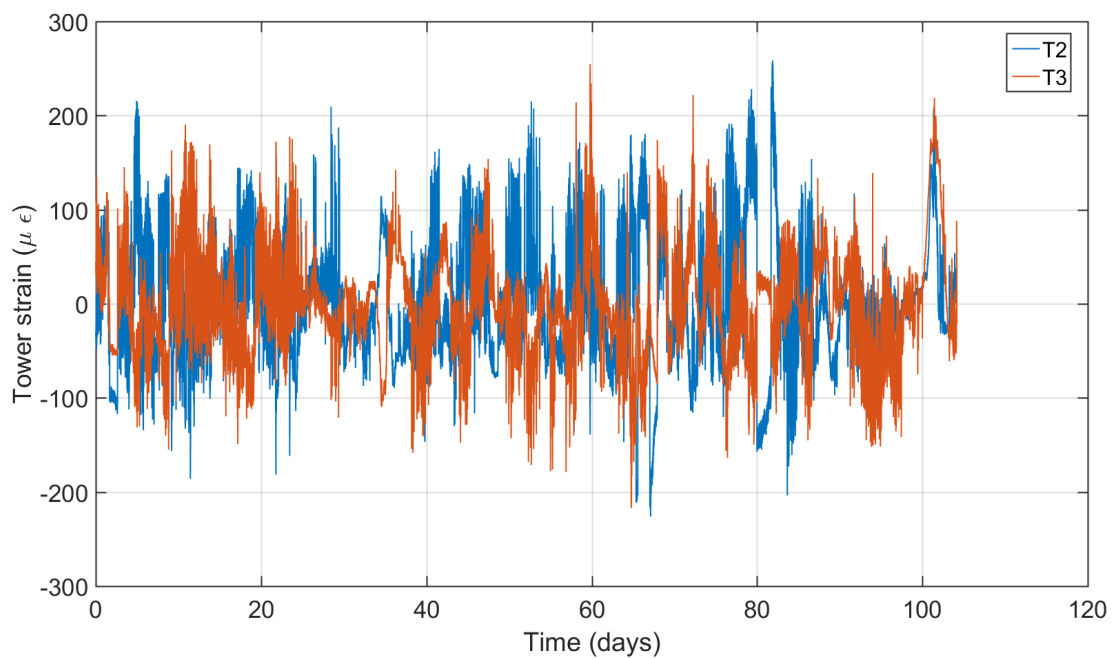
Figure 10.5: Late data starting 23rd August for sensor 2 and 3.

166
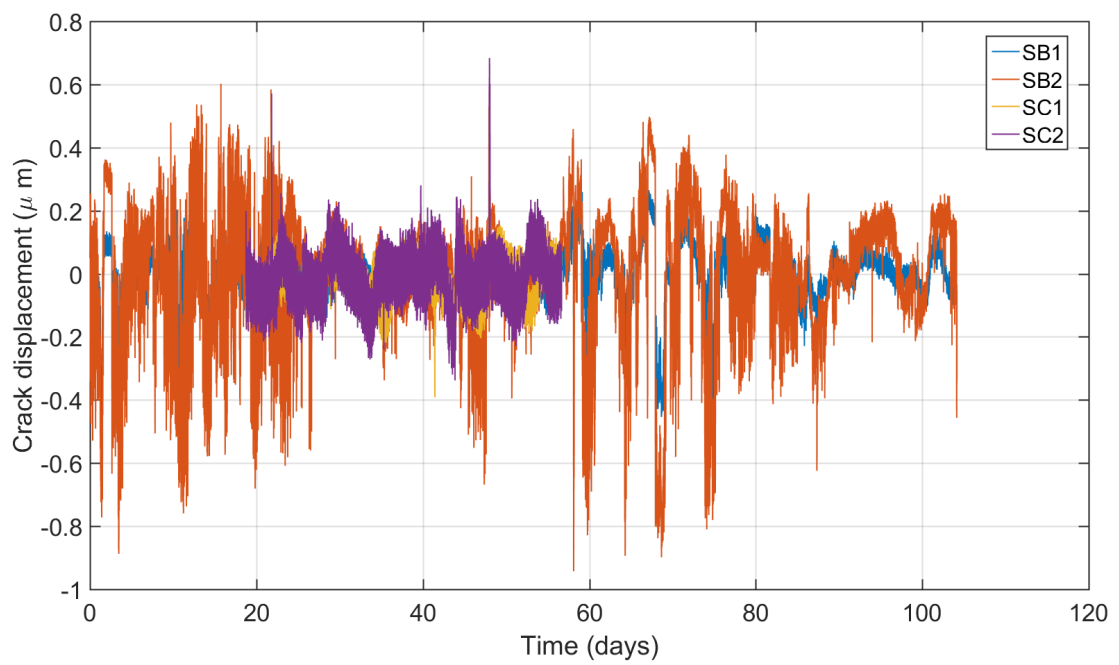
Figure 10.6: Later data starting 23rd August for modules B and C. Peak detection algorithm caused some data loss of module C.

10.4 Concrete-steel anchorage

According to ACI 355.1R-91, options for anchoring in concrete generally appear in three forms: mechanical, bonded and chemical. Mechanical refers to the use of mechanical-based attachment - such as torque-controlled, which is a bolt that essentially "expands" in the drilled hole to provide attachment. Bonded refers to using a cementitious-based adhesive inside the drilled hole to provide attachment. Chemical is similar to bonded, only the adhesive is chemical-based, such as epoxy. All methods are acceptable for anchorage in concrete, the choice mostly based on the conditions of the surrounding material and expected tensile and shear loads. According to literature review of previous crack monitoring systems, loading would be extremely small - with crack displacements never exceeding $< 10 \ \mu$m. The equivalent strain acting on the sensor for such a displacement would be $< 100\mu\epsilon$. Force can be calculated using equation 7.2 from Chapter 7:

$$F_1 = \epsilon_1 E_s A_p \tag{7.2}$$

Substituting the sensor cross-sectional area (20 mm^2) for A_p and the Young's modulus of carbon steel (200 GPa) for E_s, with strain ϵ_l of $100\mu\epsilon$ gives a force of 400 N. Therefore, HILTI HIT-RE 500-SD [194] (now replaced by HILTI HIT-RE 500 V3 [195]) was chosen and installation done according to data sheet and industrial standards [196]. This epoxy is suitable for cracked concrete and provides an easy installation process.

10.5 Fatigue machine design process

Following on from Section 7.3.2, the intended experiment is to perform $\pm$ 25 kN bidirectional 4-point loading to a 1 x 0.1 x 0.1 m concrete specimen. To do this, firstly an actuator will be chosen that meets the requirements. Secondly, a frame will be needed to both house the actuator and focus the loading on to a beam in 4-point configuration in a bidirectional form.

10.5.1 Methodology

The process in designing and commissioning the fatigue testing machine is as follows:

1. Determine the required maximum force to produce sufficient stress in predetermined test specimen. This can be exaggerated to increase specifications. For the present project, this was calculated at ± 25 kN in Section 7.3.2.

2. Review and choose preferred actuator, optimizing factors outlined in Section 7.3.2.

3. Design suitable support frame and model in CAD software.

4. Use FEM software to ensure support frame meets physical requirements. Model a test experiment with beam specimen.

5. Manufacture and install the machine, including electrical connections.

6. Commission the machine by programming and performing test experiments to compare to model, validating the support frame structure.

Following these steps the machine will be ready for further experimentation.

10.5.2 Actuator

The required force is known to be $\pm$ 25 kN, which limits possible actuator choices. The following itemized list presents the optimization factors for the actuator:

- High accuracy

- Low noise

- High reliability

- Long lifetime

- Low maintenance requirements

- Considerable customisation (capable of sinusoidal load cycle)

- User friendly interface

In addition, the variability of the stress ratio requires an adjustable control that ideally is user-friendly and software based, without any requirement to mechanically adjust the system components. For the support frame, a few factors require consideration during design:

- Actuator and beam geometry

- Yield stress

- Fatigue life

The frame must be capable of housing the actuator and beam in order to produce accurate fatigue forces (sinusoidal, trapezoidal etc.). Also, the frame itself must be adequately designed to survive the maximum stress levels over a long period. In other words, the endurance limit, σ_e, of the frame must be greater than the expected maximum stresses during fatigue operation.

Possible actuators include pneumatics, hydraulics and linear and servo actuators. Linear actuators are not suitable because they do not allow a variable speed application to adjust the testing frequency. With regards to pneumatic drives, machine parts are generally cheaper, require less maintenance and are cleaner (no oil) than hydraulics [197]. However, system efficiencies are significantly worse (lower possible forces) and the system experiences a time delay. The overall anticipated issue with hydraulics and pneumatics are the necessary system complexity (associated with many valves and control switches for $R = -1$ test option), reliability and maintenance concerns as well as the emitted noise of the compressor. Ultimately, it was ascertained that a servo actuator agrees with all requirements and was thus selected as the preferred fatigue drive option.

Servo actuators are selected based on the expected total lifetime travel distance at a given applied load, thus assumptions were made with regards to the lifetime travel distance and the mean applied force. A generic example testing procedure is defined in matrix x consisting of different test cycles $(1 : n)$ with the amount of cycles C at force F and the respective predicted distance travelled D. The travel distance may be derived from an FEM model.

$$
x = \begin{bmatrix} F_1 & C_1 & D_1 \\ F_2 & C_2 & D_2 \\ F_3 & C_3 & D_3 \\ \vdots & \vdots & \vdots \\ F_n & C_n & D_n \end{bmatrix} \tag{10.1}
$$

With a pre-defined testing procedure, the total lifetime travel distance can be calculated by:

$$
D_{tot} = \sum_{i=1}^{n} x_{i,2} x_{i,3}. \tag{10.2}
$$

And the mean applied load is calculated by the cubic mean load formula (fatigue exponent of 3

[198]):

$$F_{mean} = \frac{\left[\sum_{i=1}^{n} (x_{i,1})^3 x_{i,2} x_{i,3}\right]^{1/3}}{D_{tot}^{1/3}}. \tag{10.3}$$

Depending on the cubic mean force and total travel distance assessment for the lifetime expected, the appropriate servo actuator parameters are selected. In addition, depending on the intended test cycle and force (step changes with breaks vs. continuous movements), a fan might be necessary to prevent the motor from overheating.

Due to the requirement to enable different operational modes, the servo actuator further enables user-friendly and adjustable control. The latter can be controlled by readings from a load cell that is intended to be installed between the actuator and specimen, implemented through a feedback loop to the actuator controller.

10.5.3   Support frame

Various methods can be adopted for loading a beam specimen, such as direct tension/compression, 3-point bending or cantilever. Since an objective of this work is to test sensors, it is crucial that the maximum stress position has adequate space for sensors. For this reason, 4-point bending was chosen, as the centre of the beam remains clear. This means the support frame will require fixed constraints at each end of the beam, but incorporate the capability of using a linear-single point motion from the actuator to perform 4-point bending. It is also a requirement that the beam is loaded in both directions. In other words, a single face of the beam (top or bottom) undergoes tension and compression in a single cycle. This will allow more thorough analysis and testing of the specimen, specifically with cracks, and any attached sensors. With these additional requirements following the actuator choice, the frame can be designed.

10.5.3.1   CAD model

Figure 10.7 a) shows a rendered completed frame with inserted beam and actuator whereas 10.7 b) shows an exploded isometric CAD model of the outer frame in black and the inner 4-point bending frame in red. Some key dimensions are as follows: width of frame 1.5 m, height is 1.16 m, depth is 0.254 m. The outer frame is designed to provide the necessary reactionary compression and tension forces of the linear actuator that is vertically inserted between the top two I-beams. For the outer shell, conventional sized structural steel I-beams are selected as this element enables significant tensional and compressive resistance while allowing easy sourcing without additional machining of complex parts. At each corner the I-beams are cut at an angle of 45° and in-plane full penetration butt-welded together with a steel plate in between. Welding is carried out according to the British standards [199]. The top section is manufactured out of two parallel smaller I-beams in order to fit the servo actuator, while the top and bottom plates are necessary to distribute tension and compression forces onto both I-beams.

The 4-point bending frame is mostly composed of hollow squares, but the top two elements
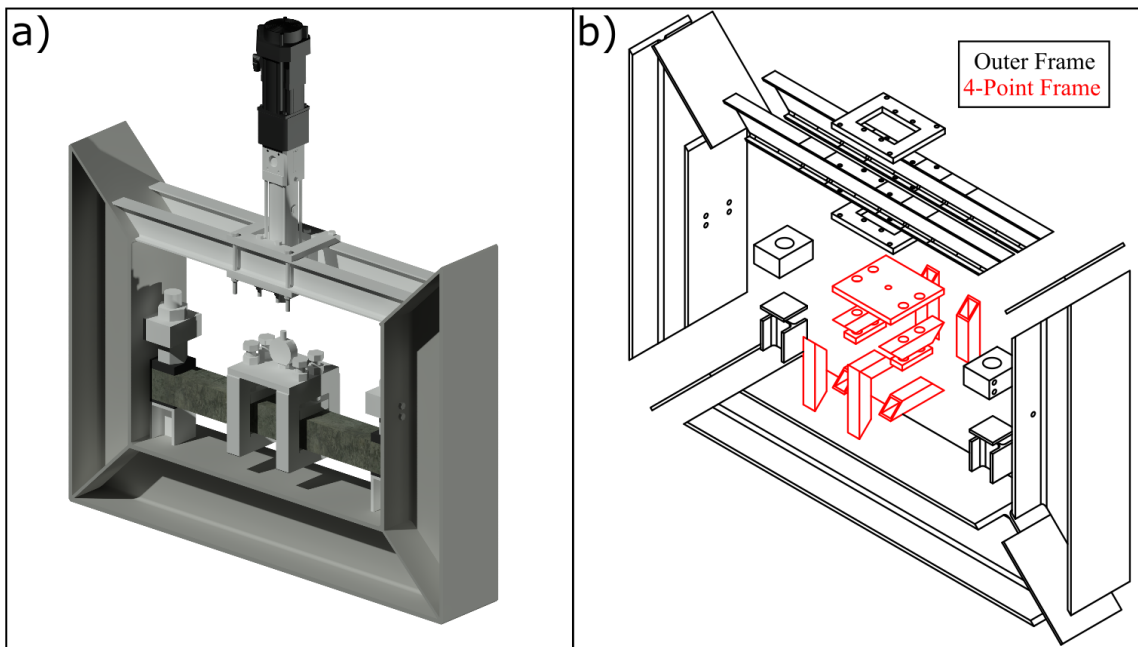
Figure 10.7: Isometric views of a) rendered machine and b) exploded frame.

are made of solid pieces with threaded holes to allow fixing of variably sized testing samples using bolts and to enable $R = -1$ testing. The 4-point bending frame could potentially be exchanged with a simple foot to enable 3-point bending tests in tension-tension configuration.

The frame is mounted onto the floor with 2 steel foot elements bolted at an angle of $90°$. The beams intended for testing are fixed by two bolts protruding from the middle sections to allow holding variably sized specimens. Larger elements may be tested; however, this would require an adjusted 4-point bending frame.

10.5.3.2   FEM model

Following the discussed requirements in Section 7.3.2, it is essential to ensure stress levels in the support frame do not exceed mechanical limits during maximum loading. Fatigue life of the frame will also require consideration. The frame can mechanically be separated into two parts, the outer and 4-Point bending frame, as exemplified in Figure 10.7 b). The 4-point frame can be modelled as a singularly welded component. The outer frame consists of 3 separate interactions: at the actuator attachment and at the bottom and top beam supports. To simplify simulations, the structure is assumed to also be singularly welded. To reduce computational requirements all holes and bolts will be removed - meaning real-world stress levels will differ from simulations. These simulations act as an approximate guide of the expected stress levels the frame will be subjected to.

Outer frame

The geometry of the outer frame is inserted into an FEM modeling software. Figure 10.8 shows
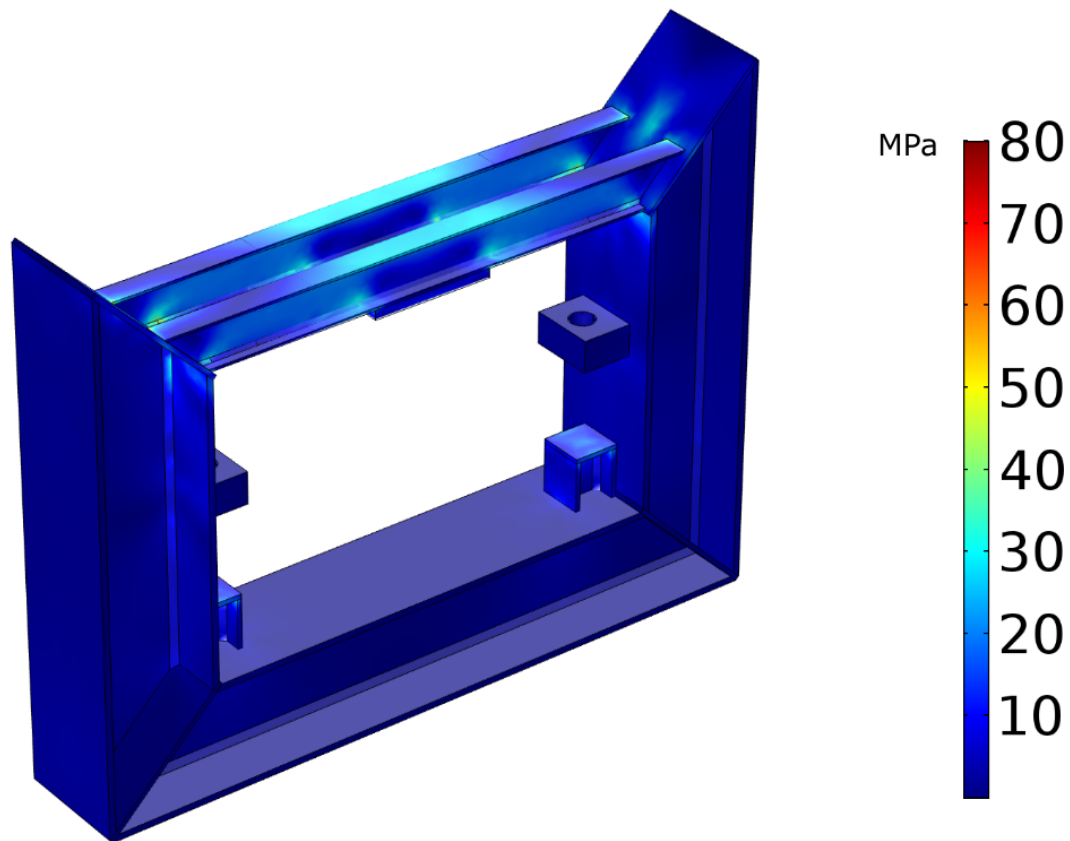
Figure 10.8: Stress distribution during 25 kN forces acting in all interfaces.

the stress distribution during a 25 kN load applied in 5 positions: upwards against the top I-beams and the two top supports as well as downwards against the two bottom supports. Any deformation is exaggerated for illustrative purposes.

The scale shows the maximum stress level is 80 MPa; however, it is clear that the majority of stress in the components is below 50 MPa. This is well below both the yield stress $\sigma_y = 250$ MPa of structural steel and will also be within the endurance limit σ_e. According to Kucharczyk et al. [200] experiments on structural steel with yield limit of 430 MPa showed no endurance limit less than 260 MPa. A general approximation of $\frac{\sigma_y}{2}$ for σ_e can be used as a guideline. This means a stress of less than 125 MPa is desired to ensure long operational lifetime. Most of the stress is witnessed in the top I-beams. It is important to also consider the welded sections, as the endurance limit will differ to that of steel. In the case of the outer frame - the stress is focused on the attachment point of the actuator, thus welds of I-beams are not of concern. This may require more in depth study for the 4-point frame. To acquire a more accurate value for maximum stress, the actuator attachment point with bolt interactions are separately modelled. Figure 10.9 shows the stress distribution for the actuator attachment during a 25 kN load in the downward direction.

According to Figure 10.9, the absolute maximum stress magnitude occurs at the contact point
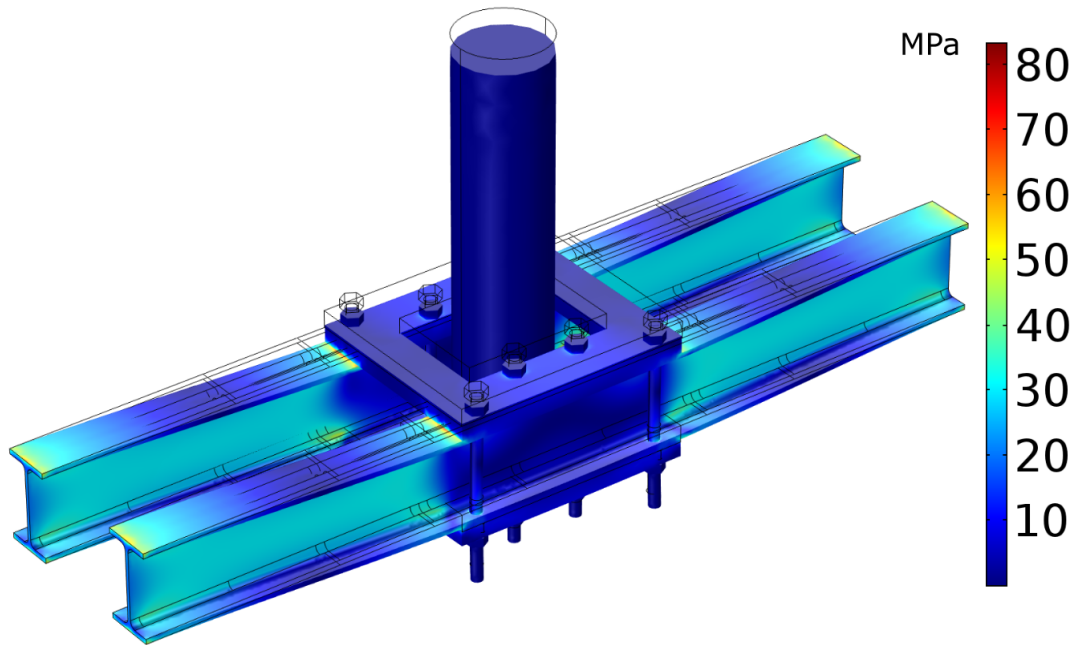
Figure 10.9: Stress distribution of maximum stress component: actuator attachment.

of the actuator attachment plates to I-beams. This matches the stress limit from Figure 10.8. The model calculates a value of ≈ 70 MPa at this point. This is well below the estimated endurance limit of the steel, $\sigma_e = 125$ MPa. It is also possible to minimise the stress at this contact point with the introduction of a soft material, such as rubber. With stress levels in the majority of the I-beams below 40 MPa the outer frame should survive indefinitely under continuous maximum loading conditions.

4-point frame

Following the same process, the FEM model of the 4-point frame is established by applying the maximum possible load to the bottom, shown in Figure 10.10.

Again stress levels are well below the approximate endurance limit, $\sigma_e = 125$ MPa. The weld interface between the hollow beams is the weakest point of this section. According to EN 1993-1-9 [201], the endurance limit for welds, σ_{ew} with detail category, $\Delta\sigma_C = 100$ can be calculated as:

$$\sigma_{ew} = 0.549 \cdot 0.737 \cdot \Delta\sigma_C \tag{10.4}$$

Providing a smaller endurance limit of 40.5 MPa when compared to that of steel. From Figure 10.10 the stress is up to 35 MPa in this region. With this information, the 4-point frame should also survive indefinitely under continuous maximum loading conditions. In the worst case scenario, according to curves shown in [201], the 4-point frame may fail after several million cycles. Since this is a significant amount of time and replacement cost would be low - this is of little concern.
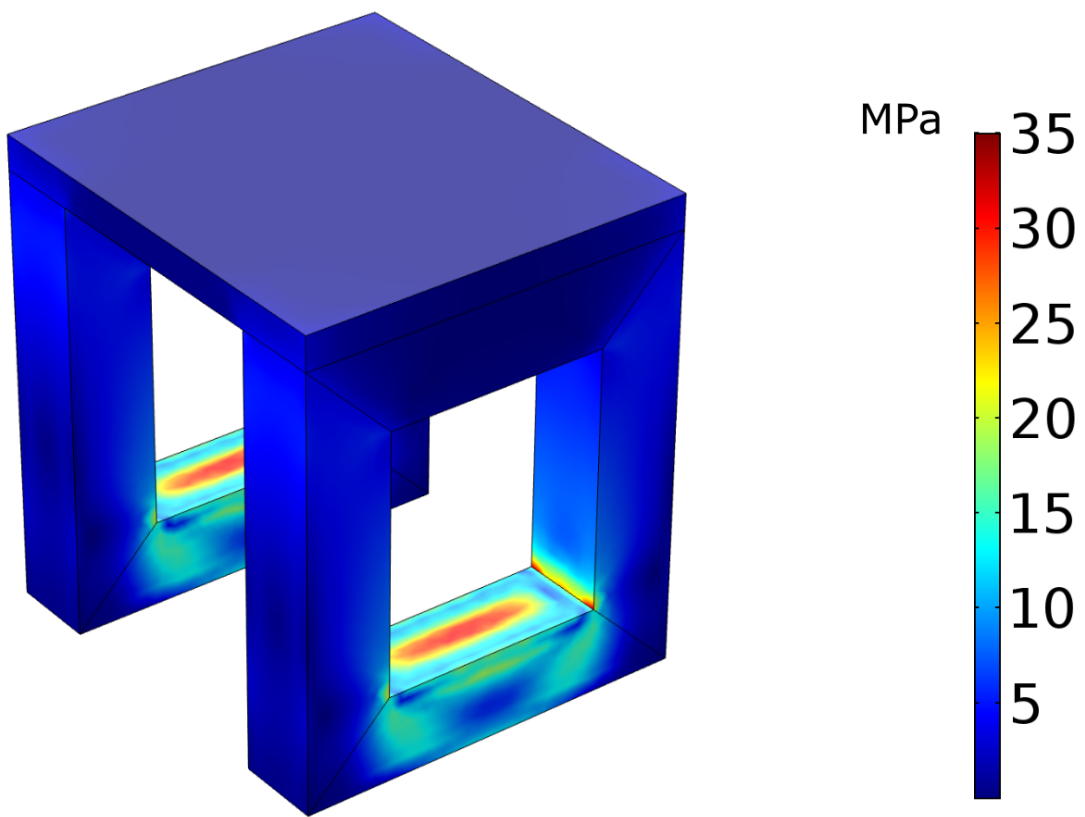
Figure 10.10: Stress distribution in 4-Point frame during maximum loading.
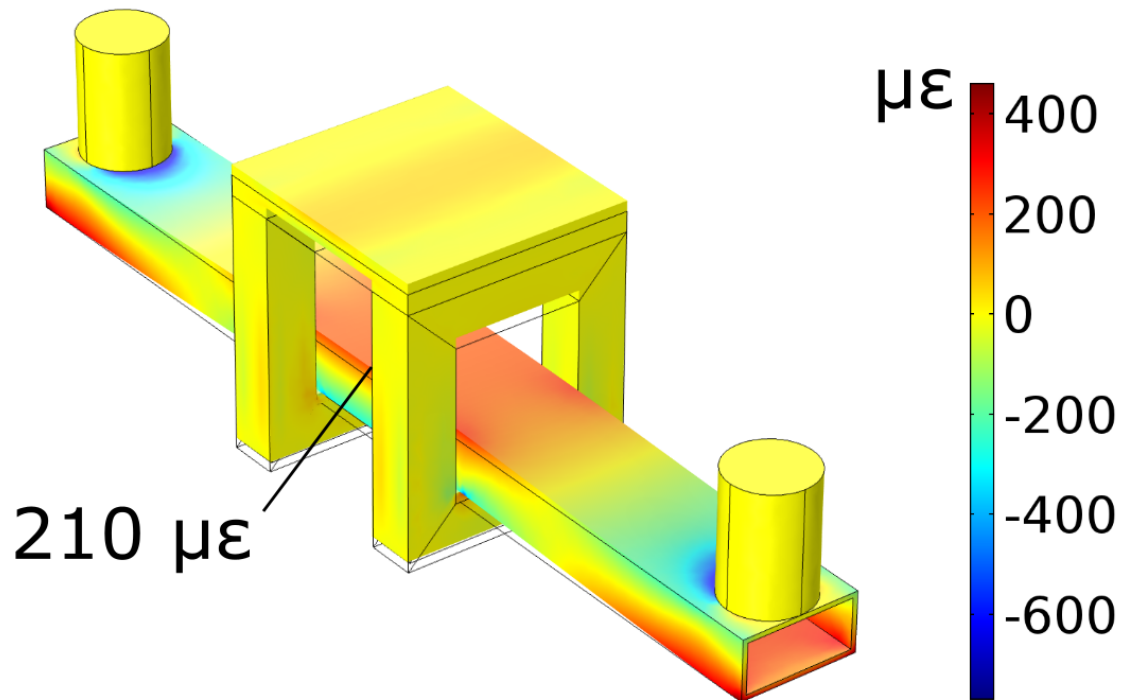
Figure 10.11: Strain distribution of steel specimen.

Beam model

As discussed in Section 7.3.2, the machine is designed to test beams of 10 cm width and height and 1 m length of any material. To validate both the force capability of the actuator and the simulations of stress levels in frame sections, it is possible to simulate and perform a single beam experiment for comparison. If strain levels witnessed in the beam during both cases are similar - this provides confidence that the frame FEM models are also accurate without the need to install more sensors. Also, it would be highly beneficial to carry out simulations prior to any experimentation in order to determine the maximum possible strain that can be subjected to the specimen. Any new specimen can then simply be inserted into the pre-existing model and expected strains will be known prior to experimentation.

A hollow steel beam of 1 m length, 120 mm width, 60 mm height and 5 mm thick walls was chosen as a test specimen. These dimensions were firstly inserted into the FEM software, results shown in Figure 10.11. A tension strain of 210 $\mu\epsilon$ was witnessed in the simulation at the mid-point of the steel specimen, as annotated. This will be validated against a future lab experiment on the same specimen.

10.5.4 Installation and commissioning procedure

Prior to lab experimentation, the machine requires installation and initial commissioning. This includes:
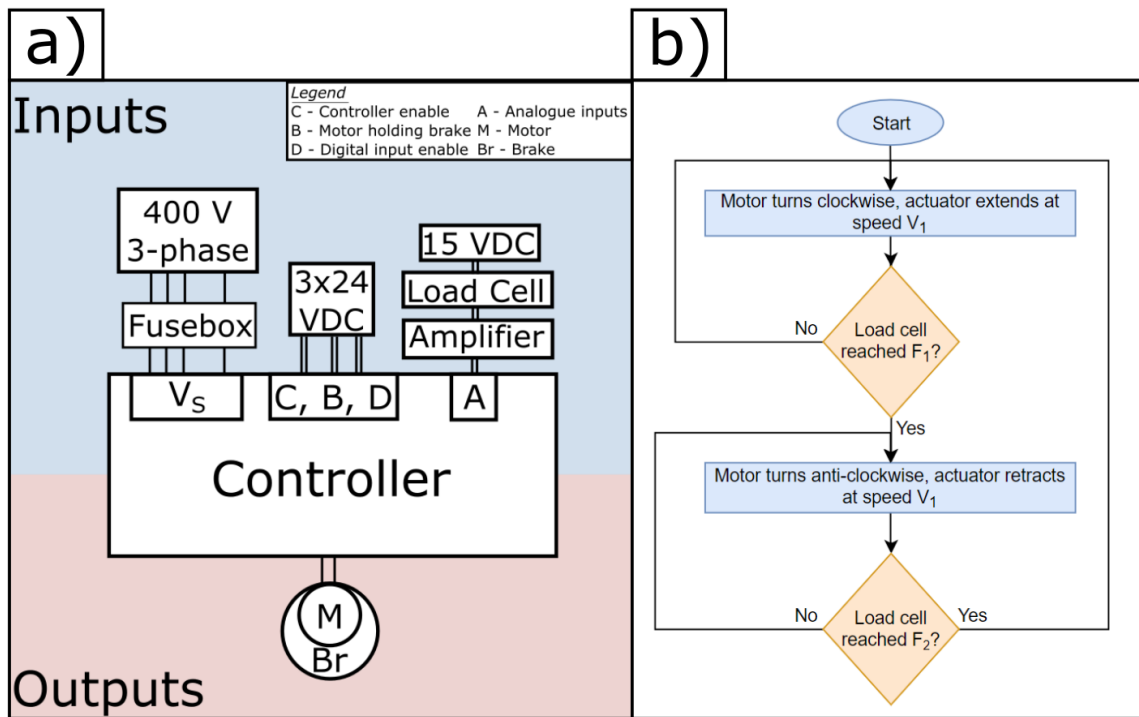
Figure 10.12: a) Circuit diagram of controller setup, b) flow chart of simple load cell feedback control program. F_1, F_2 and V_1 are force and speed values set by user.

- Physical fitting of the frame, actuator, controller and PC

- Wiring of controller, actuator, power supplies and load cell

- Programming of actuator control software

Following physical fitting, the electrical cabling is arranged according to Figure 10.12 a). At this stage the setup is simple, with extensive expandability in the form of analogue and digital inputs and outputs. 24 V DC supplies are required to power the controllers various features, such as the digital inputs/outputs, brake and to enable the controller itself. A 400 V 3-phase supply is used for powering the motor. A feedback loop containing the amplified load cell voltage is used to determine the direction of the motor. A program is created for simple trapezoidal movement dependent on set force limits, as illustrated in Figure 10.12 b). Three variables are set, compression force, F_1, tension force, F_2 and maximum speed, V_1. During either retraction or extension, the direction of motor rotation is reversed once the set force is reached. The actuator acceleration is also customisable but was set at the default value in this work. This simple program will allow initial testing of a specimen to ensure machine meets design requirements.

10.5.5 Testing results

Figure 10.13 shows the experimental set up of the steel beam and frame, similar to the simulation in Figure 10.11. The program shown in Figure 10.12 b) was run with the force limits, F_1 and F_2, set

at $\pm 25kN$ and an arbitrary speed. The sensor applied to the steel specimen was an epoxied fibre Bragg grating (FBG). The attachment method used was previously characterized and reported in [21]. Using the sensitivity of 0.89 $nm/m\epsilon$, the strain at the centre point of the steel specimen is shown in Figure 10.14, with a more detailed view of the cycle inserted. The frequency of cycles is controlled by the set speed of actuator extension. Maximum linear speed of actuator is quoted as 500 mm/s. In this test, speed was set at 50 mm/s which produced a cycle frequency of 0.5 Hz. Therefore, the maximum frequency of this load cycle is 5 Hz, although emphasis is made on the previous statement of requiring lower frequency when testing concrete. One must also consider the temperature of the controller and actuator, which may limit the cycle frequency further. An external fan is used to reduce motor temperature and was not required during the test in this work. Future work will investigate temperatures over an extended testing period. Load cell limits can be easily adjusted, allowing variable magnitude load cycles. Load and speed variables were varied during testing to ensure successful operation over the entire range. Overall the load cycle remains stable throughout, with a tension peak of ≈ 220 $\mu\epsilon$ which when compared to the simulation (210 $\mu\epsilon$) is in close agreement (+4.7%). The slight increase is most likely due to geometric differences of the specimen compared to the model - the corners are filleted for example. This was omitted in simulations to reduce computational requirements. It is clear the cycles are not sinusoidal or triangular from the insert: this will be improved on by modifying the program to include a smoother transition. The accuracy of the machine can be ascertained by analysing the spread at the peaks of the load cycle. In other words, the deviation over time of the peak loading. Extracting the peak values of each individual cycle in this test provided an accuracy of $\sigma_\epsilon/\mu_\epsilon = 0.74\%$ where σ_ϵ and μ_ϵ are the standard deviation and mean of strain peaks respectively. To compare this to similar machines is difficult as commercial machines would require significant customisation to provide similar load tests. One commercial machine was used in previous work [22] for tensile loading of a steel specimen. Results from this produced an accuracy value of 1.08% which is comparable to the machine in this work. Overall this simulation and testing provides confidence in the previous FEM simulations, the survivability of the frame and the overall design.
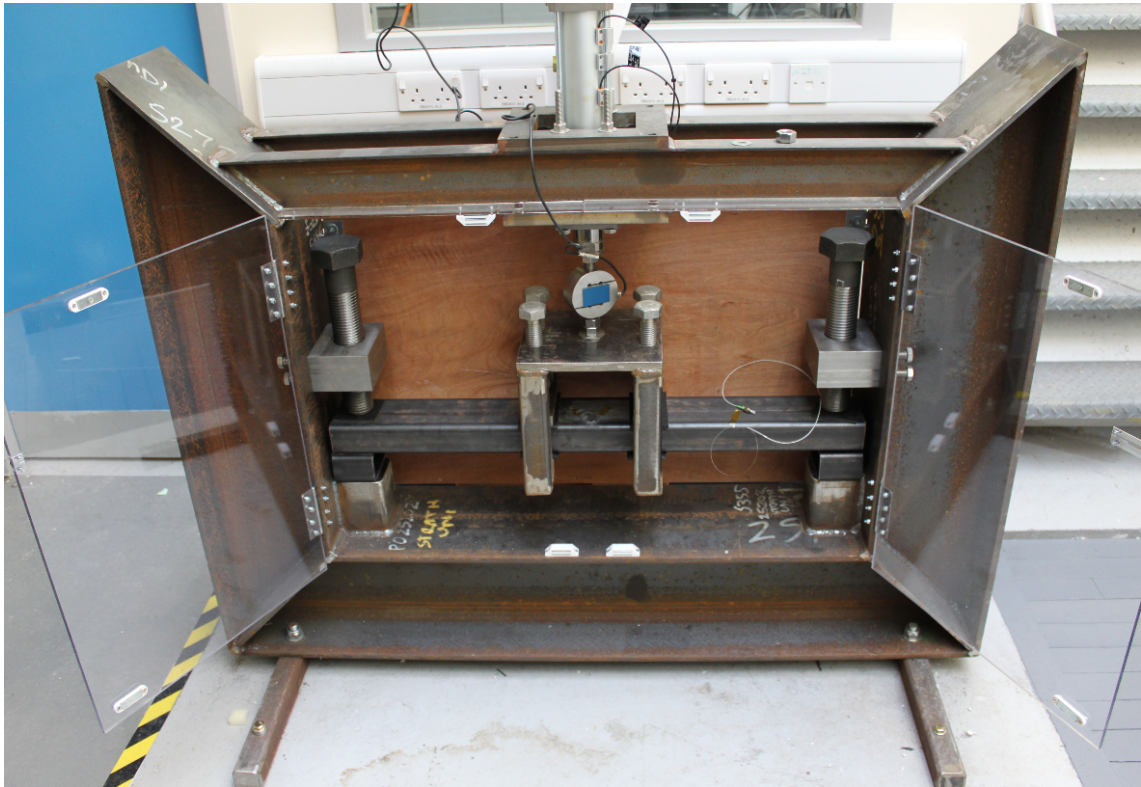
Figure 10.13: Experimental set up of test specimen.
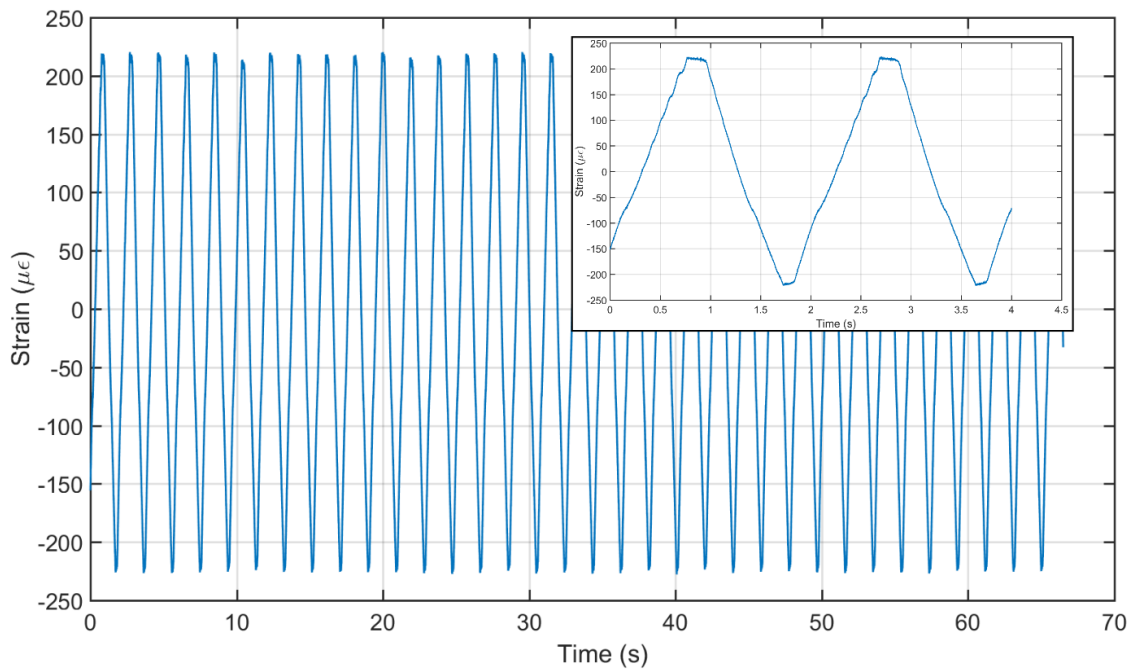
Figure 10.14: Strain at centre of steel beam, insert: detailed view of cycle.

10.6 Moving average

The moving average method for removing trends is perhaps the most simple to perform. As the name suggests, data is filtered through a window of size, N_m where the mean of the window is subtracted from the rest of the data. The window is then shifted and repeats for the entire window. Mathematically, this can be described for strain data by the following:

$$\epsilon_n(k) = \epsilon_0(k) - \frac{1}{N_m} \sum_{n=k}^{(N_m-1)+k} \epsilon_0(n) \tag{10.5}$$

where ϵ_n and ϵ_0 are the total strain and noise respectively for $k = p, p+1, ..., (N_m - 1)$ where p is the start point of the current window, $p = 0, 1, 2, ..., (M - N_m)$ for data of length M. To illustrate this, Figure 10.15 demonstrates a moving average window of 5 data points applied to 100 data points of strain data, the original data and extracted means are shown in a) with final noise shown in b). In this method, most data points will be shifted more than once, adjusting for changes based on surrounding data points.
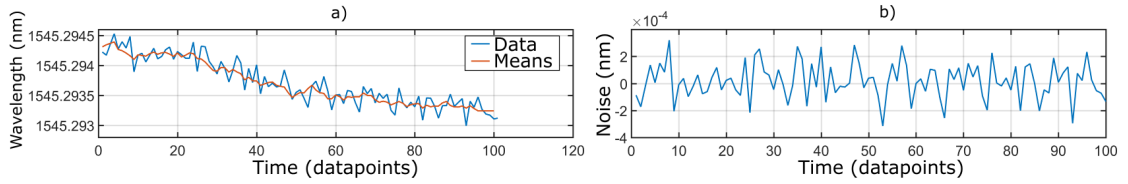
Figure 10.15: a) data and extracted means for each window, b) final noise.

10.7 Freeze cycles

From the seven cycles of supercooled water freezing, four showed apparent predictions when using DF. The additional three cycles are shown in Figure 10.16, using a window size of 10,000. Varying the window size does not significantly improve results. In cycle 3, the rise occurring after 40 minutes could possibly be a prediction indication; however, in the cycles with apparent predictions, the ACF indicator rose and did not drop until immediately after the freezing point. In this case, the the indicator rises and drops before freezing point and does not rise again. Similarly, during SA three of the cycles showed no apparent predictions, shown in Figure 10.17.
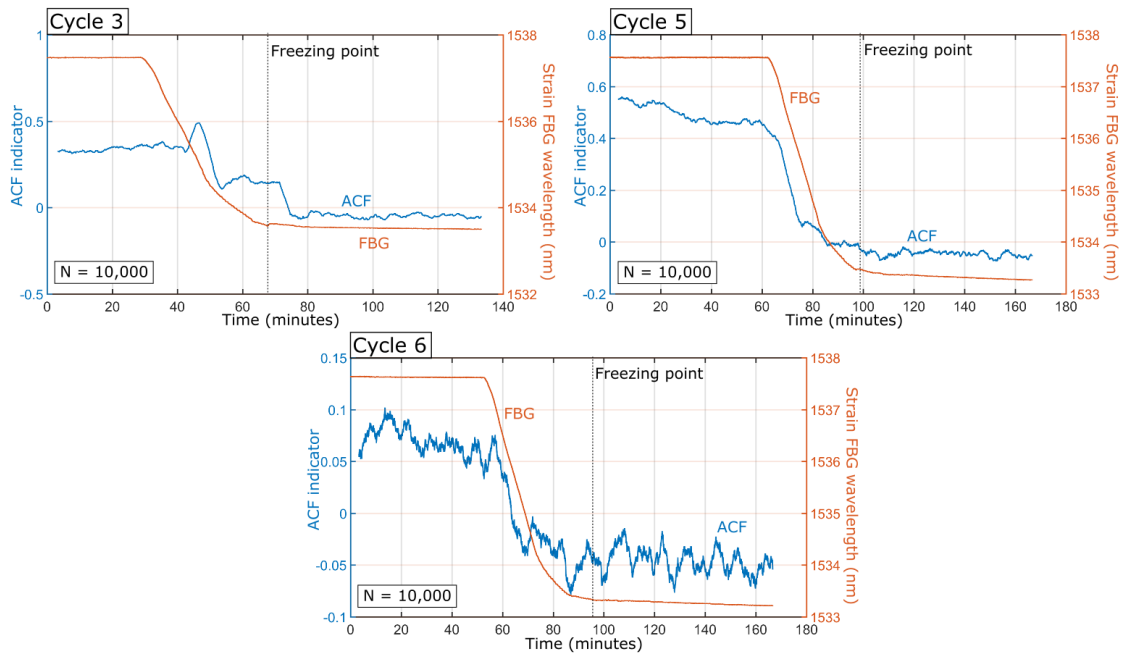
Figure 10.16: ACF of cycles 3, 5 and 6 which showed no apparent prediction.
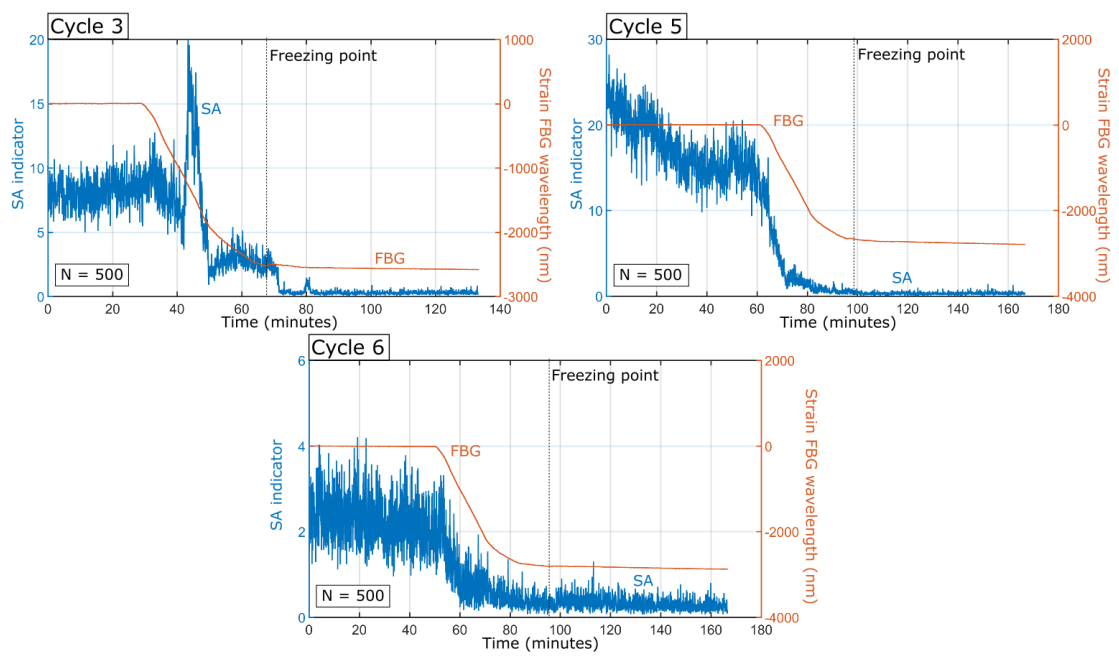
Figure 10.17: SA of cycles 3, 5 and 6 which showed no apparent prediction.

References

[1] Z. Daniele, G. Branko, and A. Sigrid, "Value of information: impact of monitoring on decision-making," *Structural Control and Health Monitoring*, vol. 21, no. 7, pp. 1043–1056, 2013. [Online]. Available: https://onlinelibrary.wiley.com/doi/abs/10.1002/stc.1631

[2] D. Agdas, J. A. Rice, J. R. Martinez, and I. R. Lasa, "Comparison of visual inspection and structural-health monitoring as bridge condition assessment methods," *Journal of Performance of Constructed Facilities*, vol. 30, June 2016.

[3] C. Cappello, D. Zonta, and B. Glisic, "Expected utility theory for monitoring-based decision-making," *Proceedings of the IEEE*, vol. 104, no. 8, pp. 1647–1661, Aug 2016.

[4] International Renewable Energy Agency, "Renewable capacity statistics 2017," 2017. [Online]. Available: http://www.irena.org/

[5] M. D. Reder, E. Gonzalez, and J. J. Melero, "Wind turbine failures - tackling current problems in failure data analysis," *Journal of Physics: Conference Series 753*, 2016. [Online]. Available: http://iopscience.iop.org/1742-6596/753/7/072027

[6] Elforsk, "Cracks in onshore wind power foundations - causes and consequences," 2011. [Online]. Available: http://www.caithnesswindfarms.co.uk/cracks.pdf

[7] M. Currie, "Gt2012-6 9065 Development of a Robust Structural Health Monitoring System for Wind Turbine Foundations," pp. 1–9, 2012.

[8] M. Currie, M. Saafi, C. Tachtatzis, and F. Quail, "Structural integrity monitoring of onshore wind turbine concrete foundations," *Renewable Energy*, vol. 83, pp. 1131–1138, 2015.

[9] F. Miceli, "Cracks in onshore wind turbines foundation," 2012. [Online]. Available: http://www.windfarmbop.com/tag/cracks-in-foundations/

[10] A. Kazem, E. Sharifi, F. K. Hussain, M. Saberi, and O. K. Hussain, "Support vector regression with chaos-based firefly algorithm for stock market price forecasting," *Applied Soft Computing*, vol. 13, no. 2, pp. 947 – 958, 2013. [Online]. Available: http://www.sciencedirect.com/science/article/pii/S1568494612004449

[11] Z. Hao, A. Aghakouchak, N. Nakhjiri, and A. Farahmand, "Global integrated drought monitoring and prediction system," *Scientific Data*, vol. 1, p. 140001, 03 2014. [Online]. Available: https://search.proquest.com/docview/1790110511?accountid=14116

[12] S. Kato, A. Homma, and T. Sakuma, "Easy screening for mild alzheimer's disease and mild cognitive impairment from elderly speech," *Current Alzheimer research*, vol. 15, 2018.

[13] J. Farmer and F. Lafond, "How predictable is technological progress?" *Research Policy*, vol. 45, 2016.

[14] C. Rodrigues, D. Inaudi, and B. Glisic, "Long-gauge fibre optic sensors: performance comparison and applications," *International journal of lifecycle performance engineering*, vol. 1, 2013.

[15] J. McAlorum, M. Perry, G. Fusiek, P. Niewczas, I. McKeeman, and T. Rubert, "Deterioration of cracks in onshore wind turbine foundations," *Engineering structures*, May 2018. [Online]. Available: https://www.sciencedirect.com/science/article/pii/S0141029617329644

[16] J. McAlorum, T. Rubert, G. Fusiek, P. Niewczas, and G. Zorzi, "Design and demonstration of a low-cost small-scale fatigue testing machine for multi-purpose testing of materials, sensors and structures," *Machines*, July 2018. [Online]. Available: http://www.mdpi.com/2075-1702/6/3/30

[17] J. McAlorum, I. McKeeman, M. Perry, L. Clayburn, and P. Niewczas, "Predicting freeze-thaw damage using tipping point analysis of strain data," *Fourth international conference on smart monitoring, assessment and rehabilitation of civil structures*, 2017.

[18] J. McAlorum, T. Rubert, G. Fusiek, I. McKeeman, L. Clayburn, M. Perry, and P. Niewczas, "Comparison of epoxy and braze-welded attachment methods for fbg strain guages," *16th International IEEE Sensors conference*, 2017.

[19] M. Perry, J. McAlorum, G. Fusiek, I. McKeeman, T. Rubert, and P. Niewczas, "Crack monitoring of operational wind turbine foundations," *MDPI Sensors*, vol. 17, 2017.

[20] M. Perry, G. Fusiek, P. Niewczas, T. Rubert, and J. McAlorum, "Wireless concrete strength monitoring of wind turbine foundations," *MDPI Sensors*, vol. 17, 2017.

[21] T. Rubert, "A decision support tool to assist with lifetime extension of wind turbines," *Renewable Energy*, vol. 120, 2017.

[22] G. Fusiek, T. Rubert, P. Niewczas, J. McAlorum, and M. Perry, "Preliminary characterization of metal-packaged fiber bragg gratings under fatigue loading," *2017 IEEE International Instrumentation and Measurement Technology Conference (I2MTC)*, 2017.

[23] A. Lacis, G. Schmidt, D. Rind, and R. Ruedy, "Atmospheric co2: Principal control knob governing earth's temperature," *Science*, vol. 330, 2010.

[24] The National Aeronautics and Space Administration (NASA), "Global climate change - carbone dioxide," 2017. [Online]. Available: https://climate.nasa.gov/vital-signs/carbon-dioxide/

[25] British Petroleum and Federal Institute for Geosciences and Natural Resources, "Coal reserves," 2016. [Online]. Available: https://www.bp.com/en/global/corporate/energy-economics/statistical-review-of-world-energy/coal/coal-reserves.html

[26] Renewable energy policy network for the 21st century, "Renewables 2017 global status report," 2017. [Online]. Available: http://www.ren21.net/status-of-renewables/global-status-report/

[27] M. M. A. Bhutta, N. Hayat, A. U. Farooq, Z. Ali, S. R. Jamil, and Z. Hussain, "Vertical axis wind turbine - a review of various configurations and design techniques," *Renewable and Sustainable Energy Reviews*, vol. 17, 2012.

[28] M. G. Molina and P. E. Mercado, "Modelling and control design of pitch-controlled variable speed wind turbines," in *Wind Turbines*, I. Al-Bahadly, Ed. Rijeka: IntechOpen, 2011, ch. 16. [Online]. Available: https://doi.org/10.5772/15880

[29] Enercon, "Enercon e-126." [Online]. Available: https://www.enercon.de/en/products/ep-8/e-126/

[30] Siemens, "Siemens swt-2.3-93." [Online]. Available: https://www.siemens.com/content/dam/internet/siemens-com/global/market-specific-solutions/wind/data_sheets/data-sheet-wind-turbine-swt-2.3-93.pdf

[31] Nordex, "Nordex n117/3600." [Online]. Available: http://www.nordex-online.com/en/produkte-service/wind-turbines/n1173600.html

[32] Vestas, "Vestas v117-4.2 mw." [Online]. Available: http://nozebra.ipapercms.dk/Vestas/Communication/Productbrochure/4MWbrochure/4MWProductBrochure/?page=12

[33] Doosan, "Doosan winds8000." [Online]. Available: http://www.doosanheavy.com/download/pdf/products/energy/DHI_Wind_Power_Brochure_Eng.pdf

[34] Goldwind, "Goldwind repower 48/750." [Online]. Available: https://en.wind-turbine-models.com/turbines/704-repower-48-750

[35] The USGS Water Science School, "Three gorges dam: The world's largest hydroelectric plant," 2016. [Online]. Available: https://water.usgs.gov/edu/hybiggest.html

[36] UK Government, "Energy consumption in the uk," 2017. [Online]. Available: https://www.gov.uk/government/collections/energy-consumption-in-the-uk

[37] B. L. Cohen, "Breeder reactors: A renewable energy source," *American journal of physics*, vol. 51, 1983.

[38] P. R. I. System, "France power generation," 2017. [Online]. Available: https://pris.iaea.org/PRIS/CountryStatistics/CountryDetails.aspx?current=FR

[39] Nuclear Energy Institute, "World nuclear generation and capacity statistics," 2017. [Online]. Available: https://www.nei.org/Knowledge-Center/Nuclear-Statistics/World-Statistics/World-Nuclear-Generation-and-Capacity

[40] Floating Power Plant. [Online]. Available: http://www.floatingpowerplant.com

[41] M. Hutchins, "Solar panels for worlds first combined hydro and floating pv project installed in portugal," 2017. [Online]. Available: https://www.pv-magazine.com/2017/03/03/panels-for-worlds-first-combined-hydro-floating-pv-project-installed-in-portugal/

[42] Kite Power Systems. [Online]. Available: http://www.kitepowersystems.com

[43] European commission, "Renewable energy progress report," 2017, Brussels.

[44] R. D. Woodson, *Concrete Portable Handbook.* Elsevier, 2011.

[45] Henan Fote Heavy Machinery Co., Ltd (FTM), "Rotary kiln." [Online]. Available: http://www.ftmmachine.com/products/cement-plant/53.html

[46] G. M. Productions, "Time lapse wind turbine foundations." [Online]. Available: www.goldenmedia.co.uk

[47] B. P. Hughes and B. Bahramian, "Some factors affecting the compressive strength of concrete," *Magazine of Concrete Research*, vol. 19, no. 60, pp. 165–172, 1967. [Online]. Available: https://doi.org/10.1680/macr.1967.19.60.165

[48] ACI Committee 224, "Cracking of concrete members in direct tension," 1993, Reapproved 1997, ACI224.2R-92.

[49] A. T. Zehnder, *Fracture mechanics.* Springer Netherlands, 2012, vol. 62.

[50] N. Perez, *Fracture Mechanics.* Springer, 2017.

[51] S. Rolfe, "Fracture and fatigue control in steel structures," *Engineering Journal / American institute of steel construction*, 1977.

[52] S. Kumar and S. Barai, *Concrete Fracture Models and Applications.* Springer, 2011.

[53] G. C. Sih and A. DiTommaso, *Fracture mechanics of concrete: Structural application and numerical calculation.* Martinus Nijhoff publishers, 1985.

[54] Z. P. Bažant and B. H. Oh, "Crack band theory for fracture of concrete," *Matériaux et Construction*, vol. 16, no. 3, pp. 155–177, May 1983. [Online]. Available: https://doi.org/10.1007/BF02486267

[55] B. Peeters, J. Maeck, and G. D. Roeck, "Vibration-based damage detection in civil engineering: excitation sources and temperature effects," *Smart materials and structures*, vol. 10, 2001.

[56] H. Sohn *et al.*, "A review of structural health monitoring literature: 1996-2001," 2004.

[57] G. W. Housner *et al.*, "Structural control: past, present and future," *Journal or Engineering Mechanics*, vol. 123, 1997.

[58] N. Stubbs, S. Park, C. Sikorsky, and S. Choi, "A global non-destructive damage assessment methodology for civil engineering structures," *International journal of systems science*, 2000.

[59] A. Rytter, "Vibrational based inspection of civil engineering structures," Ph.D. dissertation, Aalborg University, 1993.

[60] J. K. Vandiver, "Detection of structural failure on fixed platforms by measurement of dynamic response," *Proceedings pf the 7th annual offshore technology conference*, 1975.

[61] R. D. Begg, A. C. MacKenzie, C. J. Dodds, and O. Loland, "Structural integrity monitoring using digital processing of vibration signals," *Proceedings of the 8th Annual Offshore Technology Conference*, 1976.

[62] O. Loland and C. J. Dodds, "Experiences in developing and operating integrity monitoring system in the north sea," *Proceedings of the 8th Annual Offshore Technology Conference*, 1976.

[63] H. Crohas and P. Lepert, "Damage detection monitoring method for offshore platforms is field tested," *Oil and Gas Journal*, 1982.

[64] A. K. Pandey, M. Biswas, and M. M. Samman, "Damage detection from changes in curvature mode shapes," *Journal of Sound and Vibration*, 1991.

[65] J. Chance, G. R. Tomlinson, and K. Worden, "A simplified approach to the numerical and experimental modeling of the dynamics of a cracked beam," *Proceedings of the 12th International Modal Analysis Conference*, 1994.

[66] R. D. Adams, P. Cawley, C. J. Pye, and B. J. Stone, "A vibration technique for non-destructively assessing the integrity of structures," *Journal of Mechanical Engineering Science*, 1978.

[67] X. Wu, J. Ghaboissi, and J. H. Garrett, "Use of neural networks in detection of structural damage," *Computers and Structures*, 1992.

[68] M. F. Elkordy, K. C. Chang, and G. C. Lee, "A structural damage neural network monitoring system," *Microcomputers in Civil Engineering*, 1994.

[69] M. Kaouk and D. Zimmerman, "Structural damage assessment using a generalized minimum rank perturbation theory," *AIAA*, 1994.

[70] A. C. 318, "Building code requirements for structural concrete," ACI 318-95, section 8.5.

[71] M. Abdo, *Structural health monitoring, history, applications and future. A review book.* Open Science, 2014.

[72] J. Wilson and T. Kenny, *Sensor Technology Handbook.* Elsevier, 2005.

[73] B. Glisic, "Influence of the gauge length on the accuracy of long-gauge sensors employed in monitoring of prismatic beams," *Measurement Science and Technology*, vol. 22, no. 3, p. 35206, 2011.

[74] S. A. Neild, M. S. Williams, and P. McFadden, "Development of a vibrating wire strain gauge for measuring small strains in concrete beams," *Strain*, 2005.

[75] B. Glisic and D. Inaudi, *Fibre Optic Methods for Structural Health Monitoring.* John Wiley & Sons, 2007.

[76] Y. Rao, "In-fibre Bragg grating sensors," *Measurement Science and Technology*, vol. 8, no. 4, pp. 355–375, 1997. [Online]. Available: http://dx.doi.org/10.1088/0957-0233/8/4/002

[77] K. O. Hill and G. Meltz, "Fiber bragg grating technology fundamentals and overview," *Journal of Lightwave Technology 15(8)*, 1997.

[78] P. Orr, P. Niewczas, A. DyÅ›ko, and C. Booth, "Fbg-based fibre-optic current sensors for power systems protection: Laboratory evaluation," *Universities Power Engineering Conference (UPEC)*, 2009.

[79] G. Meltz, W. Morey, and W. Glenn, "Formation of bragg gratings in optical fibres by transverse holographic method," *Optics Letters*, vol. 14, 1989.

[80] R. Kashyap, *Fibre Bragg Gratings*, 2010, second Edition.

[81] A. Khare and J. Singh, "Design and study of chirped fibre bragg grating for sensing of hazardous gases," *International journal of computer applications*, 2011.

[82] Y. Okabe, R. Tsuji, and N. Takeda, "Application of chirped fiber bragg grating sensors for identification of crack locations in composites," *Composites Part A: Applied Science and Manufacturing*, vol. 35, 2004.

[83] T. Gao, A. Ivanov, C. Chen, and J. Albert, "Temperature-independent tilted fiber grating vibration sensor based on cladding-core recoupling," *Optics Letters*, vol. 33, 2008.

[84] R. Kashyap, R. Wyatt, and C. R. J., "Wideband gain flattened erbium fiber amplifier using a photosensitive fiber blazed grating," *Electronics letters*, vol. 29, 1993, pp: 154-156.

[85] C. Caucheteur, C. Chen, J. Albert, and P. Megret, "Use of weakly tilted fiber bragg gratings for strain sensing purposes," *Optical Sensors*, 2008.

[86] J. Albert, L. Shao, and C. Caucheteur, "Tilted fiber bragg grating sensors," *Laser and photonics reviews*, 2013.

[87] S. Sengupta and S. K. Ghorai, "Design of superstructure fiber bragg grating with efficient mode coupling for simultaneous strain and temperature measurement with low cross-sensitivity," *IEEE Sensors*, vol. 16, 2016.

[88] T. Erdogan, "Fiber grating spectra," *Journal of Lightwave Technology*, 1997.

[89] A. D. Kersey, M. A. Davis, H. J. Patrick, M. LeBlanc, K. P. Koo, C. Askins, M. A. Putnam, and E. J. Friebele, "Fiber grating sensors," *Journal of lightwave technology*, vol. 15, 1997.

[90] A. D. Kersey, T. A. Berkoff, and W. W. Morey, "High-resolution fibre-grating based strain sensor with interferometric wavekength-shift detection," *Electronics letters*, vol. 28, 1992.

[91] M. Kreuzer, "Strain measurement with fiber bragg grating sensors," S2338-1.0 e; HBM GmbH: Darmstadt, Germany, 2006.

[92] D. Inaudi, N. Casanova, S. Vurpillot, P. Kronenberg, G. Martinola, G. Steinmann, and M. J. F., "Sofo: Structural monitoring with fiber optic sensors," *FIB, Monitoring and safety evaluation of existing concrete structures*, 1999, vienna, Austria.

[93] D. Inaudi, "Sofo sensors for static and dynamic measurements," *1st FIG International Symposium on Engineering Surveys for Construction Works and Structural Engineering*, 2004.

[94] J. Ranz *et al.*, "Monitoring of freeze-thaw cycles in concrete using embedded sensors and ultrasonic imaging," *MDPI Sensors*, 2014.

[95] C. N. Sathyanarayana, S. Raja, and R. H. M., "Procedure to use pzt sensors in vibration and load measurements," *Smart materials research*, vol. 2013, 2013.

[96] T. Stepinski, T. Uhl, and W. Staszewski, *Advanced structural damage detection: from theory to engineering application.* John Wiley & sons, 2013.

[97] F.-K. Chang, *Structural Health Monitoring 2000.* Technomic Publishing Company, Inc, 2000, proceedings of the 2nd International Workshop on Structural Health Monitoring, Stanford University, Stanford, CA.

[98] Brannan, "Liquid in glass laboratory thermometers." [Online]. Available: https://www.brannan.co.uk/laboratory-thermometers

[99] Lascar, "Easylog el-usb-2-lcd." [Online]. Available: https://www.lascarelectronics.com/easylog-data-logger-el-usb-2-lcd/

[100] Z. Zhou *et al.*, "Smart film for crack monitoring of concrete bridges," *Structural health monitoring*, 2010.

[101] N. A. Hoult, P. R. A. Fidler, P. G. Hill, and C. R. Middleton, "Long-term wireless structural health monitoring of the ferriby road bridge," *Journal of Bridge Engineering*, 2010.

[102] H. Lima *et al.*, "Structural health monitoring of the church of Santa Casa da MisericOrdia of Aveiro using FBG sensors," *IEEE Sensors Journal*, vol. 8, no. 7, pp. 1236–1242, 2008.

[103] J. M. Ko and Y. Q. Ni, "Structural health monitoring and intelligent vibration control of cable-supported bridges: Research and application," *KSCE Journal of Civil Engineering 7(6):701-716*, 2003.

[104] T. H. T. Chan, L. Yu, H. Y. Tam, Y. Q. Ni, S. Y. Liu, W. H. Chung, and L. K. Cheng, "Fiber Bragg grating sensors for structural health monitoring of Tsing Ma bridge: Background and experimental observation," *Engineering Structures*, vol. 28, no. 5, pp. 648–659, 2006.

[105] F. Ansari, *Sensing issues in civil structural health monitoring.* Springer, Netherlands, 2005.

[106] C. Zhou, K. Li, and X. Pang, "Geometry of crack network and its impact on transport properties of concrete," *Cement and Concrete Research*, vol. 42, no. 9, pp. 1261–1272, 2012.

[107] J. M. W. Brownjohn, M. Bocciolone, A. Curami, M. Falco, and A. Zasso, "Humber bridge full-scale measurement campaigns 1990-1991," *Journal of Wind Engineering and Industrial Aerodynamics*, vol. 52, no. C, pp. 185–218, 1994.

[108] M. Nagasawa, H. Kinuhata, H. Koizuka, and K. Miyamoto, "Mechanical fatgiue of epoxy resin," *Journal of Materials Science*, vol. 30.

[109] Y. Ni, Y. Xia, and X. Ye, "Structural health monitoring of a tall building with huge floating platform," *Advances in Science and Technology*, September 2012.

[110] C. P. Fritzen and K. Bohle, "Application of model-based damage identification to a seismically loaded structure," *Smart materials and structures*, 2001.

[111] W. K. *et al.*, "Cost action f3 on structural dynamics: benchmarks for structural health monitoring," *Proceedings of the international conference on noise and vibration engineering*, 2002.

[112] S. Hunt and I. Hebden, "Validation of the eurofighter typhoon structural health and usage monitoring system," *Smart materials and structures*, September 2000.

[113] Daniele Inaudi; Branko Glisic, "Long-Range Pipeline Monitoring by Distributed Fiber Optic Sensing," *Journal of Pressure Vessel Technology*, vol. 132, no. 011701, p. 9, 2010.

[114] B. Han, X. Yu, and J. Ou, "Chapter 1 - structures of self-sensing concrete," in *Self-Sensing Concrete in Smart Structures*, B. Han, X. Yu, and J. Ou, Eds. Butterworth-Heinemann, 2014, pp. 1 – 11. [Online]. Available: https://www.sciencedirect.com/science/article/pii/B9780128005170000010

[115] B. Zhang *et al.*, "Crack width monitoring of concrete structures based on smart film," *Smart Materials and Structures*, vol. 23, March 2014.

[116] M. J. Blanch and A. G. Dutton, "Acoustic emission monitoring of field tests of an operating wind turbine," *Key engineering materials*, 2003.

[117] A. Dutton *et al.*, "Acoustic emission condition monitoring of wind turbine rotor blades:laboratory certification testing to large scale in-service deployment," *Proceedings of the 2001 european wind energy conference*.

[118] D. Tcherniak and L. L. Molgaard, "Vibration-based shm system: Application to wind turbine blades," *Journal of physics: Conference series*, 2015.

[119] Southern cross drones, "Pro-drone automated wind turbine inspection." [Online]. Available: http://www.southerncrossdrones.com/pro-drone-wind-turbine-blades-inspection.html

[120] R. suddath photography, "Wind turbine condition monitoring." [Online]. Available: http://www.robertsuddarth.com/drone-photography/services/wind-turbine-condition-monitoring/

[121] Fraunhofer, "Inspecting rotor blades with thermography and acoustic monitoring." [Online]. Available: https://www.fraunhofer.de/en/press/research-news/2017/december/inspecting-rotor-blades-with-thermography-and-acoustic-monitoring.html

[122] B. Wondra, M. Botz, and C. U. Grosse, "Wireless monitoring of structural components of wind turbines including tower and foundations," *Journal of physics: Conference series*, 2016.

[123] B. Kerkez, S. D. Glaser, R. C. Bales, and M. W. Meadows, "Design and performance of a wireless sensor networkfor catchment-scale snow and soil moisture measurements," *Water resources research*, 2012.

[124] H. Kawai, K. Michishita, and A. Deguchi, "Design wind loads on a wind turbine for strong wind," *In proceedings of the BBAA VI International Colloquium on: Bluff bodies aerodynamics and applications*, July 2008.

[125] C. Montavon, I. Jones, C. Staples, C. Strachan, and I. Gutierrez, "Practical issues in the use of cfd for modelling wind farms," *European wind energy conference*, January 2009.

[126] C. Woude and S. Narasimhan, "Dynamic structural modelling of wind turbines using comsol multiphysics," *Proceedings of the COMSOL Conference*, October 2010.

[127] J. Irwin, "A theoretical variation of the wind profile power-law exponent as a function of surface roughness and stability," *Atmosphere Environment*, 1979.

[128] T. Burton, N. Jenkins, D. Sharpe, and E. Bossanyi, *Wind Energy Handbook*, 2nd ed. Wiley, 2011.

[129] P. Brondsted and R. Nijssen, "Advances in wind turbine blade design and materials," *Elsevier*, 2013.

[130] T. Barszcz and R. Randall, "Application of spectral kurtosis for detection of a tooth crack in the planetary gear of a wind turbine," *Mechanical Systems and Signal Processing, vol. 23, no. 4, pp. 1352-1365*, 2009.

[131] C. Loraux and E. Brühwiler, "The use of long term monitoring data for the extension of the service duration of existing wind turbine support structures," *Journal of Physics: Conference Series 753*, 2016. [Online]. Available: http://iopscience.iop.org/1742-6596/753/7/072023

[132] S. G. Taylor, K. Farinholt, M. Choi, H. Jeong, J. Jang, G. Park, J.-R. Lee, and M. D. Todd, "Incipient crack detection in a composite wind turbine rotor blade," *Journal of Intelligent Material Systems and Structures 2014, Vol. 25(5) 613â€"620*, 2013.

[133] A. P. Sarbach, "Fallen turbine," 2002. [Online]. Available: http://www.windaction.org/posts/6014-fallen-turbine#.W5fEFehKjcs

[134] C. News, "Nearly all 22 turbine foundations cracked," 2011. [Online]. Available: https://ontario-wind-resistance.org/2011/02/03/nearly-all-22-turbine-foundations-cracked/

[135] K. Audenaert, G. D. Schutter, L. Marsavina, and V. Boel, "Influence of cracks and crack width on penetration depth of chlorides in concrete," *European Journal of Environmental and Civil Engineering*, 2009.

[136] C. Kurkjian, J. Krause, and M. Matthewson, "Strength and fatigue of silica optical fibers," *Journal of lightwave technology*, 1989.

[137] S. Adhikari and S. Bhattacharya, "Dynamic analysis of wind turbine towers on flexible foundations," *Shock and Vibration*, 2012.

[138] J. Crisp and B. J. Elliott, *Introduction to Fiber Optics*, 3rd ed., October 2005.

[139] J. Bernardo and A. Smith, *Bayesian theory*, 1st ed. Wiley.

[140] M. W. Vanik, J. L. Beck, and S. K. Au, "Bayesian probabilistic approach to structural health monitoring," *Journal of Engineering Mechanics*. [Online]. Available: https://doi.org/10.1061/(ASCE)0733-9399(2000)126:7(738)

[141] K. Gallo, R. Hale, D. Tarpley, and Y. Yu, "Evaluation of the relationship between air and land surface temperature under clear- and cloudy-sky conditions," *Journal of applied meteorology climatology*, 2010.

[142] J. Tempel and D. Molenaar, "Wind turbine structural dynamics â€" a review of the principles for modern power generation, onshore and offshore," *Wind engineering*, vol. 26, 2002.

[143] ACI Committee 355, "State-of-the-Art Report on Anchorage to Concrete: ACI 355.1R-91," 1991.

[144] J. Breen, E. Eichinger, and W. Fuchs, "Anchoring to concrete: The new ACI approach," *International symposium on connections between steel and concrete*, 2001, stuttugar, Germany, pp. 31-44.

[145] M. Johnson, H. Lew, and L. Phan, "Literature review of post-installed anchorage in concrete," *U.S. Dept. of Commerce, National Bureau of standards*, 1988.

[146] M. Perry, G. Fusiek, I. McKeeman, P. Niewczas, and M. Saafi, "Metal-packaged fibre Bragg grating strain sensors for surface-mounting onto spalled concrete wind turbine foundations," vol. 9634, p. 963466, 2015. [Online]. Available: http://proceedings.spiedigitallibrary.org/proceeding.aspx?doi=10.1117/12.2190188

[147] G. Fusiek, M. Perry, and M. Johnston, "Deformation monitoring in prestessing tendons using fibre Bragg gratings encapsulated in metallic packages," *23rd International Conference on Optical Fibre Sensors*, vol. 9157, pp. 14–17, 2014.

[148] I. McKeeman, G. Fusiek, M. Perry, M. Johnston, M. Saafi, P. Niewczas, M. Walsh, and S. Khan, "First-time demonstration of measuring concrete prestress levels with metal packaged fibre optic sensors," *Smart materials and structures*, vol. 25, 2016.

[149] M. Perry, P. Niewczas, M. Johnston, K. Cook, and J. Canning, "Induction brazing of type-I fiber bragg gratings into kovar ferrules exploiting curie transition," *IEEE Sensors Journal*, vol. 13, no. 2, pp. 816–823, 2013.

[150] Met Office UK, "The climate of the united kingdom and recent trends," 2009. [Online]. Available: https://ukcip.ouce.ox.ac.uk/wp-content/PDFs/UKCP09_Trends.pdf

[151] A. Wexlar and S. Hasegawa, "Relative humidity-temperature relationships of some saturated salt solutions in the temperature range 0° to 50° c," *Journal of research of the national bureau of standards*, vol. 53, no. 1, 1954.

[152] Y. L. Lee, "Fatigue Damage Theories," in *Fatigue Testing and Analysis*, 2005.

[153] R. I. Stephens, A. Fatemi, R. R. Stephens, and H. O. Fuchs, *Metal Fatigue in Engineering*, 2nd ed.   John Wiley and Sons, 2000.

[154] Y.-L. Lee, P. Jwo, H. Richard, and M. Barkey, *Fatigue Testing and Analysis: Theory and Practice*, revised ed.   Butterworth-Heinemann, 2011.

[155] S. Suresh, *Fatigue of materials*.   Cambridge: Cambridge University Press, 1994.

[156] H. A. Richard and M. Sander, *Fatigue Crack Growth: Detect - Assess - Avoid.*   Springer, 2016.

[157] Y. Kondo, "Fatigue Under Variable Amplitude Loading," in *Comprehensive Structural Integrity*, B. L. Ritchie and Y. Murakami, Eds.   Elsevier, 2003.

[158] G. P. Tilly, "Fatigue of Steel Reinforcement Bars in Concrete: a Review," *Fatigue and Fracture of Engineering Materials and Structures*, vol. 2, no. 3, pp. 251–268, 1979. [Online]. Available: http://doi.wiley.com/10.1111/j.1460-2695.1979.tb01084.x

[159] J. Schijve, *Fatigue of structures and materials*, 2009.

[160] British standards institution, *Guide to fatigue design and assessment of steel products. BS 7608:2014*, 2014.

[161] S. Lee, "Stress analysis and design for a structural fatigue testing machine Self-Heating-Induced Deterioration of Electromechanical Performance in Polymer-Supported Metal Films for Flexible Electronics," *Journal of Mechanical Science and Technology KSME Journal*, vol. 1015, no. 2, pp. 115–124, 1991. [Online]. Available: https://www.researchgate.net/publication/227230167

[162] M. K. Vincent, V. Varghese, and S. Sukumaran, "Fabrication and Analysis of Fatigue Testing Machine," *The International Journal Of Engineering And Science*, pp. 2319–1813. [Online]. Available: www.theijes.com

[163] O. P. Bhatkar, S. Y. Mhatre, A. S. Pilankar, V. S. Desai, and M. J. Katlikar, "Design and fabrication of combined fatigue testing machine."

[164] E. Pach, I. Korin, J. P. Ip Na, and C. E. Pach, "Simple Fatigue Testing Machine for Fiber-Reinforced Polymer Composite," *Experimental techniques*, no. 36.

[165] Cooper technology, "Large hydraulic four point bending machine." [Online]. Available: https://cooper.co.uk/shop/asphalt-testing/large-hydraulic-four-point-bending-machine/

[166] Instron, "Dynamic and fatigue testing systems." [Online]. Available: http://www.instron.us/en-us/products/testing-systems/dynamic-and-fatigue-systems

[167] W. C. Young and R. G. Budynas, *Roark's formulas for stress and strain*, 7th ed. McGraw-Hill, 2002.

[168] Lenze, "9400 series servo inverters." [Online]. Available: http://www.lenze.com/en-gb/products/frequency-and-servo-inverters/frequency-and-servo-inverters-for-control-cabinet-installation/9400-series-servo-inverters/

[169] N. physics laboratory, "Moving existing reactive structural health monitoring systems towards a preventive model," February 2017, web news, available: https://phys.org/news/2017-02-reactive-health.html.

[170] B. L. Bowerman, T. O'Connell, and E. S. Murphree, *Regression Analysis: Unified Concepts, Practical Applications, and Computer Implementation.* Business expert press, 2015.

[171] BBC News, "Can we teach robots ethics?" 2017, magazine article. [Online]. Available: https://www.bbc.co.uk/news/magazine-41504285

[172] Cade Metz, New York Times, "How driverless cars see the world around them," 2018. [Online]. Available: https://www.nytimes.com/2018/03/19/technology/how-driverless-cars-work.html

[173] E. Alpaydin, *Introduction to machine learning*, 3rd ed. MIT Press, 2014.

[174] M. Perry, V. Livina, and P. Niewczas, "Tipping point analysis of cracking in reinforced concrete," *Smart materials and structures*, 2016.

[175] V. Dakos *et al.*, "Methods for detecting early warnings of critical transitions in time series illustrated using simulated ecological data," *PLoS ONE*, vol. 7, 2012, https://doi.org/10.1371/journal.pone.0041010.

[176] A. R. Ives and D. Vasilis, "Detecting dynamical changes in nonlinear time series using locally linear state-space models," *Ectosphere*, vol. 3, 2012.

[177] V. N. Livina, G. Lohmann, M. Mudelsee, and T. M. Lenton, "Forecasting the underlying potential governing the time series of a dynamical system," *Physica A: Statistical Mechanics and its Applications*, vol. 392, no. 18, pp. 3891–3902, 2013.

[178] V. N. Livina and T. M. Lenton, "A modified method for detecting incipient bifurcations in a dynamical system," *Geophysical Research Letters*, vol. 34, no. 3, 2007.

[179] V. N. Livina, P. D. Ditlevsen, and T. M. Lenton, "An independent test of methods of detecting system states and bifurcations in time-series data," *Physica A: Statistical Mechanics and its Applications*, vol. 391, no. 3, pp. 485–496, 2012. [Online]. Available: http://dx.doi.org/10.1016/j.physa.2011.08.025

[180] J. Prettyman, T. Kuna, and V. Livina, "A novel scaling indicator of early warning signals helps anticipate tropical cyclones," *Europhysics letters*, vol. 121, 2018.

[181] V. N. Livina, F. Kwasniok, and T. M. Lenton, "Potential analysis reveals changing number of climate states during the last 60 kyr," *Climate of the Past Discussions*, vol. 5, no. 5, pp. 2223–2237, 2010.

[182] A. Gholaminejad and R. Hosseini, "A Study of Water Supercooling," *Journal of Electronics Cooling and Thermal Control*, vol. 3, no. March, pp. 1–6, 2013. [Online]. Available: http://dx.doi.org/10.4236/jectc.2013.31001$\delimiter"026E30F$nhttp://www.scirp.org/journal/jectc

[183] K. Li, *Durability design of concrete structures - Phenomena, Modeling, and Practice*, 1st ed. John Wiley & Sons, 2016.

[184] T. A. Harrison, B. V. Brown, J. D. Dewar, and B. B. Brown, *Freeze-thaw resisting concrete - its achievement in the UK*. Construction Industry Research & Information Association, 2001.

[185] R. Cattin *et al.*, "Evaluation of ice detection systems for wind turbines," 2015. [Online]. Available: https://www.vgb.org/vgbmultimedia/392_Final+report-p-10476.pdf

[186] M. Safiuddin, "Concrete damage in field conditions and protective sealer and coating systems," *Coatings*, 2017.

[187] Z. Bochnicek, "Experimental study of sudden solidification of supercooled water," *Physics education*, vol. 49, 2014.

[188] "Nucleation: theory and applications to protein solutions and colloidal suspensions," *Journal of physics: condensed matter*, 2007.

[189] S. Stott and K. J. O. M., "Visualization of intracellular ice formation using high-speed video cryomicroscopy," *Cryobiology*, 2009.

[190] T. L. Anderson, *Fracture mechanics: fundamentals and applications*, 3rd ed. CRC Press, 2005.

[191] T. Plachy *et al.*, "Monitoring of mechanical properties evolution of the cast gypsum," *Procedia Engineering*, vol. 48, 2012.

[192] G. Vekinis, M. F. Ashby, and P. W. R. Beaumont, "Plaster of paris as a model material for brittle porous solids," *Journal of Materials Science*, 1993.

[193] A. Garaga and G. M. Latha, "Intelligent prediction of the stressâ€"strain response of intact and jointed rocks," *Computers and Geotechnics*, vol. 37, no. 5, pp. 629 – 637, 2010. [Online]. Available: http://www.sciencedirect.com/science/article/pii/S0266352X10000455

[194] "HILTI HIT-RE 500-SD epoxy mortar," data sheet available. [Online]. Available: https://www.hilti.com/anchor-fasteners/injectable-adhesive-anchors/r3783

[195] "HILTI HIT-RE 500 V3 epoxy mortar," data sheet available. [Online]. Available: https://www.hilti.co.uk/anchor-fixings/injectable-adhesive-anchors/r4929903#nav%2Fclose

[196] Hilti, "Anchor fastening technical guide," 2011. [Online]. Available: https://www.buildsite.com/pdf/hilti/Hilti-2011-Anchor-Fastening-Technical-Guide-B25981.pdf

[197] D. M. Considine and G. D. Considine, *Standard Handbook of Industrial Automation.* Springer, 1986.

[198] P. Lynwander, *Gear Drive Systems: Design and Application.* CRC Press, 1983.

[199] British standards. BS EN ISO 5817:2014, *Welding - Fusion-welded joints in steel, nickel, titanium and their alloys (beam welding excluded) - Quality levels for imperfections*, 2014.

[200] P. Kucharczyk, A. Rizos, S. Münstermann, and W. Bleck, "Estimation of the endurance fatigue limit for structural steel in load increasing tests at low temperature," *Fatigue and Fracture of Engineering Materials and Structures*, 2012.

[201] "EN 1993-1-9: Eurocode 3: Design of steel structures - Part 1-9: Fatigue."